UNIVERSIDADE DE LISBOA
FACULDADE DE CIÊNCIAS

Lithospheric structure and wave propagation below the Gloria fault, NE Atlantic, from ocean bottom seismic data

"Documento Definitivo"

Doutoramento em Ciências Geofísicas e da Geoinformação
Especialidade em Geofísica

Juan Ignacio Pinzón López

Tese orientada por:
Professora Doutora Susana Custódio
Professora Doutora Graça Silveira
Professor Doutor Frank Krüger

Documento especialmente elaborado para a obtenção do grau de doutor

2022

UNIVERSIDADE DE LISBOA

FACULDADE DE CIÊNCIAS

Lithospheric structure and wave propagation below the Gloria fault, NE Atlantic, from ocean bottom seismic data

Doutoramento em Ciências Geofísicas e da Geoinformação

Especialidade em Geofísica

Juan Ignacio Pinzón López

Tese orientada por:

Professora Doutora Susana Custódio

Professora Doutora Graça Silveira

Professor Doutor Frank Krüger

Júri:

Presidente:

- Doutor João Manuel de Almeida Serra, Professor Catedrático e Presidente do Departamento de Engenharia Geográfica, Geofísica e Energia da Faculdade de Ciências da Universidade de Lisboa.

Vogais:

- Doutora Ana Margarida Godinho Ferreira, Professor Faculty of Mathematical and Physical Sciences da University College London;
- Doutor Martin Schimmel, Senior Researcher Geosciences Barcelona (Geo3BCN – SCIC);
- Doutor Frank Krüger, Senior Researcher Instituto of Geosciences da University of Postdam (orientador);
- Doutor João Daniel Casal Duarte, Professor Auxiliar Facultade de Ciências da Universidade de Lisboa.

Documento especialmente elaborado para a obtenção do grau de doutor

Documento financiado pela Fundação para a Ciência e a Tecnologia
(SFRH/BD/135069/2017)

2022

"Imagination is more important than knowledge. Knowledge is limited. Imagination encircles the world"

Albert Einstein

Acknowledgements

This work presented in this thesis was developed over the past five years in the Instituto Dom Luiz, at the Faculty of Science of the University of Lisbon. This would never have been possible without the unconditional help of the following people.

I will always be grateful to my supervisor Professora Susana Custódio for trusting me and for always being aware of my progress, giving me ideas, tools and for her friendship throughout this thesis. I also thank my supervisor Professora Graça Silveira for her unconditional help throughout my thesis in every way, from the emotional to the intellectual part and also for her friendship. I also thank Professor Luis Matias who, although he is not my official advisor, has always been attentive to my progress, contributing ideas and pushing me to get the best out of me. Finally, I thank my supervisor Professor Frank Krüger because also despite the distance he was always in our meetings contributing excellent ideas on how to continue with this thesis. To all of you my sincere gratitude for letting me work with you.

I thank with all my soul to God and my family, especially my mother who is now in heaven and unfortunately could not see the end of this thesis. To her who always supported me unconditionally throughout my entire life and without her I would not be here. To my mother, this work is for you. To my father who inculcate in me since I was a child to follow the path of study to be better people and contribute knowledge to the society. Also, without his support I would not be finishing my Ph.D. To my brothers Francisco and Liliana who always told me that they were proud to see me here doing a PhD, I could not have had better brothers. To my grandparents Catalina and Lorenzo who were also like parents to me and who always asked me how my work was going and who taught us that to get ahead we must be united as a family. I am very fortunate to have a very united family and that even though some very important members of the family are no longer here, we continue to support each other. To Carmen who is also like a mother to me and who always supported me a lot in finishing my thesis.

To my girlfriend Ilse who has always supported me and has been patient in the good and bad times since I came from Mexico. Thank you for being by my side all these years.

To all my friends from the faculty: Martin, David, Inês, Hannah and Jaime that thanks to them I had a nice PhD sharing office with them and who also insisted me a lot to finish

the thesis.

To Francisco and Lourdes who always gave me all the support to come to study in Lisbon. Also during my PhD, they were important pillars on the development of my thesis. Thank you very much for being always there with me.

To the Dom Luiz Institute that provided me with the facilities and resources to carry out and complete my PhD.

To the researchers I met at the University of Potsdam who helped me with new ideas for my thesis work and allowed me to stay for 3 months during which time I made many friends.

To all my friends in Mexico, especially to my colleagues at SISVOC who also encouraged me to come to study in Portugal.

To the Foundation for Science and Technology that gave me a scholarship to do my PhD in this great country with number SFRH/BD/135069/2017.

To the the scope of project UTAP-EXPL/EAC/0056/2017 for allow me the opportunity to participate in international meetings.

We thank the German instrument pool for amphibian seismology (DEPAS) pool for providing the instruments for the Deep OCean Test ARray (DOCTAR) project, which was funded by the DFG (KR1935/13, DA 478/21-1) and by the Leitstelle für Mittelgroße Forschungsschiffe (Poseidon cruises 416 and 431); to the Integrated observations from NEAR SourcES of Tsunamis (NEAREST) project, whose instruments were also provided by DEPAS, and to the an investigation on the geometry and deep signature of Cape Verde mantle plume (CV-PLUME) project, whose data was collected using instruments of GIPP (Geophysical Instrument Pool Potsdam) (*Weber et al.*, 2007) and DEPAS.

Abstract

The Gloria fault is a strike-slip fault that separate the Eurasian and Nubian tectonic plates and has an extension of ∼1000 km. In the past, at least three major earthquakes occurred in the Gloria fault domain: 1931, Ms=7.1; 1939, Ms=7.1; and 1941, Mw=8.3. This work uses data from the Deep OCean Test ARray (DOCTAR), a mid- aperture temporary broadband ocean bottom seismometer array located 70 km in the north central section of the Gloria fault. The array lies within oceanic crust that is 75 to 85 Ma old. Previous studies, also using the DOCTAR data, inferred 1-D velocity models at each station, which revealed an increase in oceanic thickness and a decrease in the shear-wave velocity in the direction of the Gloria fault, as well as evidence of the lithosphere-asthenosphere boundary. In this thesis, Empirical green's functions were extracted from the ambient seismic noise to obtain the group and phase velocity dispersion curves of the Rayleigh and Love waves at short periods (≤14 s). In addition, Rayleigh and Love wave phase-velocity dispersion measurements were obtained between 14 s and 45 s using the two-station method. Coda wave analysis was also applied, but the dispersion curves were not used for the final inversion because of the lack of enough earthquakes measurements. It was systematically investigated how short- to mid-period (≤20 s) surface waves are affected when they travel through water domains. Different transitions were modelled and compared with the results of observations from three different regions of the North Atlantic, namely from the deep ocean, ocean islands and a continent-ocean transition. Water thickness was found to strongly influence the short to mid- period Rayleigh waves. This strong sensitivity of Rayleigh waves to the water layer blocks their sensitivity to the solid Earth structure. Love waves are not affected by the water layer but are very sensitive to the oceanic shallow sedimentary structure that is pervasive in oceanic domains. It has been shown that special attention is needed when modelling paths where the thickness of the water layer varies, as such variations can strongly distort short- to mid-period surface waves and lead to misleading tomographic models for the shallow structure. A 1-D shear-wave velocity model (Vs) was obtained by inversion of Rayleigh wave phase velocities at longer periods (two-station method), the Love wave group (ambient noise) and phase velocity measurements using ambient noise and the two-station method. The 1-D Vs model shows an oceanic crust with thickness between 6 km and 9 km and velocities between 3.3 km/s and 4.5 km/s. The model reaches a maximum velocity of 4.9 km/s

for depths between 15.6 km and 35 km, which may result from an abundant 20 km thick layer with the presence of harzburgite, a residue of enhanced melting due to the proximity between the Mid-Atlantic Ridge and the Azores hotspot. For greater depths, the velocity decreases reaching a low-velocity zone ∼65-70 km depth, interpreted as the lithosphere-asthenosphere boundary.

The 3-D tomographic model was obtained by inversion of 2-D Love wave group velocity maps as a function of depth, complemented with the average Love wave phase velocity obtained from ambient noise (4 s to 9 s) and the average Raleigh and Love wave phase velocities calculated by the two-station method. Thicker oceanic crust is observed mainly in the west and southwest of the DOCTAR area, which is associated with strong negative anomalies. In contrast, thinner oceanic crust is observed in the south and center of the array, associated with positive anomalies. The 2-D profiles of the tomographic model revealed the presence of oscillations of the Vs isocurves from 3.5 to 4.5 km/s every 25-30 km. These oscillations can be associated with changes in mantle upwelling and flow, detachment faulting and mantle thermal and/or compositional heterogeneities during the formation of the lithosphere of the study area. Furthermore, there is an additional deformation in the DOCTAR area caused by the proximity to the Gloria fault, which also influences the changes in oceanic crustal thickness.

keywords: Gloria fault, Ambient seismic noise, Two station method, Coda wave, 1-D and 3-D tomography.

Resumo

A falha de Glória é uma falha de desligamento que separa as placas tectónicas Euroasiática e Núbia com uma extensão de ∼1000 km. No passado, ocorreram pelo menos três grandes sismos nesta região: 1931, Ms=7.1; 1939, Ms=7.1 e 1941, Mw=8.3. Neste trabalho, foram analisados os dados registados em sismómetros instalados no fundo oceânico no âmbito do projeto Deep OCean Test ARray (DOCTAR). Esta rede temporária esteve instalada a cerca de 70 km na secção central norte da falha de Glória e era constituída por 12 sensores de banda larga e hidrofones. A rede encontrava-se numa região onde crosta oceânica apresenta idades entre 75 Ma e 85 Ma. Estudos anteriores, utilizando os mesmos dados, permitiram obter modelos 1-D de velocidade das ondas S (Vs) sob cada uma das estações. Os modelos revelaram um aumento da espessura oceânica, uma diminuição da velocidade Vs na direção da falha de Gloria e permitiram identificar a interface litosfera-astenosfera.

No presente trabalho as curvas de dispersão das velocidades de grupo e de fase das ondas superficiais (Rayleigh e Love) foram determinadas a através da análise das funções empíricas de Green, obtidas a partir da correlação cruzada do ruído sísmico ambiente ($\leq$14 s). Foram ainda calculadas a velocidade de fase das ondas de Rayleigh e Love entre 14 s e 45 s, a partir da análise de telessismos, utilizando o método das duas estações. Recorreu-se ainda à coda das ondas superficiais numa tentativa de complementar as medidas de dispersão. Contudo estes últimos resultados não foram utilizados na análise subsequente devido à ausência de uma boa cobertura azimutal de telessismos.

Foi feita uma análise sistemática do impacto da camada de água nas medidas de dispersão nos períodos inferiores a 20 s. Os resultados da modelação em três cenários distintos no Atlântico Norte, nomeadamente oceano profundo, entre ilhas oceânicas e em transição oceano-continente mostraram que as ondas de Rayleigh, nesta banda de períodos são fortemente afetadas pela camada de água e que essa banda de períodos depende da espessura dessa camada. Esta forte sensibilidade das ondas de Rayleigh à camada de água bloqueia a sua sensibilidade à estrutura mais superficial da Terra sob os fundos oceânicos. Por sua vez, as ondas de Love não são afetadas pela camada de água, mas são muito sensíveis à camada sedimentar, praticamente omnipresente em domínios oceânicos. Mostrou-se também que deve ser dada especial atenção aos trajetos entre pares de estações ao longo dos quais a espessura da camada de água varia, uma vez que tais variações distorcem

as ondas superficiais nos períodos mais curtos podendo introduzir erros nos modelos tomográficos da crusta e do topo do manto superior.

O modelo 1-D da velocidade das ondas S foi obtido a partir da inversão das velocidades de fase e de grupo das ondas de Love a partir da análise do ruído sísmico ambiente para períodos inferiores a 10 s, e das velocidades de fase das ondas de Rayleigh e de Love obtidas pelo método das duas estações para períodos superiores a 14 s. O modelo obtido mostra uma crusta oceânica com uma espessura entre 6 km e 9 km e velocidades Vs entre 3.3 km/s e 4.5 km/s. O modelo atinge uma velocidade máxima de 4.9 km/s entre 15.6 km/s e 35 km/s de profundidade. Interpretou-se esta alta velocidade como resultante da possível presença de harzburgitos, um resíduo de derretimento melhorado devido à proximidade entre a dorsal mesoatlântica e o hotspot dos Açores. Para profundidades superiores a velocidade diminui e atinge-se uma zona de baixa velocidade a ∼65-70 km de profundidade, interpretada como a interface litosfera-astenosfera. Um modelo 3-D de velocidade das ondas S foi obtido pela inversão em profundidade da distribuição lateral das velocidades de grupo das ondas de Love, calculadas por inversão 2-D dos trajetos entre pares de estações para os diferentes períodos. Foram ainda incluídas a velocidade de fase média das ondas de Love obtidas da análise do ruído ambiente (4 − 9 s) e a velocidade de fase média das ondas de Rayleigh e Love calculadas pelo método das duas estações. Observou-se a presença de uma crosta oceânica mais espessa nos sectores oeste e sudoeste sob a as estações DOCTAR, também associada a anomalias negativas na velocidade das ondas S. A Sul e no centro desta mesma região verifica-se que a crosta parece ser menos espessa e aparece associada a anomalias positivas. A representação do modelo em perfis 2-D, em função da profundidade, permitiu identificar a presença de oscilações das isolinhas de Vs entre 3.5 km/s e 4.5 km/s a cada 25-30 km provavelmente relacionadas com alterações no fluxo do manto, falhas de deslocamento e heterogenias térmicas e/ou composicionais durante a formação da litosfera nesta região.

Além disso, existe uma deformação adicional na área do DOCTAR causada pela proximidade da falha de Gloria, que também influencia as mudanças na espessura da crosta oceânica.

Palavras-chave: Falha de Glória, Ruído sísmico ambiente, Método das duas estações, Onda Coda, Tomografia.

Contents

List of Figures

List of Tables

List of Acronyms and abbreviations

1-D one-dimensional 4

2-D two-dimensional 116

3-D three dimensional 1

ANT Ambient Noise Tomography 68

ATJ Azores Triple Junction 6

CC Cross-correlation 11

CCGN cross-correlation geometrically normalized 25

CV-PLUME an investigation on the geometry and deep signature of Cape Verde mantle plume 70

DEPAS German instrument pool for amphibian seismology 12

DAS Distributed acoustic sensing 2

DOCTAR Deep OCean Test ARray 8

EIGEN Normal-mode eigenfunctions 71

EGFs Empirical Green's functions 23

FTAN Frequency-time analysis 34

FMST Fast Marching Surface Tomography 116

FMM Fast Marching Method 116

GCadiz Gulf of Cadiz imbricated wedge 70

GEBCO General Bathymetric Chart of the Oceans 8

GF Gloria fault 6

HAP Horseshoe Abyssal Plane 81

LAB lithosphere-asthenosphere boundary 8

LOBSTER Long-term OBS for Tsunami and Earthquake Research 12

MERMAIDS Mobile Earthquake Recording in marine areas by independent divers . . . 2

MFT Multiple filter technique 33

MTR Madeira Tore Rise 6

NEAREST Integrated observations from NEAR SourcES of Tsunamis 70

OBS Ocean Bottom Seismometers 1

OBSIP The Ocean Bottom Seismograph Instrument Pool 2

PCC Phase cross-correlation 24

PEM-O Oceanic Parametric Earth Model 5

PREM Preliminary Reference Earth Model 47

PM primary microseismic 19

PPSD Probabilistic Power Spectral Densities 11

RAMN Running Absolute Mean Normalization 26

RMS root mean square 54

SAC Seismic analysis code 24

SLAT2D Normal-mode summation as a sequence of 1D blocks 78

SM secondary microseismic 19

SNR Signal-to-Noise Ratio 25

SPECFEM3D Spectral element method 78

SYN-E Synthetic seismograms by normal-mode summation 71

Chapter 1

Introduction

Ocean seismic observations are handled differently from those on land. They are mainly influenced by the conditions of the installation site and after recovering the data we have to deal with a different processing to make corrections than those on land.

The seismological applications carried out on the continents are basically the same as those that can be applied in the ocean to study the structure of the Earth. To characterize the oceanic crust and upper mantle, techniques such as surface wave tomography or array methods must be applied. The best approach to map the lateral variations of the oceanic structure is by performing three dimensional (3-D) studies. The 3-D images provide more complete information, especially if you are close to a fault. Ocean Bottom Seismometers (OBS) are used to perform these types of studies in the ocean.

1.1 Ocean seismic observations

From the beginning, seismological observations have been limited by the location of seismic stations, most of which are located on continents and islands (*Montagner et al.*, 1998; *Kohler et al.*, 2020). The oceans, which account for $\sim 70\%$ of the Earth's surface, represent a significant gap in the global seismological observation. This gap is critical for global earthquake and Earth structure studies, and specially for investigations focusing on oceanic seismicity and Earth structure beneath the oceans (*Montagner et al.*, 1998; *Webb*, 1998; *Kohler et al.*, 2020). In addition, important sites for plate tectonic (e.g., subduction zones and spreading ridges) and mantle dynamic studies (e.g., hotspots) are

located in these oceanic regions.

To meet the need for ocean seismic observations, OBS were first developed by *Ewing and Vine* (1938) in the first half of the 20th century. OBS are seismic sensors that operate on the seabed and record ground vibrations locally (*Webb*, 1998). OBS were developed in the 1980s using short-period sensors, but in the 1990s the broadband OBS were developed using the same configuration base of short-period OBSs (*Suetsugu and Shiobara*, 2014).

Usually, the OBS system is also equipped with a hydrophone to record pressure variations. For temporary deployments, the OBS are usually dropped from a ship onto the seabed, where they operate autonomously and are powered by built-in batteries. At the end of the deployment, the seismic stations are released and float to the surface where and only after the seismic data is retrieved. In permanent networks, the OBS are connected to the mainland by cables that provide both continuous power and data transmission (*Montagner et al.*, 1998; *Kohler et al.*, 2020). Permanent OBS networks currently exist or are under development in Japan, USA and Canada, among others (*Romanowicz et al.*, 2009; *Kelley et al.*, 2014; *Kawaguchi et al.*, 2015). Recently, alternative technologies for ocean seismic monitoring have been proposed, including Mobile Earthquake Recording in marine areas by independent divers (MERMAIDS) (*Simons et al.*, 2006) and fiber-optic technology (*Zhan*, 2019). MERMAIDS is an autonomous robot that floats freely in the oceans and is able to record earthquake signals with a hydrophone while swimming at a depth of 1.5 km and rise to the surface to transmit the seismograms by satellite. The data obtained is already being used for seismic tomography. Distributed acoustic sensing (DAS), on the other hand, is an emerging technology that reuses a fiber-optic cable as a dense array of strain sensors. In this technology, a fiber is repeatedly bombarded with laser pulses, measuring optical phase changes in Rayleigh backscattered light. Hence DAS has been used to record earthquake waves and other seismic signals.

In addition, OBS is gradually becoming accessible to the scientific community and can be deployed worldwide on a regular and intermittent basis (e.g., The Ocean Bottom Seismograph Instrument Pool (OBSIP) (https://www.iris.edu/hq/programs/obsip)).

After decades of experimental development, OBS observations currently have a quality high enough to detect useful signals over a wide range of frequencies. The data recorded by OBS are quite different from those recorded on land. Among others, they show signals

originating from tilt noise, compliance noise, microseismic noise, sediment resonance, ships and whales. (*Webb*, 1998; *Crawford and Webb*, 2000; *Bell et al.*, 2015; *Matias and Harris*, 2015; *Janiszewski et al.*, 2019).

Tilt noise comes from ocean currents on the seafloor interacting with the OBS. This noise can be corrected by a transfer function between the vertical and horizontal components (*Crawford and Webb*, 2000) or by rotating the horizontal components to find the maximum coherence with the vertical component (*Bell et al.*, 2015).

Compliance noise on the other hand, is the deformation of the seafloor due to long-wave pressure fluctuations generated by infragravity oceanic waves at the sea surface (*Crawford and Webb*, 2000; *Bell et al.*, 2015; *Janiszewski et al.*, 2019). Additionally, the compliance noise is related to ocean wave amplitude, OBS depth and sediment thickness (*Crawford et al.*, 1998). The observed compliance signal depends on the frequency and depth and is only significant when the wavelength is greater than the water depth. To calculate at what maximum frequency compliance noise affects the data, it is used the following expression:

$$f_{max} \approx \sqrt{\frac{g}{2\pi d}} \tag{1.1}$$

where g is the gravitational acceleration and d is the depth of the OBS.

Following *Janiszewski et al.* (2019), the compliance noise is significant at periods < 25 s in shallow waters (< 1000 m) and at periods > 50 s in deep water at depths > 4000 m. Similar to the tilt noise correction, we need a transfer function of the coherence between the vertical and pressure components to perform the correction (*Crawford and Webb*, 2000; *Bell et al.*, 2015; *Janiszewski et al.*, 2019). Figure 1.1 illustrates how the compliance noise is generated in the vertical component of the OBS.

Furthermore, the current orientation of OBS is usually unknown, as OBS is simply dropped on the seabed. Therefore, the orientation of OBS is usually determined *a posteriori* from polarization analysis of body and surface waves (*Stachnik et al.*, 2012; *Scholz et al.*, 2017; *Doran and Laske*, 2017; *Zhu et al.*, 2020), cross-correlation of ambient noise (*Zha et al.*, 2013) or airgun shots (*Anderson et al.*, 1987). Decoding the characteristics of seismic data recorded on the seabed is key to properly exploring these unique datasets.

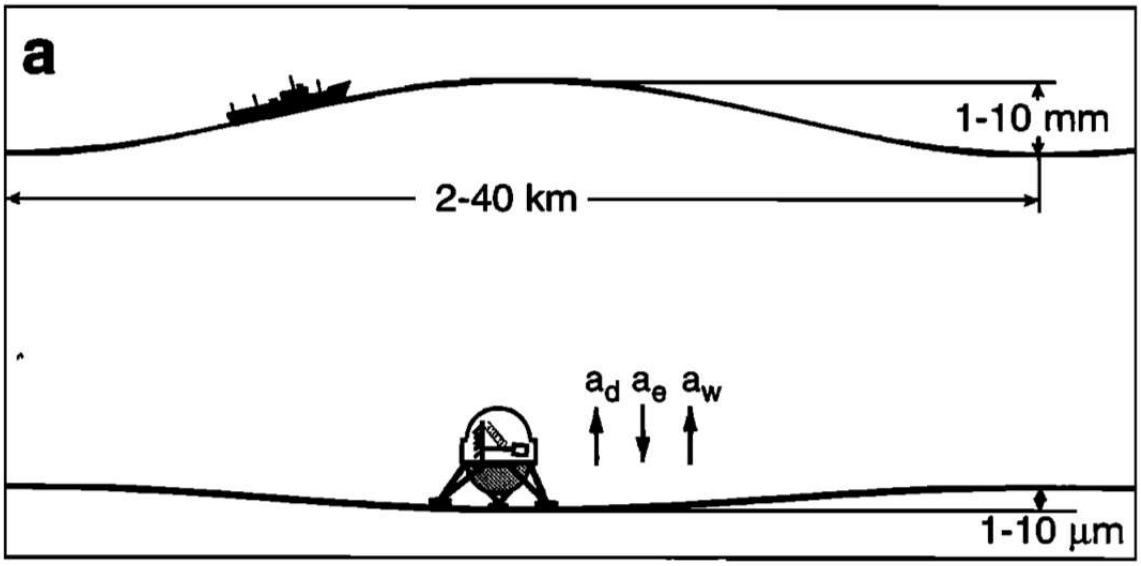

Figure 1.1: The compliance noise is introduced by the deformation of the seafloor due to the pressure of the ocean surface waves. Illustration taken from *Crawford et al.* (1998)

Despite the challenges associated with analyzing OBS data, new insights into seismicity and Earth structure have been gained through various OBS studies, including studies based on seismic refraction (e.g., *Sallarès et al.*, 2011, 2013), local earthquake studies and tomography (e.g., *Yao et al.*, 2011; *McGuire et al.*, 2012; *Hannemann et al.*, 2016; *Corela et al.*, 2017), receiver functions (e.g., *Hannemann et al.*, 2017) and shear wave splitting (e.g., *Lynner and Bodmer*, 2017; *Lynner and Porritt*, 2017), among others.

Computing one-dimensional (1-D) velocity models using OBS for the oceanic crust are not sufficient to map the lateral variations and image the earth structure below the array. Therefore, the 3-D study provides a more complete hint of the oceanic crust.

1.2 Study area

1.2.1 Normal oceanic crust structure

After numerous seismological surveys carried out in the ocean since the 1960s to determine the oceanic crustal structure, the results show that the thickness of the oceanic crust is very uniform throughout the world ocean on average (*White*, 1984) except for Islands or oceanic ridges.

Dziewonski et al. (1975) proposed several global reference models, including an oceanic, a continental and an average model. The oceanic model, also called Oceanic Parametric Earth Model (PEM-O) is a model specifically for the average oceanic structure of the Earth. PEM-O consists of an average water layer, followed by 1 km of sediments and a 6 km thick oceanic crust. This model is identical to the others one at the top of the mantle transition zone at a depth of 420 km. The data used to generate this velocity model were seismic overtones observations at very long periods, travel times of body waves and surface waves dispersion curves.

Later, *White et al.* (1992) developed an oceanic model by acquiring ∼800 seismic refraction profiles around the world to characterize the oceanic crust and uppermost mantle. This model consists of one layer of sediments and two layers for the oceanic crust averaging 2.11 ±0.55 km and 4.97 ±0.90 km for the Pacific and Atlantic Oceans, respectively.

CRUST1.0 (*Laske et al.*, 2013) is an improved version of the earlier versions CRUST5.1 and CRUST2.0, published by *Mooney et al.* (1998) and *Bassin* (2000), respectively. This improved version is a global model of the Earth's crust and lithosphere with a spatial resolution of 1 x 1 arc-deg (*Laske et al.*, 2013). In general, CRUST1.0 consists of layers of ice, water, a maximum of three sediment layers, three oceanic crust layers and a final mantle velocity, including parameters such as Vp, Vs and density. Moho depth was determined using data from active sources and receiver functions. In places where there are no seismic surveys, like Antarctica, gravity data were used to constrain the velocity in depth. In addition, there were places with no information where the crustal structure was determined by extrapolating the average crustal properties. Crust1.0 model was taken in a point at the North Atlantic North of the Gloria fault (see Figure 1.3 black dot inside the square).

These three oceanic models are shown in the figure 1.2 for Vp and Vs. In general, the three velocity models are very close in terms of oceanic crust thickness and velocity. Crust1.0 and PEM-O are reference models that consist in layers while *White et al.* (1992) (henceforth called 'White's model') is a model in gradient velocities. In the sedimentary layer, the PEM-O model has 1 km, Crust1.0 only 100 m and White's model 500 m of sediments thickness. The oceanic crust of White's model is divided into two layers of constant gradients that in total has a crustal thickness of 7.08 km. PEM-O consist in a

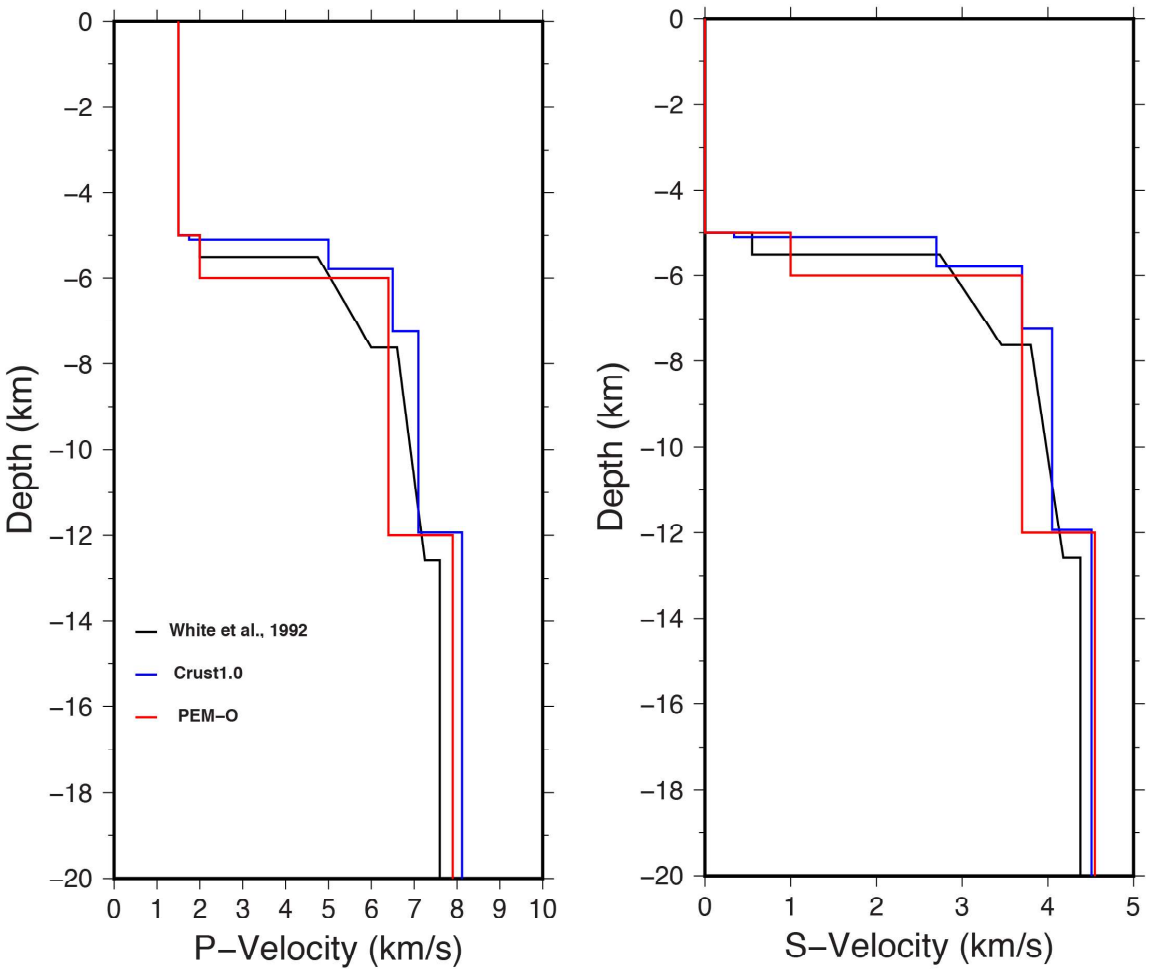

Figure 1.2: Velocity models for typical oceanic crustal structures. White's model (black), Crust1.0 (blue) and PEM-O (red).

single layer for the oceanic crust of 6 km thickness. Finally, Crust1.0 has a total crustal thickness of 6.93 km divided into three layers. This velocity model has 100 m of sediment, but in fact the average sediment layer in this area is ∼600 m according to *Hannemann et al.* (2016), but the velocity model for this layer was not changed in this thesis. When it is compared CRUST1.0 and White's model, we find that if these 100 m sediments were changed to 600 m, the two models would converge at the interfaces of the lower crust and the Moho, except that White's model runs in gradients and is slightly slower.

1.2.2 Gloria fault domain

The Gloria fault (GF) is a strike-slip fault extending from the west in the Azores Triple Junction (ATJ) to the east in the Madeira Tore Rise (MTR). It has a right-lateral motion at the west and ending with an oblique convergence motion at the east, with ∼1000 km long (Figure 1.3). This fault is the boundary between the Eurasian and Nubian tectonic

plates with a relative plate velocity motion of $\sim$ 4 mm/y (*Fernandes et al.*, 2003, 2006; *DeMets et al.*, 2010).

The first author to observe the GF was *Laughton et al.* (1972), who mapped the fault using long-range side-scan sonar and seismic reflection records and named it the Gloria fault because his sonar equipment was named GLORIA.

A complete study of seismicity and focal mechanism for the Azores-Gibraltar boundary was carried out by *Udías et al.* (1976); *Buforn et al.* (1988) for earthquakes with M $\geq$7.0. During the last century, at least three main earthquakes have been identified in the GF domain, on 20 May 1931, Ms=7.1; on 8 May 1939, Ms=7.1 and on 25 November 1941, Mw=8.3, with their focal mechanisms being mainly strike-slip solutions (Figure 1.3). An intraplate earthquake occurred 200 km south of the fault in 1975 with Ms=7.9. (*Udías et al.*, 1976; *Buforn et al.*, 1988; *Reis et al.*, 2017; *Batista et al.*, 2017). The age of the oceanic crust in the area of the GF domain changes from $\sim$ 50 Ma in the west to $\sim$ 120 Ma in the east (*Luis and Miranda*, 2008).

We can divide the GF into three segments with different strikes, from west to east with lengths of 455, 271 and 278 km, respectively (*Baptista et al.*, 2017; *Batista et al.*, 2017), if only bathymetry is considered (Figure 1.3). *Baptista et al.* (2017) applied a scaling law between fault displacement and fault length of the GF domain (Figure 3 of *Baptista et al.* (2017)). They assumed that the faults are completely vertical and with a thickness of 40 km and with a high rigidity modulus of 5×10^{10} Pa. They conclude that for each GF segment, the maximum magnitudes for earthquake generation are 8.5, 8.1 and 8.1, respectively.

1.2.3 Marine seismic profiles and other studies near DOCTAR area

The DOCTAR experiment was located $\sim$70 km north between the second and third segments of the GF domain (Figure 1.3). According to *Müller et al.* (2008), the DOCTAR is located at a lithospheric age between 75 and 85 Ma.

A seismic profile study was carried out $\sim$300 km west of the DOCTAR area in the first segment of the GF domain by *Batista et al.* (2017) to obtain new information on the GF

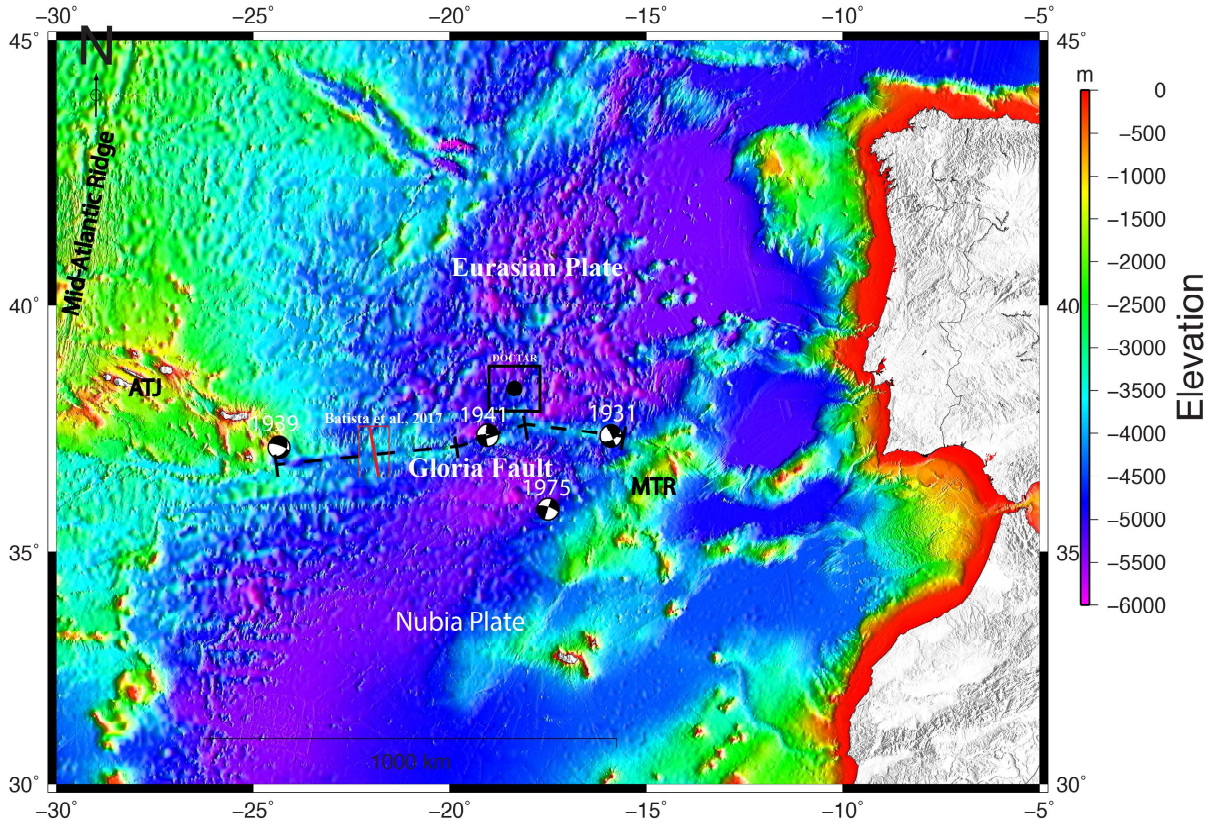

Figure 1.3: Tectonic settings of the GF domain: the black dashed line denotes the GF, which is divided into three segments and has an length of ∼1000 km between the ATJ in the west and the MTR in the east. The focal mechanism are the main historical earthquakes with Mw > 7. The black square shows the location of the Deep OCean Test ARray (DOCTAR) dataset used in this work. The red line indicates the seismic profile from *Batista et al.* (2017). Bathymetry downloaded from General Bathymetric Chart of the Oceans (GEBCO) (www.gebco.net).

structure (Figure 1.3). The seismic refraction and reflection results show that the oceanic crust has a thickness of ∼8.5 km below a sediment layer of 1 km thickness 1.4b. In addition, the authors found a petrological Moho layer of 4 km thick, which is a transition zone that separates the mafic rocks above (crust) and the ultramafic rocks below (upper mantle). The compressional velocity, shear velocity and Poisson´s ratio values found in this layer indicate not only partial serpentinization but also gabbro composition.

On the other hand, *Hannemann et al.* (2017) used DOCTAR data to find the Moho boundary at a depth between 5 and 8 km using the Receiver Functions technique. In addition, they observed the lithosphere-asthenosphere boundary (LAB) at ∼70-80 km depth and mantle discontinuities. *Hannemann et al.* (2016) observed an increase in oceanic crust thickness from ∼5 km to ∼8 km in the direction of the GF using P-wave polarization analysis (Figure 1.4a). They also observed a decrease in mantle Vs from ∼5.5 km/s to ∼4.5 km/s in the GF direction. They concluded that the decrease in shear velocity and the

increase in thickening were related to the deformation caused by the fault. *Hannemann et al.* (2016) could not draw a firm conclusion due to limited azimuthal data coverage, but they mention that serpentinization is probably the strongest reason for the decrease in shear-wave velocities.

Other studies for the Mid-Atlantic Ridge using gravity measurements like *Bonatti et al.* (2003) conclude that when the oceanic crust is not subjected to secondary processes that produce a thinning of the crust (for instance, as a metamorphic core complexes), crustal thickness oscillations are observed due to periodic changes in mantle upwelling and flow. *Bonatti et al.* (2003) reported that these temporal variations in the crustal thickness pattern have periods of ∼3-4 Ma. Other studies that found oscillations of crustal thickness in the Mid-Atlantic Ridge are *Pariso et al.* (1995); *Tucholke et al.* (1997); *Shinevar et al.* (2019). Recent studies presented by *Shinevar et al.* (2019) also show oscillations in a 1400 km long profile in which they concluded that these changes in the thickness of the oceanic crust are due to a combination of detachment faulting, mantle source heterogeneities (thermal and/or compositional), and variations in upper mantle flow.

These Vs changes and lateral variation in the thickness towards the GF are not completely resolved that is my main motivation in using surface waves technique and coda wave to better constrain the structure of the GF domain.

1.3 Thesis aims and organization

This PhD dissertation aims to characterize and image in 3-D the oceanic crust and upper mantle structure to map lateral variations caused by the GF. Previous studies done for *Hannemann* (2016) show 1-D velocity models under each OBS and two profiles N-S and E-W (Figure 1.4a) that give us an idea of the influence of the GF. This study is focused on the same study area than *Hannemann* (2016) using other methods. To achieve this, we performed a joint 3-D surface wave tomography using ambient seismic noise, teleseismic earthquakes and coda using DOCTAR dataset that was located 60 km North of the central section of the GF.

This thesis structure is organized as follow:

Chapter 2 details about the preparation of the DOCTAR dataset, such as corrections in

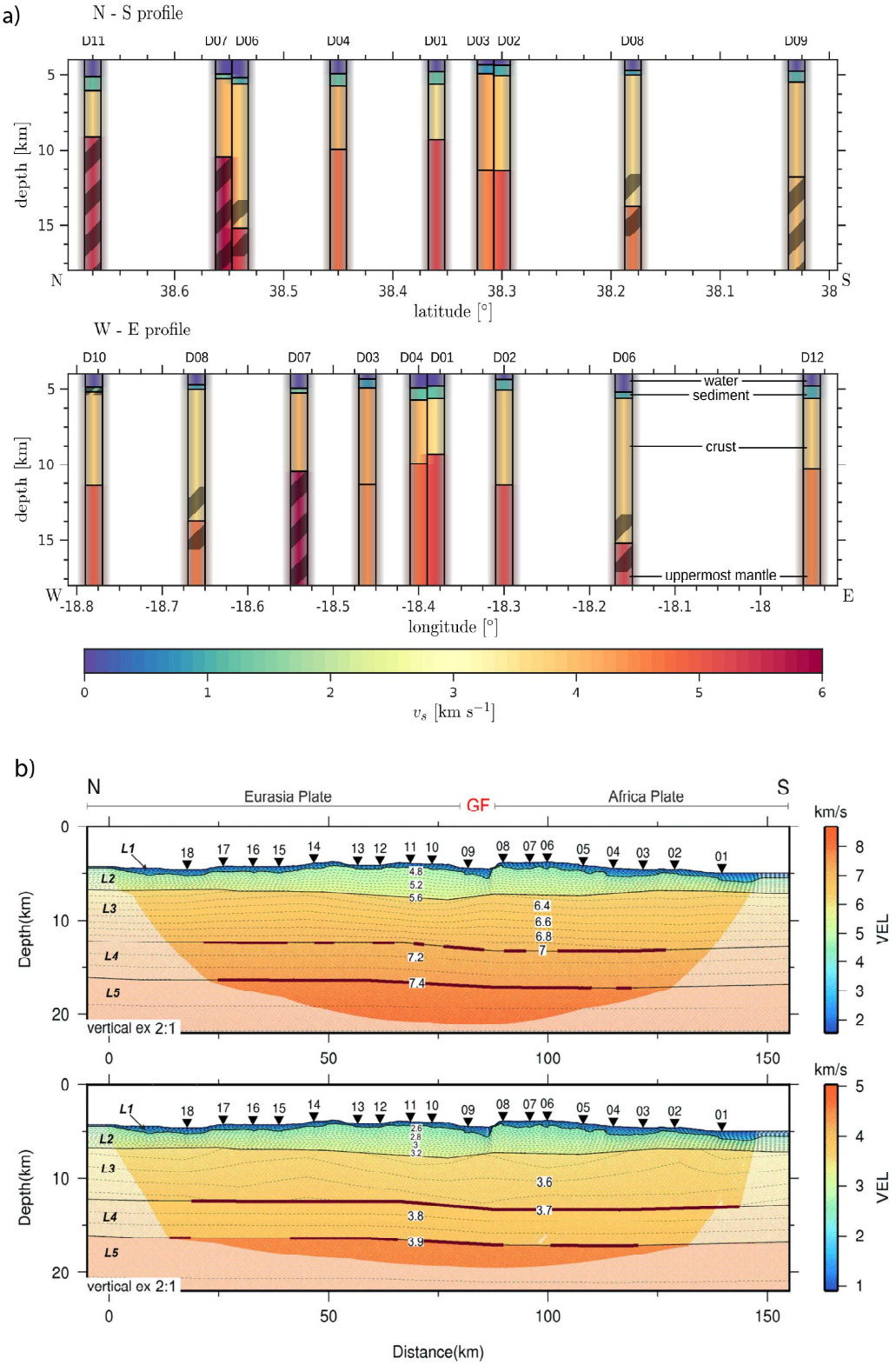

Figure 1.4: Final velocity models for two studies recently done near the GF. a) Shear wave velocity profile of *Hannemann et al.* (2016) showing the lateral variations, especially towards the GF. b) *Batista et al.* (2017) velocity model also showing an increase in the thickness in the northern side of the seismic profile.

the time drift, orientations for the horizontal components and Probabilistic Power Spectral Densities (PPSD) analysis are given. In the PPSD we have different noise sources at different period bands, which it is described here. For this thesis we are more interested in the short and long period bands (1 s - 50 s).

Chapter 3 describes the extraction of the Empirical green's functions for group and phase velocity analysis of Rayleigh and Love waves. For the cross-correlation, it was compared first the classical cross-correlation with the phase cross-correlation and after that it was compared the linear stack versus the phase weighted stack.

Chapter 4 introduces the surface wave two-station method in general and the process for the teleseismic earthquake selection criteria with visible surface waves. In addition, the extraction of phase velocity dispersion curves of Rayleigh and Love waves and anisotropy are described.

Chapter 5 is presented the seismic coda wave method, how the Cross-correlation (CC) of the coda wave were performed and the results of the dispersion curves found with this technique.

Chapter 6 shows new insights about the influence of the water in the Rayleigh wave group and phase velocity dispersion curves of synthetic seismograms and real data. In addition, it is showed the effect of the sediments, the oceanic structure, the lateral varying media, and Love waves in simple modeling and full waveform modelling in the dispersion curves.

Chapter 7 present the code and initial parameters used to perform the inversions. In addition, it was tested several initial models and inversions of several datasets of the dispersion curves available. Finally, a final 1-D shear-wave velocity inversion it is introduced and compared with other oceanic models.

Chapter 8 describe the FMST method and how the resolution analysis and regularization parameters were tested to find the optimal solution of our model. In addition, it was computed velocity maps of the ambient noise available data and finally 3-D shear velocity model of the study area were obtained.

Finally, in the last **Chapter 9** are the conclusions of each chapter and the final conclusions about the results found in this study.

Chapter 2

Data

2.1 DOCTAR Data

For this thesis study it was used data from the DOCTAR, a temporary broadband OBS array located ∼70 km north of the GF. Figure 2.1 summarize the entire array. DOCTAR was provided by the German instrument pool for amphibian seismology (DEPAS) with 12 instruments Long-term OBS for Tsunami and Earthquake Research (LOBSTER) type. The OBSs were installed north of the transition of the GF domain between the second and third segments at depths between 4.5 km and 5.5 km (Table 2.1). The array has a maximum interstation distance of ∼73 km and the interstation spacing average is between 10 km and 20 km. Each OBS was equipped with a data logger (Send Geolon MCS, 24 bits, 1-1000 Hz, 20 GB), a broadband seismometer (Guralp CMG-40T, with a corner period of 60 s) and a hydrophone (HighTechInn HTI-04-PCA/ULF, with a corner period of 100 s). The sampling rate for the seismometer and the hydrophone was set to 100 Hz. Calibration pulses were set every 14 days. The equipment recorded data continuously for a period of ∼10 months between 30 June 2011 and 22 April 2012.

The seismometer at station D05 was not used for this study because two components were jammed, between the vertical and one of the horizontal, but the hydrophone was used instead even though it failed one month before the recovery.

Two important steps in OBS data pre-processing are time correction and orientation of the horizontal components. Both these steps were done previously for the DOCTAR

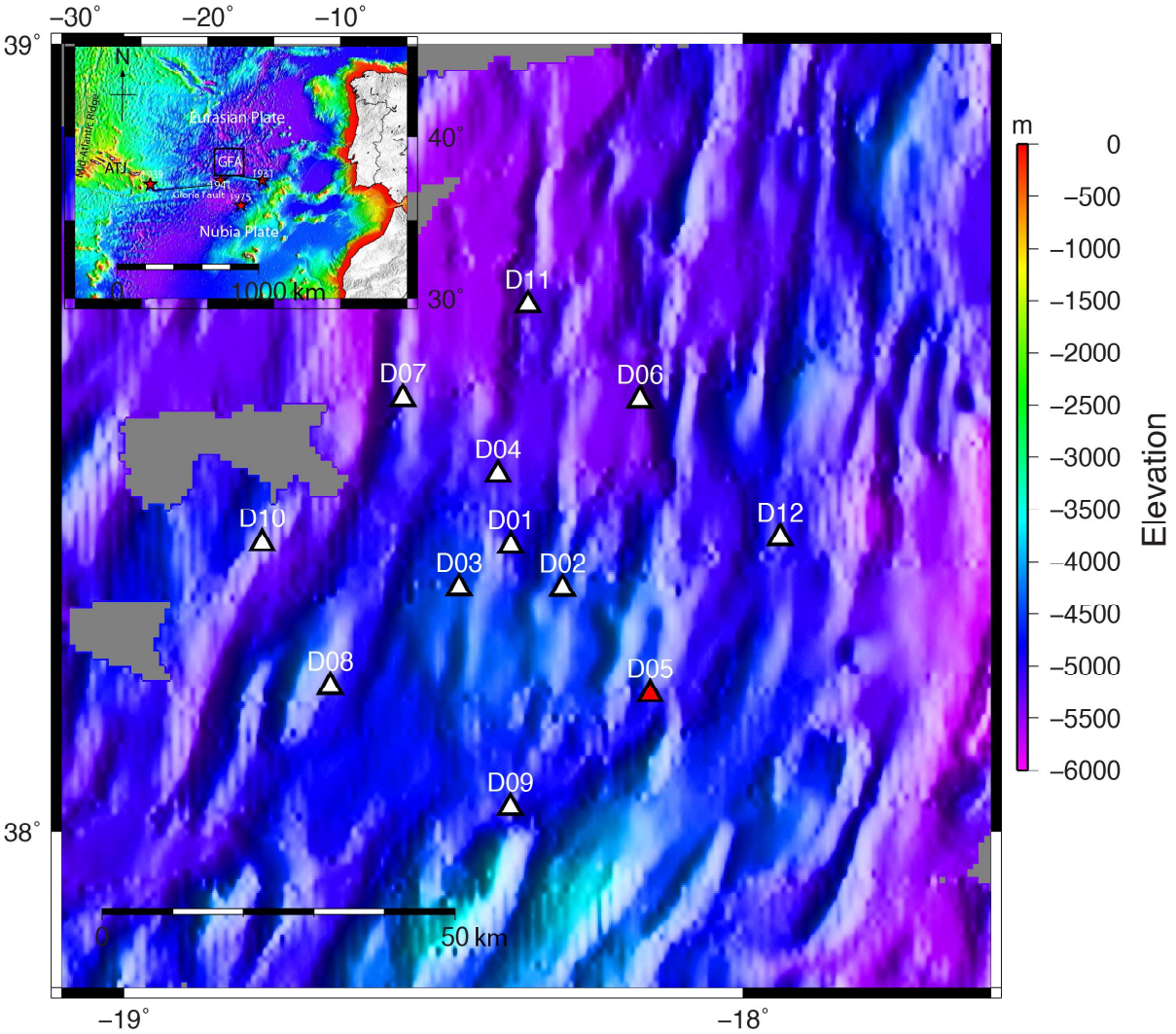

Figure 2.1: Distribution of the deployment of OBS in the mid-eastern Atlantic Ocean. The seismometer of station D05 (red triangle) was not used, only the hydrophone.

Table 2.1: Locations of the OBS stations of the DOCTAR.

Station name	Latitude	Longitude	Depth (m)
D01	38.36485	-18.37490	-4888
D02	38.30933	-18.29168	-4453
D03	38.30990	-18.45837	-4420
D04	38.45495	-18.39590	-5018
D05	38.17517	-18.14993	-4721
D06	38.54985	-18.16673	-5283
D07	38.55133	-18.54950	-5036
D08	38.18512	-18.66660	-4814
D09	38.03018	-18.37538	-4860
D10	38.36763	-18.77677	-4973
D11	38.67020	-18.34738	-5215
D12	38.37497	-17.94013	-4892

dataset by *Hannemann et al.* (2013, 2017).

Correction by the time drift was done using ambient noise with long correlation windows and GPS synchronization times to correct for static time deviations. Station D08 had the highest time drifts with 20 minutes with respect to the other stations (see Figure 2 of *Hannemann et al.* (2013).

As mentioned in Chapter 1, there are different methods to determine the orientation of the OBS after recovery. The orientation was done based on the polarization of the P and Rayleigh phases of the largest teleseismic events, following the work of *Stachnik et al.* (2012) (Figure A1 of the supplement of *Hannemann et al.* (2017)). Based on the orientations found in the work of *Hannemann et al.* (2017), the data were rotated to verify the orientation by particle motion plots. Figure 2.2 shows the 20 March 2012 earthquake in Mexico with a back azimuth of 277° before and after rotation. We selected a window containing only the Rayleigh waves to compare with the vertical component. The particle motion shows the horizontal components before and after rotation and the vertical and radial component to show the elliptical motion of the Rayleigh waves. The polarization before rotation has an orientation NE-SW (Figure 2.2a) and after rotating to the great circle path is polarized in the radial component (Figure 2.2b). The results are in agreement with the expected polarization of Rayleigh wave in the vertical and radial components.

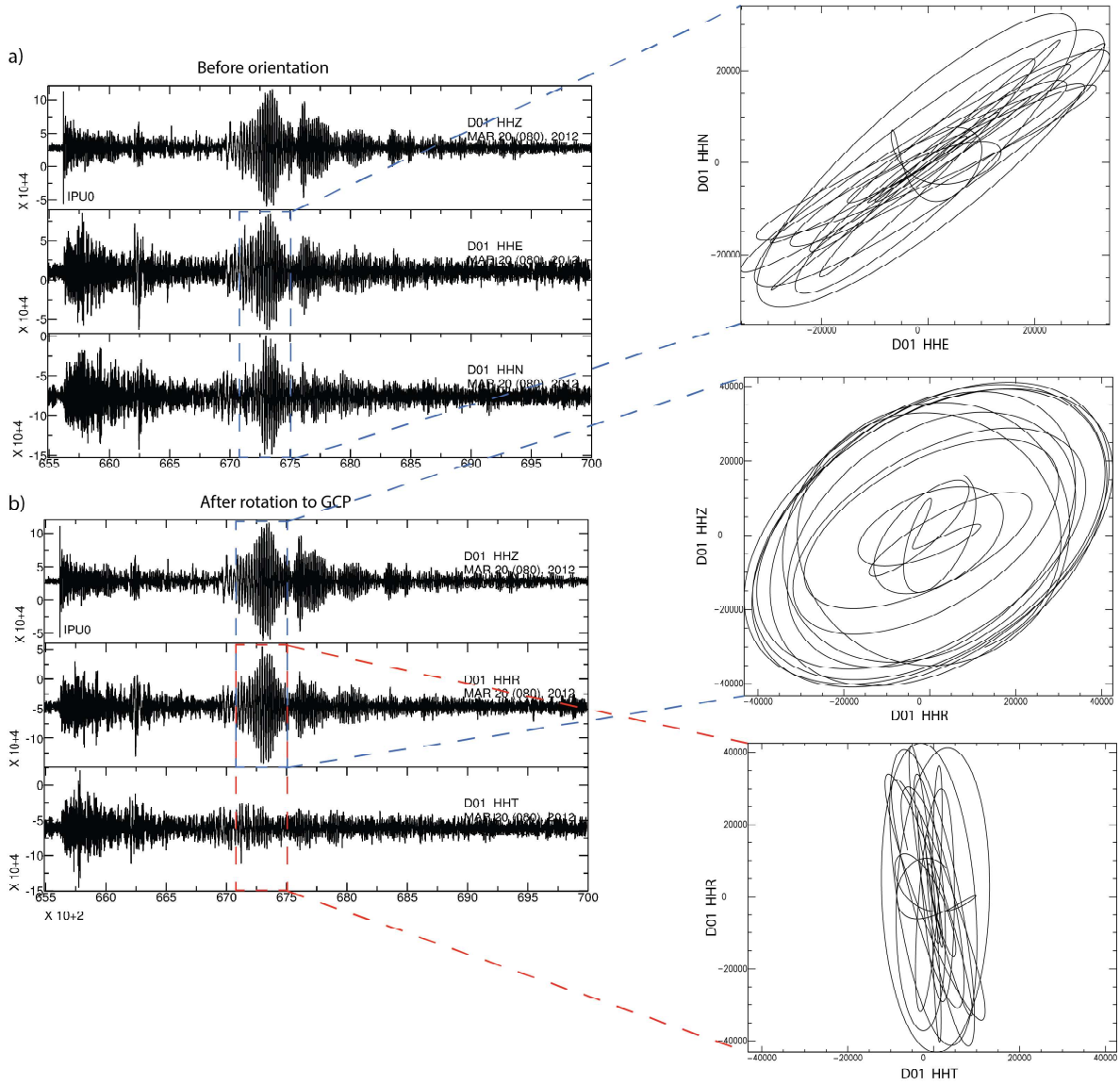

Figure 2.2: The 20 March 2012 teleseismic event on the west coast of Mexico without filter for station D01 before adding the values of the orientation and after rotating to the great circle path of the horizontal components. a) Shows the particle motions polarized in the NE-SW direction. b) Results of the orientation after rotating the radial and transverse components polarized in the radial direction. In addition, it is plotted the vertical-radial showing the retrograde Rayleigh wave motion.

2.2 Power spectral densities

In order to evaluate the quality of the DOCTAR dataset, the distribution of seismic noise levels in the spectral domain was assessed using a PPSD analysis. Before calculating the PPSD, a correction of the transfer functions in the dataless for the seismometer and the hydrophone was necessary. The transfer function for the hydrophone and the seismometer were converted from rad/s to Hz to obtain the real gain of the instruments. In addition, the sensitivity gain was also changed multiplying by 1×10^6 for the hydrophone to visualize it in the PPSD.

We used the software ObsPy (https://docs.obspy.org) to calculate the PPSD of all OBSs for all components, including the hydrophone. In addition, spectrograms were used in different period ranges to get a more complete picture of the seismic noise variations.

The ambient vibrations recorded by the OBSs are due both to the OBS frame design and to the noise generated by the earth vibrations, as seismic signals. For example, in the figure 2.3 for the vertical components of three OBS stations, D01, D06 and D08 for the whole period the array was deployed, it is observed different types of noise such as the local noise, the microseismic noise, the calibration pulse and the self-noise.

Local noise is the noise source that occurs at frequencies above 1 Hz. In the oceans, the signals identified are different from those on land. For example, the 24 hours helicorder of the figure 2.4 show signals from ships, whales, local earthquakes, etc. Figure 2.5 shows a day plot of the teleseismic Sumatra earthquake of 11 April 2012 with Mw 8.6. This rare strike-slip earthquake is considered the largest of the rare great intraplate earthquakes of the instrumental era. The earthquake occurred at 08:38 UTC and was followed by another earthquake of Mw 8.2 at 10:43 UTC.

Self-noise is a particular noise at periods $\geq$10 s for the DEPAS seismometer instruments, which is caused by a combination of tilt and instrument self-noise in the horizontal and the vertical component, respectively *Stähler et al.* (2016).

Another type of signal observed in the PPSD is the re-levelling and autocenter pulse for the DOCTAR seismometer, which has been set to do these every 14 days.

The microseismic noise is generated by pressure fluctuations that propagates in the ocean

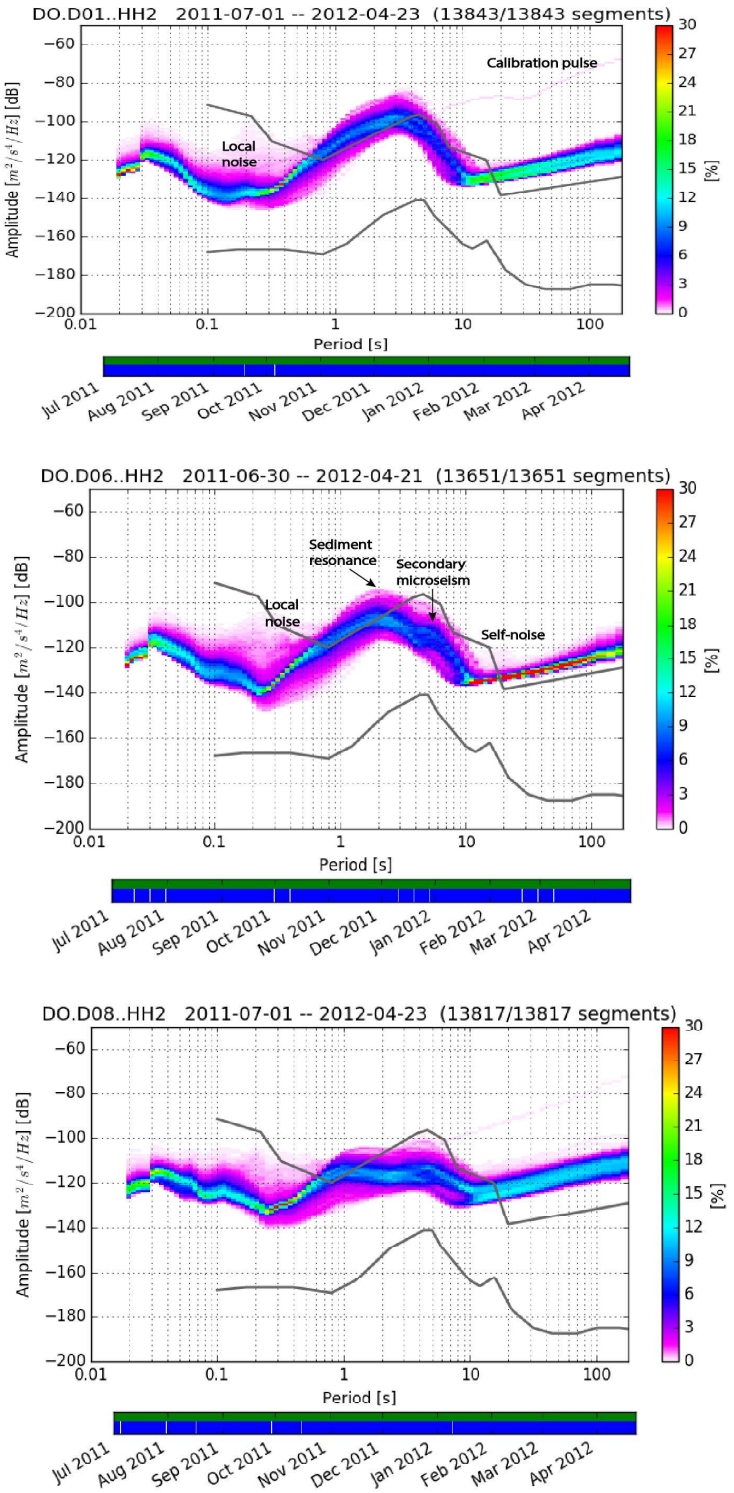

Figure 2.3: PPSD of three OBSs showing the distribution of seismic energy due to different noise sources.

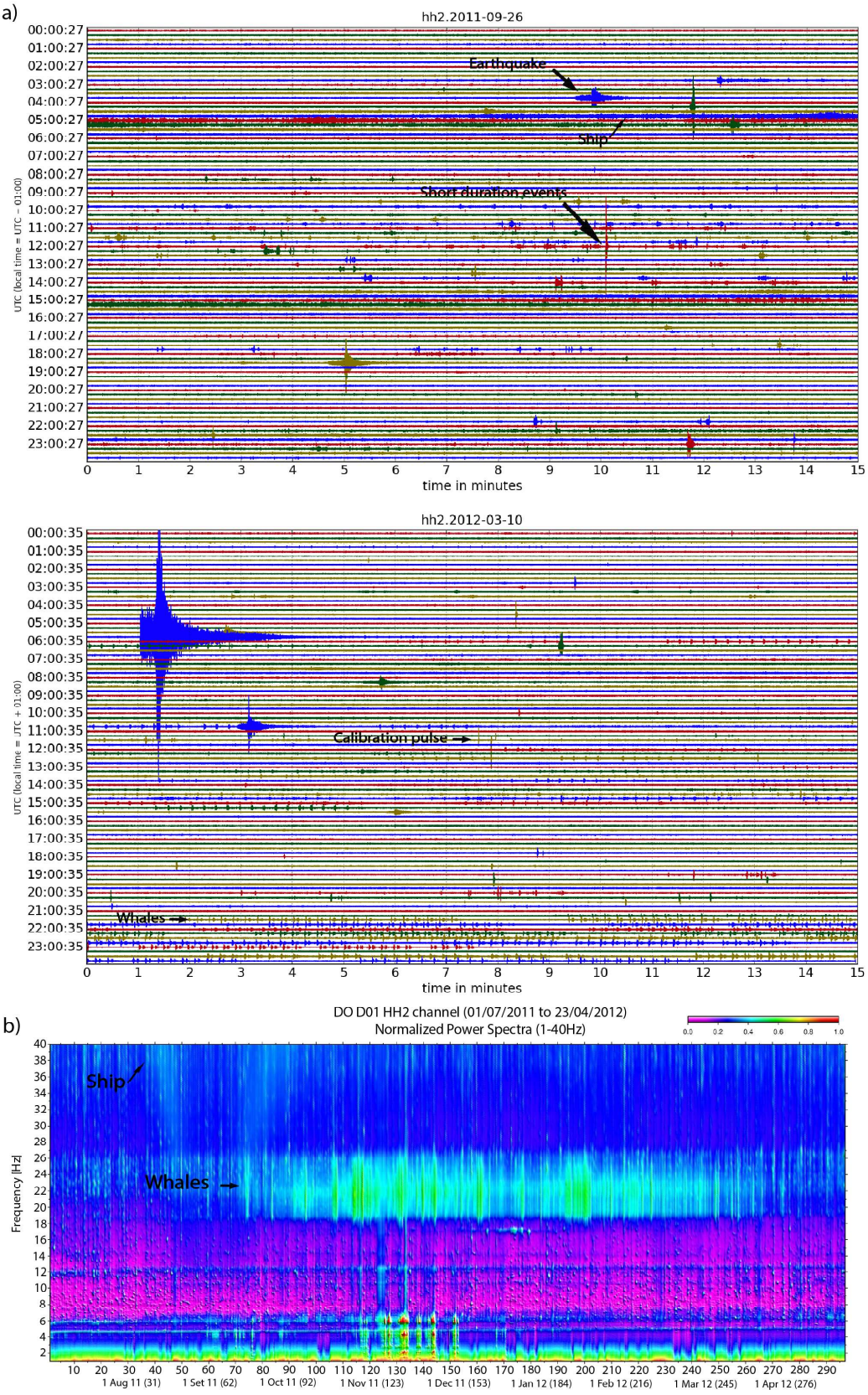

Figure 2.4: 24-h helicorder plot of station D01 with various features of the noise. The data was band-pass filtered between 10-40 Hz (a). The spectrogram shows the signals recorded between 1Hz and 40 Hz (b).

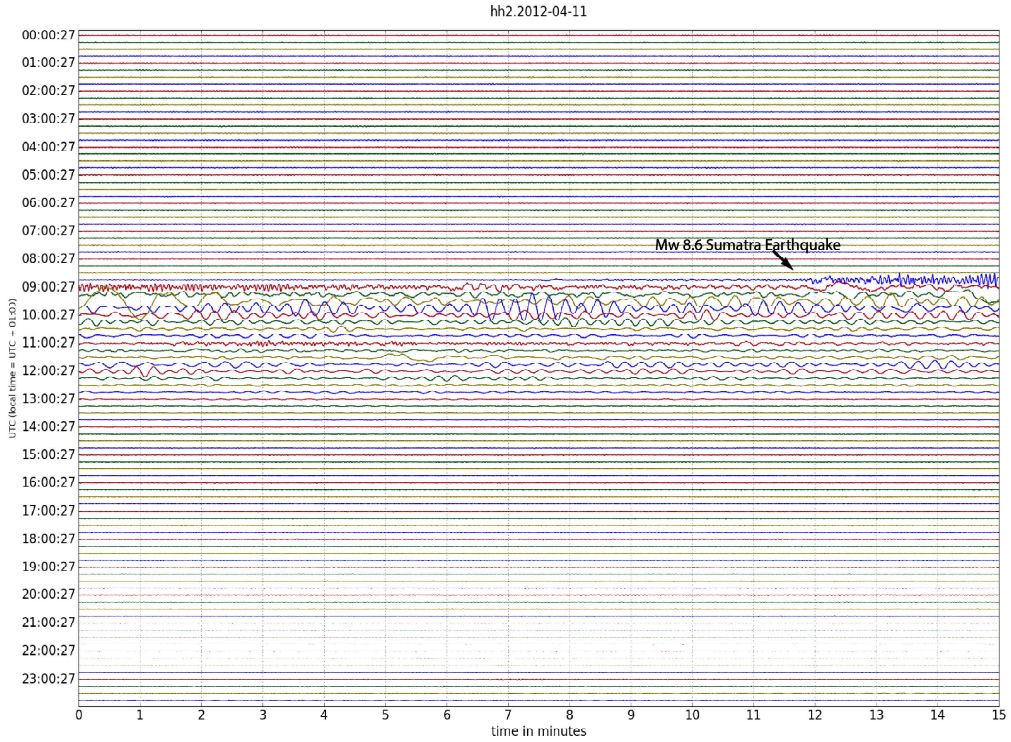

Figure 2.5: One-day helicorder plot of station D01 showing the 11 April, 2012 Mw 8.6 and 8.2 earthquakes on the west coast of North Sumatra. The daily plot was bandpass filtered between 1-50 s.

and reach the solid Earth around the world (*Ardhuin et al.*, 2011; *Gualtieri et al.*, 2013). The microseismic noise in the vertical component is mainly dominated by Rayleigh (*Tanimoto and Alvizuri*, 2006) and P-waves (*Barruol et al.*, 2006). However, some authors, analyzing the transverse components, have also identified Love waves in the secondary microseismic (SM) band (*Nishida et al.*, 2008; *Tanimoto et al.*, 2015).

The SM has a period band between 3 s and 10 s (*Longuet-Higgins*, 1950), while primary microseismic (PM) is between 8 s and 20 s (*Hasselmann*, 1963). The PM noise is generated by the direct pressure of the ocean waves against the sloping seabed in coastal areas *Hasselmann* (1963), while the SM noise is thought to be generated by second-order water fluctuations due to colliding waves (*Longuet-Higgins*, 1950).

The PPSD of station D01, vertical component, shows a prominent peak between 3 s and 4 s, which is confirmed by the spectrogram with a line trend of the noise between 3.5 s and 4s (Figure 2.6). According to *Hannemann et al.* (2016), the noise is observed as an increase in PPSD amplitude due to resonance in the sediments, as energy is trapped there. In the hydrophone, however, the energy peak is largely dominated by the SM

noise, but in the spectrogram we still see resonance. Similarly, the hydrophone shows some anomalies in the PPSD, for example station D03 in Figure 2.6c, with a scattering of noise at different frequencies, while in the spectrogram we can see that this station did not work properly compared to hydrophone D01. Figure 2.7 shows the PPSD for the hydrophone (HH1), the vertical (HH2) and the horizontal components (HH3) of stations D04, D07, D09 and D10. Some stations show two energy peaks in the vertical component, such as the vertical component of station D07, one peak at about 2 s, which is thought to be related to sediment resonance, and the other peak at ∼5 s, which is related to the SM noise. The component HH3 shows a similar distribution of noises with the vertical component except at periods ≥7 s where the noise levels are too high and mask in some stations the microseismic band. In addition, the PPSD of the seismometer show that after ∼10 s period starts losing sensitivity and this might impact in the analysis especially at longer periods.

Summarizing, the SM noise can be observed in all stations for the vertical components, but the noise is clearer in the hydrophone. The PM noise is not obvious in the PPSD due to the distance from the continental slope (∼800 km), but some energy can be seen in the spectrogram at ∼12 s. Horizontal components are too noisy that can limit the ability to analyse these components. Hydrophone has shown to be very reliable in almost all the OBSs for all the frequencies due to a wider response of the instrument.

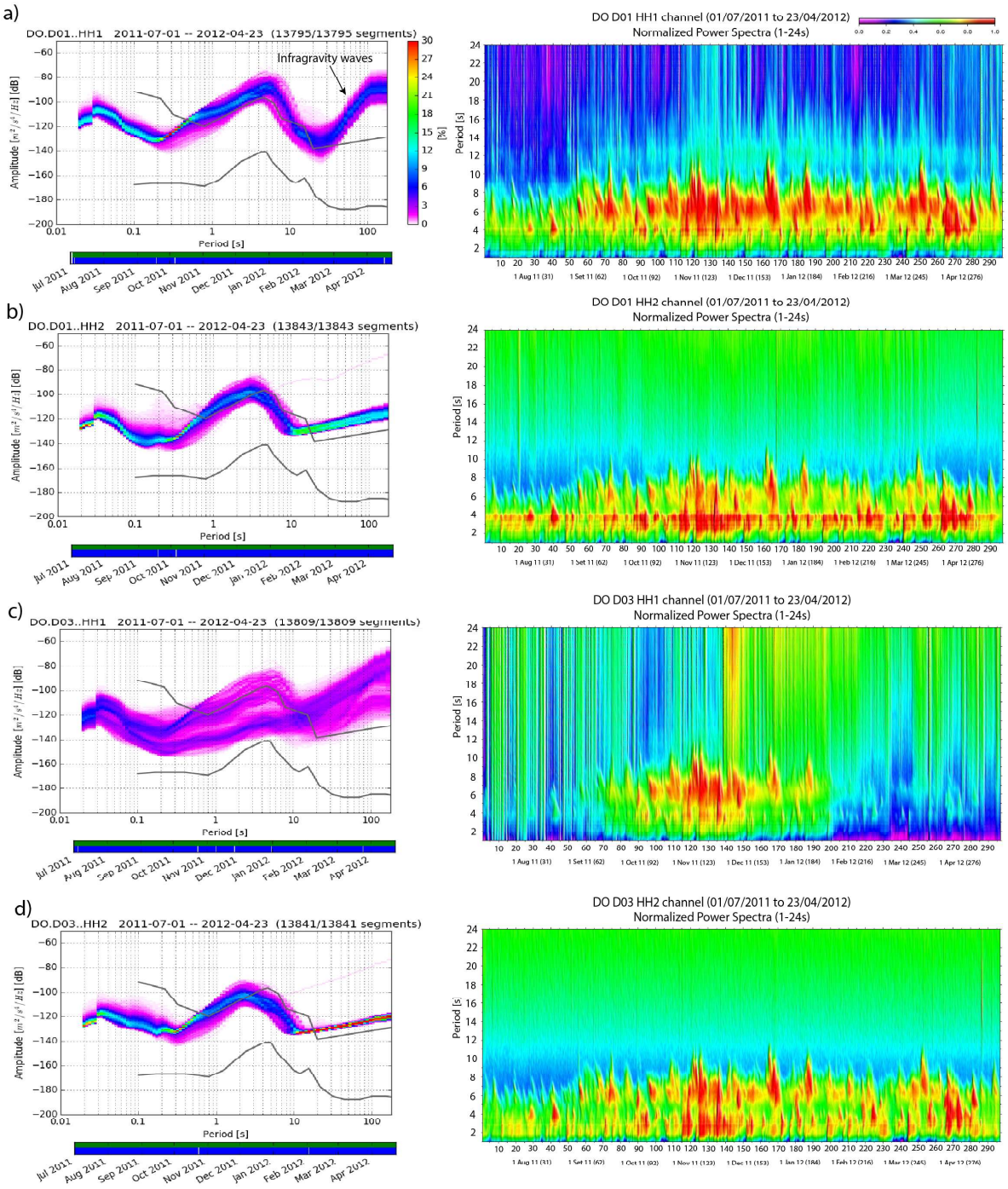

Figure 2.6: PPSD (left) and spectrogram (right) of seismic data recorded at stations D01 and D03 for the hydrophone and vertical component. a,c) PPSD and spectrogram of the hydrophone, where at station D03 is evident that the hydrophone did not work properly. Station D01 of the hydrophone shows the secondary microseismic energy and noise levels during the entire time OBS was deployed on the seabed, for the period band of 1-24s. b,d) Shows the vertical components, with especial attention at station D01 that shows the sediment resonance in the spectrogram at ∼4 s and is also seen in the peak of the PPSD.

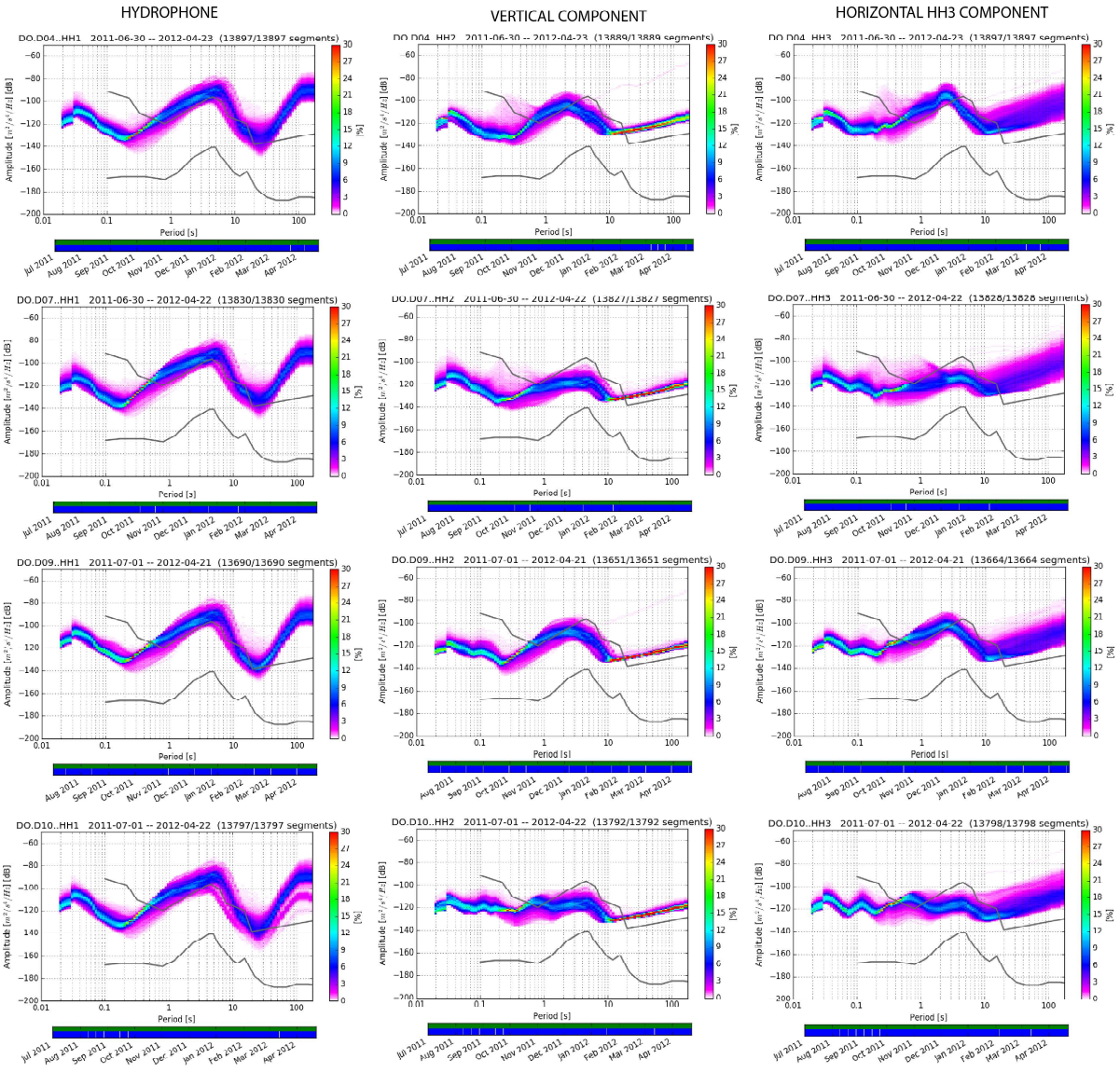

Figure 2.7: PPSD of the hydrophone, vertical and one horizontal component of the seismometer.

Chapter 3

Surface wave dispersion calculations using ambient seismic noise

3.1 Empirical Green's functions retrieved from ambient noise

For a long time, seismic noise was not thought to contain important information about the structure of the Earth because it was considered to contain unwanted energy that contaminated the seismic signals of interest, namely those of earthquakes and explosions. Later, it was realized that ambient seismic vibrations also contain useful information. *Aki* (1957) proposed to investigate the earth's structure using noise records. Nowadays, with the development of broadband seismic sensors sensitive enough to record ambient vibrations, ambient noise seismology has evolved and is one of the most widely used methods for imaging the Earth's structure.

The cross-correlation between seismic data recorded at two stations can be used to extract the Empirical Green's functions (EGFs) from random seismic wavefields. This principle has been successfully applied to ambient seismic noise (*Shapiro and Campillo*, 2004) and to the seismic coda (*Campillo and Paul*, 2003). The successful determination of EGFs from random wavefields requires the averaging of a large number of cross-correlations. The advantage of extracting ambient seismic noise is that the scattering is well distributed homogeneously. On the other hand, one of the disadvantages of this method is the bandwidth

that it is often limited.

In this chapter, ambient noise cross-correlations were computed for every pair of stations of the DOCTAR area to reconstruct the EGFs (*Shapiro and Campillo*, 2004; *Schimmel et al.*, 2011). The data were preprocessed as follows:

1. Necessary information of the stations was added in the header of the DOCTAR data, namely seafloor station coordinates, station name and components in Seismic analysis code (SAC).

2. The instrument response was removed in the frequency limits from 0.005882 Hz to 12 Hz.

3. For each pair of stations, the data were synchronized and trimmed the edges according the maximum begin of the two station pairs to get all the data with the same start and end time, as well as number of data points.

4. Finally, the data was downsampled to 10 samples per second to reduce computation time. We also consider the Nyquist frequency to avoid clipping some signals because we are only interested in the frequency band from 0.25 s to 25 s.

3.1.1 Cross-correlations of ambient noise

Next, we followed the method of Phase cross-correlation (PCC) described in *Schimmel et al.* (2011). This processing technique performs PCC as presented by *Schimmel* (1999), where the PCC is amplitude independent and therefore no preprocessing is required. PCC is a mathematical operation to quantify the phase coherence between two analytical signals. The analytical signal $S(t)$ is obtained by assigning the real time series $u(t)$ to the real part of $S(t)$ and applying the Hilbert transform $H(u(t))$ to the imaginary part of $S(t)$.

$$S(t) = u(t) + iH(u(t)) = a(t) \cdot e^{i\Phi(t)} \tag{3.1}$$

where $a(t)$ represents the envelope of the phase and $\Phi(t)$ is the instantaneous phase. PCC are thus defined in *Schimmel* (1999); *Schimmel et al.* (2011) as follow:

$$PCC(t) = \frac{1}{2T} \sum_{\tau=\tau_0}^{\tau_0+T} (|e^{i\Phi(t+\tau)} + e^{i\Psi(\tau)}|^\nu - |e^{i\Phi(t+\tau)} - e^{i\Psi(\tau)}|^\nu) \tag{3.2}$$

where $\Phi(\tau)$ and $\Psi(\tau)$ are the instantaneous phases of u_1 and u_2, t is the lapse time of PCC, τ_0 is the start time and T is the correlation window length.

In general, the classical cross-correlation geometrically normalized (CCGN) requires pre-processing such as normalization and spectral whitening of the data to eliminate energetic signals (e.g. earthquakes) that will otherwise dominate the correlations (*Bensen et al.*, 2007). The advantage of using PCC is that it is more sensitive than CCGN to determine the maximum correlation using the maximum number of samples, which is more sensitive to aligning the signals with the largest amplitudes. PCC improves the amplitude signal of the CC but may reduce the absolute correlation values (*Schimmel et al.*, 2011). Depending on the aim of the study, it is possible to decide which method to use: PCC or CCGN. For example, to find the highest energy signals the CCGN is a more recommended option.

The PCC script developed by *Schimmel et al.* (2011) can perform two types of cross-correlation: i) for the CCGN it applies a bandpass filter followed by normalization and spectral whitening of the data if desired (*Bensen et al.*, 2007) and ii) for PCC it simply applies a bandpass filter and then processes PCC.

3.1.2 Stacking of ambient noise cross-correlations

After obtaining the cross-correlation for each pair of stations by either PCC or CCGN, it can be applied two types of stacking: the linear stack and the time-frequency Phase weighted stack (tf-PWS) (*Schimmel and Gallart*, 2007; *Schimmel et al.*, 2011).

With the linear stack, only the signal amplitude is taken into account, regardless of whether the signal is coherent or not. On the other hand, the tf-PWS is a non-linear stacking that attenuates incoherent signals and allows for better signal identification, improving the Signal-to-Noise Ratio (SNR) (*Schimmel and Gallart*, 2007; *Schimmel et al.*, 2011). This method was first introduced by *Schimmel and Paulssen* (1997) to identify signals by their coherence. tf-PWS uses the S-transform (*Stockwell et al.*, 1996) to convert each cross-correlogram into the time-frequency domain (τ, f) with a Gaussian window function $\omega(\tau - t, f)$ centered at time τ and whose width is proportional to $|1/f|$. The

tf-PWS is written as follows:

$$c_{ps}(\tau, f) = |\frac{1}{N}\sum_{j=1}^{N}\frac{S_j(\tau, f)e^{i2\pi f\tau}}{|S_j(\tau, f)|}|^{\nu}, \tag{3.3}$$

where $S_j(\tau, f)$ is the S-transform of the j-th cross-correlogram trace and N is the number of PCCs. The stacking in the time-frequency domain $S_{pws}(\tau, f)$ is defined as a multiplication of the phase coherence $c_{ps}(\tau, f)$ with the S-transform of the linear stack of all the PCCs in the following way:

$$S_{pws}(\tau, f) = c_{ps}(\tau, f)S_{ls}(\tau, f) \tag{3.4}$$

Finally, the inverse of the S-transform is used to transform the stack from the time-frequency domain to the time domain.

3.2 Results

All cross-correlation and stacking was done using software developed by *Schimmel et al.* (2011). Before deciding on a method for cross-correlation and stacking, we ran a test on the data. In this test, the data was downsampled to 1 Hz and a bandpass filter was applied from 4 s to 20 s. Figure 3.1 shows an example of the test results of the different methods for extracting the EGFs using the PCC and CCGN as well as linear stacking and tf-PWS, for the station pair D03-D08. For CCGN, two types of normalization were used, 1-bit normalization and Running Absolute Mean Normalization (RAMN). The results show that the EGFs retrieved using PCC and tf-PWS have higher amplitude signal than the others. The linear stack is noisy for all types of cross-correlation, but the signal is still good enough to identify and extract the EGFs, at least for this pair of station. Results are also good with CCGN, RAMN and tf-PWS. Using the tf-PWS in the PCC or CCGN improves the signal significantly. However, the decision on which stacking method to use should depend on the goals and the type of signal to process.

In this case for ambient noise, it was decided to use PCC and tf-PWS to extract the EGFs from ambient noise with a time lags from -200 s to 200 s.

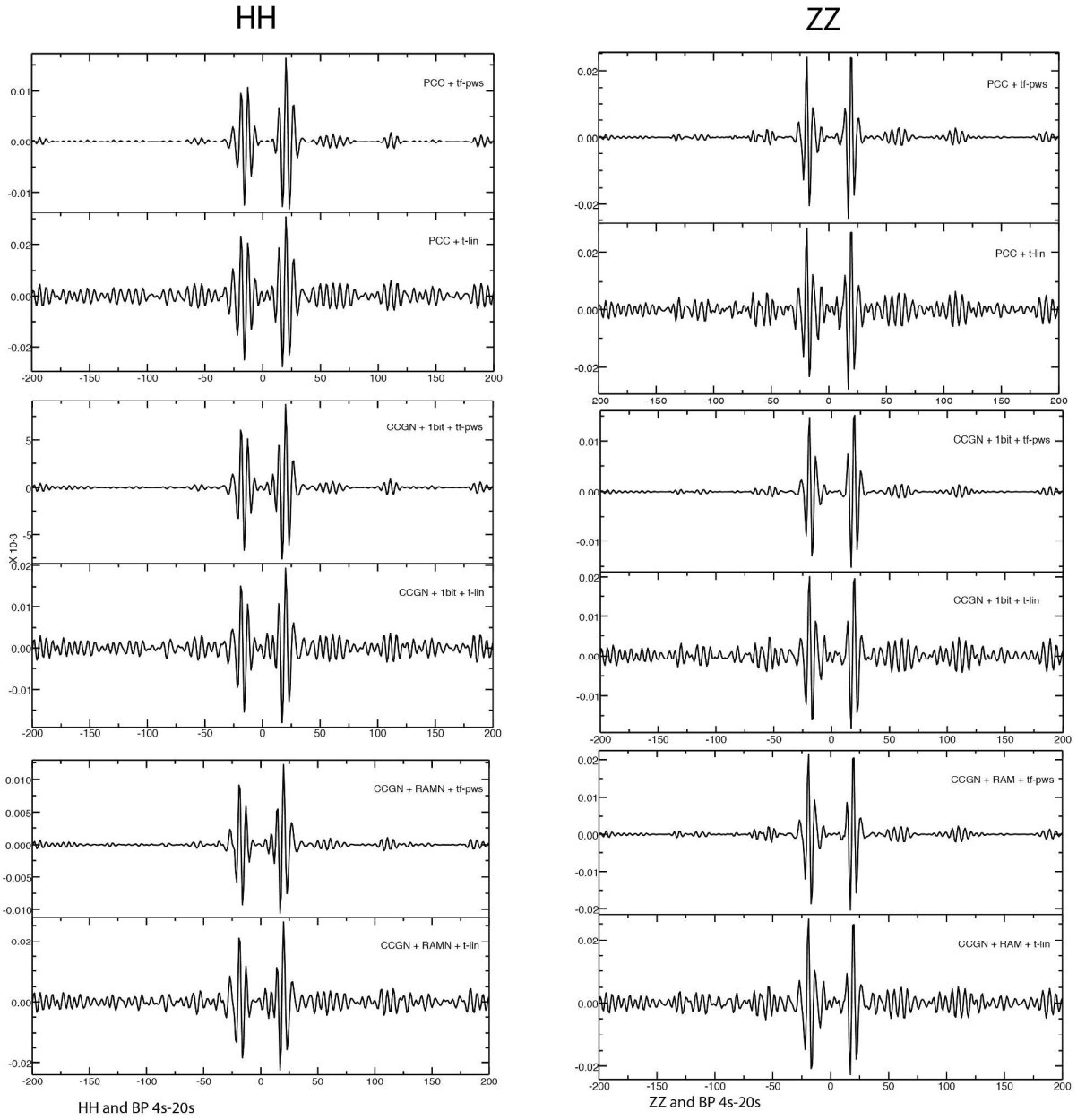

Figure 3.1: Comparison of different cross-correlations and stacking for the hydrophone and vertical with a bandpass filter from 4 s to 20 s. The cross-correlations were computed using the PCC and the classical cross-correlation applying a normalization and a whitening to the data. The stacking process were computed with the tf-PWS and linear stack. In general, using PCC+tf-PWS for ambient noise shows a higher amplitude signal in the extraction of the EGFs than the CCGN.

3.2.1 Empirical Green's Functions

Figure 3.2 shows the evolution of the ambient noise cross-correlations in time, for the hydrophone, over the period when the OBSs were installed. On top is the bathymetry profile between the two stations. This figure was stacked every 20 days and shifted by one day. For the first 50 days, the microseismic noise energy was not very strong as it was not the storm season for the North Atlantic Ocean. Towards the middle of August, the energy increased and remained more stable during the rest of the time. Station pair D01-D09, indicates that the noise is not homogeneously distributed in the medium. The noise distribution can also be affected by the bathymetry between stations. First, in the causal part, the energy is traveling from station D01 to D09 located at South (Figure 2.1) and the acausal part is the noise energy traveling from station D09 to D01. Between stations D09 to D01 it is observed one small mountain, which also affects the energy traveling from south to north. On the other hand, for the station pair D01-D11 there is a good recovery of the EGFs on both sides. In addition, the bathymetry between the stations is almost flat, which allows energy to travel from one station to another without any restrictions. The lack of successful extraction of the EGFs in the station pair D01-D09 is probably related to the directivity of the noise, bathymetry or to local site effects, such a very strong attenuation. To observe the dominant direction of propagation energy noise in the array, we plotted the maximum amplitudes of each EGFs of the acausal and causal sides with the direction of seismic energy propagation. Figure 3.3 show the results with most of the energy coming from the northwest propagating towards the southeast.

The figure 3.4 shows the results of the cross-correlation of ambient noise as a function of distance for the hydrophone and the vertical component. The results show a much clearer EGFs for the hydrophone than for the vertical component due to the higher amplitude signal of the hydrophone. However, in the vertical component it is possible to identify the fundamental mode and another mode with less energy and faster speed. In all four cross-correlograms, the moveout is $\sim$1.3 km/s. As observed in the PPSD and spectrograms of the chapter 2, some sediment resonance is seen in the period band of the microseismic noise in the vertical component complicating the extraction of the EGFs from the seismometer records.

On the other hand, the horizontal components were downsampled to 1 Hz, since for

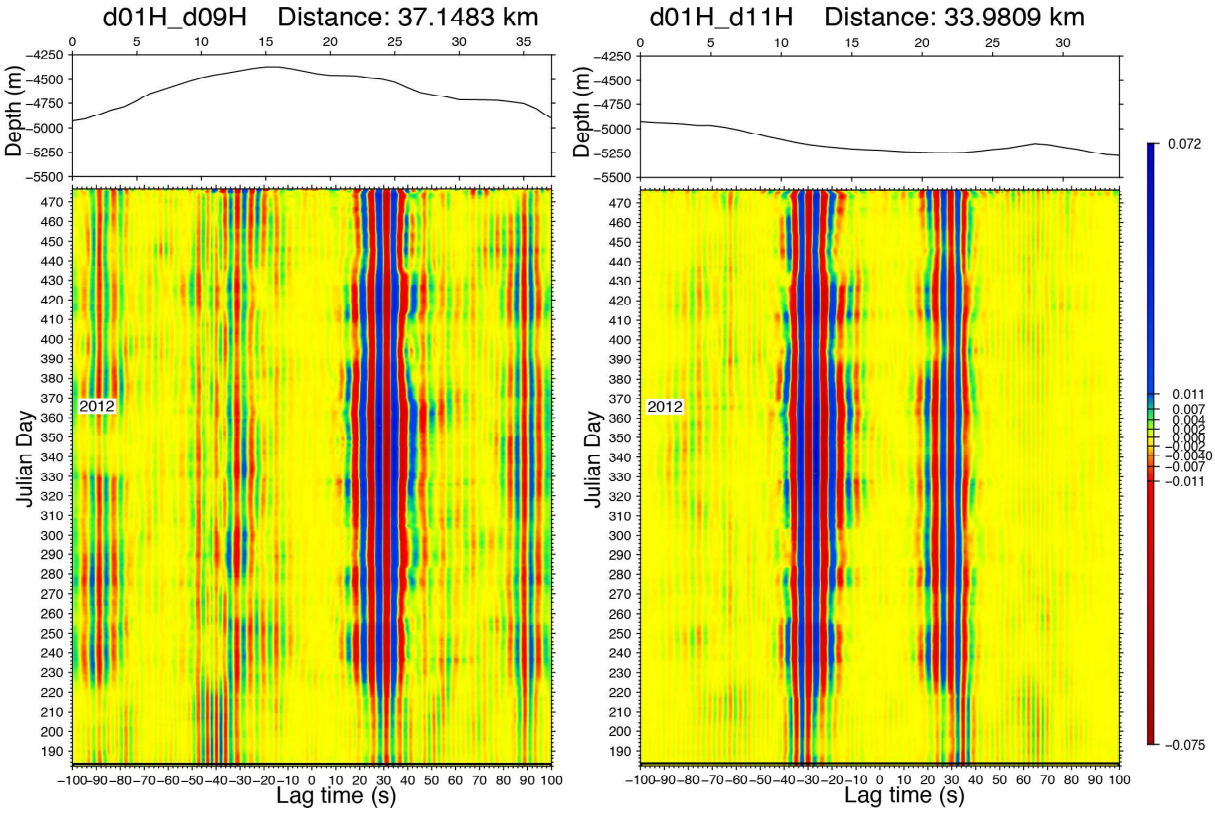

Figure 3.2: Stack of ambient noise cross-correlations between two different pairs of stations: D01H-D09H and D01H-D11H. The stack is computed using a moving window with a length of 20 days and shifted by one day over a total of 10 months of data. On top of each stacking are the bathymetry profile between the two stations. The noise sources fluctuated during the period when the OBS were installed. Noise sources were weak for the first 50 days and then again in February and mid-March. There is a clear asymmetry for the station pair D01H-D09H in the EGFs, which could result from the direction of propagation of the noise or from local site effects. On the other hand, the station pair D01H-D10H shows a more symmetric recovery of the wavefield on both sides.

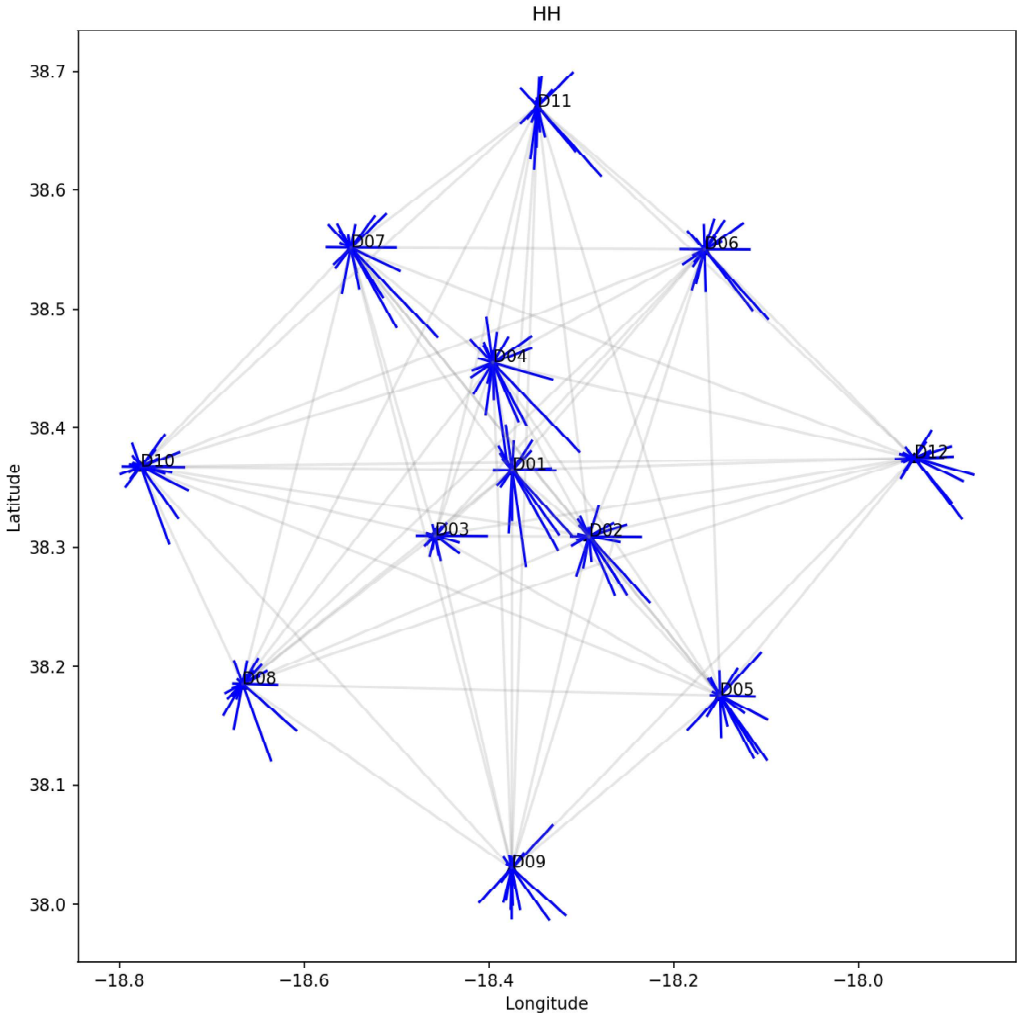

Figure 3.3: Illustration of the direction of the seismic energy propagation of the hydrophone for the causal and the acausal part, where the units are arbitrary. The dominant energy comes from the northwest and propagates towards the southeast.

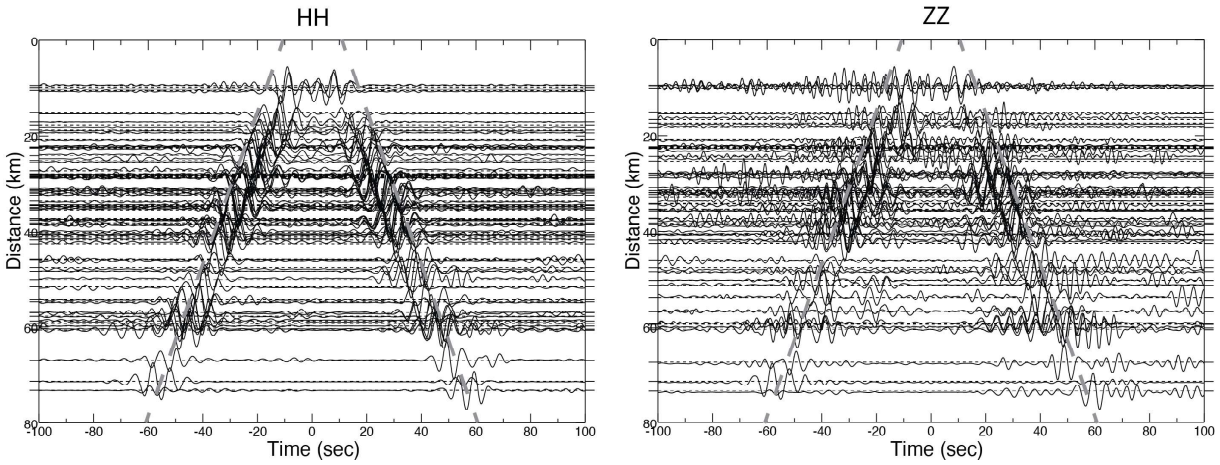

Figure 3.4: EGFs as a function of inter-station distance for the hydrophone and the vertical components. The EGFs were computed using the PCC and the tf-PWS for the 10 months in which the OBS were deployed. These components were downsampled to 10 sps and a bandpass filter from 4 Hz to 0.04 Hz were applied. The figure clearly show that the hydrophone has a much clear and less noisy extraction of the EGFs.

this component the main interest is focused on the period band of the surface waves. The horizontal components were rotated to extract the EGFs of the radial and transverse components using a bandpass filter from 4 s to 25 s. The results are shown in the figure 3.5, where is observed the propagation of signals with two different velocities for the radial component. In the transverse component is observed the Love wave fundamental mode. Because of the proximity between the OBS stations, the velocities of the fundamental mode of the Rayleigh wave on the radial component and the fundamental mode of the Love wave on the transverse component appear to be very similar in velocities, but with the Love waves having slightly higher velocities.

Considering the reciprocity theorem, the Green's functions between two stations should be the same, independently of the direction of wave propagation. However, this does not happen due to the inhomogeneous distribution of noise sources such as storms. In order to obtain symmetric cross-correlations, the mean of the the acausal and causal parts of the cross-correlations were calculated (Figure 3.6). Symmetric stacking provides a more complete information about the path in both directions because it averages out the effect of inhomogeneously distributed noise sources and increases the arrival energy of coherent phases over incoherent signals.

To obtain the symmetric correlation with tf-PWS, the acausal and causal parts of the daily cross-correlogram were truncated. The waveform of the acausal part was reversed

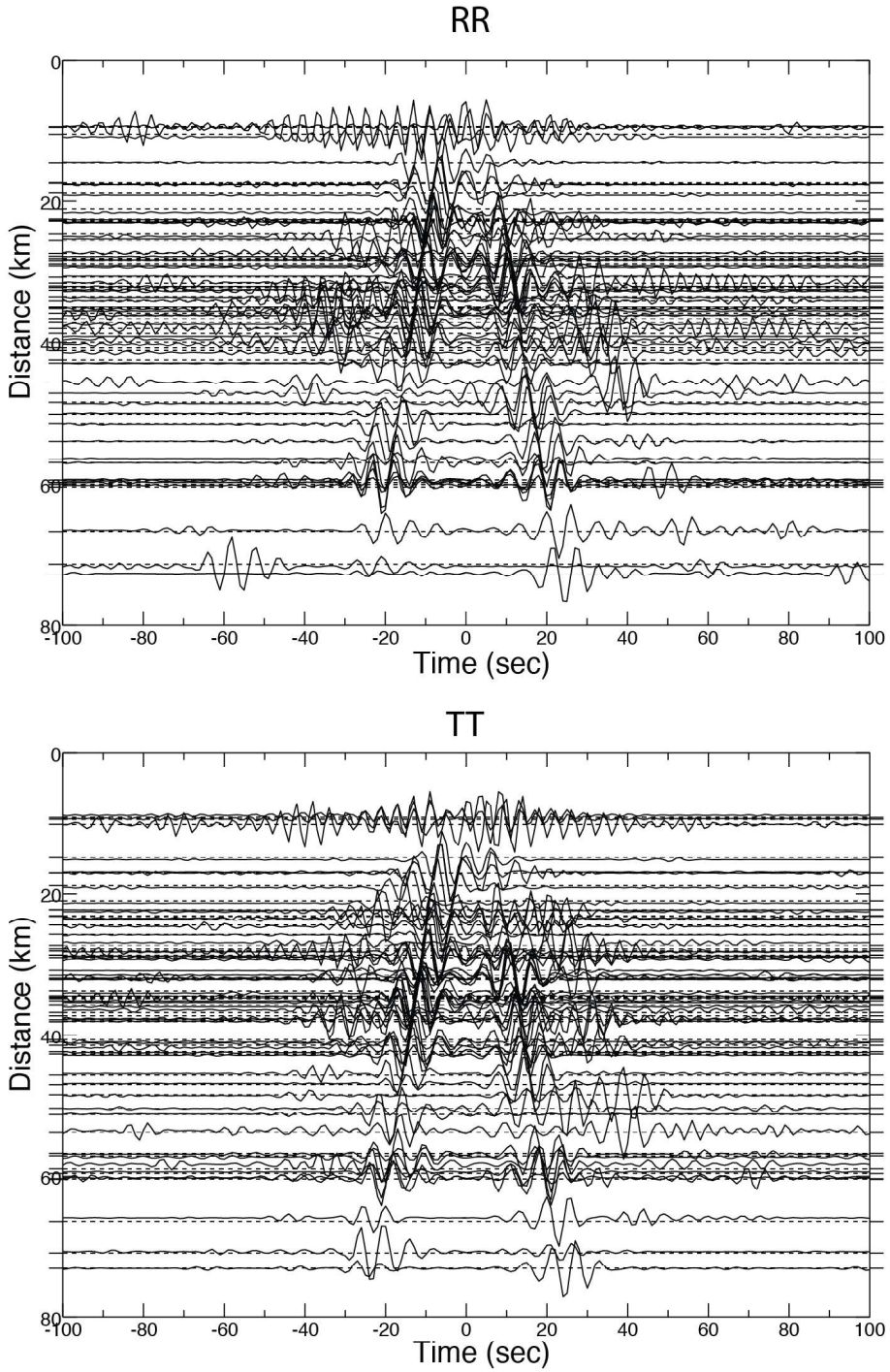

Figure 3.5: EGFs as a function of interstation distance for the horizontal components. These components were downsampled to 1 and a bandpass filter from 4 s to 25 s were applied. The figure show in the radial component the fundamental mode and the first higher mode of the Rayleigh waves. On the contrary, the transverse component only shows the fundamental model of the Love wave.

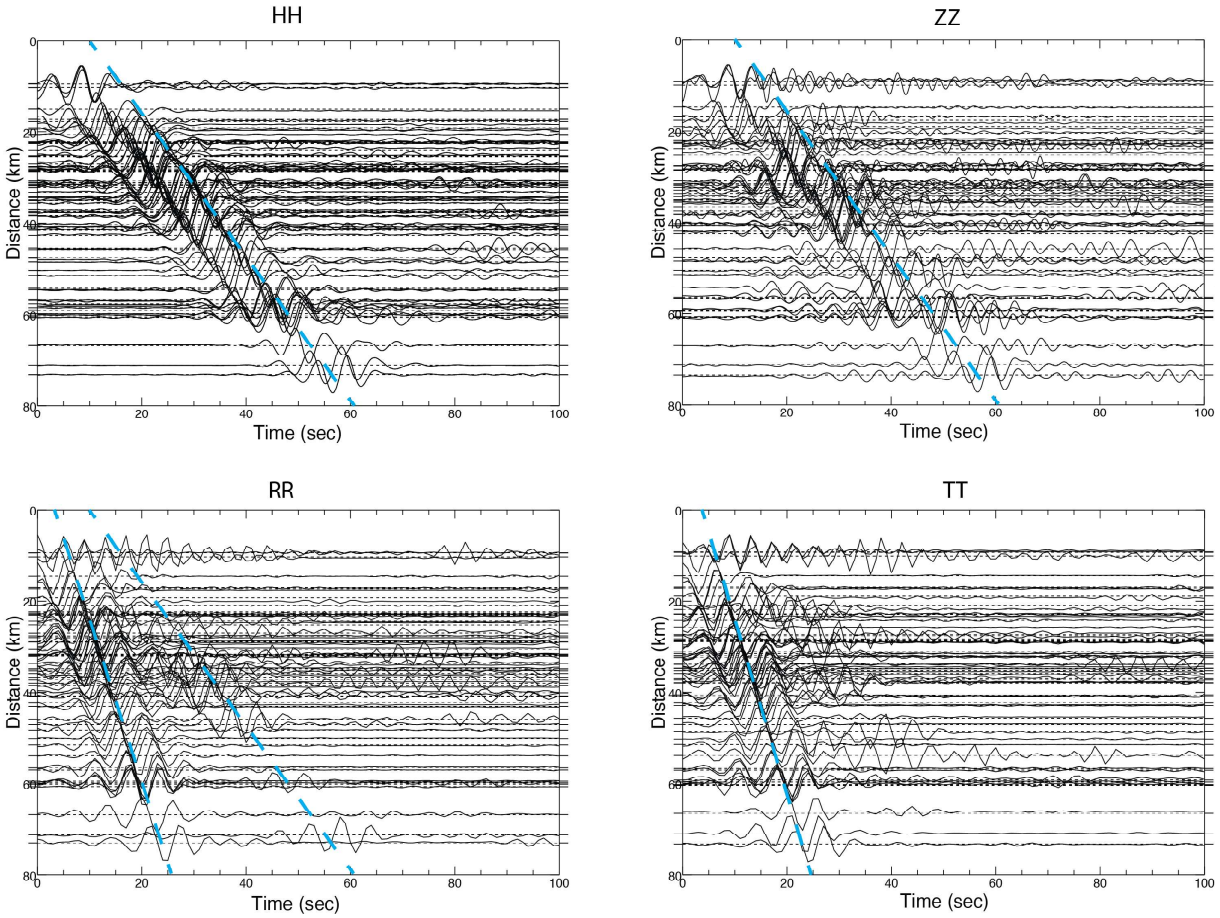

Figure 3.6: Symmetric stacking of the EGFs as a function of the interstation distance for all the components used in this study. Dashed blue lines show the moveout for each component. The figures show the fundamental mode for all the components and for the radial shows additionally the first higher mode.

and the reversed acausal and causal parts were stacked. Figure 3.6 shows the results of the symmetric EGFs as a function of distance. The fundamental mode of the Rayleigh wave has a moveout of $\sim$ 1.3km/s, as observed in the hydrophone, in vertical and radial components. The radial component shows the first higher mode of Rayleigh waves with a moveout of 3.1 km/s. Finally, in the transverse component, the fundamental mode of Love waves can be seen with a velocity of $\sim$3.3 km/s.

3.2.2 Group and phase velocity measurements

Once the EGFs were extracted, the dispersion curves of group and phase velocities were measured. In order to calculate group velocity, it was used the Multiple filter technique (MFT) (*Dziewonski et al.*, 1969; *Herrmann and Ammon*, 2002). In the MFT, the waveform is filtered in a sequence of narrow bandpass bands with a Gaussian filter (*Dziewonski et al.*, 1969). Then, the group velocity is measured based on the narrow

band seismograms. Unfortunately, when measuring the group velocity with the MFT, the correct dispersion curve had to be selected manually, which was time-consuming. This procedure allowed the selection of not only the dominant mode but also other modes.

In addition, the measurement of group velocity was tested using the method of *Schimmel et al.* (2017). This method uses the random sampling and subset stacking strategy to stack the daily cross-correlations and robustly estimate the maxima group velocity. The group velocity is determined in the time-frequency representation (TFR) by finding the maximum amplitude as a function of frequency for each subset. The tracing of the group velocity curve starts at the lowest frequency and the largest maximum energy and gradually moves to the higher frequencies after the previous measurement of the group velocity. The user can decide how many subsets of tf-PWS will be used. In this case, it was selected 30 subsets for the test. A minimum of 60 percent of the required number of detections clustered around the medium group velocity were chosen. The median of the group velocity subsets is calculated as a function of frequency and the final group velocity curve is shown in black along the likelihood of the possible group velocities for each subset in white.

Figure 3.7 and 3.8 shows the dispersion curves for two pair of stations, D01-D10 and D09-D11, obtained with the MFT and the time-scale phase-weighted stack for 0 slowness & group velocity (ts-pws0-ug). The hydrophone and vertical components in figure 3.7 show similar results in the extraction of the group velocity dispersion curves, with the difference that ts-pws0-ug automatically obtains the dispersion curve according to the maxima energy but does not extract other modes. In figure 3.8 it is shown the results for the horizontal components, displaying more modes, especially in the radial component where is observed the fundamental and the first higher mode. With MFT the surface wave modes of the Earth can be selected manually based on the experience of the analyst.

To measure phase velocity, it was used the automated Frequency-time analysis (FTAN) (*Levshin and Ritzwoller*, 2001). Similar to MFT, FTAN applies a series of narrowband Gaussian filters to the EGFs by first constructing a 2-D plot of the power of the signal as a function of time in the raw signal. The method selects the arrival based on the local power maximum along the period or frequency axis; this selection is called 'raw'. Then the method applies a phase-matched filter or antidispersion based on the initial parameters

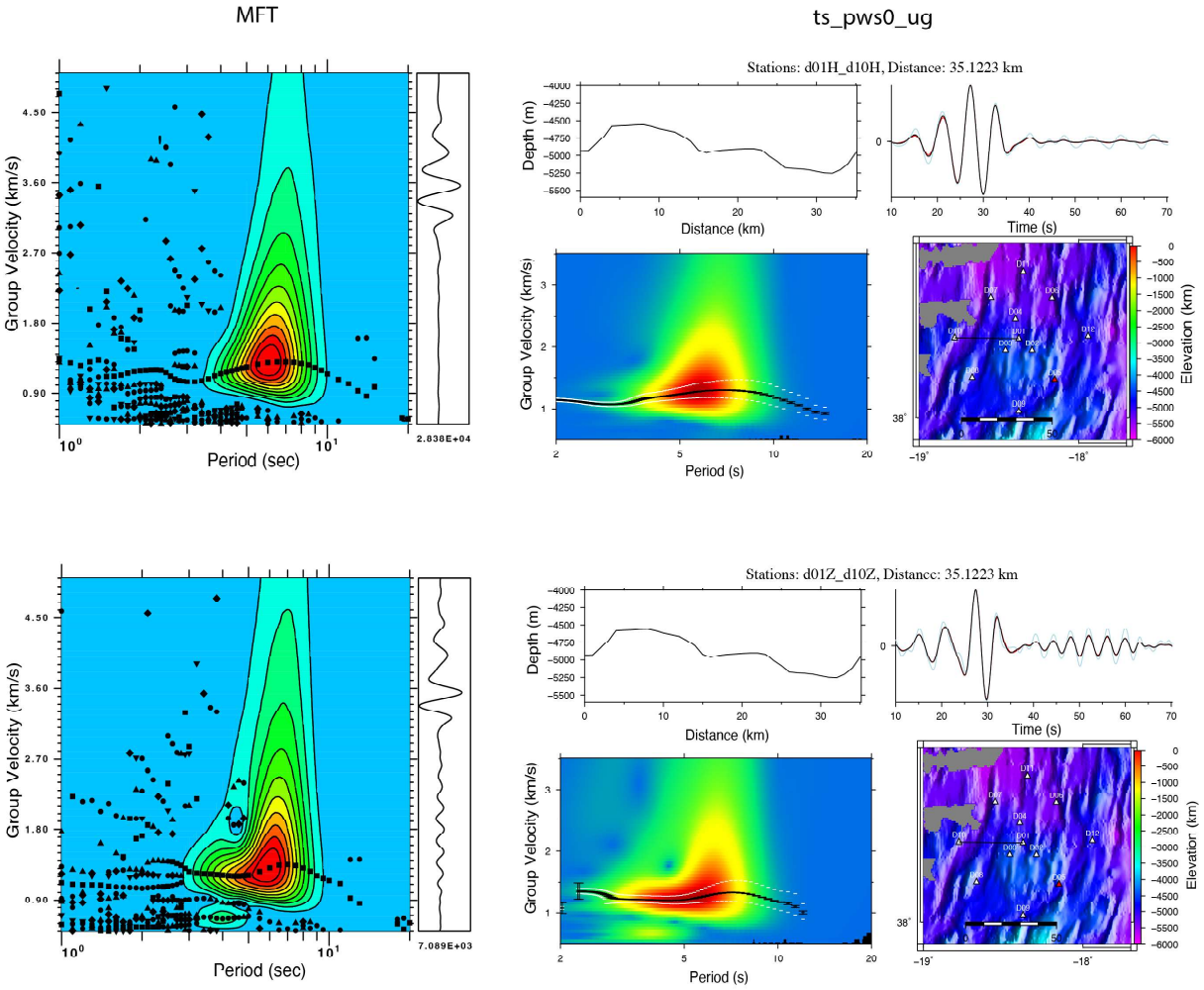

Figure 3.7: Extraction of group velocity using two different methods: MFT and ts-pws0-ug, for station pair D01-D10, hydrophone and vertical components. The selection of the group velocity is easier in the hydrophone data because of the higher amplitude signals.

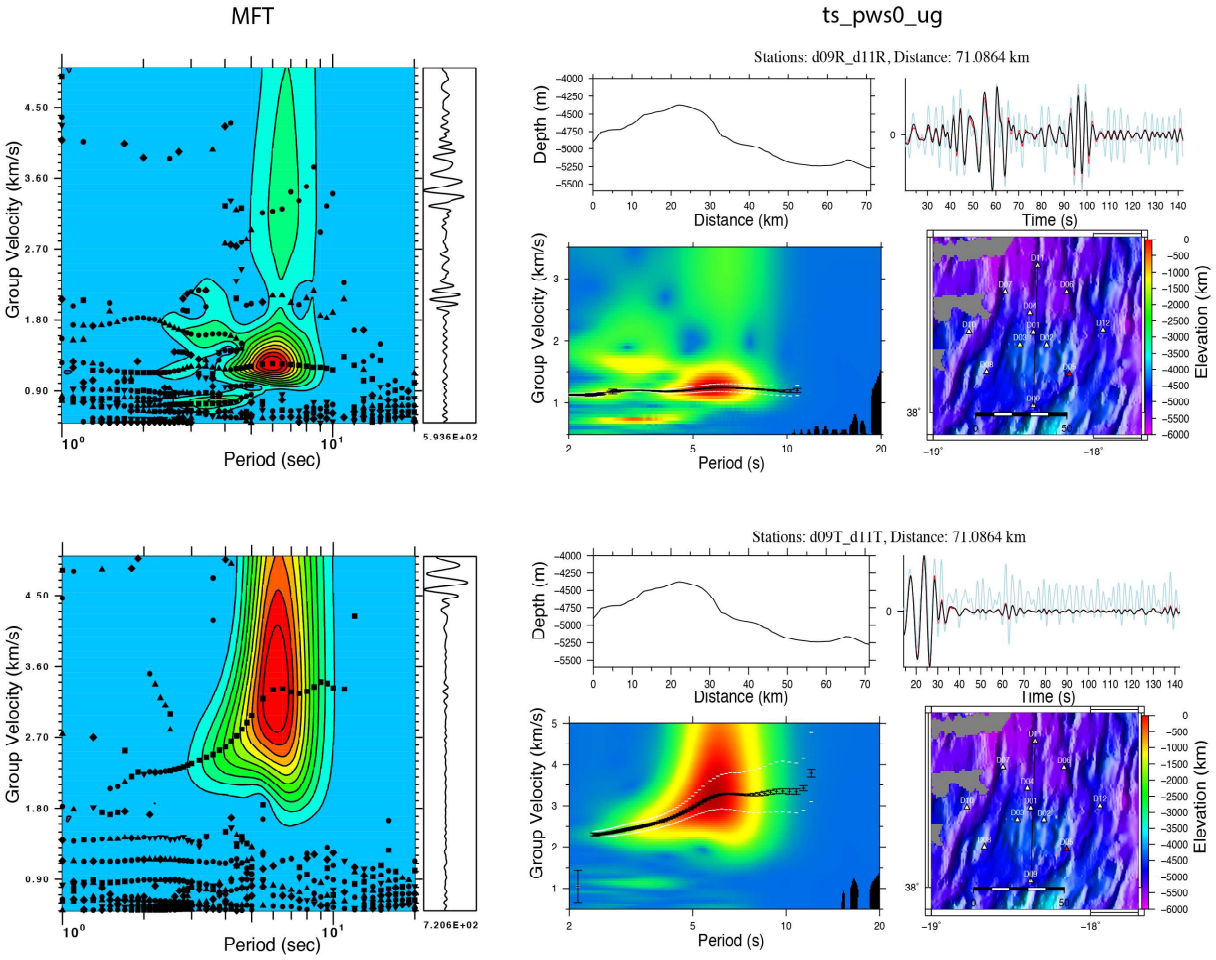

Figure 3.8: Comparison of the extraction of group velocity using two different methods: MFT and ts-pws0-ug, for the station pair D09-D11, using the horizontal components. In the radial component, ts-pws0-ug selects only the dispersion curve with the maxima energy, ignoring other higher modes. MFT performs better in this case because we can manually select all observed modes.

such as the phase-matched filter and the period band of interest. The phase-matched filter applies a series of wider Gaussian filters to improve the frequency resolution. The method later identifies and removes the contaminating noise from the signal. Finally, FTAN again creates a 2-D plot, now using the clean waveform by tracking the dispersion curve. The group velocity can also be determined by FTAN using the time derivative of the phase velocity plus a constant.

3.2.3 Surface waves modelling

To compare the fit between modelling and the group and phase velocities observations as a function of the period, synthetic eigenfunctions were computed (*Takeuchi and Saito*, 1972; *Dahlen and Tromp*, 1998; *Yang et al.*, 2010). The initial model to compute synthetic eigenfunctions was obtained by averaging all stations for each layer from Figure 1.4a.

Figure 3.9 shows all the dispersion curves obtained with ambient noise for the hydrophone, vertical and horizontal components for group and phase velocity of Rayleigh and Love waves. The phase velocity dispersion curves for the hydrophone and vertical components were extracted using the phase-matched filtering of FTAN.

Figure 3.9a,c, compare the group and phase velocities dispersion curves of Rayleigh waves for the hydrophone and vertical components with the eigenfunctions. It is observed a good fit between the data and the eigenfunctions. Conversely, in the group and phase velocities of the Love waves, the eigenfunctions are slightly faster than the results and do not strictly fit the dispersion curves. This is because the Love waves are more sensitive to the Earth's structure, so even a small change in the velocity of the solid Earth affects the dispersion curves. The Rayleigh wave group velocity dispersion curves below 4 s is more scattered due to sediment thickness, and also beyond 10 s where minimum velocity is related to the water layer thickness above each OBS.

In addition, in the Figure 3.9b,d shows similar dispersion curves, but with the average (yellow curve) of the observed dispersion curves for group and phase velocities of Love and Rayleigh waves of the hydrophone and vertical components. The period range of extracted group velocity of Rayleigh wave is between 4 s and 12 s. On the other hand, the Love wave of group velocity measurements ranges from 3 s to 9 s for the average dispersion curves. For the velocity maps of group velocity of Love wave, it is only used

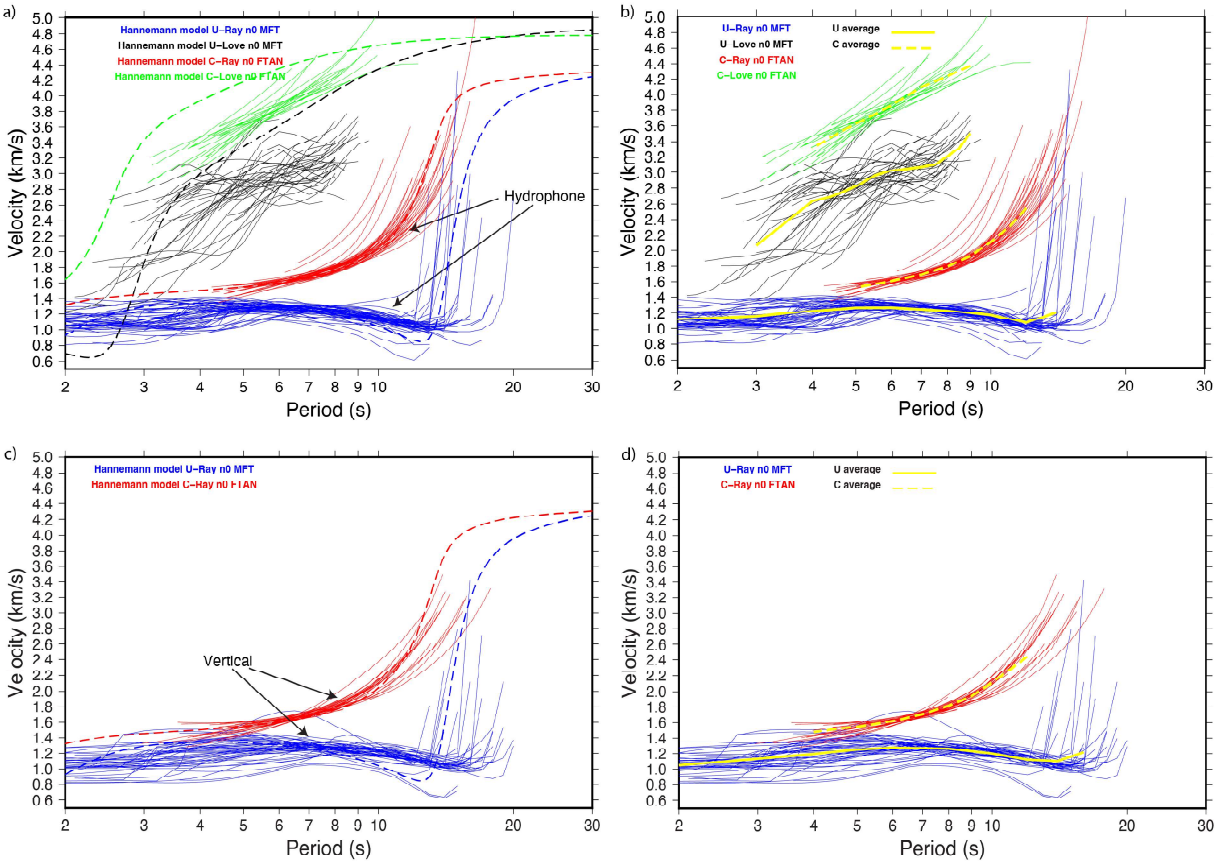

Figure 3.9: Group and phase velocities dispersion curves of Rayleigh and Love waves extracted from ambient noise. a) Synthetic eigenfunctions obtained for Rayleigh and Love wave (Dashed lines). b) Plot of the average of each set of dispersion curves extracted. c) and d) Same as a) and b) but for the vertical component.

dispersion curves between 4 s and 8.5 s. For phase velocity of Rayleigh wave, the period range extracted for the hydrophone is on average between 5 s and 12 s. Finally, the phase velocity of the Love waves, only the average range between 4 s and 9 s were used for the shear velocity inversion in chapter 7 because of the lack of many dispersion curves to obtain the velocity maps.

3.3 Summary

In general, it was used the PCC and the tf-PWS to extract the EGFs from ambient noise. The dominant energy comes from the northwest and propagates towards the southeast. The hydrophone showed a higher amplitude signal in comparison with the vertical component. The horizontal components were rotated and cross-correlated to extract the EGFs in the radial and transverse component. Symmetric stacking was applied to increase the arrival energy of all the paths of the station pairs.

It was applied MFT to obtain group velocity and FTAN to calculate phase velocity dispersion curves. Figure 3.9 shows all the ambient noise dispersion measurements extracted with seismic ambient noise to investigate the lithospheric structure of the study region.

In addition, data obtained with the hydrophone was used due to the number of dispersion curves are higher than those for the vertical component and the higher amplitude signal in the CC step.

Appendix section

Noise fluctuations for pairs of stations. The noise sources are stronger in the NW-SE direction so when the stations pairs are perpendicular to the direction of propagation of the energy, the recovery of the EGFs are better in terms of amplitude. On top of each figure are the bathymetry profile between stations.

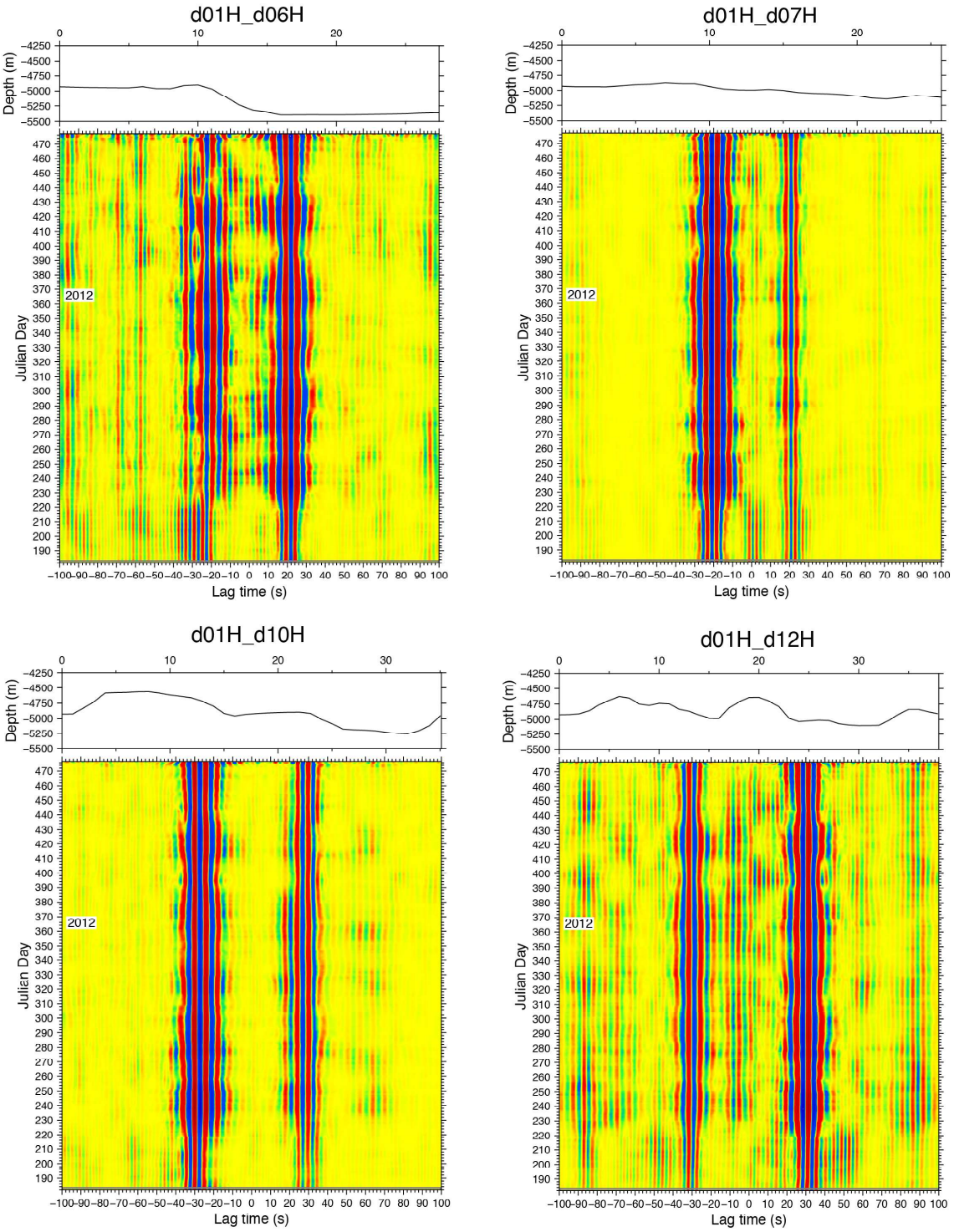

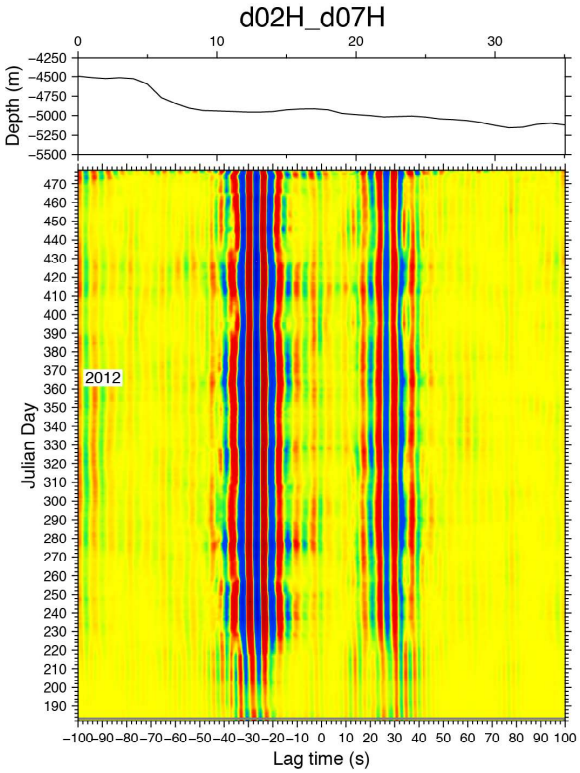
d02H_d07H
Depth (m)
Julian Day
2012
Lag time (s)

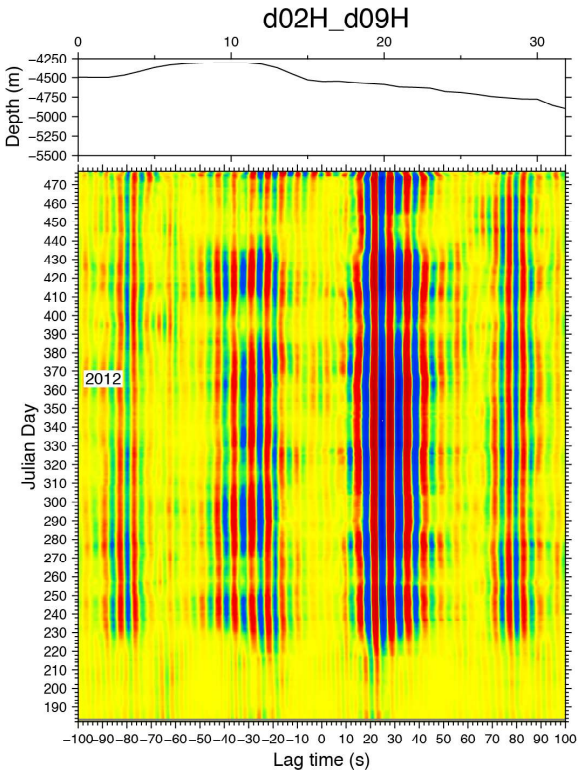
d02H_d09H
Depth (m)
Julian Day
2012
Lag time (s)

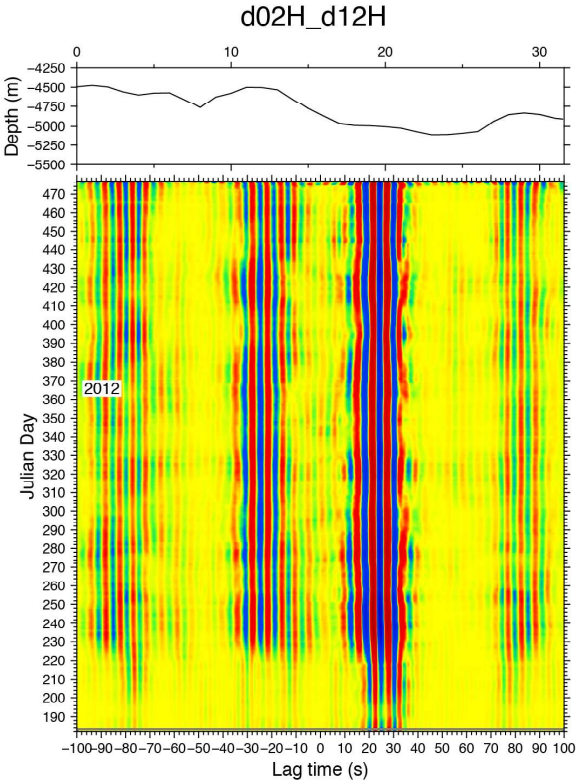
d02H_d12H
Depth (m)
Julian Day
2012
Lag time (s)

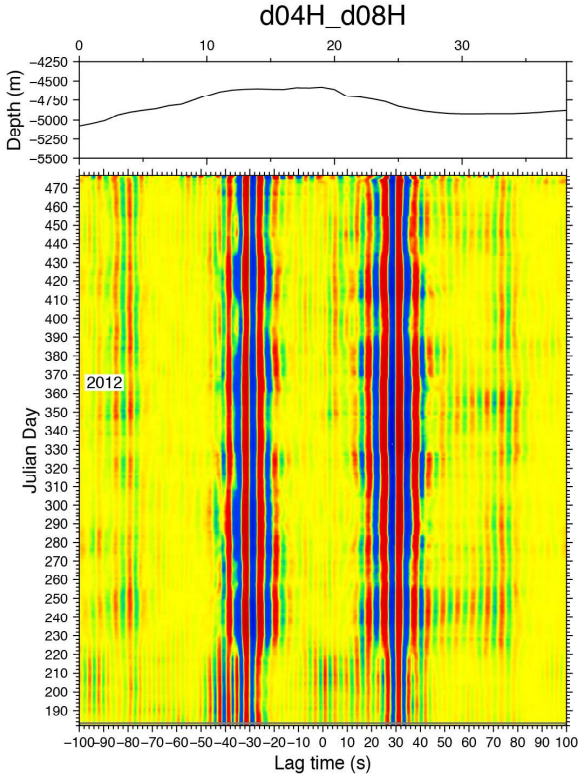
d04H_d08H
Depth (m)
Julian Day
2012
Lag time (s)

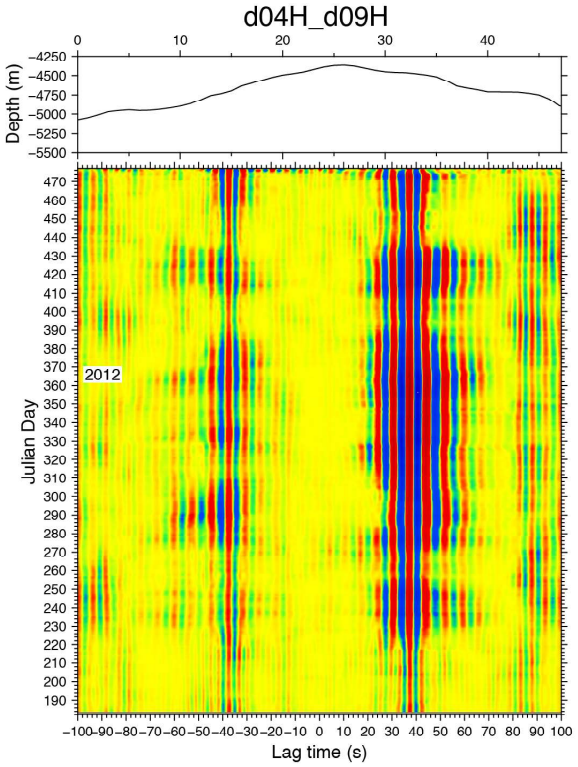
d04H_d09H
Depth (m)
Julian Day
2012
Lag time (s)

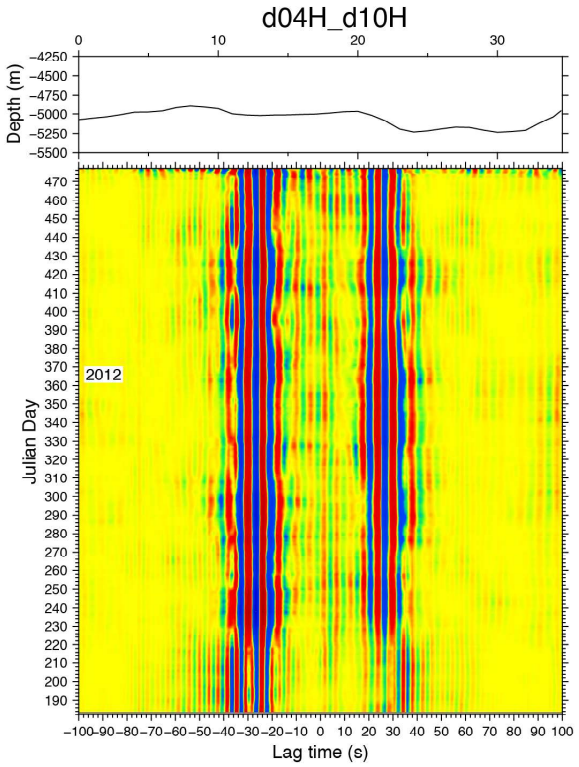
d04H_d10H
Depth (m)
Julian Day
2012
Lag time (s)

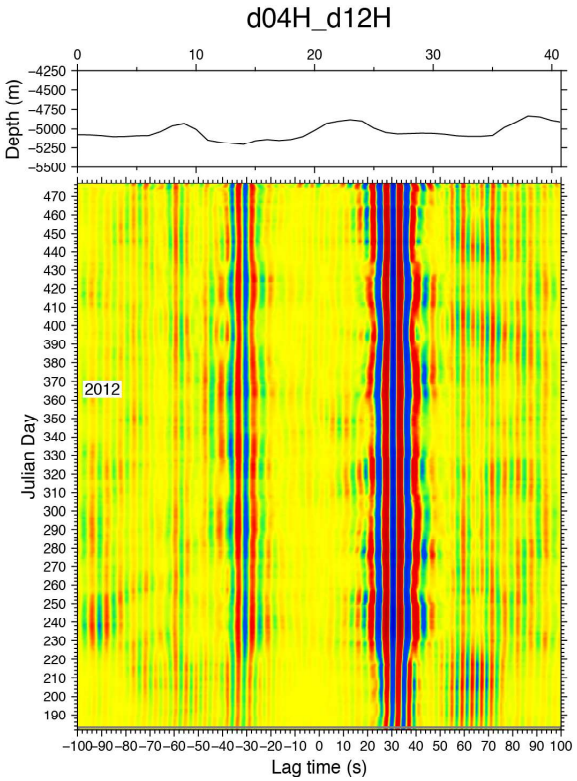
d04H_d12H
Depth (m)
Julian Day
2012
Lag time (s)

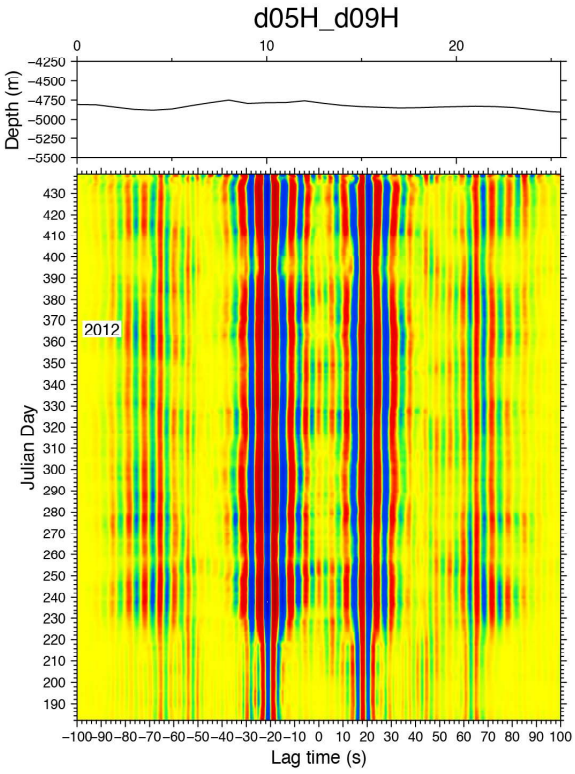
d05H_d09H
Depth (m)
Julian Day
2012
Lag time (s)

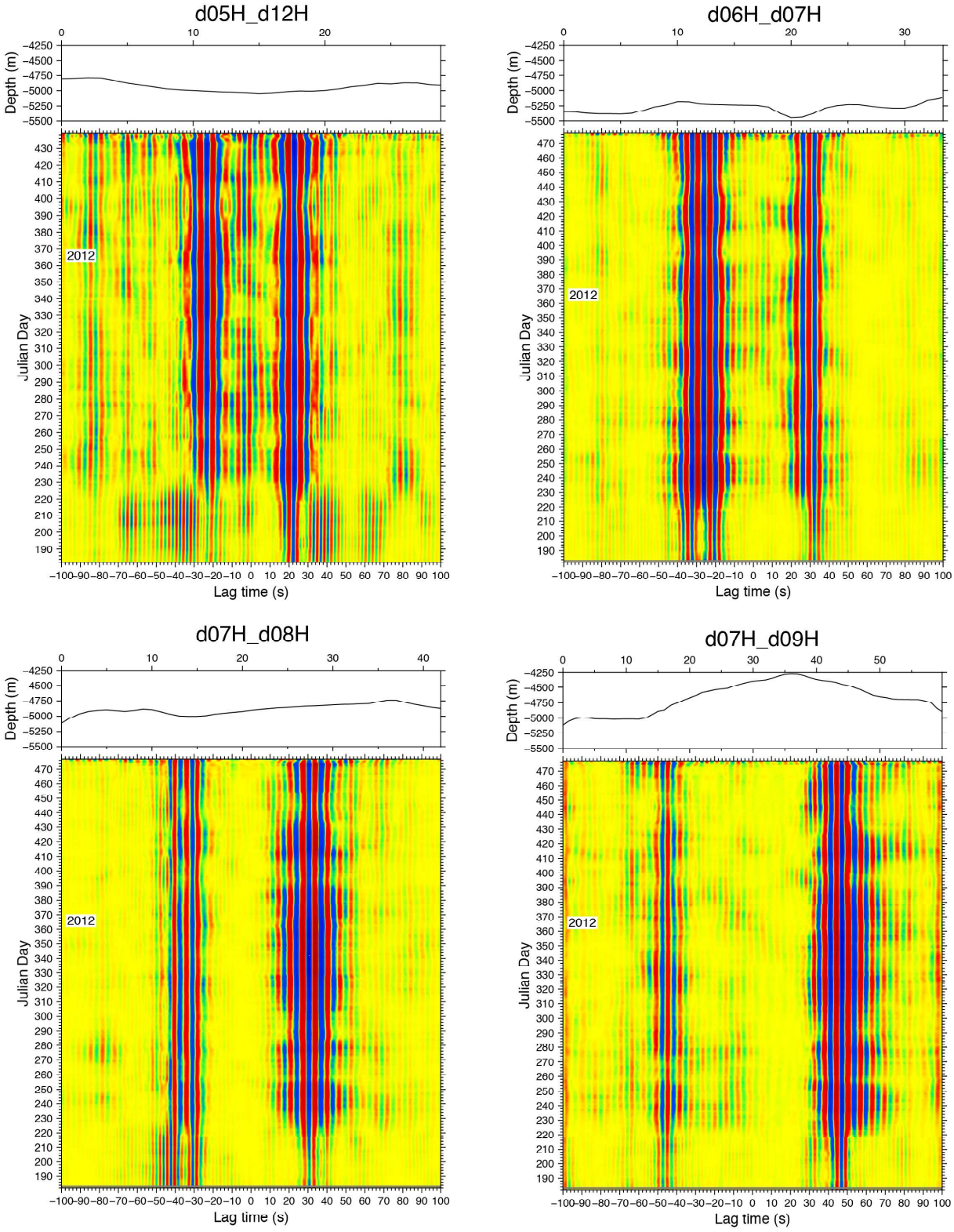
d05H_d12H
d06H_d07H
d07H_d08H
d07H_d09H
Depth (m)
Julian Day
Lag time (s)
2012

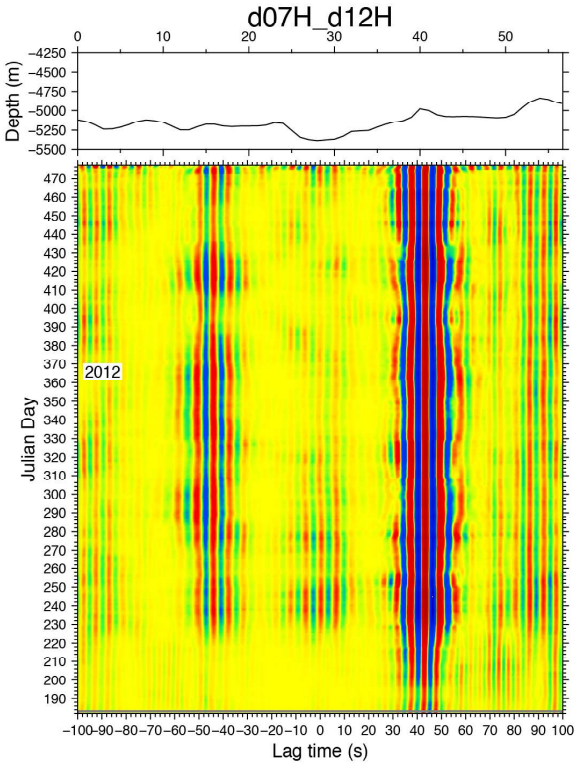
d07H_d12H
Depth (m)
Julian Day
2012
Lag time (s)

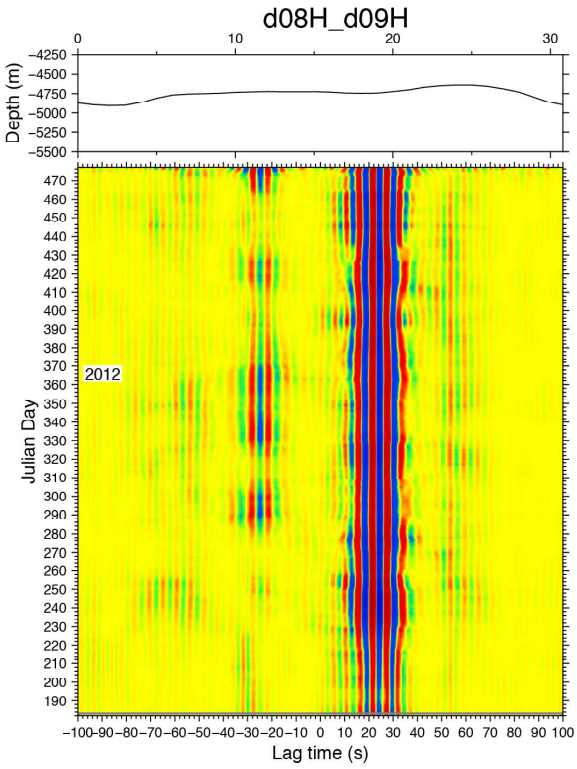
d08H_d09H
Depth (m)
Julian Day
2012
Lag time (s)

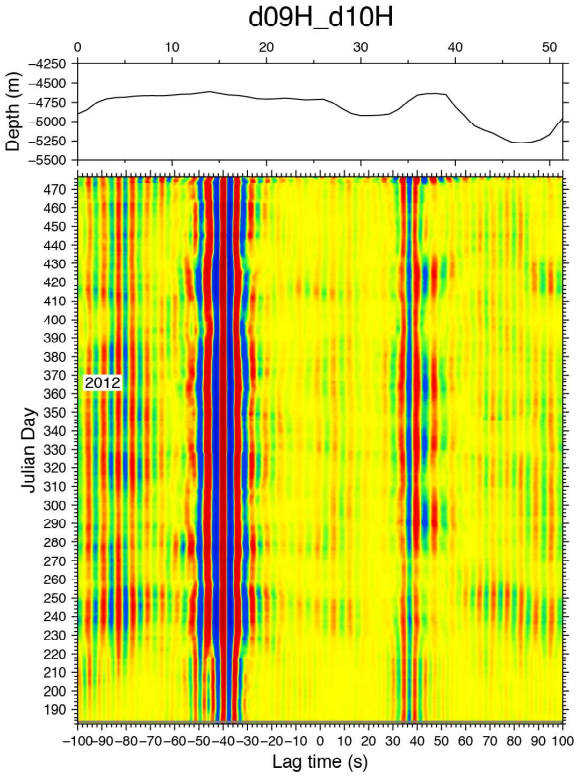
d09H_d10H
Depth (m)
Julian Day
2012
Lag time (s)

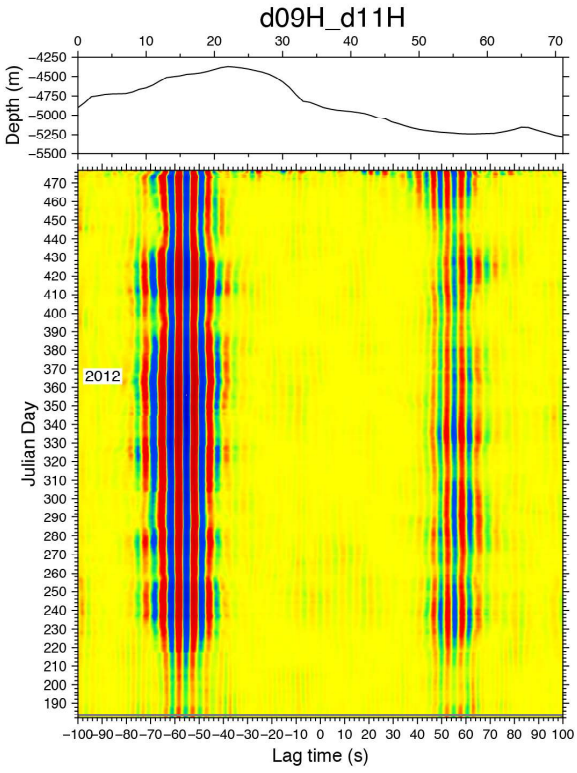
d09H_d11H
Depth (m)
Julian Day
2012
Lag time (s)

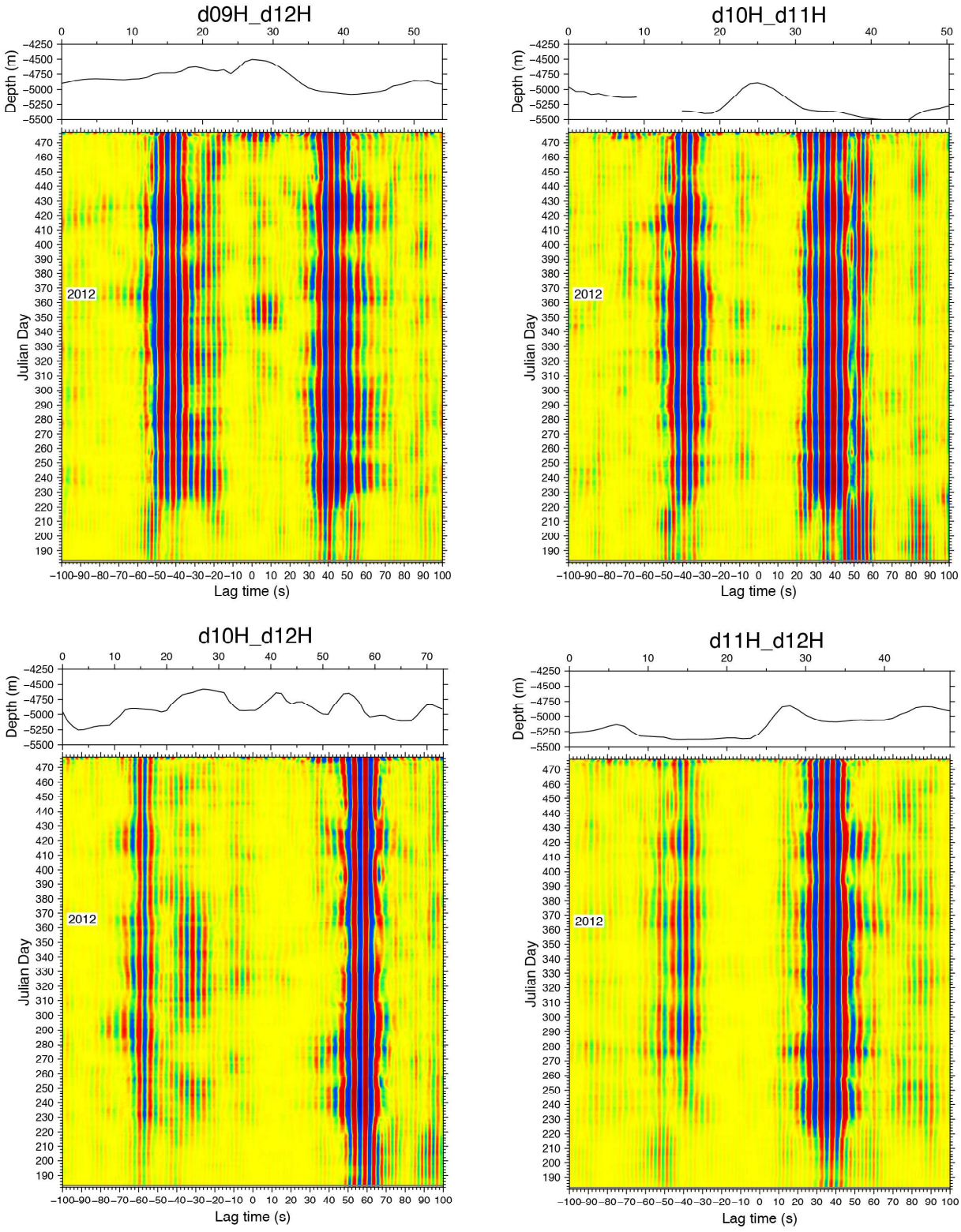
d09H_d12H
d10H_d11H
d10H_d12H
d11H_d12H
Depth (m)
Julian Day
Lag time (s)
2012

Chapter 4

Two-station method

4.1 Introduction

The two-station method uses the signal from distant high-magnitude earthquakes to study the average local structure between the two seismic stations. This method was first presented by *Sato* (1955), and then applied in several local studies. Decades later, the method was improved by *Meier et al.* (2004) and automated by *Soomro et al.* (2016). The two-station method reduces the influence of the uncertainty of the source parameters and decreases the problem of the 2π ambiguity of the phase velocity measurements due to the relatively small distances between the stations. For each pair of stations, the teleseismic records are cross-correlated, from which the phase velocity can be measured.

Due to the limitation of the phase velocity dispersion curves with ambient noise extracted only at short periods, the two-station method will complement the computation on the dispersion curves at longer periods.

4.2 Method

When assessing the dispersion corresponding to the path between two stations, the phase difference of Love and Rayleigh waves propagating alongside the great circle path between two stations, is measured in the transverse and vertical components, respectively.

An approximation to calculate the average phase velocity $c(\omega)$ is given by (*Sato*, 1955):

$$c(\omega) \approx \frac{\omega(\Delta_2 - \Delta_1)}{\phi(\omega) + 2n\pi} \tag{4.1}$$

where $\phi(\omega)$ is the fundamental mode phase spectra at stations 1 and 2, and Δ_1 and Δ_2 represent the epicentral distances for stations 1 and 2. The epicentral distances are used instead of the distances between the stations to remove the bias in the phase velocity if the event is slightly outside the great circle between the two stations. Due to the ambiguity of the phase, the correct n must be determined by comparing the calculations with the phase velocity of a background model. From equation 4.1, there are two sources of error in estimating the phase velocity. One is the wavefront, which deviates when the lateral heterogeneity between the two stations is not smooth. The other is related to the errors in the estimation of the phase difference between the fundamental and the first higher modes. In order to isolate the fundamental mode from the other modes, a transformation in the time-frequency domain should be performed. The higher modes are thus downweighted to obtain a cleaner time-frequency representation that contains the fundamental mode.

The phase $\phi(\omega_n)$ is obtained from the complex spectrum of the cross-correlation function filtered with a frequency-dependent Gaussian bandpass filter and weighted in the frequency domain. This procedure yields several candidates for phase velocity curves due to the 2π ambiguity of the phase measurement. Manual processing requires the analyst to select the correct dispersion curve, which is easily identified by its proximity to a reference 2π branch. The reference branches are generated by the Preliminary Reference Earth Model (PREM) (*Dziewonski and Anderson*, 1981), which takes into account the structures to which the surface waves are sensitive, such as the Moho interface and a sedimentary layer. Figure 4.1 displays an example of the two-station method processing for the station pair D01H-D06H. The figure shows the waveforms of the teleseismic earthquake recorded at the two stations, the CC and TFR. In addition, the results show the phase velocity dispersion curve of the event to be selected manually, and some examples of the dispersion curves already selected manually.

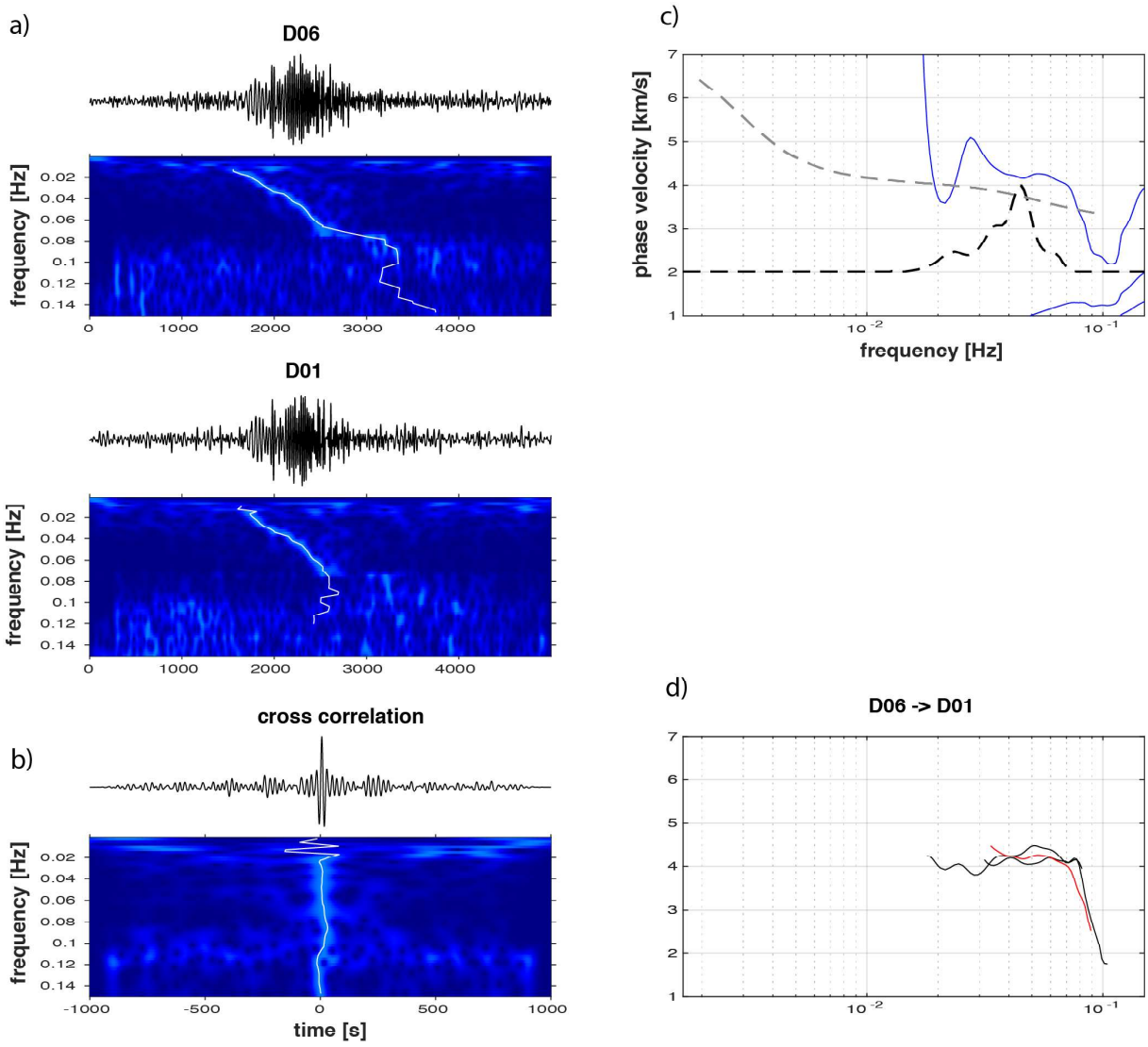

Figure 4.1: Example of Rayleigh wave phase velocity measurement for the pair of stations D01H-D06H (see Fig. 2.1). a) Waveform of the same teleseismic earthquake recorded at stations D01 and D06 and the TFR of the group arrival. b) Cross-correlations between the waveforms recorded at the two stations and their respective TFR. c) 2π ambiguous measured phase velocity dispersion curve (blue lines) plotted together with the reference model (thick grey dashed line) and the normalized amplitude spectrum of the cross-correlation function (black dashed line). d) Selected phase velocity dispersion curves for these two pair of stations.

4.3 Earthquake selection

For this study, were selected 126 earthquakes with Mw $\geq$ 6.0 for the analysis. From them, those with visible surface waves in all the OBS were selected for further processing using the two-station method. In addition, all the components of each station were downsampled to 1 Hz and cut into segments with a total length of 5000 s containing only the surface waves. The horizontal components were rotated into the radial and transverse components for each pair of stations. A bandpass filter from 20 s to 50 s was applied. The maximum backazimuthal deviation of 10° were chosen for all the interstation great circle paths.

In the hydrophone, which has a higher amplitude signal than the vertical component, 38 earthquakes were located within the 10° backazimuthal deviation and had a good amplitude signal compared to the normal noise (Figure 4.2). After applying the cross-correlation and TFR, 32 events remained for which it is possible to select the phase velocity dispersion curves (see table 4.1). It was not possible to select any measurement in any combination with station D03 (Figure 4.3), due to the reasons previously explained in section 2.2.

For the vertical component, originally 26 events were within the 10° range, but after the extraction of the dispersion curves we were left with 23 earthquakes. For the horizontal components, the amplitude signal of the events was poor due to tilt noise, which made it difficult to observe the surface waves. Only for 12 events it is observed a surface wave with reasonable amplitude signal that was within the 10° range. After applying the two-station method, it is possible to extract the phase velocity dispersion curves of only 8 events in the radial and transverse components.

4.4 Dispersion curves

Figure 4.4 shows all phase velocity dispersion measurements obtained using the two-station method. Thus, it was possible to select more dispersion curves from the hydrophone than from the vertical component because it has a higher amplitude signal. However, the dispersion curves of the hydrophone are more scattered than those from the vertical component of the seismometer. The average phase velocity dispersion curve

Table 4.1: Earthquakes used for the two-station method analysis.

#	Date	Time	Latitude (°)	longitude (°)	Depth (km)	Mw	Hydrophone	Vertical	Radial	Transverse
01	2011-07-06	19:03:18	-29.54	-176.34	17.0	7.6	-	X	X	X
02	2011-07-10	00:57:10	38.03	143.26	23.0	7.0	-	X	X	X
03	2011-07-11	20:47:04	9.51	122.17	19.0	6.4	X	-	-	-
04	2011-07 19	19:35:43	40.08	71.41	20.0	6.1	X	-	-	-
05	2011-07-26	17:44:20	25.10	-109.53	12.0	6.0	X	-	-	-
06	2011-07-30	18:53:50	36.94	140.96	38.0	6.3	X	-	-	-
07	2011-80-17	11:44:08	36.77	143.77	9.0	6.1	X	-	-	-
08	2011-08 20	16:55:02	-18.36	168.14	32.0	7.2	-	-	-	-
09	2011-08-20	18:19:23	-18.31	168.22	28.0	7.1	-	-	-	-
10	2011-08-24	17:46:11	-7.64	-74.53	147.0	7.0	X	-	-	-
11	2011-09-02	10:55:53	52.17	-171.71	32.0	6.9	X	X	-	-
12	2011-09-03	22:55:40	-20.67	169.72	185.0	7.0	-	-	-	-
13	2011-09-05	09:52:01	-15.29	-173.62	37.0	6.2	X	-	-	-
14	2011-09-05	17:55:11	2.96	97.89	91.0	6.7	-	X	-	-
15	2011-09-09	19:41:34	49.53	-126.89	22.0	6.4	X	X	-	-
16	2011-09-16	19:26:40	40.27	142.78	30.0	6.7	X	X	-	-
17	2011-09-18	12:40:51	27.73	88.16	50.0	6.9	X	X	-	-
18	2011-10-14	03:35:14	-6.57	147.88	37.0	6.5	X	X	-	-
19	2011-10-21	17:57:16	-28.99	-176.24	33.0	7.4	X	X	-	-
20	2011-10-23	10:41:23	38.72	43.51	18.0	7.1	X	X	-	-
21	2011-10-28	18:54:34	-14.44	75.97	24.0	6.9	X	X	-	-
22	2011-11-08	02:59:08	27.32	125.62	224.0	6.9	-	-	-	-
23	2011-12-27	15:21:56	51.84	95.91	15.0	6.6	X	X	X	X
24	2012-01-09	04:07:14	-10.62	165.16	28.0	6.4	X	-	-	-
25	2012-01-10	18:36:59	2.43	93.21	19.0	7.2	X	X	X	X
26	2012-01-15	13:40:19	-60.95	-56.11	8.0	6.6	X	-	-	-
27	2012-01-30	05:11:00	-14.17	-75.64	43.0	6.4	X	-	-	-
28	2012-02-02	13:34:40	-17.83	167.13	23.0	7.1	X	X	-	-
29	2012-02-06	03:49:12	10	123.21	11.0	6.7	X	X	-	-
30	2012-02-26	06:17:19	51.71	95.99	12.0	6.7	X	X	-	-
31	2012-03-14	09:08:35	40.89	144.94	12.0	6.9	X	X	-	-
32	2012-03-20	18:02:47	16.49	-98.23	20.0	7.4	X	X	X	X
33	2012-03-25	22:37:06	-35.2	-72.22	40.0	7.1	X	X	X	X
34	2012-04-11	08:38:36	2.33	93.06	20.0	8.6	X	X	X	X
35	2012-04-11	10:43:10	0.80	92.46	25.0	8.2	X	X	-	-
36	2012-04-12	07:15:48	28.70	-113.10	13.0	7.0	X	X	X	X
37	2012-04-17	03:50:15	-32.62	-71.36	29.0	6.7	X	-	-	-
38	2012-04-21	01:16:52	-1.62	134.28	16.0	6.7	-	X	-	-

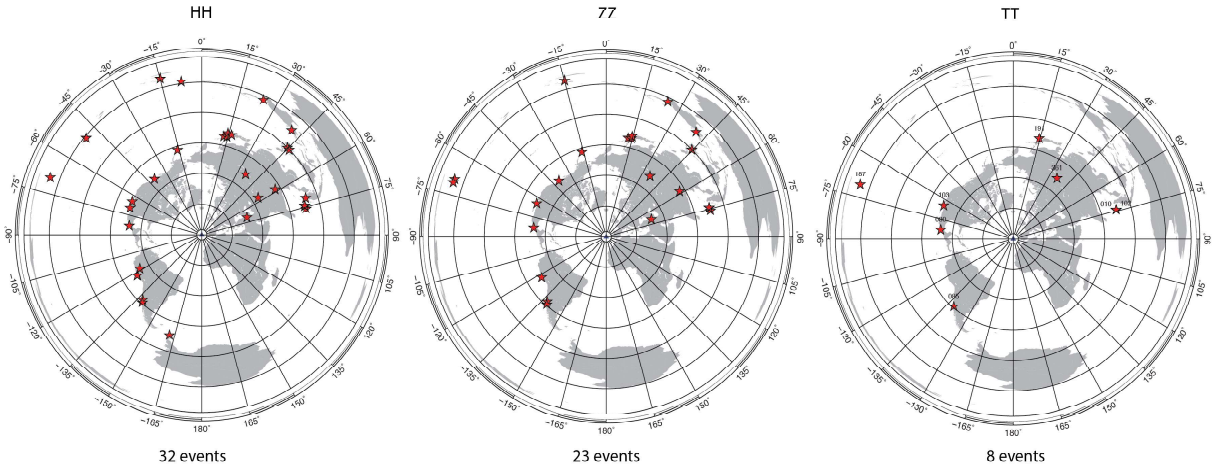

Figure 4.2: Map of processed earthquakes (red stars) using the two-station method for the hydrophone, vertical and transverse components. Since the hydrophone has a higher amplitude signal, it was possible to select more phase velocity dispersion curves than from the vertical component. Due to the tilt noise in the horizontal components, only 8 events were used for the radial and the transverse components.

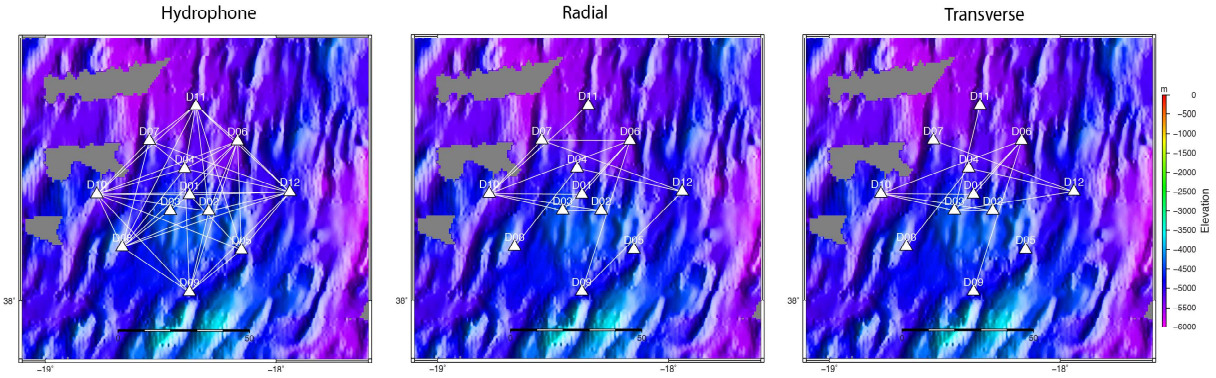

Figure 4.3: Maps of interstation paths used in this thesis for the hydrophone, radial and transverse components. For the horizontal components, it was not possible to select more interstation paths due to the high noise levels.

extracted from the hydrophone tends to be flatter for longer periods (15 s to 75 s) than for the vertical component. The average period range imaged for the hydrophone is from 9.5 s to 100 s and for the vertical component from 10 s to 133 s. The waveforms were not restituted because the instrument was the same in all the OBSs. From the horizontal components we could only extract fewer phase velocity dispersion measurements due to the high noise level in these components. The radial component in Figure 4.4 has more dispersion measurements (22) than the transverse component (18). The average velocity and standard deviation of the transverse component is slightly faster than the radial component due to the emergence of Love waves. In both the radial and transverse components, the averaged minimum and maximum observed periods are between 12 s and 42 s.

The average dispersion curves obtained by the two-station method were later inverted together with the ambient noise data in section 7.

4.5 Azimuthal anisotropy

Azimuthal anisotropy is used to draw conclusions about past and present deformation in the lithosphere and asthenosphere. It is difficult to detect azimuthal anisotropy using surface waves because many measurements are required along different azimuths across the array (*Forsyth and Li*, 2005). A disadvantage of surface wave methods is their very poor lateral resolution compared with shear-wave splitting, which has an excellent lateral resolution but poor vertical resolution. However, an advantage of surface waves anisotropy is the good resolutions analysis regarding different depths determined by the period.

In the hydrophone component were chosen different azimuthal ranges based on the number of events used (Figure 4.2) and the interstation paths that we obtained in DOCTAR area. Unfortunately, there is a significant gap to the southwest, as no earthquakes of sufficient magnitude occurred in that direction during the recording period. Figure 4.5a shows the observed phase velocity averaged by backazimuth together with the average velocity of all the interstation phase velocity dispersion curves, as well as the modeled eigenfunctions considering the velocity structure of the *Hannemann et al.* (2016) model. Additionally, it is shown a phase velocity dispersion curve using the two-station method from a synthetic seismograms with an interstation distance of 100 km. Synthetic seismograms were done

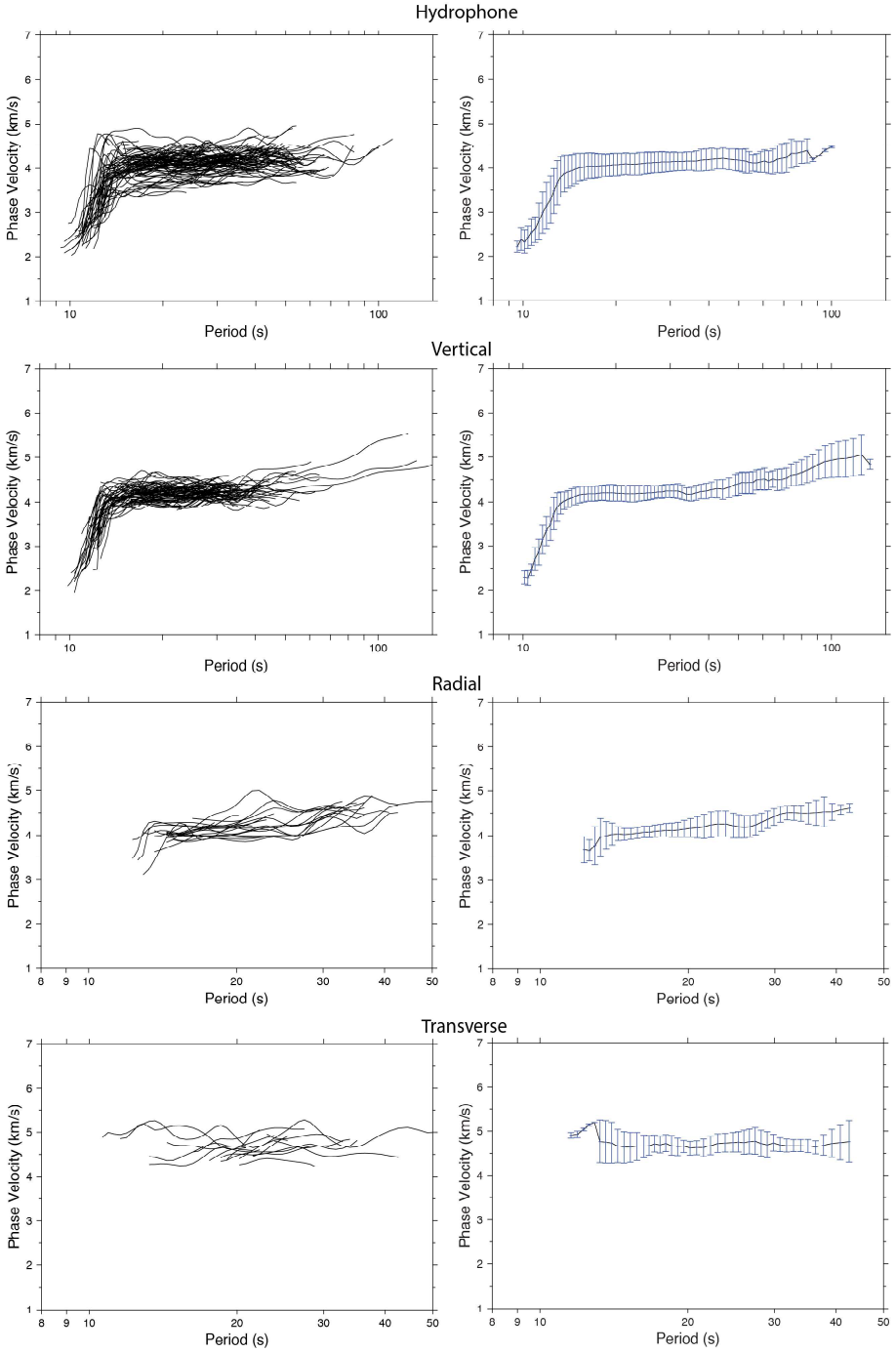

Figure 4.4: Selected phase velocity dispersion curves for the hydrophone and the three components of the seismometer. The transverse component has a slightly higher average velocity because this component extracts the phase velocity Love waves.

with the normal-mode summation (*Herrmann*, 2013) using the Hannemann model as a reference model with 4.881 km of water thickness and with an epicentral distance of 1000 km. The source was located 1 km below the seafloor and the stations located 1 m below the seafloor. The dispersion curve obtained with the synthetic seismogram match perfectly the Hannemann eigenfunction at periods ≥15 s with faster velocities compared with the azimuthal ranges. This higher velocity is related to the half-space velocity for the mantle in the Hannemann model, which has a Vs=4.91 km/s. Between 11 s and 15 s, the synthetic seismogram curve is less steep than the Hannemann eigenfunction. This synthetic test allows us to trust in the longer periods dispersion curves because of the small array aperture, which limit our ability to solve the longer periods. Between 20 s and 50 s, the velocity curves ranging from 0 to 75 degrees and 200 to 245 degrees are faster. On the other hand, lower velocities are obtained for the averaged curves in the range of 270 to 360 degrees.

In addition, the phase velocities at 20 s period were extracted from earthquakes over all directions to observe changes in velocity as a function of backazimuth. To observe if there is some anisotropy in the velocities, a grid search was done varying the amplitude and the phase. Also, the root mean square (RMS) were calculated and compared it with the isotropic model (Figure 4.5b). It was also added to the figure a cosine function $C = Amp * cos(x) + d$; where C is the Phase velocity and d is the shift. The best fit of the cosine function were obtained with an Amplitude = 0.1, phase = 15°, and shift = 4.1. The RMS between the isotropic and the anisotropic model are very small with values of 0.246 and 0.239, respectively. The large gap between 80 and 190 degrees and the number of observations does not allow us to observe a clear anisotropy in the study area.

4.6 Summary

The two-station method allow to extract additional phase velocity dispersion curves at longer periods, which is helpful for the shear velocity inversion to reach deeper structures in the study area. Phase velocity of Rayleigh wave dispersion curves from 15 s to 44 s were used only considering the velocity range in which the dispersion curves are already sensitive to the mantle structure. The use of this method is very straight-forward to obtain dispersion curves because it reduces the 2π ambiguity in the measurements. Even

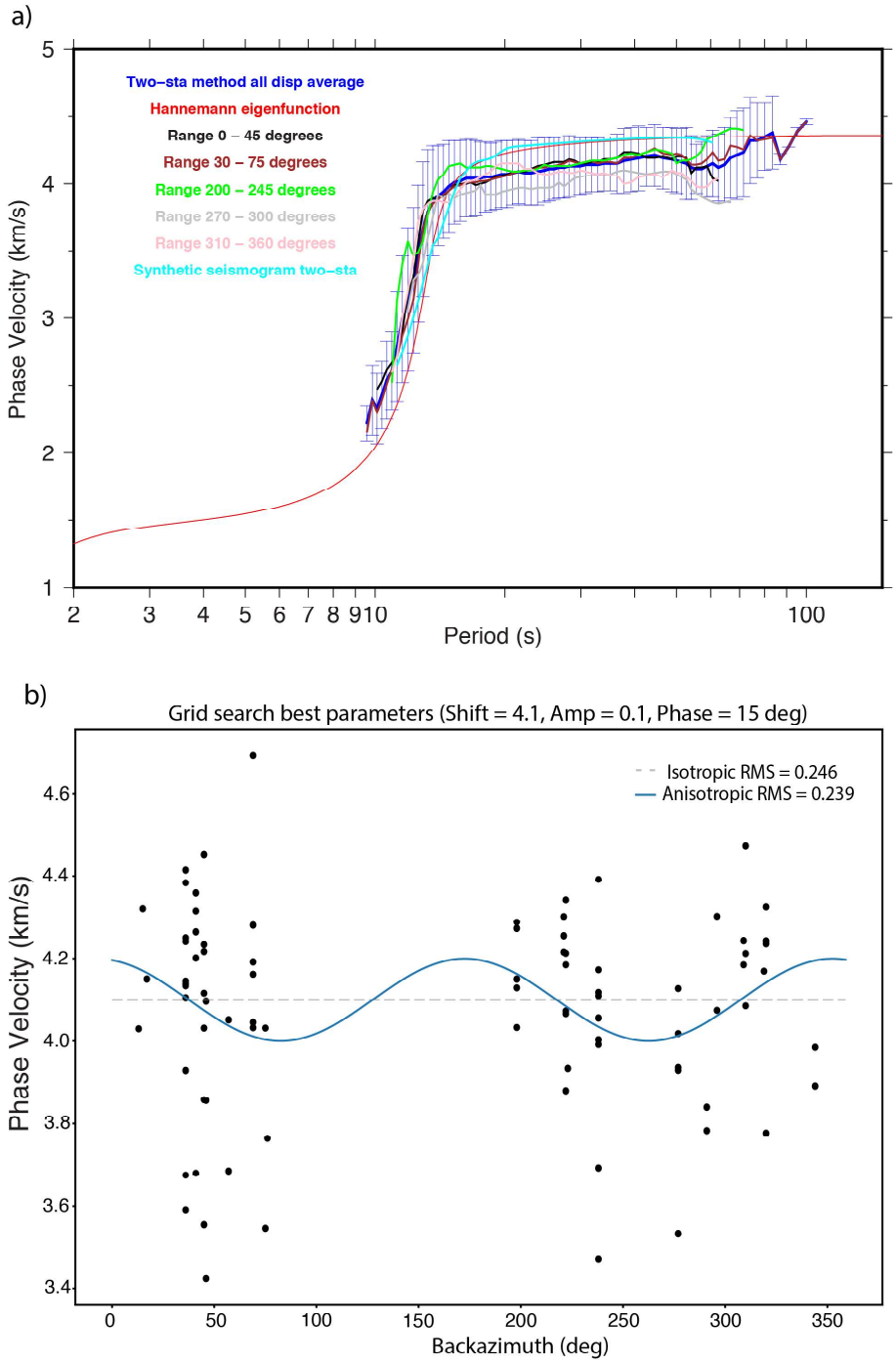

Figure 4.5: a) Averaged phase velocity dispersion curves observed in the hydrophone along different azimuthal ranges. The average of all curves, the modeled eigenfunction based on the Hannemann model, and one dispersion curve (cyan) obtained from a synthetic seismogram using the two-station method are shown for comparison. b) Phase velocity observations at 20 s period as a function of the backazimuth together with a cosine function and the best grid search parameters.

not having a great number of earthquakes to analyze, it was possible to obtain 113 phase velocity dispersion curves for the hydrophone, which in general has an average velocity of 4.1 km/s between 20 s and 45 s. At periods $\geq$ 45 s, the number of measurements to get the average decreased considerable leading to a different behavior in the average dispersion curve.

Average phase velocity dispersion curves were not used for the shear-wave velocity inversion in chapter 7 at the sharp increase (5 s to 14 s). It was decided to remove these periods of dispersion curves taking into consideration the behavior of the synthetic seismogram dispersion curve (Figure 4.5a) at short periods. It was only used the average phase velocity of Rayleigh and Love wave dispersion curves between 15 s to 45 s and 14 s to 43 s, respectively.

Using different azimuthal ranges, it is observed fast and low velocity dispersion curves at different azimuth ranges. The observations at 20 s period, which is the period with more observations, show a very small anisotropy but enough to detect anisotropy clearly. Using other methods like shear-wave splitting will help us to confirm if there is evidence of azimuthal anisotropy in the study area.

Chapter 5

Coda

5.1 Introduction

The seismic coda is the part of the earthquake seismic signal to arrive at any given location after the surface waves. It has a long-duration and a small amplitude, and its energy is supposed to be uniformly distributed around the event source (*Aki*, 1969; *Aki and Chouet*, 1975; *Sato et al.*, 2012). Some of it especial characteristic is that it has a slow temporal decay of spheroidal higher modes with large Q-values (*Maeda et al.*, 2006). Array observations have shown that the coda waves are the results of incoherent waves scattered from small-scale heterogeneities in the lithosphere (*Aki*, 1969; *Aki and Chouet*, 1975; *Campillo and Paul*, 2003; *Snieder*, 2006; *Sato et al.*, 2012). The coda excitation thus depends on the geology at the site of the recording station, and it can be 5-8 times larger in sediments than in granite (*Aki*, 1969).

Both the seismic coda and ambient seismic noise contain scattered seismic energy that can be used to study the Earth's structure. The seismic coda becomes diffuse after multiple scattering of the wavefield. Theoretically, it can be obtained the EGFs from the CC and stacking of diffuse wavefields as long as the energy arrives at the two stations coming from all directions (*Snieder*, 2006). The emergence of EGFs is only effective after averaging plenty of cross-correlograms of the scattered wavefield. In the case of diffuse coda waves, the averaging is performed over several sets of earthquakes (*Campillo and Paul*, 2003; *Paul et al.*, 2005).

Yao et al. (2009) analyzed the symmetry and travel-time properties of EGFs in a broadband array in the Tibet, using CC in different windows: ambient noise, direct surface waves, and surface wave coda. Results show similar dispersion characteristics, which demonstrate that the EGFs can be recovered from direct wavefields (e.g., ambient noise or earthquakes) or from wavefields scattered by heterogeneities on a regional scale.

More recent studies have shown that the late-coda is more diffuse than the early surface wave coda and is usually expected to build more symmetric EGFs (*Paul et al.*, 2005; *Lin and Tsai*, 2013; *Poli et al.*, 2017). On the other hand, *Poli et al.* (2017); *Wang and Tkalčić* (2020) demonstrated that cross-correlating the late coda of events along the same great circle plane (max $\sim 5^{\circ}$ deviation) results in a much better contribution to coda-correlation's formation. Additionally, it can recover appropriately the EGFs with a large number of stations and sufficient earthquakes coming from all directions in case of a good azimuthal coverage (*Wang and Tkalčić*, 2020).

The introduction of the long-range correlation of seismic coda has allowed progress in studies of near-surface imaging (*Campillo and Paul*, 2003; *Shapiro et al.*, 2005) and inferences of the Earth's deep interior *Poli et al.* (2012, 2015).

In this chapter, it was intended to reconstruct the EGFs of the seismic coda using the largest earthquakes recorded in the DOCTAR area. The coda of large earthquakes may enable to recover dispersion curves at long periods by the following arguments: 1) The earthquake source radiates energy at long periods something that the oceanic microseismic does not do. 2) The Guralp CMG-40T sensors have high self-noise at long periods as shown in chapter 2, and thus, large amplitudes are necessary to overcome this problem. 3) Coda waves have better path coverage.

5.2 Cross-correlation of coda wave

To generate EGFs from the coda of teleseismic events, we followed the methodology described by *Campillo and Paul* (2003); *Paul et al.* (2005).

DOCTAR data was pre-processed before computing the CC. First, earthquakes with Mw $\geq$ 6.0 were selected. Then it was visually inspected the waveforms in order to assess whether they contained visible surface coda waves in the OBS records. Table 5.1

shows the selected events for the hydrophone and each component of the seismometer. Figure 5.1 shows an example of a teleseismic event observed in the hydrophone, vertical, radial and transverse component. The hydrophone has a higher amplitude signal than the seismometer allowing to use more events for the cross-correlation. The transverse component, on the other hand, is mixed with Rayleigh and Love waves because of the scattered waves coming from all directions making more difficult to extract the EGFs.

The three components of the seismometer were first downsampled to 1 Hz and bandpass filtered between 5 s and 100 s. On the contrary, the hydrophone was downsampled but not filtered because it has a higher amplitude signal for hundreds of seconds after the surface wave train. The horizontal components were rotated to the radial and transverse directions for each station pair assuming that one station is the source the other the receiver. Coda records were used ∼200 s after the largest amplitude of the surface waves and ending when the amplitude signal of the coda was less than 3 times the normal noise level.

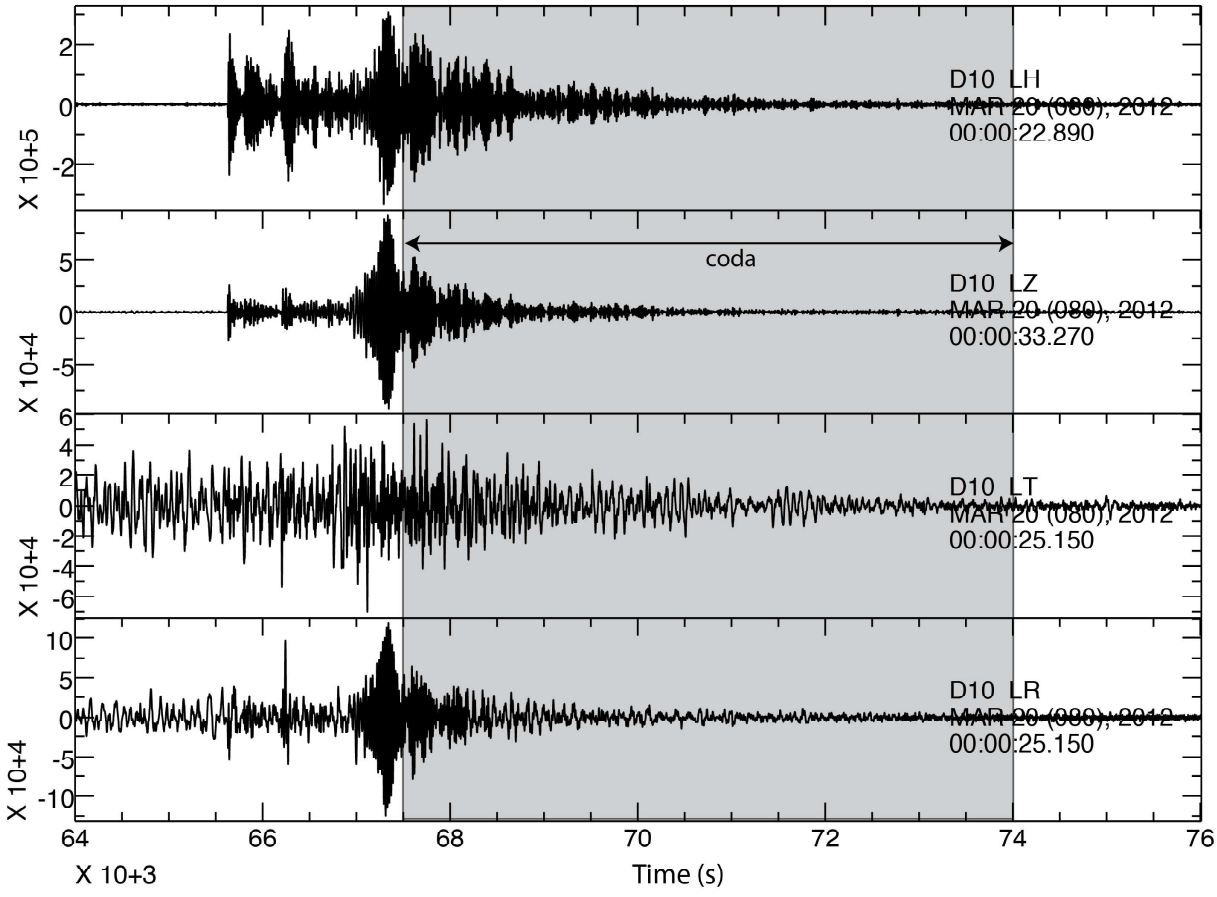

Figure 5.1: Example of a teleseismic earthquake recorded in the hydrophone and in the three components of the seismometer at station D10, highlighting the coda. Observe that the signal remains well above the noise level for several hours after the arrival of the surface waves.

Table 5.1: Earthquakes used here for the seismic coda wave study. The X means that the waveforms of the event were used for the components indicated.

#	Date	Time	Latitude (°)	longitude (°)	Depth (km)	Mw	Hydrophone	Vertical	Radial	Transverse
01	2011-07-06	19:03:18	-29.54	-176.34	17.0	7.6	X	X	X	X
02	2011-07-10	00:57:10	38.03	143.26	23.0	7.0	X	X	X	-
03	2011-07-11	20:47:04	9.51	122.17	19.0	6.4	X	-	-	-
04	2011-07 19	19:35:43	40.08	71.41	20.0	6.1	X	-	-	-
05	2011-07-26	17:44:20	25.10	-109.53	12.0	6.0	X	-	X	-
06	2011-08-24	17:46:11	-7.64	-74.53	147.0	7.0	X	X	X	-
07	2011-09-02	10:55:53	52.17	-171.71	32.0	6.9	X	-	X	-
08	2011-09-16	19:26:40	40.27	142.78	30.0	6.7	X	-	-	-
09	2011-09-18	12:40:51	27.73	88.16	50.0	6.9	X	-	-	-
10	2011-10-14	03:35:14	-6.57	147.88	37.0	6.5	X	-	-	-
11	2011-10-21	17:57:16	-28.99	-176.24	33.0	7.4	X	X	X	X
12	2011-10-23	10:41:23	38.72	43.51	18.0	7.1	X	X	-	-
13	2011-10-28	18:54:34	-14.44	75.97	24.0	6.9	X	X	X	X
14	2011-12-27	15:21:56	51.84	95.91	15.0	6.6	X	-	X	-
15	2012-01-10	18:36:59	2.43	93.21	19.0	7.2	X	X	X	-
16	2012-02-02	13:34:40	-17.83	167.13	23.0	7.1	X	X	-	-
17	2012-02-06	03:49:12	10	123.21	11.0	6.7	X	-	-	-
18	2012-02-26	06:17:19	51.71	95.99	12.0	6.7	X	X	-	-
19	2012-03-14	09:08:35	40.89	144.94	12.0	6.9	X	X	X	-
20	2012-03-20	18:02:47	16.49	-98.23	20.0	7.4	X	X	X	X
21	2012-03-25	22:37:06	-35.2	-72.22	40.0	7.1	X	X	X	X
22	2012-04-11	08:38:36	2.33	93.06	20.0	8.6	X	X	X	X
23	2012-04-12	07:15:48	28.70	-113.10	13.0	7.0	X	X	X	X

The vertical component data were split into 200 s long segments with 50% overlap to compensate for the amplitude attenuation (*Campillo and Paul*, 2003). The radial, transverse and hydrophone components were divided into segments of 500 s, also with an overlap 50%. In total, it was used 23 events for the hydrophone, 14 earthquakes for the vertical and radial, and 7 events for the transverse component (Figure 5.2). For each pair of stations, it was computed the classical CC of all the segments by applying a 1-bit normalization and a whitening to the signals. The CC results for all the events were stored for each station pair and then stacked linearly to avoid attenuating important signals.

In addition, the emergence of the EGFs were tested from the data for each station pair for the events that are only deviated from the great circle plane by a maximum of ±10° (*Poli et al.*, 2017; *Wang and Tkalčić*, 2020).

5.3 Results

Figure 5.3 shows the resulting EGFs using all the earthquakes for the hydrophone and vertical component and also bandpass filtered between 5 s and 30 s. The prominence of the Rayleigh waves in the hydrophone and vertical component are clearer with the filter.

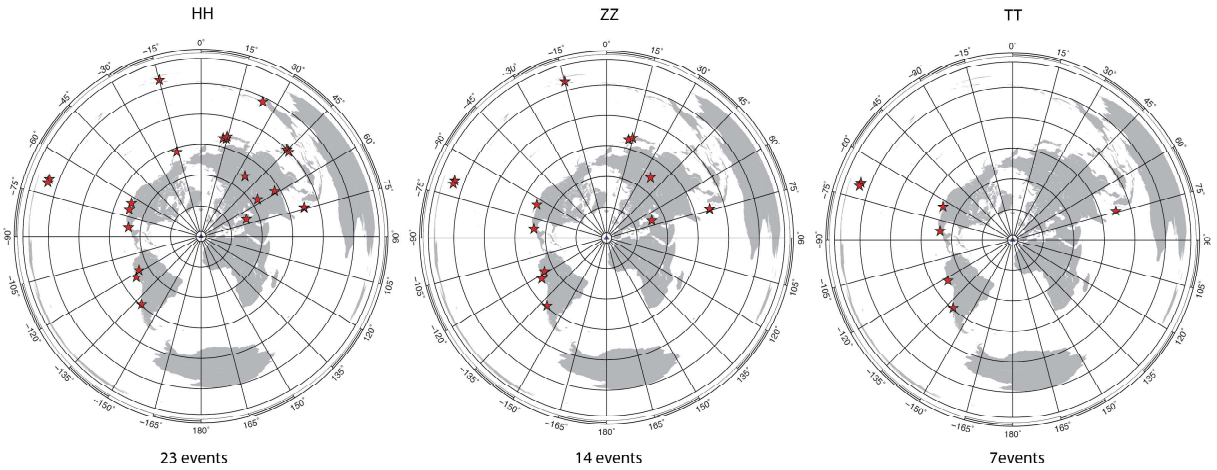

Figure 5.2: Map of earthquakes used for the seismic coda analysis in the hydrophone (HH), vertical (ZZ) and transverse (TT) components. Considering that the hydrophone has a higher amplitude signal, this allows to select more earthquakes than for the vertical component. In the horizontal components, it was more difficult to select the coda because of the high noise levels.

On the contrary, using $\pm 10°$ from the great circle plane did not improve the extraction of the EGFs because of the limited number of earthquakes and stations, and the small aperture of the DOCTAR area. Figure 5.4 highlights the difference between extracting the group velocity for all the events and only events aligned to the interstation great circle path. Essentially, the selection of the group velocity using all the events it is more clear, except for station pair D02-D08, where the results were improved by using only lined-up events. As the results were better using all the events for the extraction of the EGFs of seismic coda in the seismometer and hydrophone, the complete dataset was used.

The extraction of the group and phase velocity dispersion curves at short interstation distances (9 km to 27 km) was not successful because they are to close. Also, the hydrophone of station D03 did not work properly, making it impossible to obtain the group velocity. Additionally, the amplitude spectrum permit to identify the maximum period of scattered waves for the coda waves. Figure 5.5 display the dispersion curve of the pair of stations D10H-D11H and the amplitude spectrum. It is observed that the energy decay after 22 s, which indicates why we were only able to extract up to 22 s in the dispersion curves.

Figure 5.6 show the selected group velocity dispersion curves for the hydrophone and vertical components, together with synthetics obtained from the Hannemann velocity model as a reference. The results show that the calculations follow well the reference model between 5 s and 10 s. Beyond 10 s, the coda curves are less steep than the reference

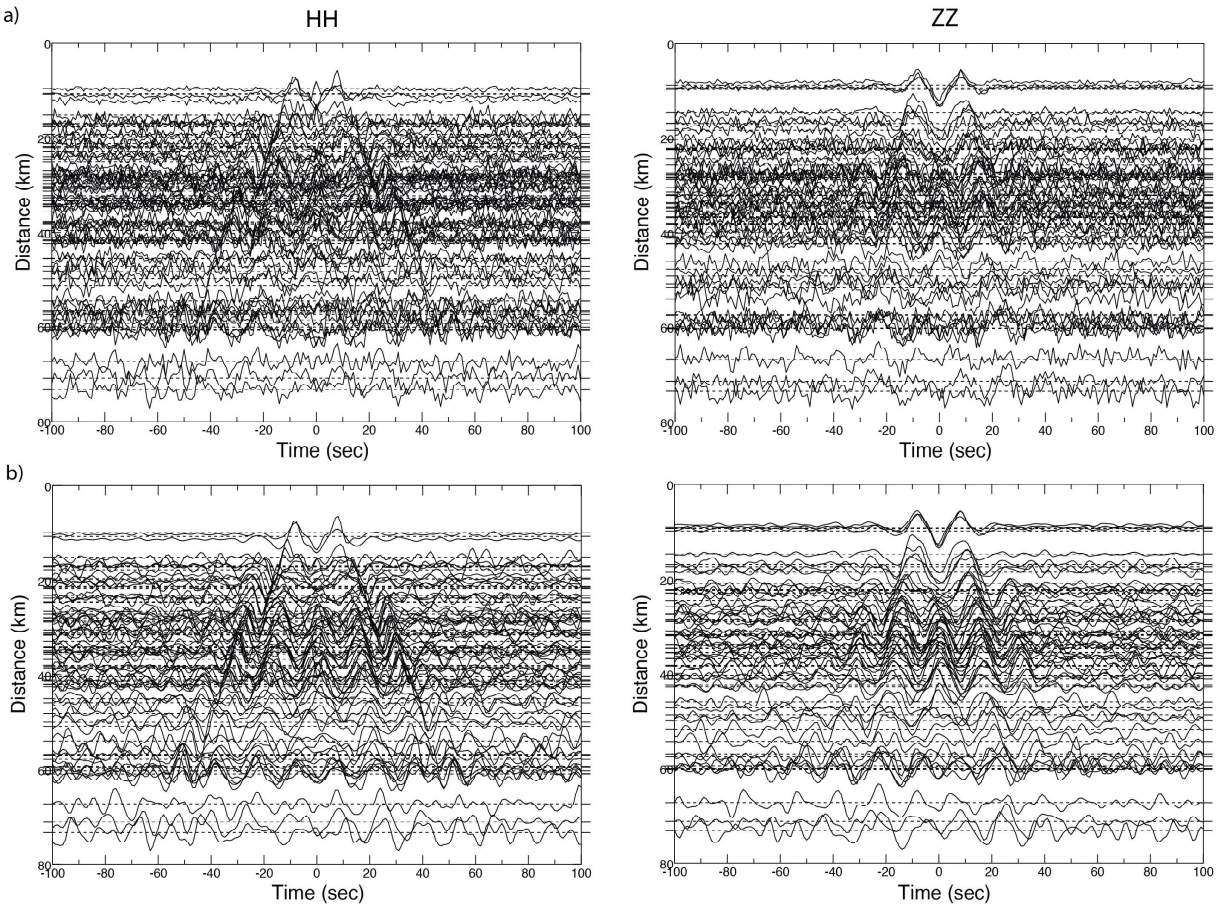

Figure 5.3: Emergence of the EGFs for the hydrophone and vertical component (a) and bandpass filtered between 5 s and 30 s (b). It was used the CCGN method normalized to a maximum amplitude of one and applied a whitening to the signals. Linear stack were used to avoid losing important signals and a bandpass filter from 5 s to 30 s were applied for a clearer identification of the fundamental mode.

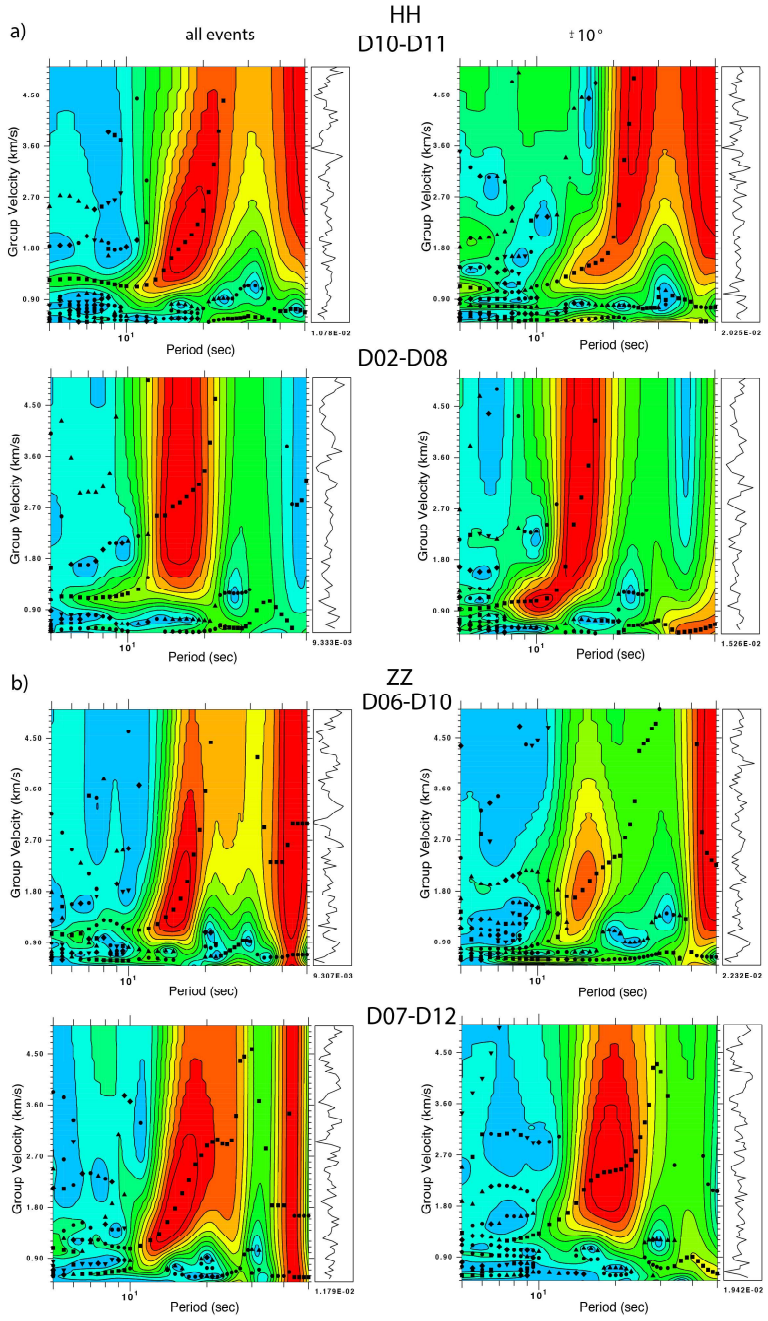

Figure 5.4: Group velocity energy diagrams and dispersion curves obtained using all the events (left) and the selection criterion of ±10° from the interstation great circle plane (right). Group velocity dispersion curves for the hydrophone (a) and vertical components (b) for selected pairs of stations. There is only one station pair that improved by using events aligned with the great circle plane (D01-D08). The rest of the stations pairs gave better results when using all the events.

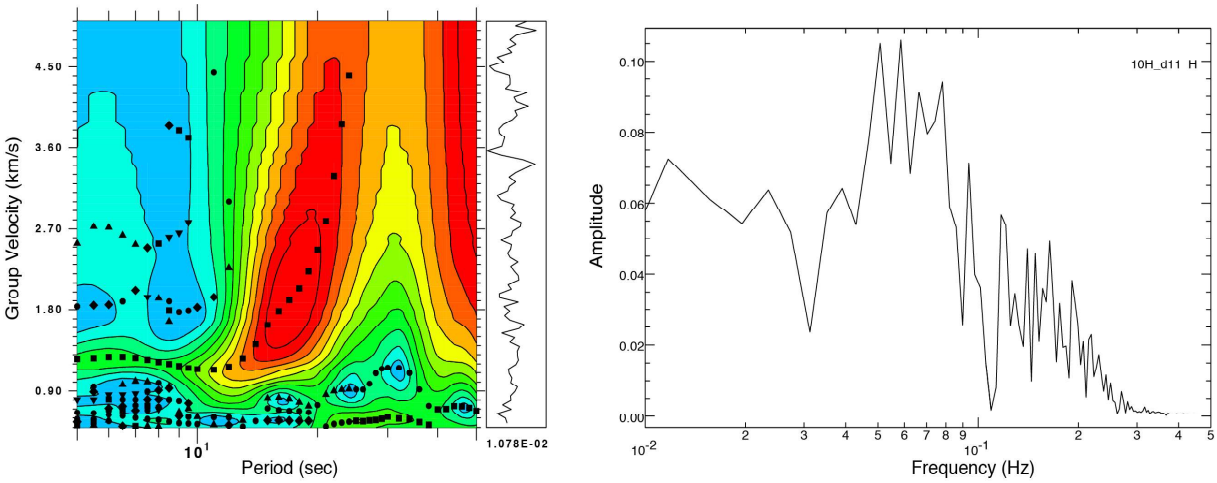

Figure 5.5: Group velocity energy diagram and amplitude-spectrum for the station pair D10H-D11H. The amplitude spectrum indicates that there is only energy until 22 s, beyond that there is a decay in the energy meaning that it was only possible to extract the dispersion curves until 22 s.

model. 39 group velocity dispersion curves were extracted from the hydrophone and 20 from the vertical seismic waveforms. Thus, the higher amplitude signal of the hydrophone permits to obtain about double the number of group velocity dispersion curves from the vertical component.

Finally, the extracted group and phase velocity dispersion curves obtained were compared by using ambient noise, the two-station method and the seismic coda (Figure 5.7). For both, the hydrophone and vertical components, group velocity dispersion curves of the coda show a similar behavior to those of ambient noise, with a decrease of the velocity between 5 s to 10 s followed by a sharp increase (Figure 5.7a) but earlier than the ambient noise. In addition, phase velocity of the coda does not fit well the dispersion curves of the two-station method but it is closer to the Hannemann reference model and the synthetic seismogram dispersion curve at periods >12 s. Alike group dispersion, also phase velocity dispersion curves tend to be less steep than the rest of the data. These observation differences in the sharp rise may be related to numerical instabilities during the extraction of the dispersion curve due to the narrow Gaussian band-pass filter and the rapid increase in velocity between one point of the extraction and the following point. Phase velocity of coda waves and the period range of ambient noise fit correctly. It was obtained 19 phase velocity dispersion curves from the hydrophone and 14 dispersion curves from the vertical components.

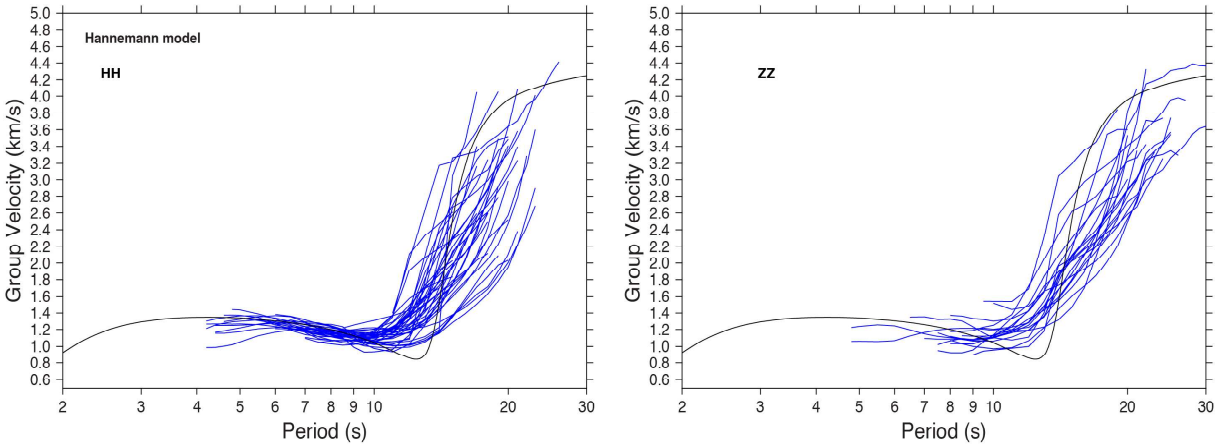

Figure 5.6: Group velocity dispersion curves obtained from the coda recorded in the hydrophone and vertical component. Because of a higher amplitude signal in the hydrophone it was possible to identify and select more group velocity measurements.

5.4 Summary

In general, it was obtained some information of the shallow earth structure only at periods between 5 s and 20 s that gives a hint of the nature of the scattered waves. Beyond 20 s period, no information was retrieved because a decay of the scattered seismic energy, which is the period that is sensitive to the upper mantle structure. Also, the array aperture limit the ability to extract dispersion curves at longer periods.

In addition, to properly recover the seismic wavefield, a good distribution of energy from all directions between the two stations is required, which in turn requires a large number of recordings. Due to the lack of enough data and the difficulties in observing the dispersion curves, 1-D velocity structure inversion were carried out by using only the measurements of the average Rayleigh wave phase velocity dispersion curves obtained with the two-station analysis from 15 s to 44 s. The average Love wave group velocity calculations of ambient noise from 3 s to 9 s and the average Love wave phase velocity dispersion curves of ambient noise and two-station method between 4 s to 9 s and 14 s to 42 s were used, respectively.

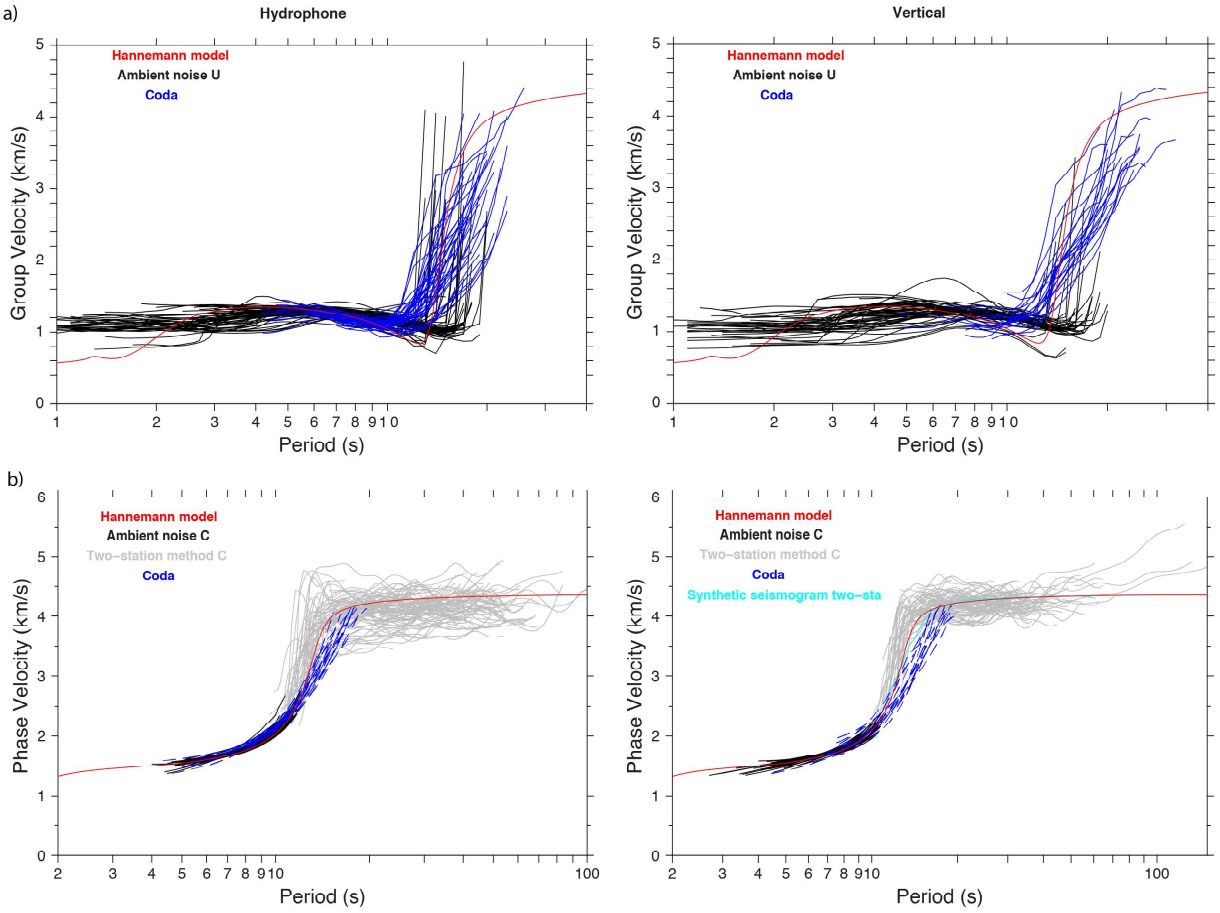

Figure 5.7: Summary of measured group and phase velocity dispersion curves for the hydrophone and vertical components of the ambient noise (black), two station method (gray) and coda results (blue). Hannemann model eigenfunction (red) for group and phase velocity dispersion curves. The number of dispersion curves for the coda is very limited due to the number of events in comparison with the number of the ambient noise and two-station method data.

Chapter 6

Impact of the oceanic structure in short- to mid-period (< 20 s) surface waves

Juan I. Pinzón, Susana Custódio, Graça Silveira, Luis Matias, F. Krüger, Joana F. Carvalho, Carlos Corela

In correction process

Summary

In this article we investigate how short- to mid-period (< 20 s) surface waves are affected when they travel through water domains. We perform systematic modeling and compare the results to calculations from three different illustrative regions of the north Atlantic, namely from the deep ocean, ocean islands and a continent-ocean transition. We show that short- to mid-period Rayleigh waves are strongly affected by the water thickness. Love waves are not affected by the water layer but are very sensitive to the oceanic shallow sedimentary structure, which is pervasive in oceanic domains. Considering a typical oceanic structure, surface waves display a domain at very short periods ($< 2-5$ s) where group and phase velocities have very low values ($\sim 0.2-0.5$ km/s) and are mostly sensitive to the shallow sedimentary structure. At periods of ∼2-15 s, Rayleigh waves display a second domain where they are mostly sensitive to the water layer and

both group and phase velocities display values of ∼1.5 km/s. This strong sensitivity of Rayleigh waves to the water blocks their sensitivity to the solid Earth structure. Finally, at longer periods (> 15 s) Rayleigh waves become sensitive to the lower crust and mantle structure. In addition, at short-periods (< 5 s) Rayleigh waves are strongly affected by the interference between fundamental and higher modes, particularly in deep waters and for group velocities. Special attention should be given to modeling paths along which the thickness of the water layer varies laterally, as such variations strongly distort short- to mid-period surface waves and can lead to misleading tomographic models for the shallow structure.

6.1 Introduction

Earth's ambient vibrations, also known as microseismic ambient noise, are dominantly generated by ocean waves that interact with the solid Earth by low-amplitude but persistent pressure variations (*Ardhuin et al.*, 2015). These pressure perturbations propagate within the solid Earth as seismic waves, which are observed in seismic stations around the globe (*Webb*, 1998; *Nishida*, 2013). Ambient noise has been demonstrated to be composed dominantly of Rayleigh waves, although Love and body waves have also been observed (*Zhao et al.*, 1997; *Roux et al.*, 2005; *Zha et al.*, 2014; *Nakata et al.*, 2015). *Shapiro and Campillo* (2004) showed that it is possible to extract EGFs between two seismic stations by cross-correlating the seismic noise recorded at those stations. From these, one can proceed to infer a 3-D seismic model of the Earth structure using common tomographic techniques (e.g., *Rawlinson et al.*, 2010). In the last 20 years, successful Ambient Noise Tomography (ANT) has been carried out in various settings, including continents (*Lin et al.*, 2007, 2008; *Bensen et al.*, 2008, 2009; *Ekström et al.*, 2009; *Lin and Ritzwoller*, 2011; *Savage et al.*, 2013; *Harmon et al.*, 2013; *Fang et al.*, 2015; *Harmon and Rychert*, 2016), oceans (*Zhao et al.*, 1997; *Harmon et al.*, 2007, 2009; *Yao et al.*, 2011; *Mordret et al.*, 2014; *Zha et al.*, 2014; *Tomar et al.*, 2018) and ocean-land domains (*Tian and Ritzwoller*, 2015; *Bowden et al.*, 2016; *Corela et al.*, 2017).

Ambient noise tomography based on OBS-recorded Rayleigh waves use either vertical seismometer data or pressure (hydrophone) data, whose records are a good proxy for vertical motion. Pressure data typically have a higher SNR than seismometer data, because

the pressure receivers are placed in the water above the seafloor and therefore are less contaminated by modes that develop at the solid-fluid interface (*Le et al.*, 2018). Love waves identified in the transverse component of the seismometer can also contribute to the inference of robust Earth structure models. However, Love waves are more difficult to observe in OBS data because the horizontal components of OBS have high noise levels due to ocean currents and sensor tilt (*Crawford and Webb*, 2000). Also, the analysis of Love waves requires a careful orientation of the horizontal components (*Lin et al.*, 2008).

Previous ANT studies based on OBS data showed that the water layer above the sensors strongly affects the dispersion of short- to mid-period ($T < 20$ s) Rayleigh waves (*Harmon et al.*, 2007; *Yao et al.*, 2011; *Zha et al.*, 2014; *Bowden et al.*, 2016; *Corela et al.*, 2017; *Tian and Ritzwoller*, 2017). The short-period dispersion of surface waves along paths that cross water domains, such as inter-island paths or paths that cross lakes with substantial water depths, is also affected in a way similar to intra-oceanic paths (*Lin et al.*, 2007). Furthermore, the dispersion of group velocities in oceanic domains is affected by mode interference, which is particularly strong for both Rayleigh and Love waves at short-periods ($T < 10$ s) (*Tomar et al.*, 2018; *Le Pape et al.*, 2021) and at long periods ($T > 25$ s) (*Nettles and Dziewoński*, 2011; *Luo et al.*, 2015; *Hariharan et al.*, 2020).

Previous OBS studies found that oceanic dispersion curves display a low-velocity domain ($\sim$1.5 km/s) at short periods ($T < 15$ s), followed by a sharp increase to velocities typical of crustal and mantle domains (*Harmon et al.*, 2007; *Yao et al.*, 2011; *Lebedev et al.*, 2013; *Zha et al.*, 2014; *Bowden et al.*, 2016; *Corela et al.*, 2017; *Tian and Ritzwoller*, 2017). This low-velocity domain results from most energy in oceanic Rayleigh waves being propagated in the water (*Yao et al.*, 2011; *Gualtieri et al.*, 2015). These oceanic waves (Scholte waves) can be advantageously used to study the sedimentary structure in marine seismology (*Bohlen et al.*, 2004; *Socco et al.*, 2010). The strong sensitivity of oceanic Rayleigh waves to the water blocks their sensitivity to the upper crustal structure. In order to account for the effect of the water, previous authors have typically inverted fundamental mode and in some cases the first higher mode of surface waves, while considering a water layer with fixed thickness and velocity (*Harmon et al.*, 2007; *Zha et al.*, 2014; *Corela et al.*, 2017).

Previous works have documented the effect of the water layer on particular datasets. However, a systematic study of the general impact of the water layer on surface waves is

missing. Here, we show how surface waves that cross water domains are affected by the water layer, sediments, crustal structure, interference of modes and laterally varying Earth structure. To this end, we perform synthetic tests, analyzing both dispersion curves, waveforms and sensitivity kernels, and showing the impact on both group and phase velocities. We further compare synthetic results for an ocean-continent transition region, both obtained using full wavefield 3-D modeling and a simpler model based on mode conservation. The comparison shows that the simple scheme allows to identify the influence of varying water thickness for a data set given the existence of reliable regional velocity models. We then compare our results with OBS and ocean island data recorded in different environments (Figure S6.5): a) deep ocean, using data of the DOCTAR recorded 60 km north of the Gloria fault, in the North Atlantic (*Hannemann et al.*, 2013); b) ocean islands, namely the Cape Verde archipelago, where we used data of the an investigation on the geometry and deep signature of Cape Verde mantle plume (CV-PLUME) project (*Weber et al.*, 2007); and c) land-ocean transition, in the Gulf of Cadiz imbricated wedge (GCadiz), offshore southwest Europe, namely data of the Integrated observations from NEAR SourcES of Tsunamis (NEAREST) project (*Alfred-Wegener-Institut Helmholtz-Zentrum für Polar- und Meeresforschung et al.*., 2017).

6.2 Modeling of oceanic short- to mid-period (<20 s) surface waves.

6.2.1 Reference deep ocean structure.

We start by computing synthetic dispersion curves for a reference oceanic velocity structure, which we took as a depth profile of Crust1.0 (*Laske et al.*, 2013) at a point in the North Atlantic inside the DOCTAR array (Figure S6.5). The structure has a water depth of 5 km, followed by 100 m of unconsolidated sediments, and a magmatic oceanic crust represented by 3 layers with increasing P- and S-wave velocities (Figure S6.6a). The upper crust (layers 1 and 2, with a total thickness of 2.2 km) are basaltic pillow lavas and sheeted dikes, while the lower crust (layer 3, with a thickness of 4.71 km) has a gabbroic composition.

In order to generate synthetic dispersion curves, we used three different approaches.

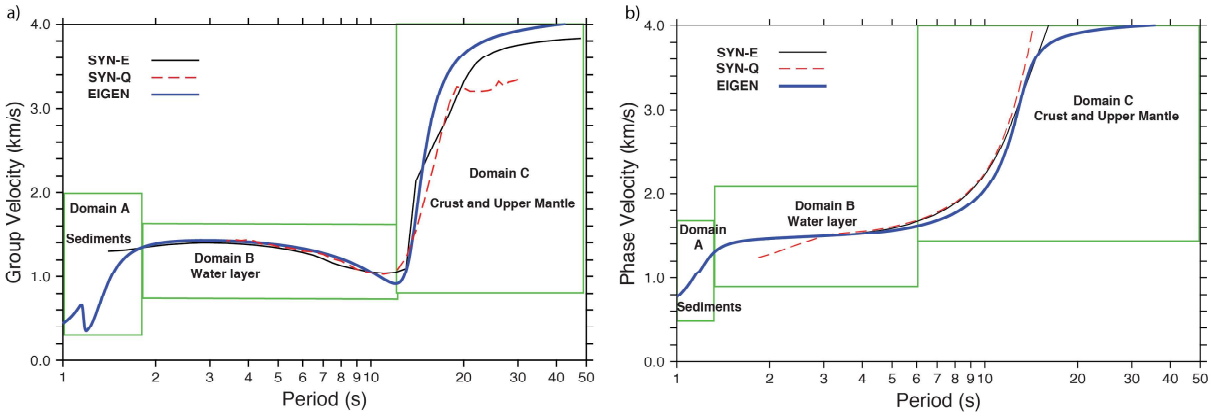

Figure 6.1: Rayleigh wave fundamental-mode dispersion curves for a reference deep ocean structure. (a) Group and (b) phase velocity dispersion curves inferred using three different computational approaches: EIGEN (thick full line), SYN-E (thin black line) and SYN-Q (dashed line). The dispersion curves can be separated into three domains corresponding to different sensitivities to the oceanic structure. Domain A is mostly sensitive to the shallow sedimentary structure, whereas domain B is strongly affected by the water layer and domain C is mostly sensitive to the lower crust and topmost mantle (see additional details in Supplementary Figure 6.6).

In the first approach, we computed group and phase velocities as a function of period directly from Normal-mode eigenfunctions (EIGEN) (*Takeuchi and Saito*, 1972; *Dahlen and Tromp*, 1998; *Yang et al.*, 2010). In the second and third approach, we computed synthetic seismograms, from which we then measured group velocity using a MFT (*Dziewonski et al.*, 1969; *Herrmann and Ammon*, 2002) and phase velocity using a FTAN (*Levshin and Ritzwoller*, 2001). In the second approach Synthetic seismograms by normal-mode summation (SYN-E), synthetic seismograms were obtained by normal-mode summation (*Herrmann*, 2013), whereas in the third approach Synthetic seismograms by QSEIS (SYN-Q), synthetic seismograms were obtained using QSEIS, a full wavefield reflectivity code (*Wang*, 1999). In order to simulate Rayleigh waves generated by oceanic microseismic sources, synthetic seismograms were computed using as source a vertical force placed 10 m below the ocean bottom. We assumed an arbitrary source-receiver distance of 75 km and placed the receiver at a depth of 1 m below the seafloor. Both sensor and source were placed slightly below the seafloor in order to avoid numerical instabilities.

Figure 6.1) shows, respectively, how group and phase velocities vary with period in our reference deep ocean structure. All computational approaches provide consistent results, with some divergence for periods above ∼20 sec due to the short inter-station distance. Figure 6.1a shows that the dispersion of fundamental Rayleigh wave group velocities can be separated into three different domains. In domain A, from ∼1 to 2 s, velocities increase from very low values of ∼0.4 km/s at T=1 s up to 1.4 km/s at T=2 s. This

domain corresponds to kernels with periods of 1-2 s, which show an extreme sensitivity to the low shear-wave of the sediments. The sensitivity to the shallow low-velocity layers decreases with increasing period, allowing velocities to increase with period.

In domain B, from ∼2 s to 12 s, group velocities are approximately flat, with a value of ∼ 1.4 km/s, from T=2 s to T=6 s. Then, group velocity shows a slight decrease from 1.4 km/s to 1.0 km/s between T=6 s and T=12 s. This domain corresponds to kernels with periods between 2 s and 12 s, which show that group velocity is not as sensitive anymore to the shallow low-velocity structure but rather becomes strongly sensitive to Vp in the water (Figure S6.6b). In general, domain B is dominated by Scholte waves, which keep most of the energy trapped in the water layer (*Pekeris*, 1948; *Bohlen et al.*, 2004). In this example, the maximum sensitivity to the water layer occurs at ∼ 12 s, where the group velocity reaches the lowest value, forming an Airy phase. *Gualtieri et al.* (2013) showed that variations of group velocity with bathymetry and period depend on the wavelength of Rayleigh waves and on water thickness. At short periods, the ocean and the sediments act as waveguides, mostly reflecting P-waves between the ocean and the sedimentary layer, but also producing elastic P and S waves in the sediments (*Gualtieri et al.*, 2014, 2015). Very little seismic energy penetrates into the upper crust, which explains the high sensitivity of group velocities to the water layer and associated low sensitivity to the upper crust.

In domain C, T>12 s, group velocities rise sharply from 1.0 km/s at T=12 s to ∼4 km/s at T> 20 s. The kernels show that group velocity becomes more sensitive to the lower crust and upper mantle, explaining the sharp increase in group velocities.

The phase velocity dispersion curve of the fundamental Rayleigh wave can also be separated into similar three domains (Figure 6.1b). In domain A, which now extends from T=1 s to T=1.3 s, velocities rise from 0.8 km/s to 1.4 km/s. The sensitivity of T=1 s confirms that at these periods the phase velocity is extremely sensitive to the low Vs of the sediments. In domain B, phase velocities show a negligible variation, maintaining a value of ∼1.5 km/s between T=1.3 s and T=6 s. The kernels confirm an abrupt increase in the sensitivity to the water layer at periods of ∼2 s, reaching a maximum sensitivity at T=12 s. In domain C, velocities rise from 1.5 km/s at T=6 s to ∼4 km/s at T>10 s. For periods longer than 12 s, the kernels show a decrease in the sensitivity to the water

layer, together with an increased sensitivity to the deeper layers of the crust, Moho and topmost mantle.

Similar steep increases in group and phase velocities are also observed for other Earth discontinuities. As an example, *Lebedev et al.* (2013) identified a steep increase in group and phase velocities, for both Love and Rayleigh waves, at ∼20 s and ∼50 s for typical continental and thickened crust, respectively, which corresponds to the crust-mantle boundary (Moho). The steep part of the dispersion curves are difficult to image because the energy is distributed over a wide time window. In addition, in deep oceanic domains, this Moho-associated increase in group and phase velocities can often not be imaged, as it falls inside domain B, where the sensitivity to crustal structure is blocked by the water.

6.2.2 Impact of water depth.

We now keep our reference deep ocean structure and vary the thickness of the water layer between 0 m (no water) and 6000 m (Figure 6.2a). The results clearly show that Rayleigh waves are substantially affected by water depth at periods below 20 s, with domain B extending up to longer periods as the water thickness increases, for both group and phase velocities. For example, for group velocities the sharp B/C transition occurs at ∼1.5 s for a water depth of 1000 m, whereas it only occurs at ∼15 s for a water depth of 5000 m. Thus, it is easier to resolve shallow crustal structure from seismic data recorded in shallow waters than in deep waters. In fact, for very shallow waters (0 m to 500 m deep), domain B disappears and we only see the direct transition from domain A, dominated by the sedimentary structure, to domain C, dominated by crustal structure. The Moho signature in the dispersion curves can only be seen in shallow waters, where at ∼4 s velocities increase from ∼3 km/s to ∼4 km/s. The dispersion of Love waves – which are insensitive to fluids – is not affected by water depth.

6.2.3 Impact of sediments.

Next, we keep our oceanic model and vary the thickness of the sedimentary layer between 100 m and 5000 m. Because deeper sediments are more compacted, they have higher Vp, Vs and density. Accordingly, we varied these values gradually by considering the depth profiles of regions with thick sedimentary layers, such as the Horseshoe Abyssal Plain and

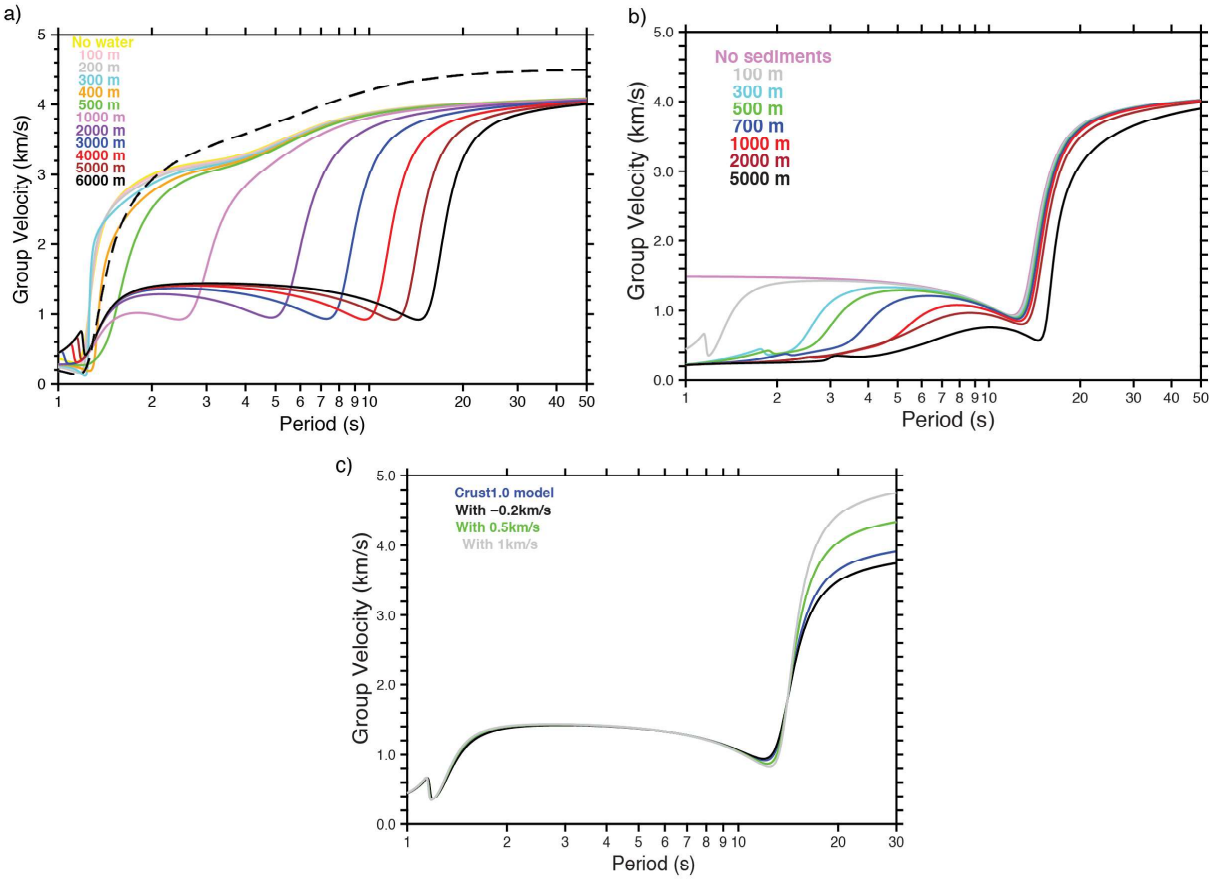

Figure 6.2: Surface wave fundamental-mode dispersion curves for varying oceanic structures calculated with EIGEN. (a) Effect of the water depth in group velocity dispersion curves. We used our reference deep ocean structure and a water layer whose thickness was varied between 0 m (no water) and 6000 m (Figure S6.7a). The dispersion of Love waves is not affected by the water layer, as Love waves do not propagate in the water (dashed line). Rayleigh wave fundamental modes are strongly affected by the water, displaying a wider domain B for deeper waters. In very shallow waters (≤500 m), domain B disappears and we can only identify domain A, which is dominated by the sedimentary structure, directly followed by domain C, which is dominated by crustal structure. (b) Effect of the sedimentary structure on group velocities. Rayleigh wave fundamental modes are strongly affected by the sedimentary structure at very short periods. The deeper the sediments, the more the low-velocity domain A extends to longer periods. (c) Effect of crustal structure on group velocities. We used our reference deep ocean structure, kept both the water and sediment layer fixed, and varied the crustal structure velocity below the sediments. The Rayleigh wave fundamental modes shows no observable sensitivity to crustal structure at short and mid periods, both in domain A (dominated by sediments) and domain B (dominated by the water). Only after the Airy phase transition to domain C, fundamental mode Rayleigh waves become visibly sensitive to the crustal structure. Phase velocities display a similar pattern (supplementary Figure S6.7).

the GCadiz, west of Gibraltar, SW Europe. Figure 6.2b shows that domain A is absent in a structure with no sediments. As sediment thickness increases, domain A extends down to longer periods, for both group and phase velocities. The A/B transition, which for group velocities occurs close to T=1 s for a sediment thickness of 100 m, occurs only at T=7 s when sediments reach a thickness of 5000 m. *Gualtieri et al.* (2015) studied the effect of seafloor sediments on surface waves and demonstrated that the reduced velocities of domain A are a consequence of reflected P-waves and transmitted P-SV waves in the water-sediment boundary. In OBS, domain A is most easily observed in pressure data, as seismometer data tend to be noisy at very short periods.

The effect of the sedimentary layer persists also in continental settings. In modeling not shown here, we observed that if we removed the water layer and kept only the solid Earth structure with a thick (5000 m) sedimentary layer, dispersion curves would still show domain A, with velocities of ∼0.4-0.5 km/s, followed directly by domain C. As an example, *Asano et al.* (2017) studied dispersion curves using data recorded in the thick Osaka sedimentary basin, onshore Japan, and found very low group velocities varying between 300 m/s and 600 m/s in the short period range (1-7 s).

6.2.4 Impact of crustal structure.

The strong sensitivity of short- to mid-period Rayleigh waves to the water and sediments begs the question of whether they are still useful to infer upper crustal structure in oceanic domains. To address this, we computed dispersion curves for a variable crustal structure, while keeping fixed both a 5000 m water layer and the sedimentary layer. We varied both Vp and Vs in the crust uniformly, from -0.2 km/s to +1.0 km/s with respect to the reference structure, below the 100 m thick sediments. Figure 6.2c and figure S6.7c shows that fundamental mode Rayleigh waves display very little to no observable sensitivity to crustal structure at short periods, both in domain A (dominated by sediments) and in domain B (dominated by water). Only after the Airy phase transition to domain C, fundamental mode Rayleigh waves become visibly sensitive to the crustal and upper mantle structure.

6.2.5 Influence of higher modes.

Previous studies in oceanic domains have shown that at short periods ($T < 10$ s) the fundamental and 1st higher mode of both Rayleigh and Love waves often interfere (*Yao et al.*, 2011; *Gualtieri et al.*, 2013, 2015; *Le Pape et al.*, 2021) . In order to investigate this interference, we again used our reference deep ocean structure and varied the water thickness between 1000 m and 5000 m. Figure S6.8 shows that Rayleigh wave phase velocities display no mode interference, although in deep waters (5000 m) the phase velocities of the two overtones approach that of the fundamental mode at periods of 1.5 s to 3 s. For Rayleigh group velocities, in shallow waters (1000 m) the dispersion curve of the fundamental mode is always separated from the two overtones, however the three approach each other at periods of 1.2 s and 2.6 s. In deeper waters (3000 m - 5000 m) we observe a clear interference between modes, particularly at short periods (1.3 - 5 s).

Figure S6.9 compares the energy diagrams of Rayleigh group velocities for the fundamental mode alone, 1st overtone alone and their sum. In the vertical component, there is an entanglement between the fundamental and 1st higher mode, with the two dispersion curves crossing at ∼5 s (Figure S6.9c). Below ∼5 s, the two curves are so close that they become difficult to separate. On the other hand, the pressure component shows more clear energy diagrams at short periods, which facilitates the selection of the fundamental mode (Figure S6.9f). Seismometers are sensitive to ground velocities, whereas pressure observations are proportional to force, and therefore acceleration. Thus, pressure data are richer in short-period energy, making it advantageous in studies of the shallow structure.

Finally, figure S6.10 compares synthetic seismograms of Rayleigh waves for the fundamental mode, 1st overtone and their sum. In all cases investigated, the fundamental mode is more energetic than the first higher mode. In addition, the radial component is more energetic than the vertical component, suggesting that it may be easier to extract the first higher mode from the radial component. As water depth increases, the arrival of the first energy becomes more strongly dominated by the 1st overtone (Figure S6.11). Therefore, in our example, it is easier to separate the fundamental and 1st higher mode in deeper waters. Nevertheless, the dominance of fundamental mode vs 1st overtone is dependent on Earth structure and generalizations are not warranted.

6.2.6 Love waves in deep ocean settings.

As discussed before, Love waves are insensitive to the water layer due to their shear motion, which in oceanic environments becomes advantageous. Figure S6.12 shows the sensitivity of Love waves to Vs in our reference deep ocean structure, together with group and phase dispersion curves for the fundamental and first higher mode. The kernels confirm that both group and phase velocities are more sensitive to the shallow sedimentary crustal structure than Rayleigh waves. Figure S6.13 shows the impact of sediment thickness in the dispersion of Love waves. The pattern is similar to that of Rayleigh waves (Figure 6.2b), with sediments originating low-velocity group and phase velocities at short periods. The thicker the sediments, the longer the periods up to which such low velocities extend. Figure S6.14 shows the effect of a varying crustal structure below fixed water and sediment layers. Both group and phase velocity dispersion are identical for all crustal structures below 2 seconds, where velocities are dominated by sediments. Above 2 s, group and phase velocities vary strongly with crustal structure, confirming that changes in the Earth structure will be easily imaged. In this example the dispersion curves of the fundamental and 1st higher mode are not entangled (Figure S6.12b). However, even small changes in velocity structure, particularly in the sediments, can lead to mode interference (*Le Pape et al.*, 2021).

6.2.7 Impact of laterally varying water depth.

In a deployment, the depth of OBS varies, sometimes dramatically, as in coastal land-ocean deployments. Changes in water depth and topography between source and receiver affect the wavefield, namely by ray bending and scattering (*Gualtieri et al.*, 2015; *Bowden et al.*, 2016; *Corela et al.*, 2017; *Tian and Ritzwoller*, 2017). A common approach is to model surface waves as if both sensor and receiver were under the same water depth, which is taken as the average depth of the two (*Harmon et al.*, 2007; *Yao et al.*, 2011). Another possible strategy is to remove from the analysis dispersion curves corresponding to paths along which depths differ substantially (e.g. *Zha et al.*, 2014). Alternatively, one may opt to model all paths, including deep-shallow water paths and ocean-land paths, in order to improve network coverage, ignoring the depth differences (*Bowden et al.*, 2016; *Corela et al.*, 2017; *Tian and Ritzwoller*, 2017).

We start by investigating paths with a laterally varying water layer using SLAT2D96 (*Herrmann*, 2013). Similar to SYN-E, is based on the Normal-mode summation as a sequence of 1D blocks (SLAT2D). It allows to model a laterally varying media as a sequence of 1-D blocks, where surface waves propagate from one block to the next without mode conversion or reflection and assuming energy conservation (*Keilis-Borok et al.*, 1989). Here, we used two 1-D blocks whose structures corresponded to our reference oceanic model (Ocean1) and to an identical solid Earth structure overlaid by a thinner 2.5-km thick water layer (Ocean2) (Figure S6.15). We placed the source in Ocean1, the receiver in Ocean2, kept the total source-receiver distance constant (100 km) and varied the width of each block. The resulting phase and group velocities show a mixed pattern between those of each individual structure. In particular, the group velocities display two Airy phases instead of just one, at T=6 s and T=12-13 s (Figure S6.15c). Group and phase velocities start to increase at T=6-7 s, corresponding to the B/C transition of the shallow water block. However, typical crustal velocities (∼4 km/s) are only achieved at T=12-13 s, corresponding to the B/C transition of the deep water block. The longer surface waves travel in the deep Ocean1 model (or conversely in the shallow Ocean2 model), the closer the dispersion pattern will be to that of a homogeneous deep water structure (or conversely to that of a shallow water structure).

The block model used in SLAT2D is a simplification of the real Earth that allows us to gain insight into the dispersion of surface waves along a path with laterally varying water depth. However, its assumption of no mode conversion is justified only for smoothly varying media. For more complete modeling, we used the Spectral element method (SPECFEM3D) that models the full wavefield (*Komatitsch and Tromp*, 1999; *Komatitsch et al.*, 2016). Now, the structure varies progressively from deep to shallow water, identical to the 3-D model of *Le Pape et al.* (2021) (Figure 6.3). The anelastic 3-D model was extended in depth to 250 km to ensure that at least 3 wavelengths corresponding to the periods of interest (3 - 20 s) were covered. The model comprises an acoustic water layer and an anelastic Earth's structure defined by the Ocean1 model, where the sediments shear wave velocity was set to Vs=610 m/s, allowing to resolve a minimum period of 2.9 s. The simulation was performed over 150 000 timesteps, with a time step of 0.008 s, corresponding to a sampling rate of 125 Hz in the synthetic signals. The source was placed 15 m below the sea surface to simulate the oceanic microseismic source and its time function was built

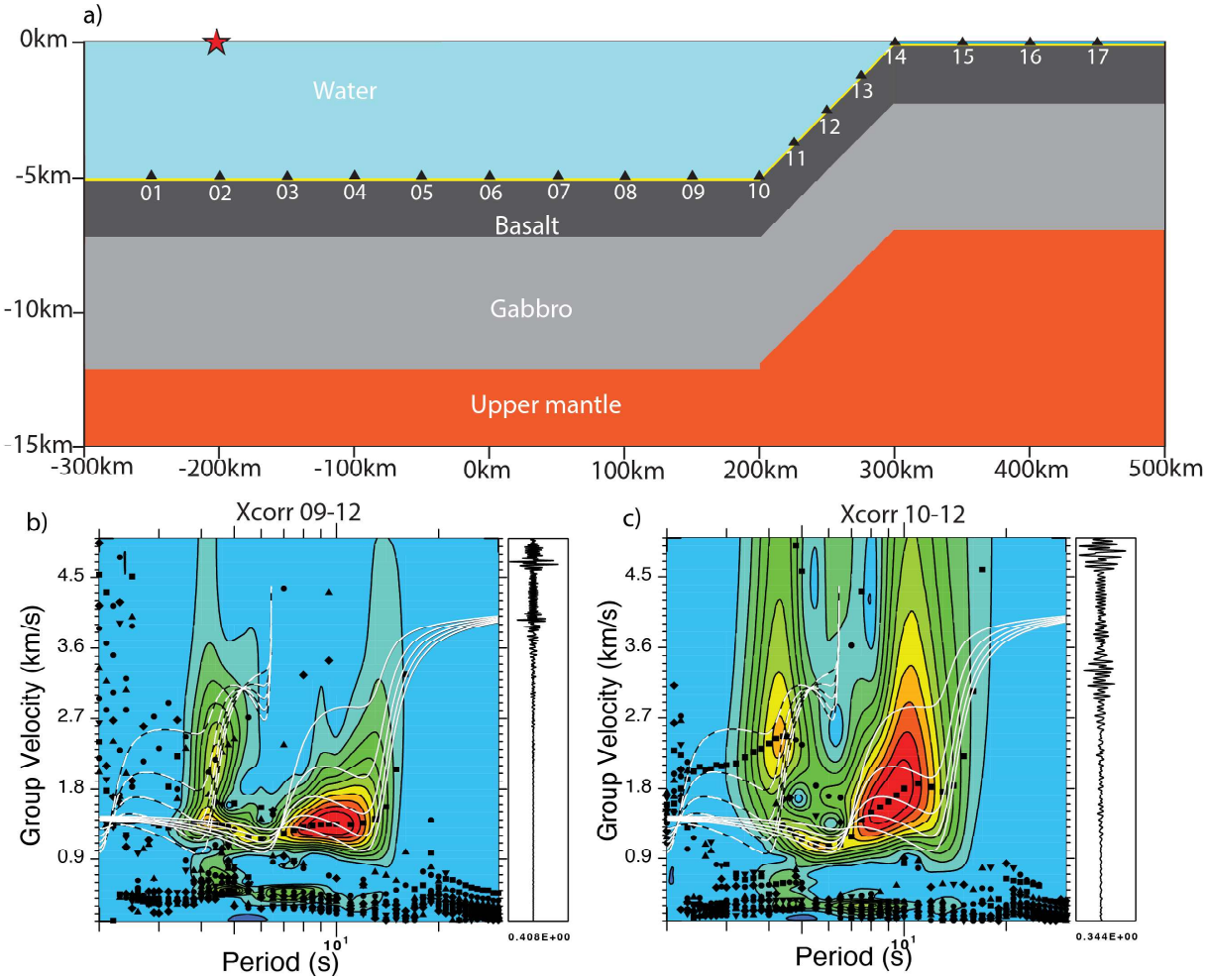

Figure 6.3: (a) Earth structure cross-section, where we used our reference oceanic structure with a varying water layer. The sediments Vs velocity was slightly increased to 610 m/s due to computational limitations. We placed 17 stations 15 m below the seabed and the source 15 m below the sea surface (red star). Energy diagrams obtained by cross-correlating synthetic surface waves recorded at station pairs (b) 09-12 and (c) 10-12. A first Airy phase is visible at 6 s, which is due to the 2.5 km water layer. A second Airy phase occurs at 13 s, corresponding to the 5 km of water layer of the deep ocean. For comparison, we added the fundamental (solid white lines) and first higher mode (dashed white lines) synthetic dispersion curves obtained using SLAT2D (see Figure S6.15c).

as a combination of simultaneous acoustic Ricker wavelets of dominant frequencies 0.12, 0.1, 0.08, 0.06 and 0.04 Hz. This source function allows to emphasize the effect of the varying water depths at longer periods. We placed 17 receivers 15 m below the seafloor along the path in order to track propagation effects.

Figure 6.3 shows the dispersion curves obtained by cross-correlating synthetics at stations 9-12 and 10-12, and the respective energy diagrams. Synthetic dispersion curves obtained with SLAT2D are also plotted. As foreseen by SLAT2D, the dispersion curves obtained with SPECFEM3D show a double Airy phase corresponding to the B/C transitions of Ocean1 and Ocean2. The energy diagram of station pair 9-12 compares better with the block model comprising 70 km of Ocean1 and 30 km of Ocean2, both corresponding to paths that include longer deep water segments. As the segment traveled in shallow water increases, as for station pair 10-12, the dispersion curve approaches the corresponding SLAT2D modeling, resulting in this case with a good fit to the block model of 50 km of Ocean1 and 50 km of Ocean2. The fit between the dispersion inferred from SLAT2D and SPECFEM3D is further improved if we model the continental slope using several consecutive blocks of progressively varying water depth, rather than just two blocks (Figure S6.16).

6.3 Real Data Observations

6.3.1 Deep ocean.

We now analyse observations from three seismic experiments located in different oceanic settings (Figure S6.5). We start by analyzing data of the DOCTAR OBS, located in the north Atlantic (Figure S6.17a). DOCTAR stations were deployed under an average water depth of ∼5000 m and all inter-station paths are purely oceanic. The seismic structure under the DOCTAR area is consistent with an oceanic crust and mantle influenced by the nearby Gloria Fault. *Hannemann et al.* (2016) found that towards the Gloria fault (south) the crust thickens from 5 km to 8 km and the mantle Vs decreases from 5.5 km/s to 4.5 km/s, hypothetically related to serpentinization processes.

Figure 6.4a shows Rayleigh group dispersion curves obtained by cross-correlating continuous hydrophone data recorded at OBS of the DOCTAR area. A synthetic dispersion

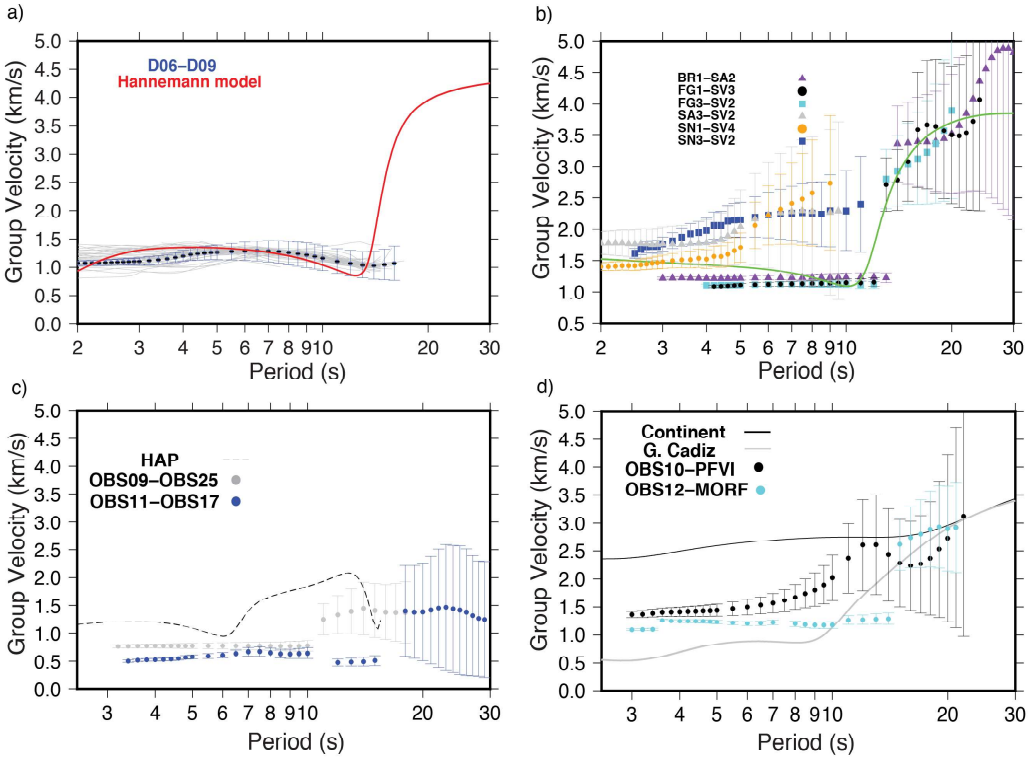

Figure 6.4: Rayleigh-wave group velocity dispersion curves observed in different oceanic settings (Figure S6.17): (a) DOCTAR, north Atlantic (deep ocean). Dispersion curves from ambient noise CC analysis observed between all pairs of stations are shown in gray. The dispersion curve between stations D06-D09, together with its error bars, for the hydrophone component, is also shown (blue). For comparison, we also show a synthetic dispersion curve (red) obtained from a local velocity model (*Hannemann et al.*, 2016). The observed variability at short periods (<6 sec) is due to sediments and water layer. (b) Cape Verde archipelago, north Atlantic (ocean islands) (*Carvalho*, 2020). Dispersion curves for station pairs BR1-SA2 (red), FG1-SV3 (black) and FG3-SV2 (cyan) correspond to paths that cross ∼4 km deep ocean. Dispersion curves for station pairs SA3-SV2 (gray), SN1-SV4 (orange) and SN3-SV2 (brown) correspond to paths between nearby islands, which only cross shallow waters. Error bars show the uncertainty of each dispersion curve. For comparison, a synthetic dispersion curve is also shown (solid green line), computed using SLAT2D for three adjacent blocks with different Earth structures: 1) a block 30-km wide representing the S. Vicente structure (NW islands); 2) a block 200-km corresponding to a deep ocean domain; 3) a block 30-km wide representing the Fogo island structure (SW islands). Inter-island paths that cross the deep water basin show a wide domain B (with velocities of ∼1 km/s), whereas paths that only cross shallow waters show a more gradual increase in velocities. (c) and (d) Land-ocean transition from SW Iberia, Europe, to the adjacent north Atlantic ocean (ocean-land domain) (*Corela et al.*, 2017). (c) Group velocity dispersion curves for station pairs OBS11-OBS17 (deep ocean, blue) and OBS09-OBS25 (mid-depth to deep ocean, red); (d) OBS10-PFVI (mid-depth to continent, black) and OBS12-MORF (deep ocean to continent, cyan). For comparison, we show synthetic dispersion curves obtained using SLAT2D corresponding to different domains: continent (solid black line), GCadiz (solid gray line) and Horseshoe Abyssal Plane (HAP) (dashed line).

curve corresponding to the local velocity model of *Hannemann et al.* (2016) is also shown. Due to the short inter-station distances and energy content of microseisms, group velocities can only be computed for T<16 sec. Further considering the thickness of the water layer, the data only images domains A and B. The B/C transition shown by our synthetic models has been well imaged in other deep ocean experiments with longer inter-station distances (e.g., *Ryberg et al.*, 2017).

In the short period range (T<4 s), the dispersion curves show some variability (0.75-1.4 km/s) that reflects the varying sedimentary structure (domain A). The comparison between energy diagrams of various OBS channels indicates that the fundamental mode is dominant and easier to identify in hydrophone than in vertical-component seismic data (see example in Figure S6.18). In addition, the first higher mode is more easily identifiable in the radial component.

6.3.2 Island-Ocean-Island.

As an example of a deployment in an oceanic archipelago, we use data of the CV-PLUME network (Figure S6.17b). The Cape Verde Archipelago consists of 10 volcanic islands in the eastern Atlantic Ocean, the origin of which has been associated with hotspot activity (*McNutt*, 1988; *Ali*, 2002). Some of the inter-station paths cross an oceanic domain with 4-km deep water (*Carvalho*, 2020). As an example of these, we plot three group velocity dispersion curves that correspond to paths between the islands of S. Antao and S. Vicente, to the northwest, and the islands of Brava and Fogo, to the southwest (BR1-SA2, FG1-SV3, FG3-SV2) (Figure 6.4b). For comparison, we also show a synthetic dispersion curve computed for a path corresponding to a laterally varying medium consisting of a first block, 30-km long, of typical S. Vicente (NW islands) structure, followed by a 200 km long ocean path, and a final 30-km long path with a structure similar to that of Fogo (SW islands). The velocity structures for the blocks of S. Vicente and Fogo were taken from *Lodge and Helffrich* (2006) and for the oceanic block from *Pim et al.* (2008); *Carvalho et al.* (2019). These three dispersion curves show a wide domain B, dominated by the water layer, with group velocities of ∼1.5 km/s, at periods of 2 s to 12 s. At T ∼12 s, the three dispersion curves show a jump to higher velocities, typical of the crustal structure (2.7-3.5 km/s), corresponding to the B/C transition. Only paths that travel through the deep ocean domain show a prominent domain B. In opposition, inter-island paths

that only cross shallow waters (SA3-SV2, SN1-SV4, SN3-SV2) display more progressive increases in velocity, indicative of the strongly laterally varying structure that they cross.

6.3.3 Continent-ocean transition.

Finally, we use data of the NEAREST project, offshore SW Europe, as an example of a continent-ocean transition (Figure S6.17c). OBS stations were placed at depths of 2000 m to 5000 m and the maximum continental elevation of land stations was 560 m. OBS stations were located over two main morphotectonic domains, the HAP and the GCadiz. The structure below the HAP consists of a very thick (4-5 km) sedimentary layer, which directly overlays serpentinized exhumed mantle. The GCadiz is underlain by a thick (3-4 km) unconsolidated sedimentary layer, followed by a layer of consolidated sediments (1-3 km) and a layer for the transition between oceanic and continental crust with a thickness of $\sim 15 km$(*Sallarès et al.*, 2011).

Figure 6.4c shows observed group velocities for: 1) a deep ocean - deep ocean path (OBS11-OBS17); 2) a deep ocean - mid-depth ocean path (OBS09-OBS25); 3) a mid-depth ocean - continental path (OBS10-PFVI); and 4) a deep ocean - continental path (OBS12-MORF). For comparison, we present synthetic dispersion curves based on three different velocity models: 1) a continental velocity model; 2) a model representative of the GCadiz; and 3) a model representative of the HAP (Figure S6.17c); In all cases, we took vertical profiles from wide-angle reflection profiles corresponding to the regions of interest (*Sallarès et al.*, 2011, 2013). The synthetic dispersion curve for the HAP shows a very wide domain A, in result of the thick 5-km layer of sediments, followed by a domain B that corresponds to the 5 km water layer. The continental synthetic dispersion curve shows group velocities above 2.5 km/s over the whole period range, as expected. The synthetic dispersion curve of the GCadiz shows a very low group velocity domain at $T < 5$ s, which corresponds to domain A, dominated by the thick sedimentary layers, followed by domain B, dominated by the water, and finally domain C, corresponding to the lower crustal structure and mantle.

The deep - deep ocean path (OBS11-OBS17), corresponding to a path that crosses the Horseshoe Abyssal Plain, shows a wide short period band ($T < 15$ s) composed of very low group velocity ($\sim$0.5 km/s) due to the very thick sedimentary layer (domain A) and

also very low velocity of ∼0.7 km/s dominated by the water layer (domain B) This wide domain leads to the interference between fundamental and first higher mode of Rayleigh waves (Figure S6.19). The short interstation distance does not allow us to image the transition to domain C. The synthetic dispersion curve for the HAP (dashed line) shows a higher group velocity at all periods than observed, suggesting that either the Vs model adopted for the HAP is not accurate or that it was not possible to correctly extract the fundamental mode from the observed energy diagram.

The deep - mid-depth ocean example corresponds to the path between OBS09, located in the HAP, and OBS25, located at the bottom of the continental slope. The group dispersion curve is similar to that of OBS11-OBS17, with the difference that domain A has a slightly higher velocity, reaching values of ∼0.8 km/s. This suggests that the sediments Vs is higher along path OBS09-OBS25 than along OBS11-OBS17.

The mid-depth ocean - continental path is illustrated by stations OBS10, located at the outer edge of the accretionary wedge, in the GCadiz, and PFVI, in mainland Portugal. This dispersion curve clearly shows the effect of the laterally varying medium. At short periods ($T < 6$ s), we observe a group velocity of ∼1.5 km/s, corresponding to domain B, dominated by the water layer. At $T = 6$ s group velocities start to rise, reaching a peak at $T = 13$ s, then decrease and later rise again. This double B/C transition corresponds to the two dominant water depths along the path, namely a shallow water depth in the continental shelf and a deep water layer in the GCadiz.

Finally, a deep ocean - continental path is exemplified by stations OBS12, located in the HAP, and MORF, in mainland Portugal. This dispersion curve shows a wide domain B, dominated by the water layer, typical of deep ocean settings, followed by an increase in group velocities to domain C at $T = 14$s. Along this path, the identification of the fundamental mode is not easy due to interference with higher modes caused by the large water depth difference between the two stations (> 5 km) and by the location of OBS12 on top of a very thick sedimentary layer (Figure S6.19).

6.4 Discussion and Conclusions

In this work we showed the impact of water depth, sediments, mode interference and laterally varying water column on short- to mid-period ($T < 20$ s) surface waves. At very short periods, the dispersion of surface waves - both Love and Rayleigh - is dominated by the sedimentary structure (domain A). Moving up in periods, we identify a second domain in which Rayleigh waves are mostly sensitive to the water layer (domain B); This domain is absent for Love waves, which are insensitive to the water. The deeper the water layer, the more domain B extends up to longer periods, reaching a maximum of $T = 15$ s for a 6000 m water layer. In domain B, the high sensitivity of Rayleigh waves to the water layer blocks their sensitivity to the upper crustal structure. Domain B ends with an Airy phase that marks the transition to domain C, which is dominated by lower crustal and upper mantle structure. When surface waves travel along a path with varying water thickness, the resulting dispersion curve is strongly distorted, displaying a behavior that is a mix of the various segments crossed. Synthetic tests where we varied the sediment and crustal structure support the conclusions of *Bensen et al.* (2008); *Lebedev et al.* (2013), who showed that at very short periods group velocities have a higher sensitivity than phase velocities, therefore allowing for a better resolution of sediments. On the other hand, at longer periods phase velocities become more sensitive to crustal structure. In Earth structures typical of oceanic domains, at short periods (<5 s) Rayleigh waves show a clear interference between fundamental and higher modes. This interference is particularly strong in deep waters and for group velocities. Love wave dispersion curves show a more clear separation between the various modes, even though some interference can exist at short periods (*Le Pape et al.*, 2021) and also at longer periods (*Nettles and Dziewoński*, 2011; *Luo et al.*, 2015; *Hariharan et al.*, 2020). Rayleigh waves observed in different oceanic settings confirm the existence of the three domains identified in synthetic tests, dominated by: (A) sediments; (B) water; and (C) lower crust/upper mantle structure, respectively. Paths between land stations that cross water domains (e.g., between islands) display similar effects to those of paths between ocean-bottom stations.

These results show that simplifying assumptions about the influence of the water layer are not warranted when computing tomographic models based on surface wave dispersion along paths that travel through water domains. In particular, the water layer, including

variations in its thickness along the path must be properly accounted for. In order to correctly interpret surface wave dispersion along paths that cross water domains, it is suggested that: 1) A special effort be dedicated to the observation of Love waves, as they are not affected by the water layer. To this end, the horizontal components must be carefully oriented and tilt noise reduced.2) Synthetic dispersion curves, including those of higher modes, should be computed using preliminary velocity models for the study region, using the appropriate water thicknesses. These will guide the seismologist in the interpretation of observations. 3) Dispersion curves should be picked or at least verified manually in the short-period band, where mode interference is likely to occur. 4) The pressure channel should be preferentially used to identify the fundamental mode, given that it is more energetic than the vertical seismometer component in the short period band. In addition, pressure dispersion curves are less affected by mode interference.

Supplement figures

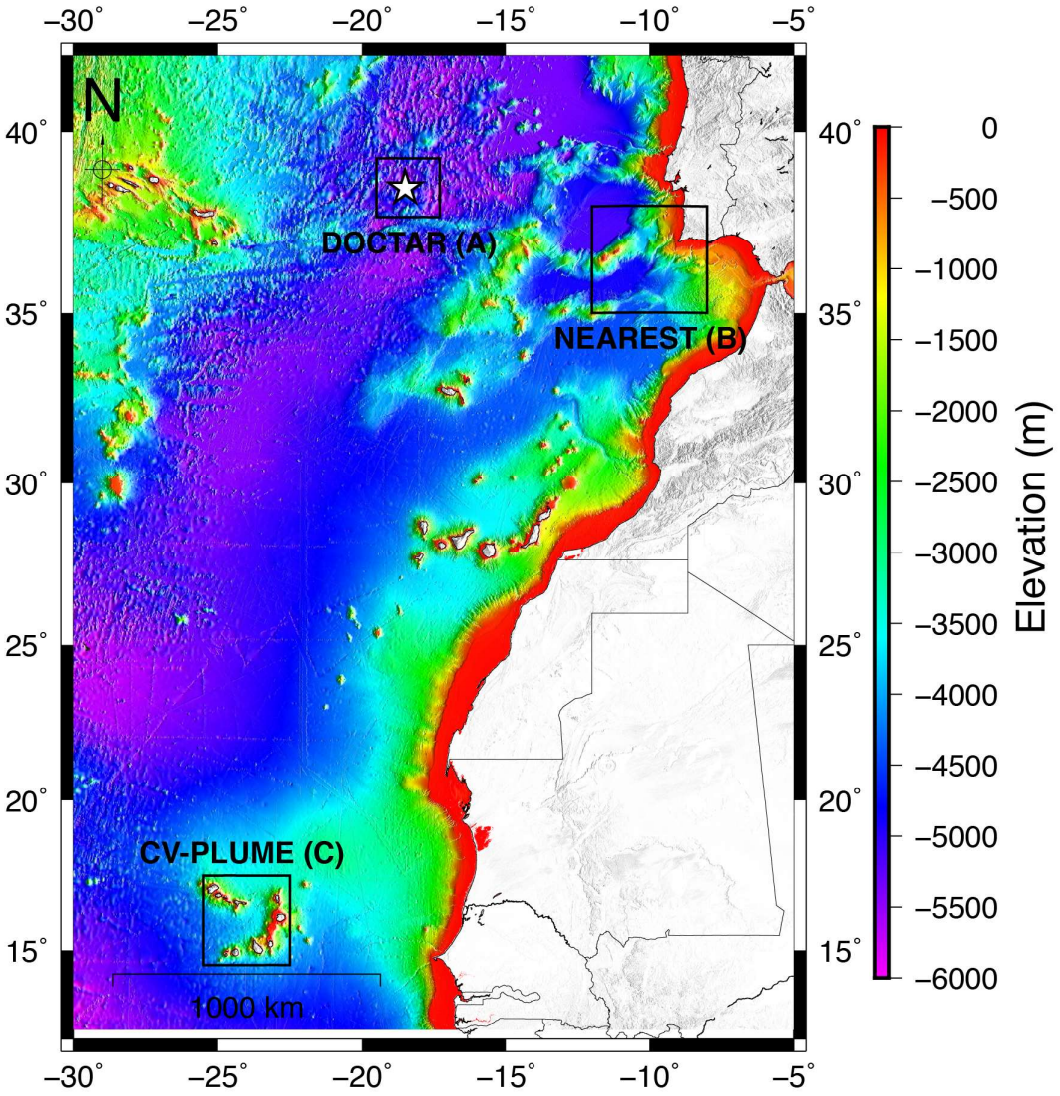

Figure 6.5: Location of the study regions for which we show the effect of the water layer on surface waves: A) Deep Atlantic ocean, DOCTAR area, 60 km north of the Gloria fault (*Hannemann et al.*, 2013); B) Ocean islands, Cape Verde archipelago, CV-PLUME project (*Weber et al.*, 2007); and C) Land-ocean transitional domain, GCadiz, offshore southwest Europe, NEAREST project (*Alfred-Wegener-Institut Helmholtz-Zentrum für Polar- und Meeresforschung et al..*, 2017). The white star marks the location where we extracted the reference oceanic velocity profile from Crust1.0 (*Laske et al.*, 2013). The background shows the global GEBCO bathymetry (*Tozer et al.*, 2019).

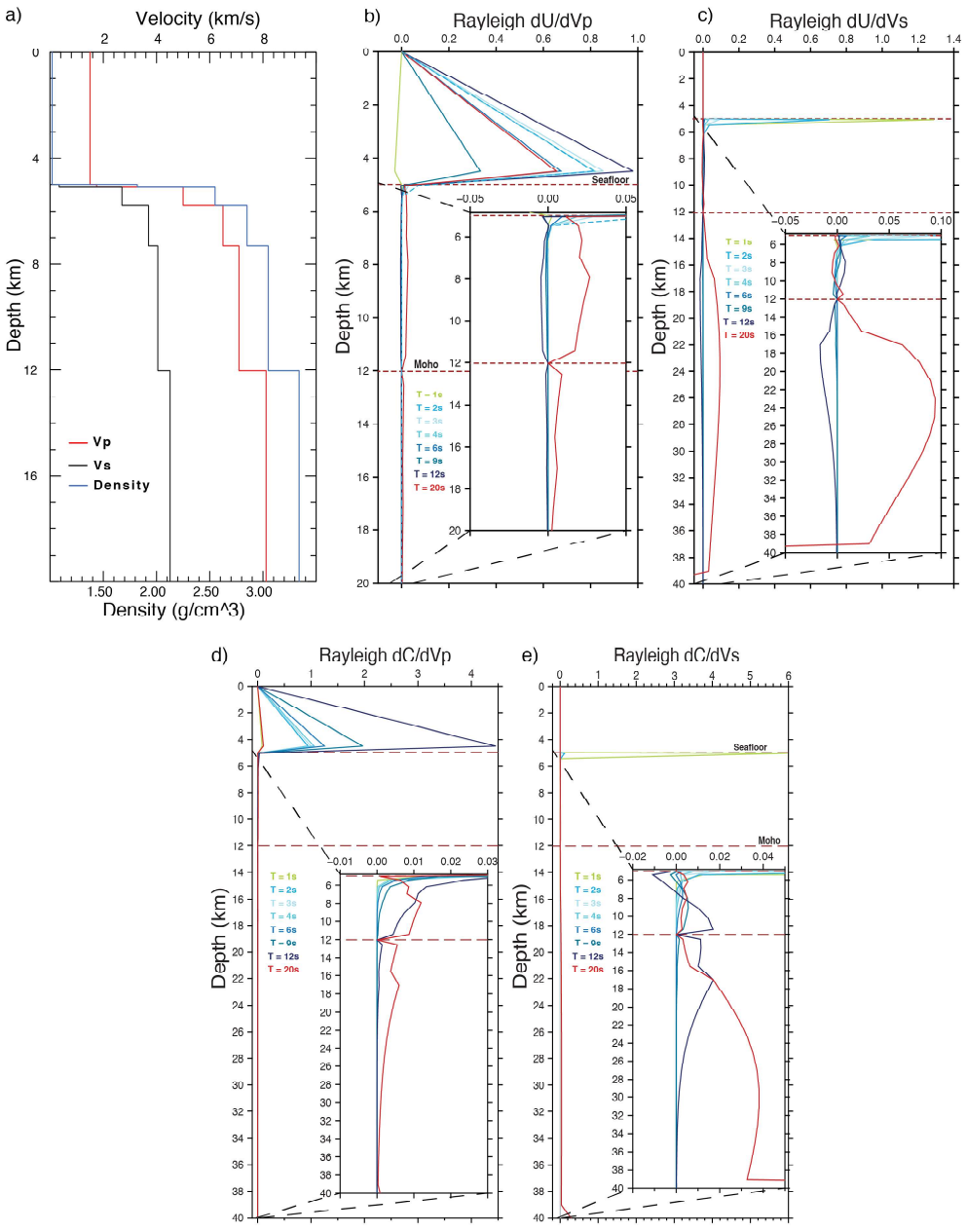

Figure 6.6: (a) Crust1.0 depth profile for Vp, Vs and density (*Laske et al.*, 2013) at a chosen location inside the DOCTAR area, deep north Atlantic (Fig. S6.5). This profile is taken as representative of a deep ocean environment. It consists of 5 km of water, followed by 100 m of unconsolidated sediments, 2.22 km of basalt (layers 1 and 2), and 4.71 km of gabbro (layer 3). (b, c) Sensitivity kernels of fundamental-mode Rayleigh wave group velocities for Vp and Vs, respectively. The two main interfaces, the seafloor and the Moho, are shown by dashed lines. The insets show a zoom of the structure below the seafloor. The colors of sensitivity kernels indicate whether they are most sensitive to the sedimentary structure (green), water layer (blue) or lower crust and topmost mantle (orange-red). (d, e) Sensitivity kernels of fundamental-mode Rayleigh wave phase velocities for Vp and Vs, respectively, also showing in dashed lines the two main interfaces.

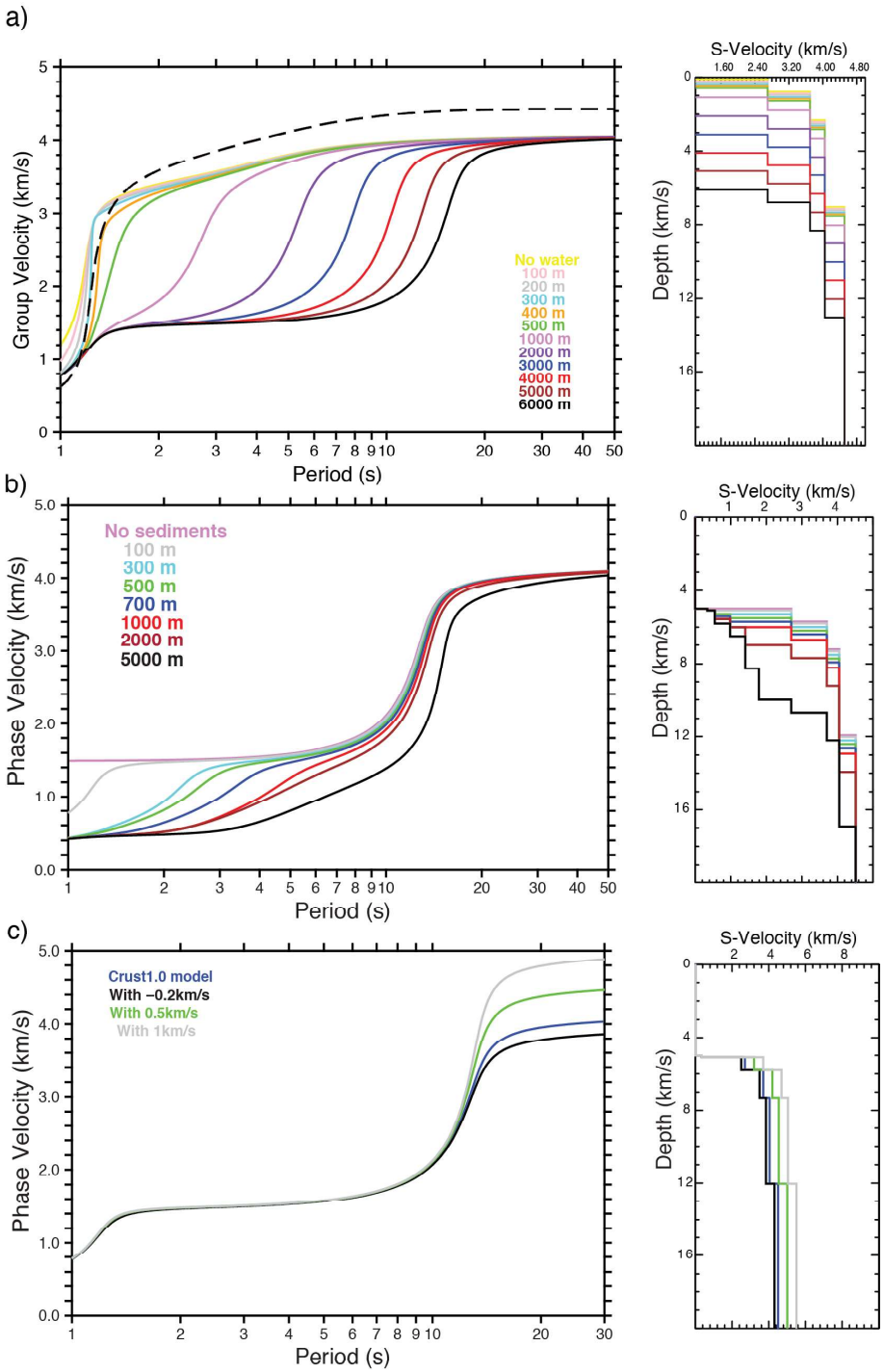

Figure 6.7: (Left) Synthetic phase velocity dispersion curves of fundamental mode Rayleigh waves obtained using EIGEN (solid lines). (Right) Velocity profiles modeled. (a) Effect of water depth in phase velocity dispersion curves. Love waves are not affected by the water layer (overlapping dashed lines). (b) Effect of the sedimentary structure. The impact of the sediments is more noticeable in group velocity than in phase velocity at short periods, in agreement with *Bensen et al.* (2008); *Lebedev et al.* (2013). (c) Effect of a varying crustal structure. Similar to group velocity, phase velocities show no observable sensitivity to crustal structure at short to mid periods.

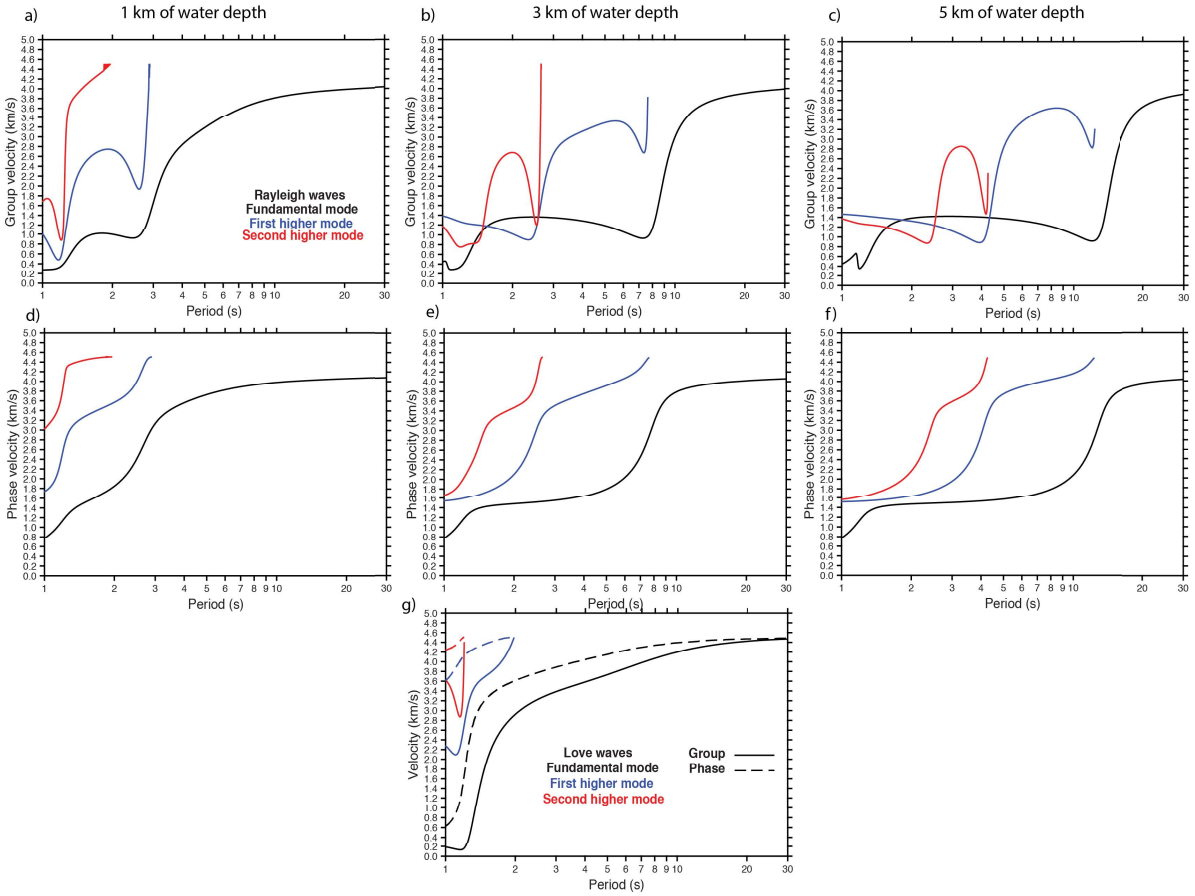

Figure 6.8: Vertical-component dispersion curves for the fundamental (black), 1st higher mode (blue) and 2nd higher mode (red) using our reference oceanic model. Group velocity dispersion curves for Rayleigh waves for water depths of: (a) 1 km; (b) 3 km; and (c) 5 km. Phase velocity dispersion curves for Rayleigh waves for water depths of: (d) 1 km; (e) 3 km; and (f) 5 km. (g) Dispersion curves for Love waves (not affected by water depth). Mode interference is clearly observed for Rayleigh wave group velocities for water depths of 3 and 5 km. The phase velocities of Rayleigh waves do not show clear mode interference, but approach each other at very short periods for water depths of 3 and 5 km. Love group and phase velocities are also not affected by mode interference.

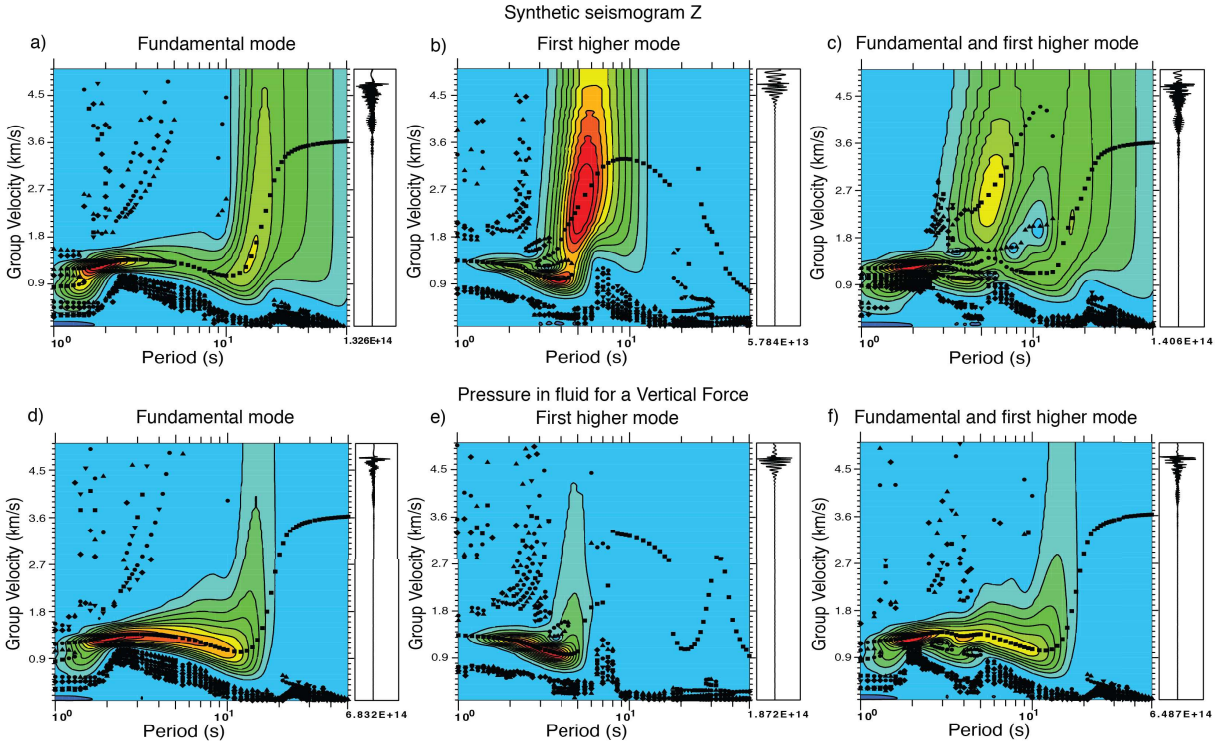

Figure 6.9: Vertical (top) and pressure (bottom) energy diagrams of Rayleigh group velocity (not normalized) extracted from SYN-E using a vertical force. (a,d) Fundamental mode; (b,e) 1st higher mode; and (c,f) fundamental and first higher mode combined. In all cases, we used a structure with a 5-km water depth and a source-receiver distance of 30 km. For pressure, the receiver was located 1 m above the fluid/solid interface. We observe clearly the fundamental and first higher mode in a) and b), but in c) the two modes becomes entangled below 5-6 s, not allowing their correct identification. Pressure energy diagrams are more clear than vertical energy diagrams at short periods.

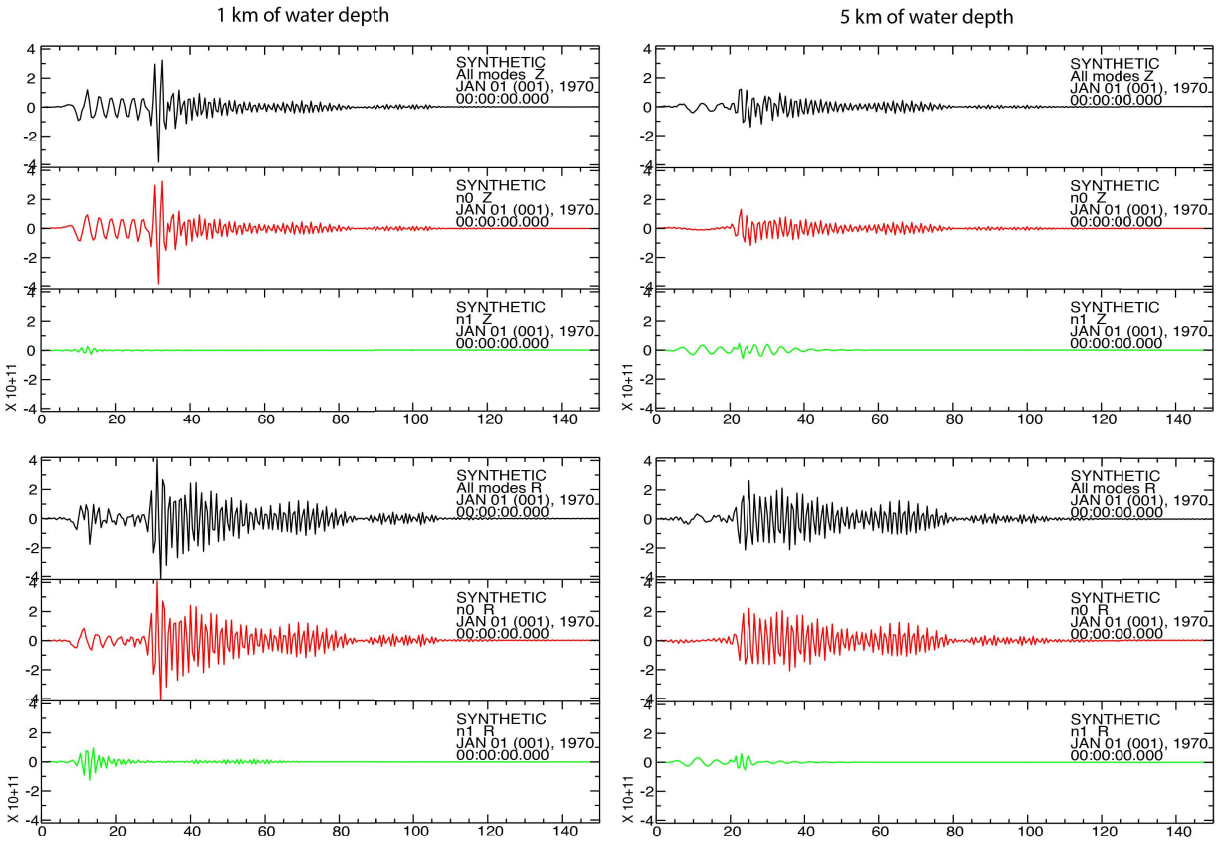

Figure 6.10: Synthetic seismograms for the fundamental (n0, red), first higher mode (n1, green) and two modes combined (black). We compare the synthetic seismograms obtained with a 1 km (left), and 5 km (right) water depth, both for the vertical (top) and radial (bottom) components. In all cases, we considered a distance of 30 km between source and receiver.

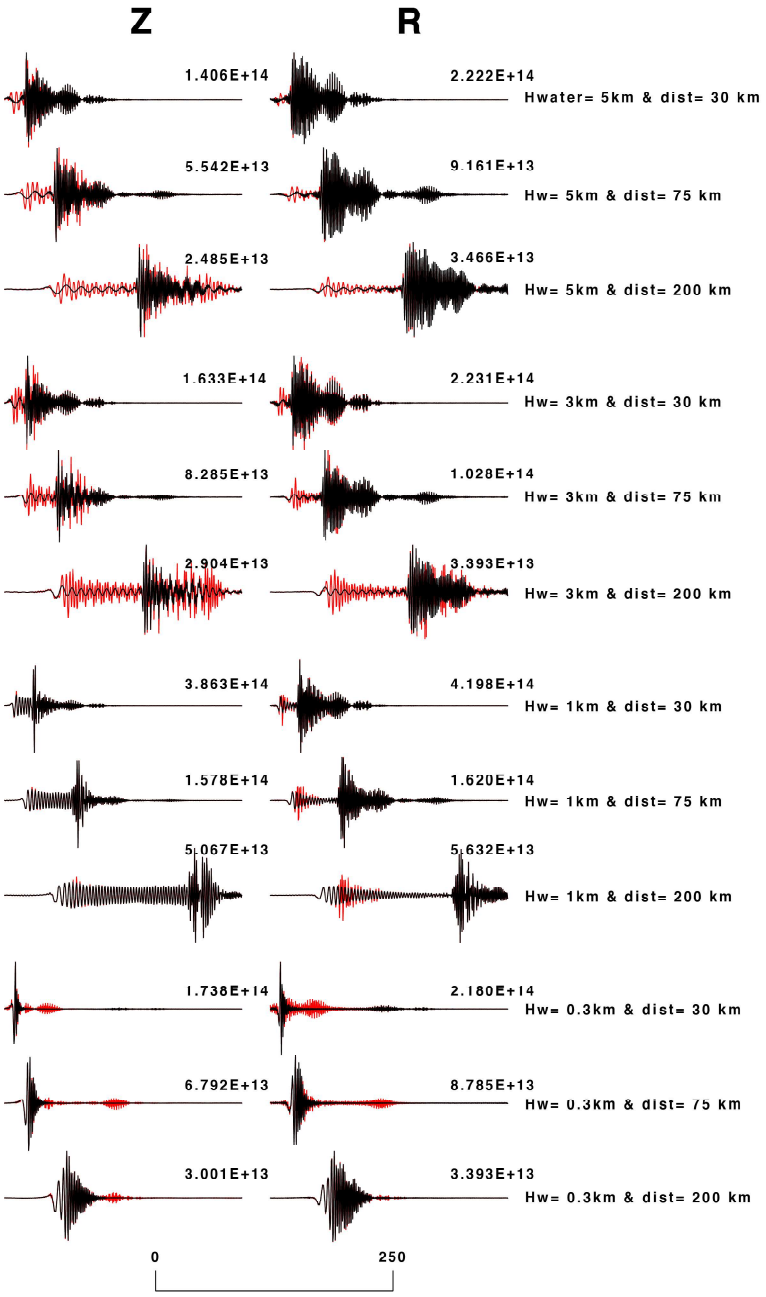

Figure 6.11: Synthetic seismograms computed with SYN-E, showing the fundamental mode (black) and the combined fundamental and first higher mode (red). We used inter-station distances of 30 km, 75 km and 200 km, and water thicknesses of 300 m, 1 km, 3 km and 5 km. The figures show both the vertical (left) and radial (right) components.

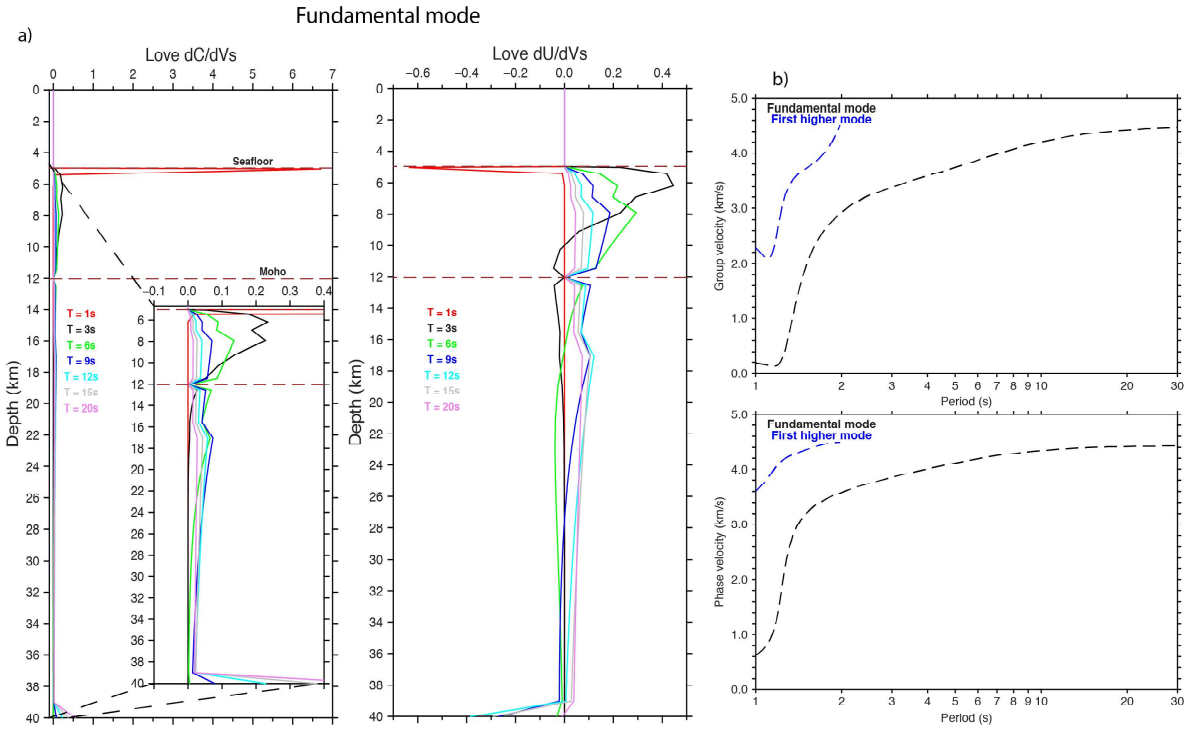

Figure 6.12: Love wave sensitivity kernels to S-wave velocity: (a) phase and group velocities, using our reference oceanic velocity model. Love wave dispersion of: (b) Group and phase velocities, for the fundamental (black) and first higher mode (blue). Love wave group velocities are more sensitive to the shallow structure (short periods) than phase velocities.

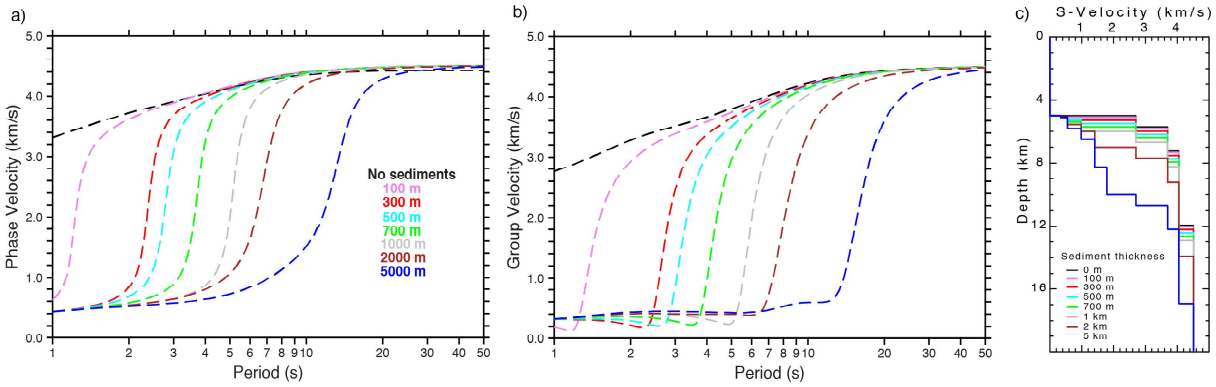

Figure 6.13: Effect of sediments on fundamental mode Love waves. Similar to Figure 6.2b, the sedimentary structure of the our reference oceanic model was varied. (a) Phase velocities. (b) Group velocities. (c) Vs profile of the various structures tested. The synthetic dispersion curves were computed with EIGEN. The deeper the sediments, the more the low-velocity domain A extends up to longer periods.

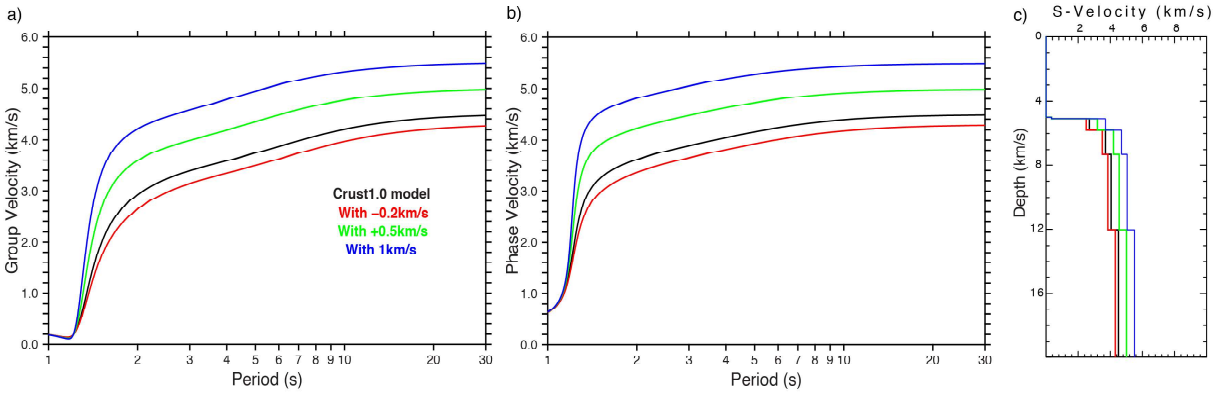

Figure 6.14: Effect of the crustal structure on fundamental mode Love waves. (a) Group velocity dispersion curves for different structures obtained by varying the structure below a fixed sedimentary layer. (b) Phase velocities dispersion curves for the same structures. (c) Vs profile of the various structures tested. Love-wave fundamental mode is very sensitive to crustal structure, as expected from purely shear-motion waves (not affected by water).

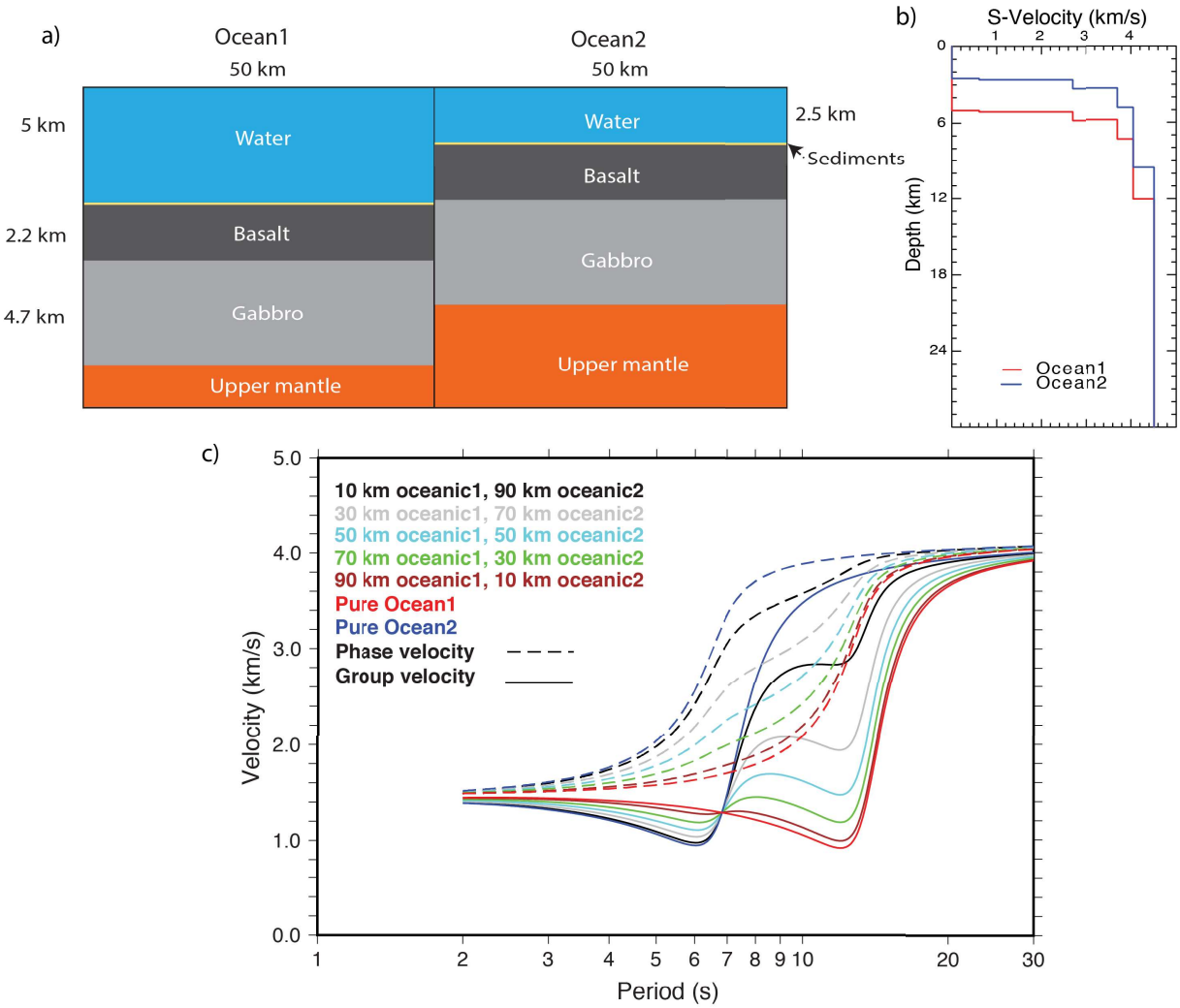

Figure 6.15: Synthetic dispersion curves were computed with SLAT2D96 (*Herrmann*, 2013), which is similar to SYN-E but allows to model a laterally varying structure. (a) Representation of the two blocks used in SLAT2D. (b) Two different velocity structures, Ocean1 and Ocean2. Ocean1 corresponds to our reference oceanic model (Figure S6.6a) except for the velocity at the layer of the sediments that were adapted to the SPECFEM3D initial model. Ocean2 has an identical solid Earth structure but a thinner 2.5-km water layer. We placed the source in Ocean1 and the receiver in Ocean2. (c) Effect of a laterally varying water thickness on fundamental mode Rayleigh waves. The source-receiver distance is kept fixed (100 km) and the widths of Ocean1 and Ocean2 are varied as shown by the colored lines. Both phase and group velocities show a pattern that is a mix of those obtained for each of the two oceanic structures. In particular, group velocities display two Airy phases, corresponding to the Airy phases of Ocean1 and Ocean2.

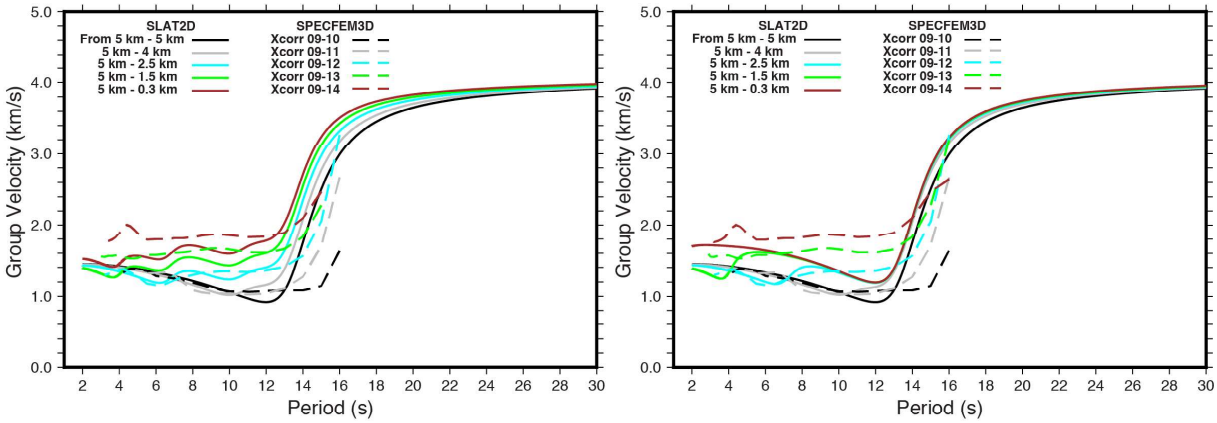

Figure 6.16: Group velocity eigenfunctions (solid lines) dispersion curves for SLAT2D and group velocity synthetic dispersion curves (dashed lines) for SPECFEM3D for stations located in the continental slope. On the left: SLAT2D eigenfunctions are computed using several blocks of 25 km width. For the last simulation of the station 09-14, six blocks where used, meaning one block for each station. The number represents the water depth for each block. For SPECFEM3D, the dispersion curves are from station 09 to the rest of the stations located in the continental slope. On the right: Only two blocks where used for SLAT2D, we only change the path proportions of each block in the simulation. We observe a much better approach of the eigenfunctions to the dispersion curves obtained with SPECFEM3D when using several blocks.

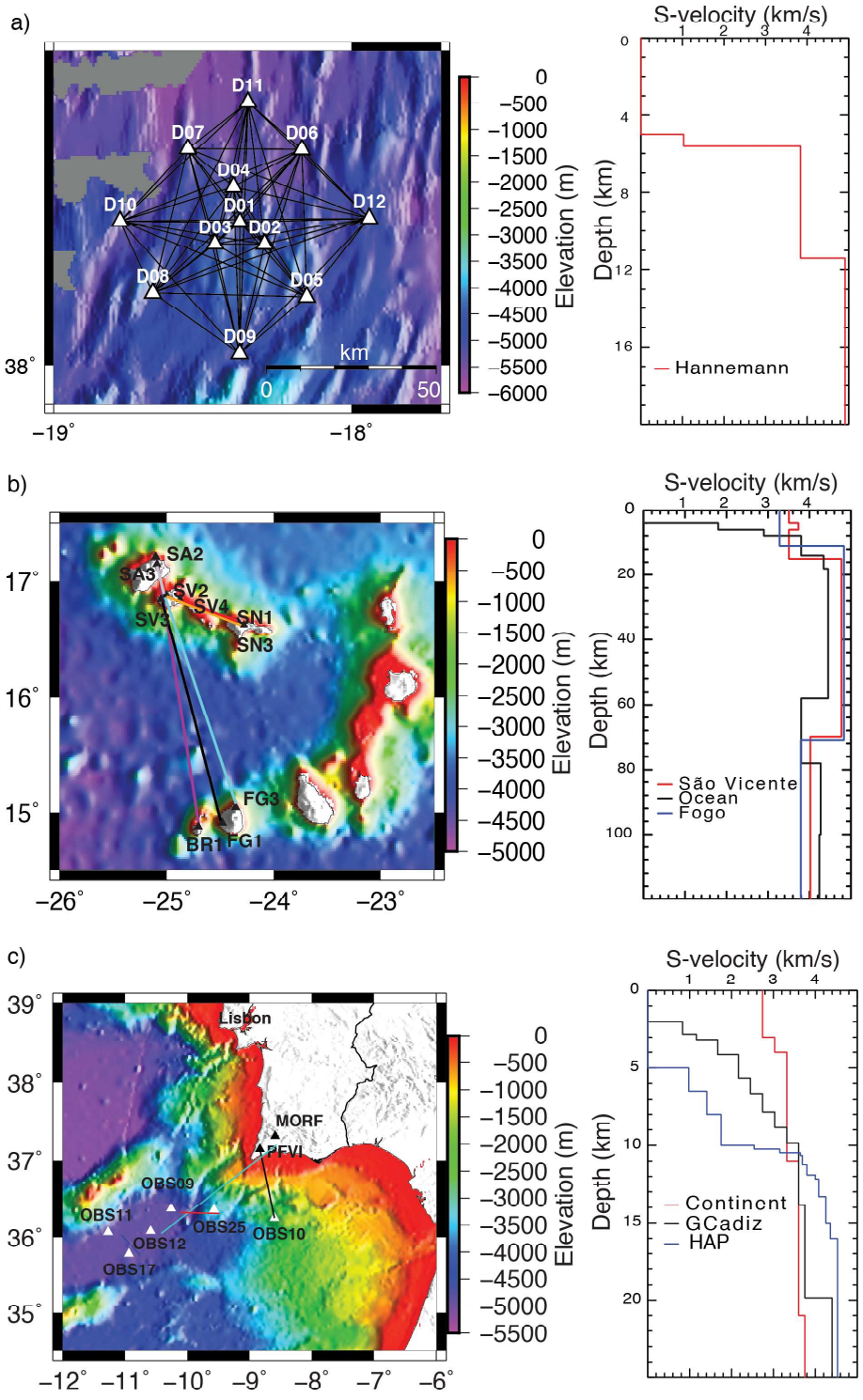

Figure 6.17: (a) Map of the DOCTAR area with the velocity model obtained from a local velocity model (*Hannemann et al.*, 2016). (b) Map of the Cape Verde islands showing the paths displayed in figure 6.4b) and velocity models used to compute the synthetic group velocity dispersion curve (*Lodge and Helffrich*, 2006; *Pim et al.*, 2008; *Carvalho et al.*, 2019). (c) Map showing station locations and inter-station paths for the Rayleigh wave group velocity dispersion curves observed in the figure 6.4c. Additionally, the different velocity models used to compute the synthetic dispersion curves shown in figure 6.4c) and d) are also shown: continent (black), GCadiz (red) and HAP (blue) (*Sallarès et al.*, 2011, 2013).

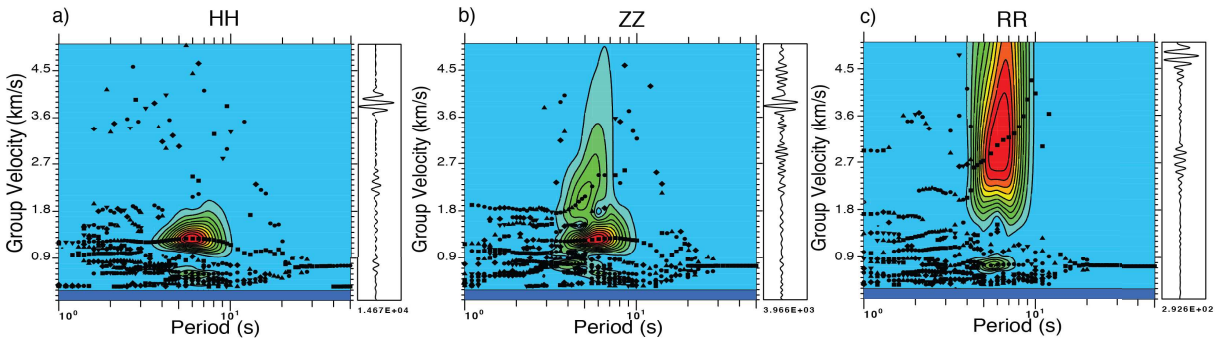

Figure 6.18: Observed energy diagrams for station pair D10-D12 of the DOCTAR area, north Atlantic (deep ocean). (a) EGFs obtained from the cross-correlation between hydrophone components; (b) EGFs obtained from the cross-correlation between vertical components; and (c) EGFs obtained from the cross-correlation between radial components. The fundamental mode is more energetic and easier to identify on the hydrophone component, whereas the first higher mode is easier to identify in the radial component. The vertical component energy diagram is the most affected by mode interference.

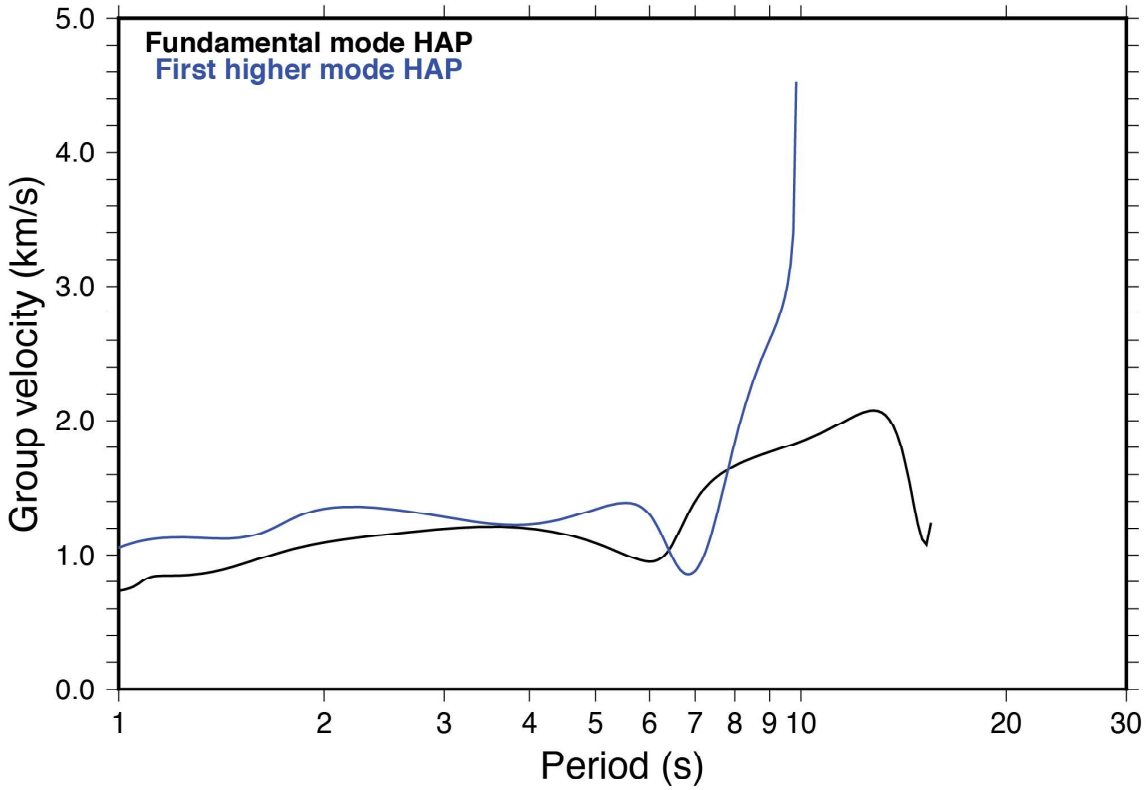

Figure 6.19: Synthetic dispersion curves for Rayleigh wave, vertical component, fundamental (black) and 1st higher mode (blue). The synthetic curves were computed based on a velocity structure representative of the Horseshoe Abyssal Plain (*Sallarès et al.*, 2013). The two curves show a clear interference between the fundamental and the first higher modes.

Chapter 7

1-D oceanic Earth structure north of the Gloria fault

The distribution of physical properties in the Earth's interior affects the propagation of seismic waves and can therefore be inferred using seismic inversion, one of the most commonly used techniques in geophysics. The physical properties to be determined include, among others, properties such as the elastic, anelastic and anisotropic parameters, as well as the density.

In this chapter, first it is presented a 1-D shear-wave velocity profile below the array using the average of the dispersion measurements obtained from ambient noise and the two-station method presented in chapters 3 and 4. To perform the 1-D shear-wave velocity inversion, it was used SURF96 (*Herrmann and Ammon*, 2002; *Herrmann*, 2013), which finds the velocity structure that best fits the observations.

7.1 Regional 1-D surface wave inversion

The estimation of a 1-D shear-wave velocity model for all the dispersion curves of the DOCTAR area is an important first step in determining the earth structure of the study area. On the one hand, it provides a robust estimation of the general local earth structure. In addition, it is also a first step towards the 3-D tomography, where it is used as a starting model.

The group and phase velocity dispersion data used for the 1-D inversion were obtained from ambient noise and the two-station method (Figure 7.1), as shown in chapters 3 and 4. The coda results were omitted as they were not considered reliable (chapter 5).

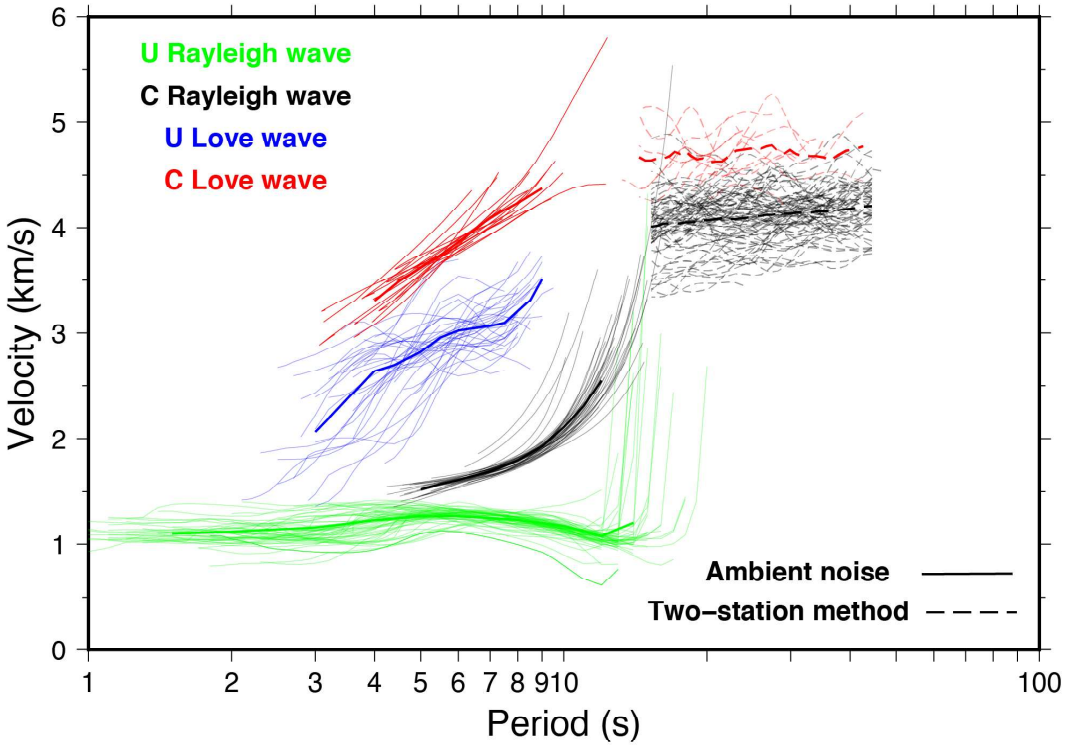

Figure 7.1: Data available for the 1-D shear velocity inversion test. Solid lines are the average of the dispersion curves obtained from ambient noise and the dashed lines represents the average of the dispersion curves inferred from the two-station method.

7.2 Method: SURF96 inversion

In this work, it was used the code SURF96 (*Herrmann and Ammon*, 2002; *Herrmann*, 2013) to perform the 1-D inversion for the velocity structure at depth based on the approach of *Rusell* (1987). SURF96 implements a linearized least squares approach to the inversion of the shear-wave velocity structure. The linearized inversion process provides a good fit to the dispersion observations but requires a good initial model. SURF96 aims to find the parameters that minimize the prediction error between the observed dispersion curves and those estimated from the model. This process is done by inversion with a weighted least squares method. The code allows to define different weights for each layer and also allows to have layers whose parameters are fixed. Knowledge of the depth of interfaces that might have been inferred from previous studies or independent observations can be used to constrain the inversion in those layers. The inversion can be done either

by fixing the layer thicknesses and inverting for the layer velocities or by fixing the velocities and inverting the layer thickness (*Herrmann and Ammon*, 2002). Additionally, the inversion process requires an input file for the observations, i.e., dispersion curves. During the inversion, at each iteration, the code computes the prediction and partial derivatives of the current model, then performs the velocity inversion and finally updates the model. In each iteration, it is possible to change the damping value according to the inversion performed.

7.3 Inversion setup

To test the reliability of the initial model, several tests were conducted. In these tests, the group and phase velocities of Love waves at short periods were used (extracted from ambient noise) and the phase velocities of Rayleigh and Love waves at long periods (extracted from the two-station method) (Figure 7.1). The short-period (ambient noise) group and phase velocities of Rayleigh waves were not used because of the dominant sensitivity to the water layer (Chapter 6).

The initial model was a half-space model topped by a sediment layer and a water layer. The sediment layer had the average sediment characteristics of the Hannemann model. The maximum depth of the model was set to 200 km, following the recommendation of *Maupin* (2011) to use a depth limit greater than that which the measured data can resolve. The model was parameterized using 51 layers: the top water layer has a thickness of 5 km, the second layer has a thickness of 600 m and represents the sediments, next we have 10 layers of 1 km thickness and finally the remaining layers have a thickness of 5 km. The weights of all the layers in our inversion process are set to 1, which is the default weighting factor, except for the water layer, whose velocity was fixed. At first, it was tested 176 different initial models. These initial models had a water layer with fixed velocity of Vp=1.5 km/s, a sedimentary layer with velocity varying from Vs=1.4 km/s to Vs=2.4 km/s, and a half-space with velocity varying from Vs=4.05 km/s to Vs=4.95 km/s, as shown in Figure 7.2. For the first 2 iterations of the inversions, a higher damping value of 10 were established to avoid overshooting in the first model estimation. After the second iteration, the damping was set to 1 for the rest of the 20 iterations.

The final shear wave models obtained from the different initial models hardly differ in the

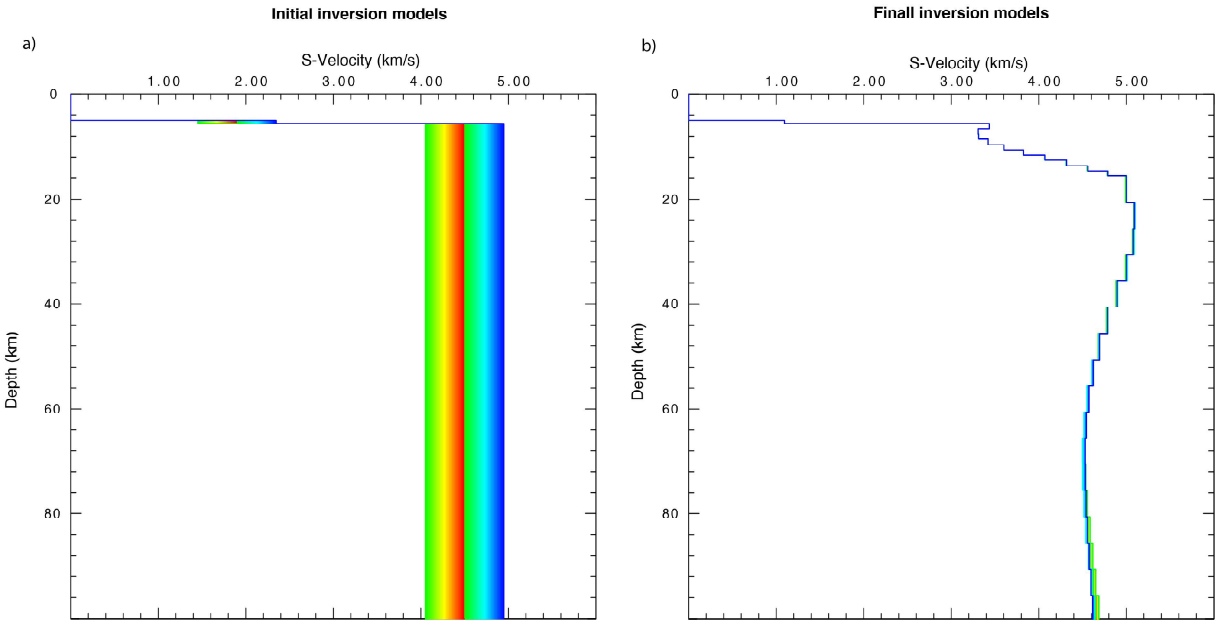

Figure 7.2: a) Shear-wave velocity models obtained using different starting models. For the different starting models, the velocity of the sediments and the half-space were varied by ± 0.5 km/s. b) The final shear-velocity models are very stable over all the depths with minor variations below 80 km. Each color represents the initial model, for instance the strong blue in the right edge has a half-space velocity of 4.95 km/s.

first 80 km, although the velocities of the initial half-space models varied by as much as 1 km/s. Below 80 km, the final inversions begin to show minor variations, which result from the limited resolution of our dataset at those depths.

The final inversion results show a very stable shear-wave model, indicating that it is possible to rely on our initial model for the following inversions. It was used the values of Vs=1.9 km/s for the sediments and Vs=4.5 km/s for the rest of the initial model, while keeping the same model parameters described above. In addition, more iterations were tested and found that the first 20 iterations seem to be sufficient to find a good signal power fit to the dispersion curves (Figure 7.3). For more than 20 iterations, the improvement in data fit is residual because the inversion starts to overfit the data, that is, to add detail to the model that has little consequence in data fit, thus not being justified by the data.

7.4 Shear-wave inversion of different datasets

Several inversions of the shear-wave 1-D velocity structure were performed using different combinations of all the dispersion curve data (Figure 7.1). The inversions were done with

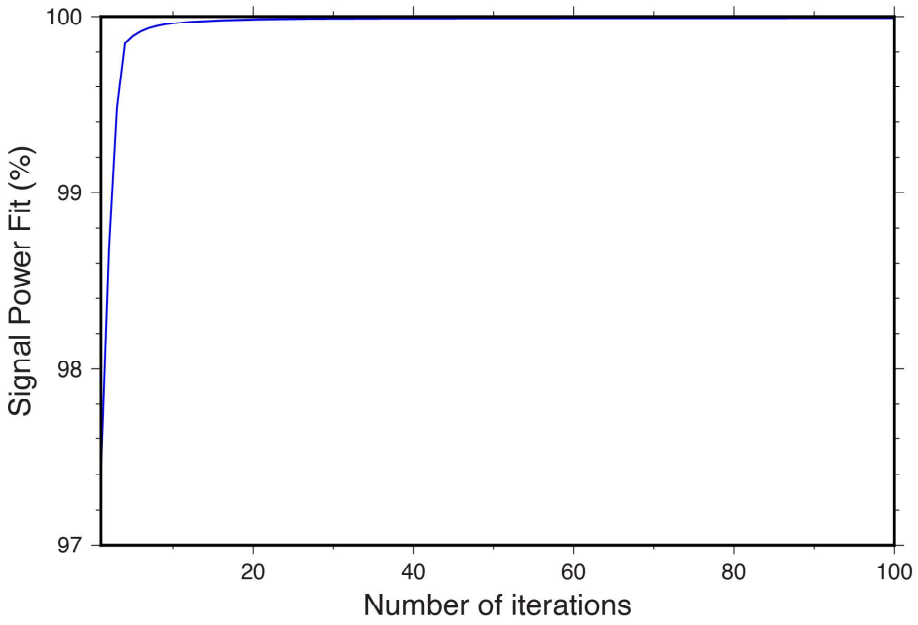

Figure 7.3: Signal power-fit vs number of iterations. After 20 iterations the model has a good signal power fit.

the same setup as above (section 7.3).

First, were inverted only the group and phase velocities of the Rayleigh and Love waves individually, using both group and phase velocities. Figure 7.4a shows the inversion using only the group and phase velocities of Rayleigh waves. After 20 iterations, it was obtained what is considered as a poor shear-wave model, with a fast velocity of 4 km/s in the first layer of the oceanic crust and a maximum velocity observed in the lithosphere of 6.5 km/s, well above typical mantle velocities. Furthermore, the model fit (red line) for the group velocity dispersion measurements is quite poor. This likely results from the observations being affected by the water layer and therefore not containing sufficient information on the crustal structure. On the other hand, the model fit of the phase velocity dispersion curves was very good. Still, the final model was strongly influenced by the group velocities. Figure 7.4b shows the inversion for only the phase velocity of the Love waves, which resulted in a much better shear-wave inversion, with a good model fit of the observations for the first 40 km depth. The combination of group and phase velocity of the Love waves also led to similar results as using only phase velocity dispersion curves of Love waves, with the exception that now a low velocity zone is observed in the first 3 km below the sediment layer (Figure 7.4c).

Next, it was inverted joint combinations of the group and phase velocity dispersion curves

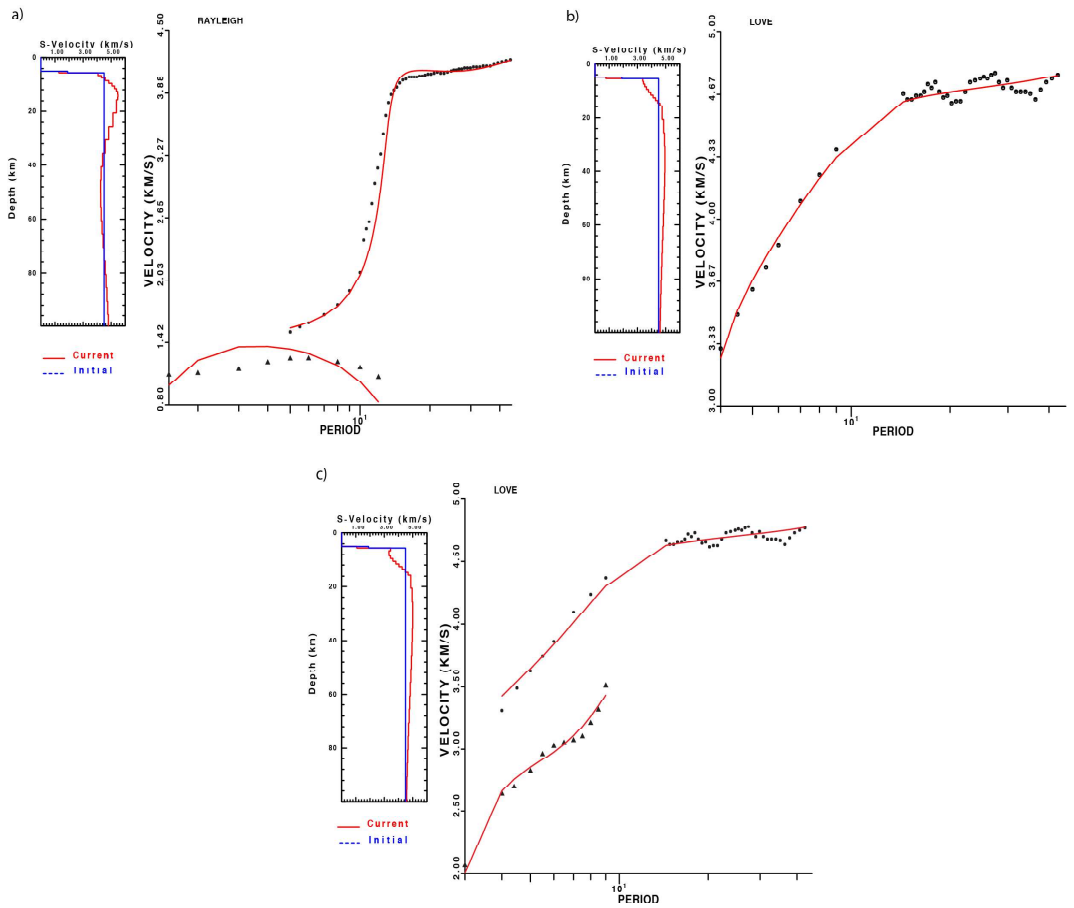

Figure 7.4: 1-D shear-wave velocity inversions based on dispersion data inferred from ambient noise and the two-station method. a) Shear-wave inversion for Rayleigh waves group and phase velocity. The average of the group velocity has observations between 1.5 s and 12 s, while phase velocity is between 5 s and 44 s period. The red line represents the dispersion curve corresponding to the best-fit model after 20 iterations. The triangles represent the group velocity and the circles the phase velocity dispersion measurements. b) Shear-wave velocity model for Love waves phase velocity between 4 s and 42 s. c) Shear-wave velocity inversion for Love waves group and phase velocity between 3 s and 9 s and 4 s and 42 s, respectively. Note that the figure changes the scale of the velocity in relation to the data used.

of Rayleigh and Love waves. Figure 7.5a shows the result of the inversion using Rayleigh wave phase velocity and Love wave group velocity dispersion measurements. The periods affected by the water layer were removed from 5 s to 14 s in the phase velocity dispersion curves, as to rely more on the periods that are more sensitive to the solid Earth structure. The resulting model of the shear waves and the fit of the model to the observations are now very good, with better resolution at greater depth due to the long-period Rayleigh waves. The inversion using only Rayleigh and Love wave phase velocity dispersion curves are observed in the Figure 7.5b. In addition, in the Figure 7.5c, dispersion curves for the Rayleigh wave phase velocity and Love wave group and phase velocity dispersion curves were used. The results show a very similar shear-wave model to that obtained with Rayleigh wave phase velocity and Love wave group velocity data for the first 10 km depth below the seafloor (Figure 7.6). Below 13 km, the model now has similar results than the inversion using Rayleigh and Love wave phase velocities and Love wave group velocity measurements, converging the three models at 30 km depth.

Finally, the inversion of the shear wave velocity was performed using the entire data set. Figure 7.7a shows the inversion of the group and phase velocities of Rayleigh and Love waves. Here it was used all the data for the Rayleigh wave phase velocity dispersion curves between 5 s and 44 s. The results show a maximum velocity of 5.35 km/s at 25 km depth and a low velocity zone at shallower depths than the other inversions (60 km depth). The model fit is not the best again for the group velocity of Rayleigh waves. In Figure 7.7b, the phase velocity dispersion curves of the Rayleigh waves were removed between 5 s and 14 s, which is the part most affected by the water layer. The results show a slight decrease of the fast velocity layer between 20 and 25 km depth compared to the previous inversion.

7.5 Final 1-D shear-wave velocity inversion

Based on the previous tests, as well as on the results of chapter 3, it was decided to rely on the ambient noise Love wave dispersion curves for the short period (<10 s) band, because Love waves are not affected by the water. At longer periods (>10 s), phase velocity measurements derived from the two-station method were used, as this method allows us to obtain more measurements from teleseismic events at longer periods. It was avoided to use the Rayleigh wave phase velocity dispersion data at the points where the curves show

Table 7.1: Table of data used for the 1-D shear-velocity inversion in frequency.

Method	Wave	frequency band (Hz)
Ambient noise	Love wave group velocity	0.111 - 0.333
Ambient noise	Love wave phase velocity	0.111 - 0.25
Two station	Love wave phase velocity	0.0238 - 0.0714
Two station	Rayleigh wave phase velocity	0.0227 - 0.0666

a sharp increase, because these parts of the dispersion curves are dominated by the water layer and not by the solid earth structure. For the ambient noise, the average of the Love wave group velocities was used between 3 s and 9 s and the average of the Love wave phase velocities between 4 s and 9 s. For the two-station method, the Love wave phase velocities were used between 14 s and 42 s and Rayleigh wave phase velocities between 15 s and 44 s (see table 7.1).

Figure 7.8 shows the final shear-wave velocity inversion model down to a depth of 80 km including the water layer and the inversion using the standard deviation of the data. In addition, the figure also shows the observations of the group and phase velocities of the Love waves and the phase velocity of the Rayleigh waves used for the inversion, as well as the degree of fit to the data. The percentage fit between the dispersion curves and the estimated model was 99.984 % out of 100 % for the last iteration, which means that the fit is good. The Figure7.9 show the sensitivity kernels of the final model for group and phase velocities using the code from *Herrmann* (2013) to observe to what depth our final model is still sensitive to the structure. In order not to put any artifacts within the initial model in the sensitivity kernels, all layers especially the 5 km layers were split into 1 km layers.

The final model (Figure 7.8a) shows a water layer of 5 km, a sediment layer with a low Vs=1.1 km/s, followed by a rapid increase to crustal velocities of 3.3 km/s up to 4.9 km/s between 5.6 km and 15.6 km depth. Surface waves are not sensitive to discontinuities, but if we use an average upper mantle shear-wave velocity of 4.5 km/s as a reference (e.g., PEM-O or Crust1.0), it is inferred a total crustal thickness of 9 km for the observed model between 5.6 km and 14.6 km depth. In contrast, using the velocity for the base of layer 4 (L4) of *Batista et al.* (2017), which is Vs=3.9 km/s, a crustal thickness of 6 km is inferred. In the group and phase velocity of the Love wave sensitivity kernels we observe a clear change at ∼15.6 km depth, which may be due to the Moho boundary, but it is 1 km thicker than the inferred crustal thickness with the reference velocity of 4.5 km/s.

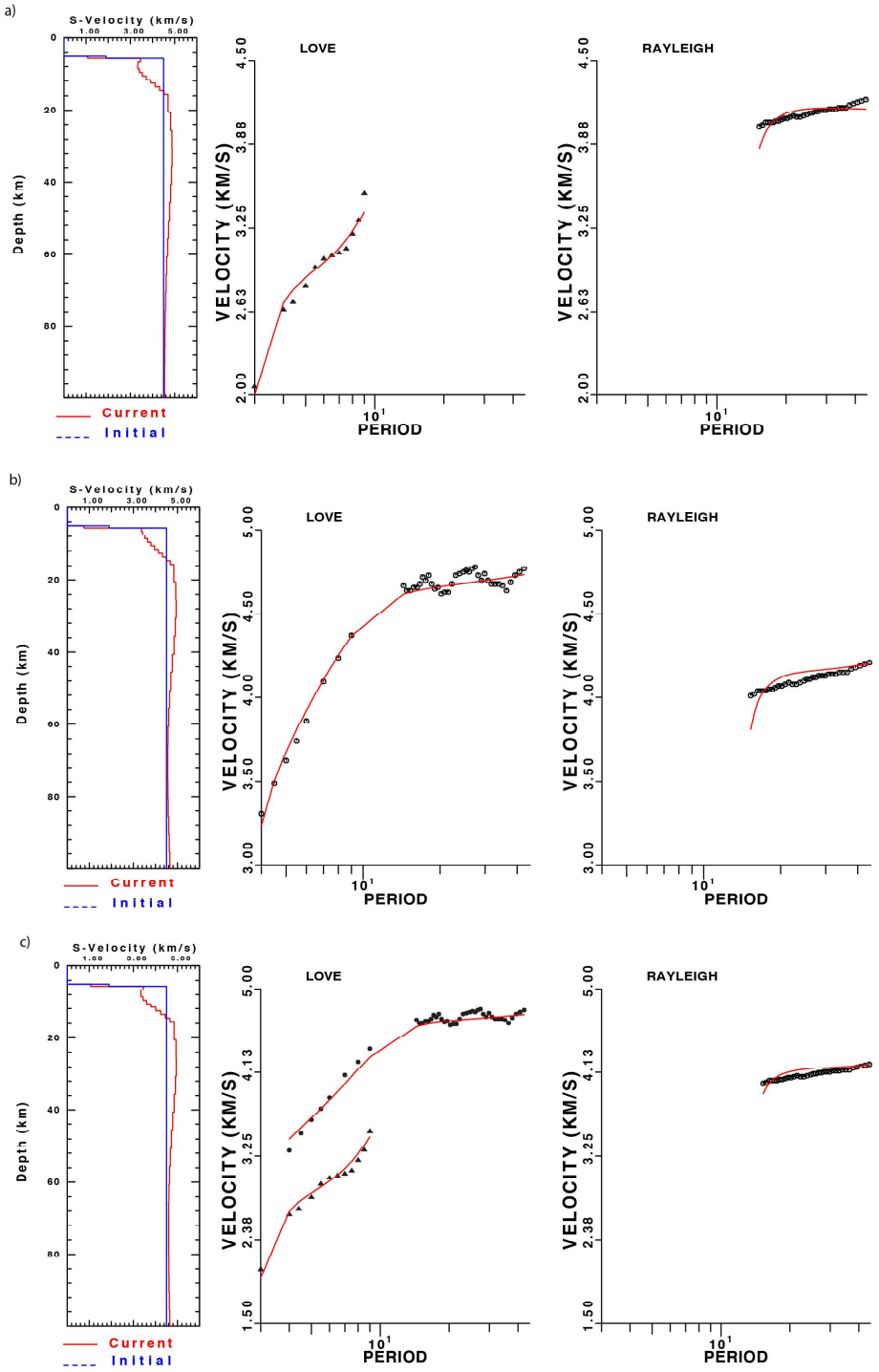

Figure 7.5: a) Shear-wave velocity inversion for Rayleigh waves long-period phase velocity and Love waves short-period group velocity. The triangles represent the group and the circles the phase velocity dispersion curves. b) Shear-wave velocity model for Rayleigh wave long-period phase velocities and Love wave short and long period phase velocities. c) Shear-wave velocity inversion for Rayleigh wave long-period phase velocities and Love wave long and short period, group and phase velocities.

The obtained profile depicts a maximum Vs $\approx$ 4.9 km/s, which is almost constant between 15.6 and 35 km depth, i.e., at the uppermost mantle where lherzolite fertile compositions would be characterized by the presence of olivine, orthopyroxene, clinopyroxene and pla-

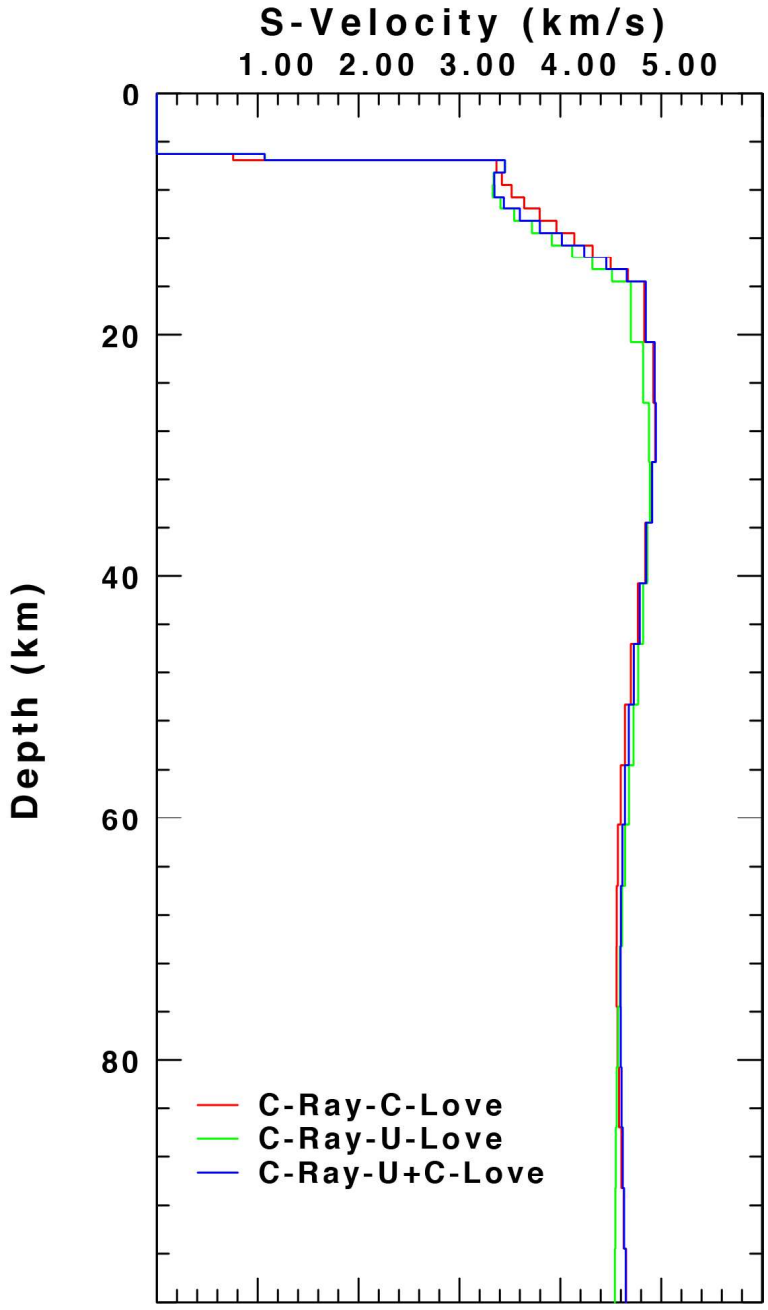

Figure 7.6: Comparison of the shear-wave velocity inversions of the three output models using different datasets. Red model represents the Rayleigh and Love wave phase velocity data. Green model correspond to the inversion using the Rayleigh waves phase velocity and the Love wave group velocity. The blue inversion is the Rayleigh waves phase velocity and the Love wave group and phase velocities. The first 5 km, the green and blue models are very similar but below 5 km, both models start to separate. Below 15 km, the red and the blue models are very alike.

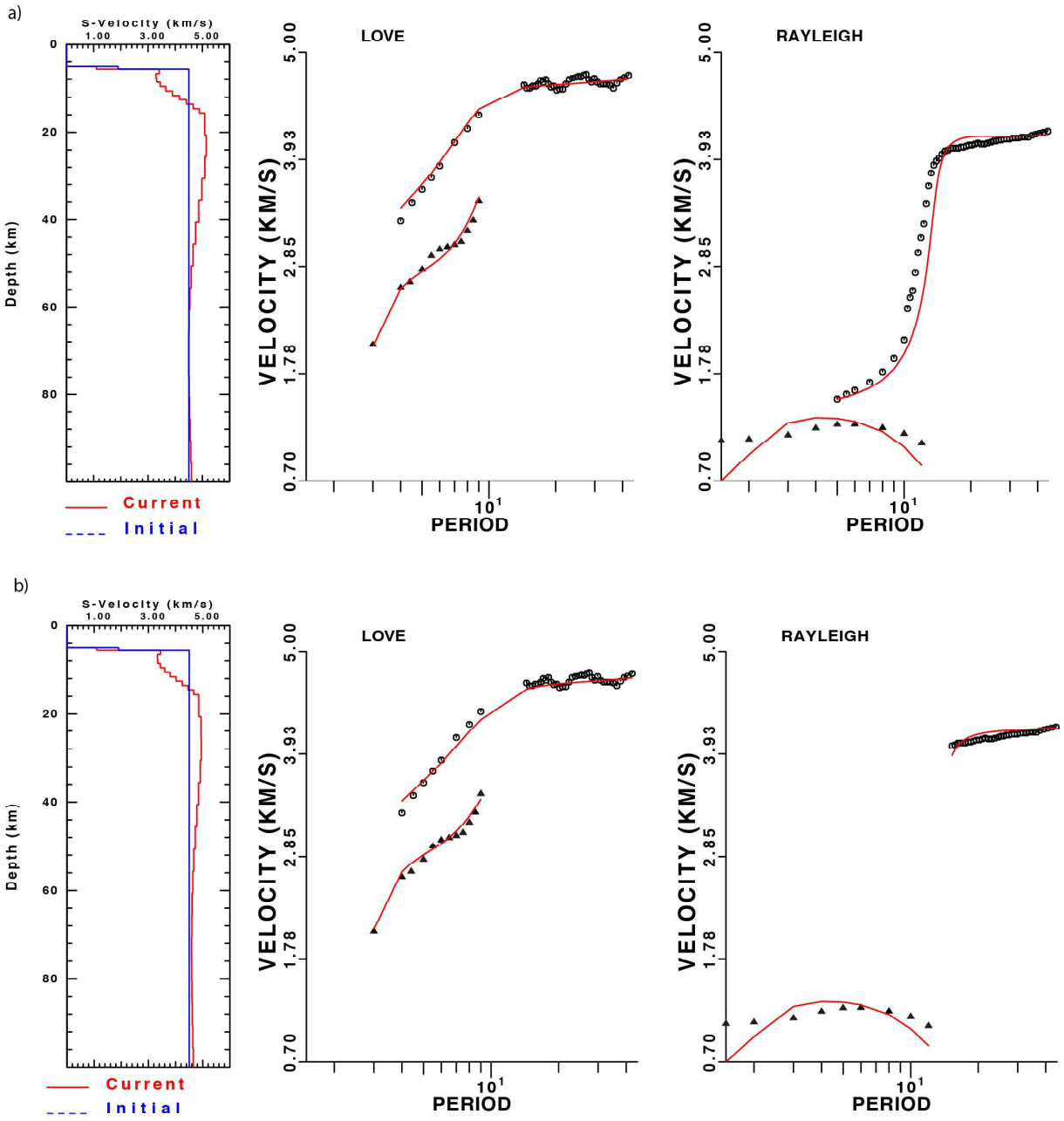

Figure 7.7: 1-D shear-wave velocity inversions using all the dispersion data. a) Shear-wave velocity inversion for Rayleigh and Love waves group and phase velocity. The phase velocity dispersion curves of Rayleigh waves are between 5 s to 44 s. Triangles represent the group and the circles the phase velocity dispersion curves. b) Same shear-wave inversion as previous but this time only taking the phase velocity of Rayleigh waves between 15 s and 44 s.

gioclase. The low Vs characterizing plagioclase (3.54 km/s) and clinopyroxene (4.66 km/s) (*Wang et al.*, 2013) suggest that the dominant mineral at those depths are olivine (4.82 km/s) and orthopyroxene (4.86 km/s) forming a harzburgite. In oceanic settings, harzburgites and dunites are not only found in subduction zones or island arc collisions, but also in mid-ocean ridges (*Kelemen et al.*, 1995; *Rospabé et al.*, 2021). Partial melting of a lherzolite can originate a residual harzburgite if partial melting is large. The spreading at the Mid-Atlantic Ridge is slow when compared with the Pacific, which would imply relatively low partial melting during the generation of mid-ocean ridge basalts (MORB). However, as initially proposed by *Dick et al.* (1984), the amount of melting at a ridge is also influenced by the presence of hotspots. So, we propose that the high Vs detected at the studied segment can be due to the presence of harzburgite, a refractory residue of enhanced melting due to the proximity between the Mid Atlantic Ridge and the Azores hotspot. The hypothetical presence of dunitic veins, usually interpreted by melt/harzburgite reaction (e.g. *Kelemen et al.* (1995)), would not alter significantly the shear-wave velocities.

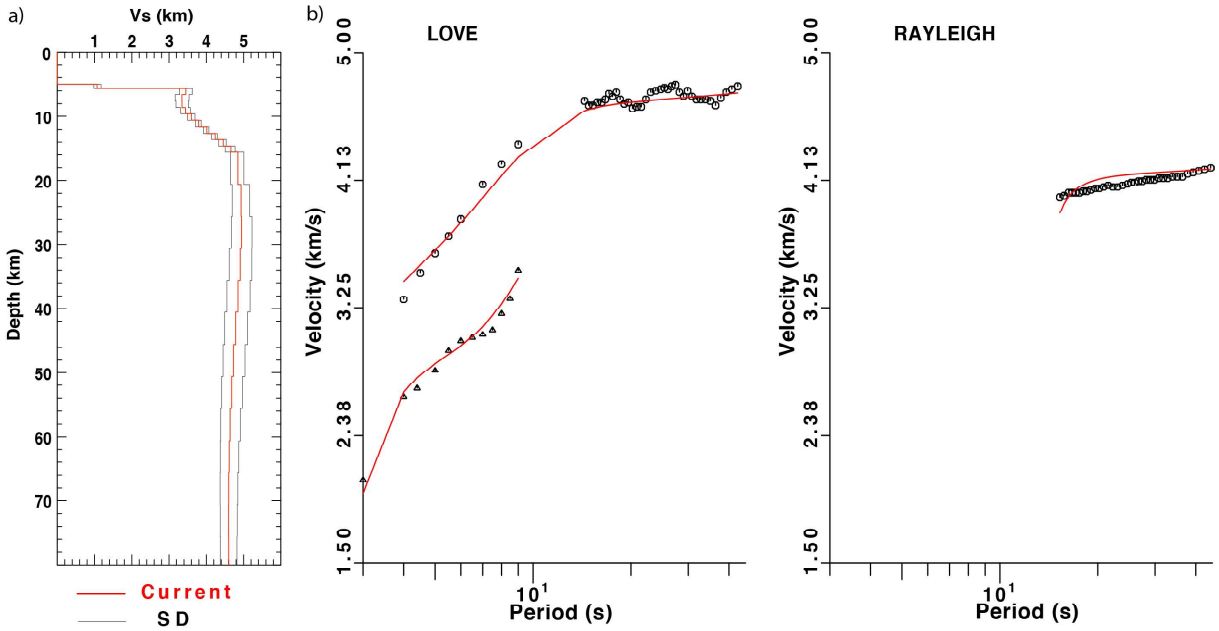

Figure 7.8: Final 1-D shear-wave velocity model based on dispersion data inferred from ambient noise and the two-station method. a) Final 1-D shear-wave model (solid red line) and the standard deviation (solid grey line) down to a depth of 80 km. b) Observed average Rayleigh and Love waves dispersion curves (circles represent the phase velocity and the triangles the group velocity measurements) and dispersion curve corresponding to the best-fit model after 20 iterations (red line).

Using receiver functions, *Hannemann et al.* (2017) imaged the LAB below the DOCTAR area at ∼70 - 80 km depth. In our final model, is observed a decrease to the velocity to a minimum Vs=4.6 km/s at ∼70km depth, likely corresponding to the LAB. One

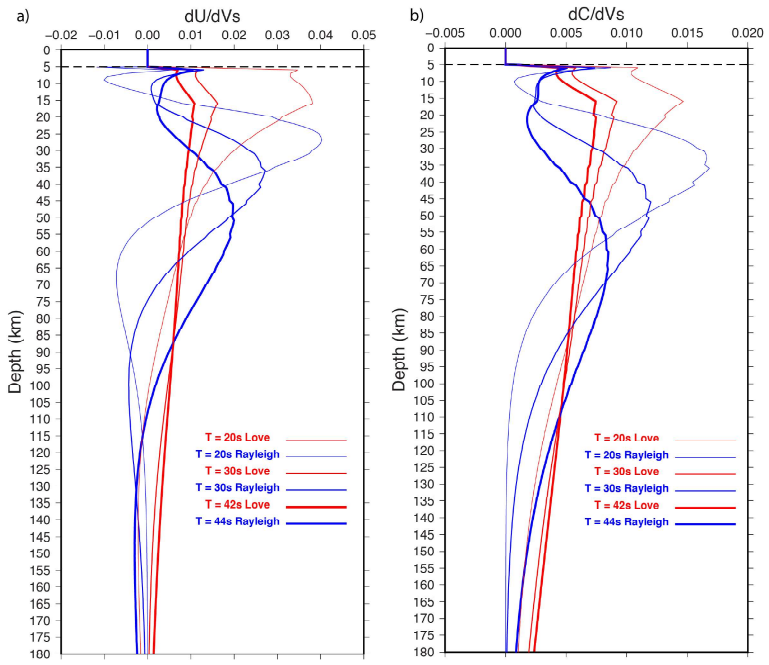

Figure 7.9: Sensitivity kernels for group and phase velocities derivatives with respect to the shear velocities at 20 s, 30 s, 42 s and 44 s periods. All layers of the final 1-D model were divided into 1 km layers.

observation is that this low velocity never reaches the initial velocity of the half-space model. However, if we analyse the sensitivity kernels, in particular the phase velocity of the Rayleigh waves at longer periods, we can see that there is still sensitivity at this depth (Figure 7.9. This decrease of the velocity in the LAB is originated by the rising of the temperature, which can be related to partial melting, changes in rheology, thermal control, anisotropy or dehydration (*Kawakatsu et al.*, 2009; *Fischer et al.*, 2010; *Olugboji et al.*, 2013).

7.6 Comparison of oceanic models

Figure 7.10 shows the final 1-D model for comparison together with two other oceanic models obtained in the same study region, namely the Hannemann (*Hannemann et al.*, 2016) and Batista (*Batista et al.*, 2017) models and a more general model of the oceanic crust from *White et al.* (1992). In the sediment layer, the model obtained in this study has similar velocities to Hannemann's model, while White's model has lower velocities. Batista's model, which is a gradient velocity model, has a similar velocity at the surface to the 1-D model, but at the base of the sedimentary layer displays a higher velocity (1.9 km/s) than the 1-D model. The thickness of the sediment layer varies between 0.5 km and

0.7 km. The 1-D model displays a high velocity in the upper crust compared to White and Batista models. However, when depth increases, roughly at 7.7 km, White's and Batista's models quickly exhibit higher velocities than the 1-D model of this study. From a depth of about 9.5 km, the 1-D velocity model increases, but very smoothly. The Hannemann model has an even higher velocity because it is a single-layer model for the entire oceanic crust. The different models have different crustal thicknesses. In the White's model, the crust is 7.08 km thick; Batista's model has an average value of 8.5 km + 4 km of a petrological layer. In comparison, Hannemann's model has an average value of 6.41 km. The 1-D model in this study was obtained from the inversion of surface wave dispersion measurements as a function of depth, and surface waves are not sensitive to discontinuities. Therefore, the thickness of the crust depends on the initial model and varies between 6 and 9 km. In the upper mantle, the 1-D model, using seismic ambient noise and teleseismic surface waves, and the Hannemann model, using Ps Receiver Functions, show velocities above 4.5 km/s.

Finally, Figure 7.11 shows the fit of the eigenfunctions obtained with the final model together with the measured dispersion curves of the group and phase velocity of Rayleigh and Love waves obtained from ambient noise and the two-station method. Comparing the Figure 3.9a with this figure we observe that our model provides a very good data especially concerning the Love waves. We used a water thickness of 4.8 km to compute the eigenfunctions and we changed the Vp of the sediments using the relationship of *Castagna et al.* (1985) for the mud-rock $V_p = 1.16 * V_s + 1.36$. For larger shear-wave velocities >2.5 km/s the relationship $V_p/V_s = 1.778$ can be used.

7.7 Summary

In this chapter, it was first tested the reliability of the initial model used for the inversion of the 1-D vertical shear-wave structure. Next, several 1-D shear-wave inversions were performed with different partial data sets based on the ambient noise and the two-station measurements. It was decided to perform the final velocity inversion using only the Rayleigh wave phase velocity data at long periods (two-station method) and the Love wave group (ambient noise) and phase velocity data (ambient noise and two-station method). The final 1-D shear-wave velocity model shows an oceanic crust with a thickness between

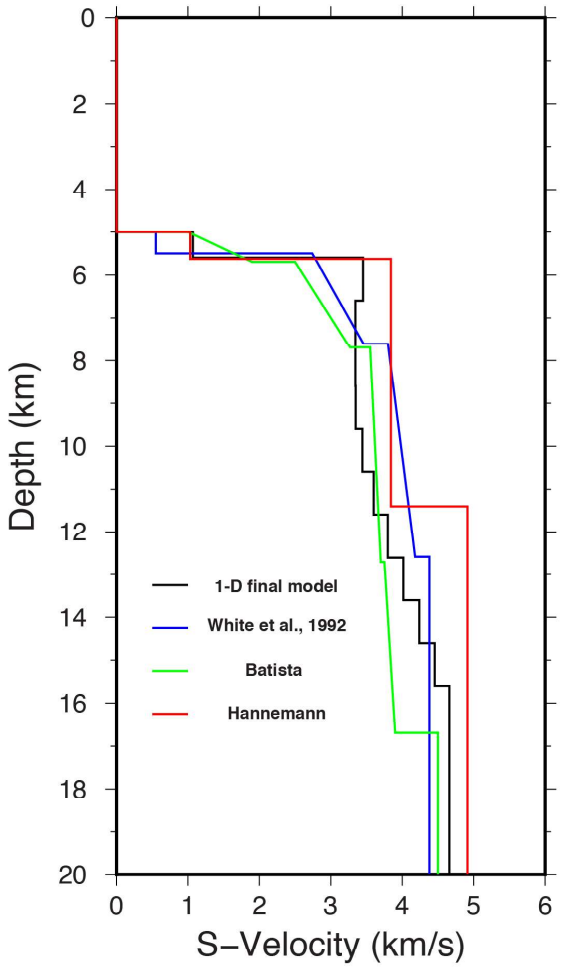

Figure 7.10: Comparison of the 1-D final shear-wave velocity model obtained in this work (black line) with other regional models such as Hannemann model (Red line) (*Hannemann et al.*, 2016), Batista model (Green line) (*Batista et al.*, 2017) and a normal oceanic model from *White et al.* (1992) (Blue line).

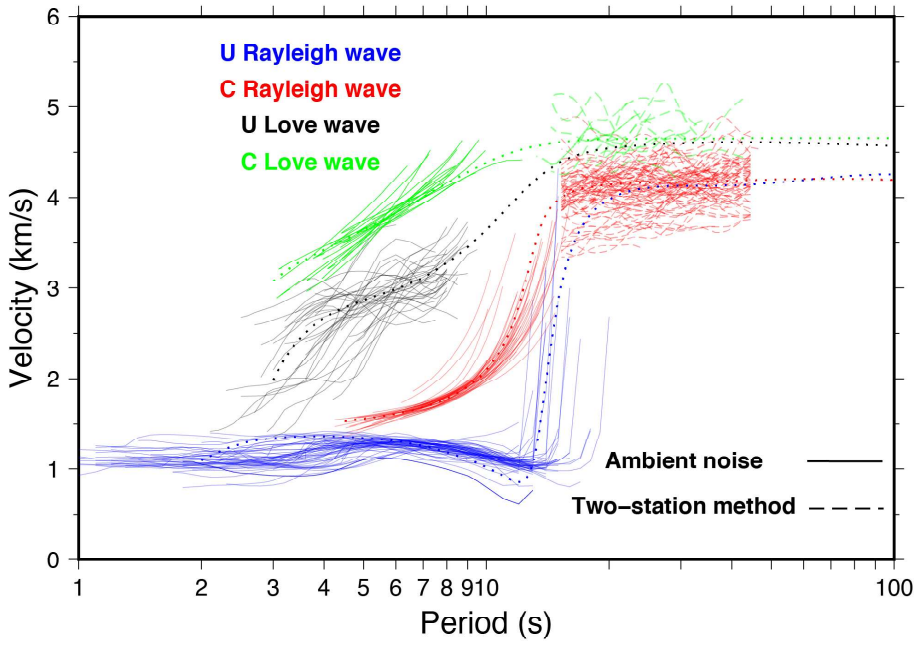

Figure 7.11: Plot of the eigenfunctions calculated with the 1-Dfinal model (dotted lines) and the dispersion curves measurements of the group and phase velocities of the Rayleigh and Love waves. The agreement of the final model with the observations is very good.

6 and 8 km and a shear-wave velocity ranging from 3.3 km/s to 4.5 km/s. This is followed by an increase in the shear-wave velocity reaching a maximum velocity of Vs=4.9 km/s between 15 km and 35 km depth, which we interpret as indicative of the presence of harzburgite, a refractory residue of enhanced melting due to the proximity between the Mid Atlantic Ridge and the Azores hotspot. The velocity then decreases reaching a minimum at ∼65-70 km depth, which is interpreted as the LAB, consistent with the results of *Hannemann et al.* (2017).

A geodynamic comparison was done with other models of the region and with a typical oceanic crust model. The average sediment thickness is 600 meters for all models, but only the Hannemann model shows similar velocities. The oceanic crust varies significantly from model to model, for example, White's model has a thickness of 7.08 km while Batista's model has an average thickness of ∼8.5 km. The Hannemann model is the one with the thinnest oceanic crust of 6.41 km on average. Our final model is not sensitive to discontinuities because it was done using surface waves but setting a reference value it can vary between 6 km and 8 km thickness. Finally, only the Hannemann model and our model present higher velocities for the upper mantle than the other models.

Chapter 8

3-D surface wave tomography

To observe the lateral variations in the oceanic crust below the DOCTAR area, a 3-D shear-wave velocity tomographic inversion was performed. To do so, computation of the two-dimensional (2-D) velocity maps were done for different periods, using the Love wave group velocity dispersion curves obtained with ambient noise. Subsequently, the average of the two-station method dispersion curves to the velocity maps were added to the velocity maps in order to invert for the shear-wave velocity as a function of the depth at each node of the 2-D grids, thus building a final 3-D tomographic model of the oceanic Earth's structure north of the GF.

So, the definitive dataset used for the 3-D inversion are as follows: the Love waves fundamental mode group and average of phase velocities from ambient noise and fundamental mode phase velocities of Rayleigh and Love waves from the two-station method. However, the phase velocity of Rayleigh waves from ambient noise were not used because of poor ray coverage. Furthermore, the group velocity of Rayleigh waves has a good ray coverage, but the periods extracted are more sensitive to the water layer than to the oceanic structure, as demonstrated in chapter 6, and therefore also were not considered.

8.1 2-D Tomography inversion

To obtain the 2-D group velocity maps for the various observation periods, it was used the Fast Marching Surface Tomography (FMST) method of *Rawlinson* (2005). This method implements an iterative non-linear inversions scheme. In particular, it uses the Fast

Marching Method (FMM) (*Sethian*, 1996; *Rawlinson and Sambridge*, 2004) to solve the forward problem, and a subspace inversion scheme (*Kennett et al.*, 1988) that allows to solve the inverse problem using the non-linear relationship between Earth's velocities and traveltimes. The FMM solves the forward problem by using the eikonal equation, using finite-differences to track the wavefront from the phase delays. One of the advantages of using the FMM for ray tracing is that it generates the minimum (or maximum) travel time in the presence of multi-pathing, which can be missed with simple ray tracing. Thus, the FMM provides stable and robust solutions in complex laterally heterogeneous media (*Rawlinson and Sambridge*, 2005).

The 2-D models are parameterized for each period by 20 $\times$ 20 velocity nodes, which are regularly spaced by 0.05° in latitude and 0.066° in longitude. The dicing factor used was 6 $\times$ 6, giving in total 13,225 nodes for the forward propagation grid. For each inverted period, the corresponding average velocity obtained in chapter 3 were used as initial background velocity to compute the velocity maps.

8.1.1 Resolution analysis

Before starting the inversion of a seismic tomography inversion, its necessary to carry out resolution tests in order to gain insight on the scale at which anomalies can be recovered given the available traveltimes. This is done through the inversion of synthetic idealized velocity structures, which typically are checkerboard and models with spikes. Checkerboards are synthetic models of alternating high- and low-velocity anomalies. The size of the grid spacing used for the actual tomography was chosen based on the checkerboard resolution tests with different grids dimensions. Figure 8.1 shows an example of two different grid sizes and the respective recovered models, after 9 iterations, using all the possible paths between sources and receivers, and using a background velocity of 3.02 km/s. We decided to use a grid of 20 $\times$ 20, corresponding to a grid spacing of 5.5 km in latitude and 7.3 km in longitude because it is possible to recover well the original anomalies at a higher resolution, especially at the center of the array.

In addition, the recovery of the checkerboard was tested in a 20 $\times$ 20 grid synthetic model for the group velocity of Love waves using only the available traveltimes. Figure 8.2 shows the group velocity of Love waves with a good recovery on the western side of the array

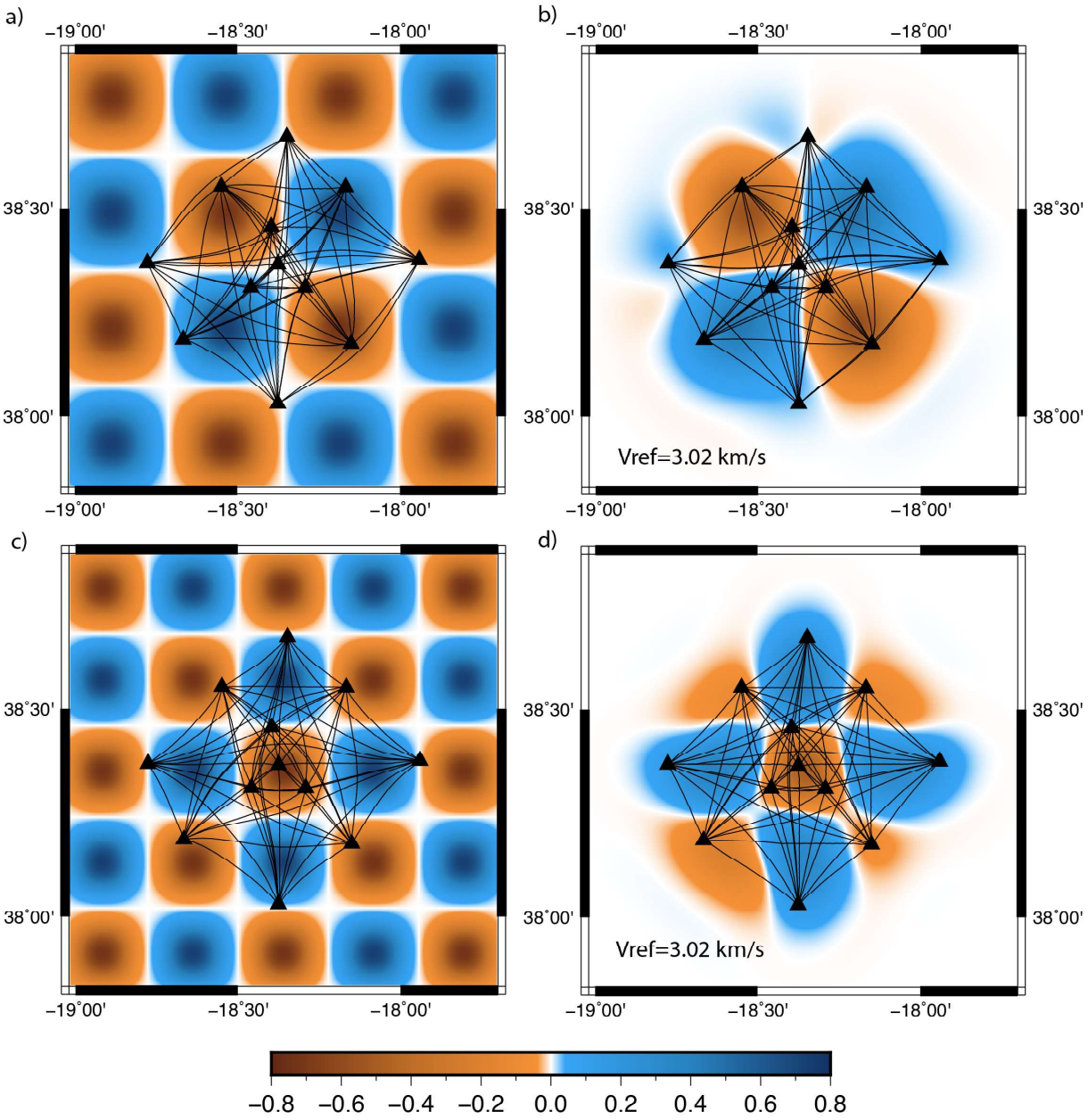

Figure 8.1: Checkerboard resolution test for two different input models, with a reference velocity of 3.02 km/s, using all the paths available given our station locations. a) 16 × 16 grid input model. b) Recovered model after 9 iterations using the 16 × 16 grid. c) 20 × 20 grid input model. d) Recovered model using the 20 × 20 grid.

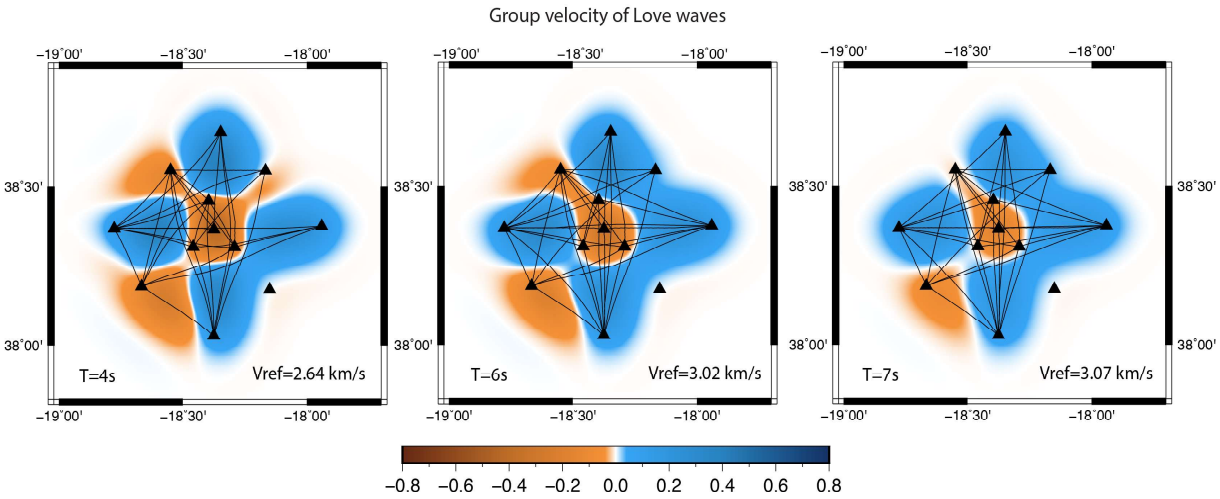

Figure 8.2: Recovery of the checkerboard synthetic model at different periods for the group velocities of Love waves at 4 s, 6 s and 7 s. The reference velocities used are of of 2.64 km/s, 3.02 km/s and 3.07 km/s, respectively.

at 4 s period with only 33 paths of the 66 possible ones. At 6 s period, similar results were obtained as at the 4 s period, only recovering very well the anomalies to the west. Additionally, at 7 s is also possible to recover appropriately the input anomalies on the west half of the array with the available trajects. This is due to the fact that most of the observed dispersion curves of group velocities of Love waves correspond to paths on the center and western side of the DOCTAR area.

Finally, a couple spike models were tested using all the trajects between the OBSs, one with a negative anomaly at the center of the array and the other with a fast velocity anomaly on the west side of the array (Figure 8.3). It can be observed a good recovery of both anomalies, even when the anomaly is at the edge of the array, indicating that the chosen grid size is suitable.

8.1.2 Regularization parameters

Important parameters that need to be carefully tuned in the tomographic inversion are the damping ϵ and smoothing η, as to find an optimal solution to the model. The damping parameter prevents the solution model from deviating too far from the initial model, on the other hand, the smoothing parameter limits the smoothness of the resulting model. To find the appropriate trade-off regularization parameters for an optimal inversion process, it is necessary to test the inversion with different values of damping and smoothing. We started by setting the damping parameter to $\epsilon = 1$ and varying η for group velocity of

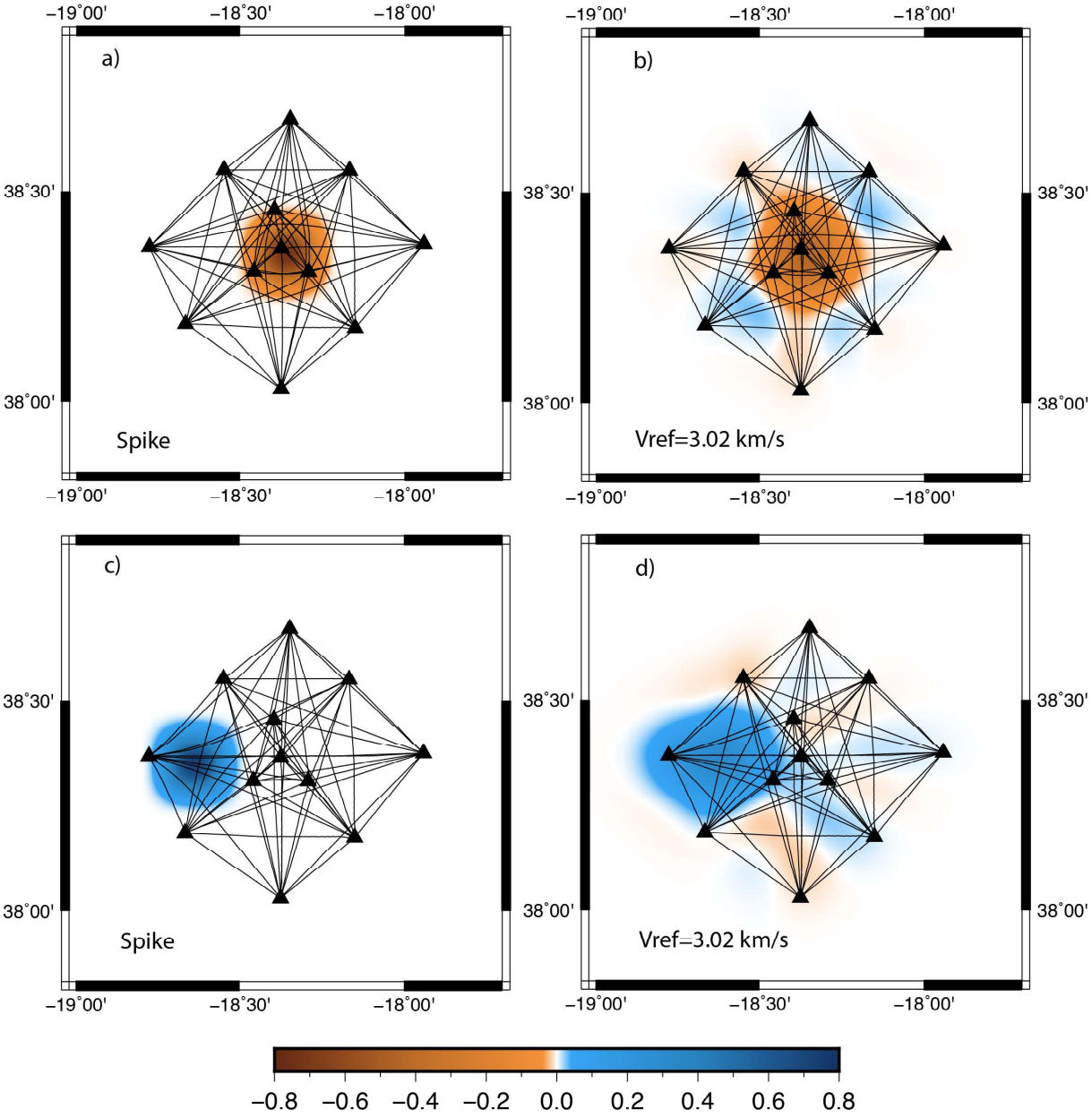

Figure 8.3: Spike resolution test for two different input models with a reference velocity of 3.02 km/s. a) Input model with a negative anomaly in the center of the array. b) Recovered model corresponding to the synthetic model shown in a). c) Input model with a fast velocity anomaly model on the left side of the array. d) Recovered model corresponding to the synthetic model shown in c).

Love waves. Figure 8.4a shows the results of the trade-off between data variance and model roughness for the group velocity of Love waves. The data variance measures the deviation of the solution model from the average model and the model roughness measures the variability of the model.

The optimal regularization parameters correspond to a model that fits well the data and is as smooth as possible, that is, which has no artificial detail. Thus, it was chosen the point where the data variance vs model roughness curves display the most accentuated curvature. For group velocity of Love wave at 6 s period, the value chosen for smoothing was $\eta = 20$. We continue the process now fixing $\eta = 20$ and varying the ϵ, resulting in an optimum parameter of $\epsilon = 15$. Finally, the number of iterations necessary to converge to the best model is 4 (Figure 8.4c). So, the best regularization parameters for the group velocity of Love wave were set to $\eta = 20$ and $\epsilon = 15$.

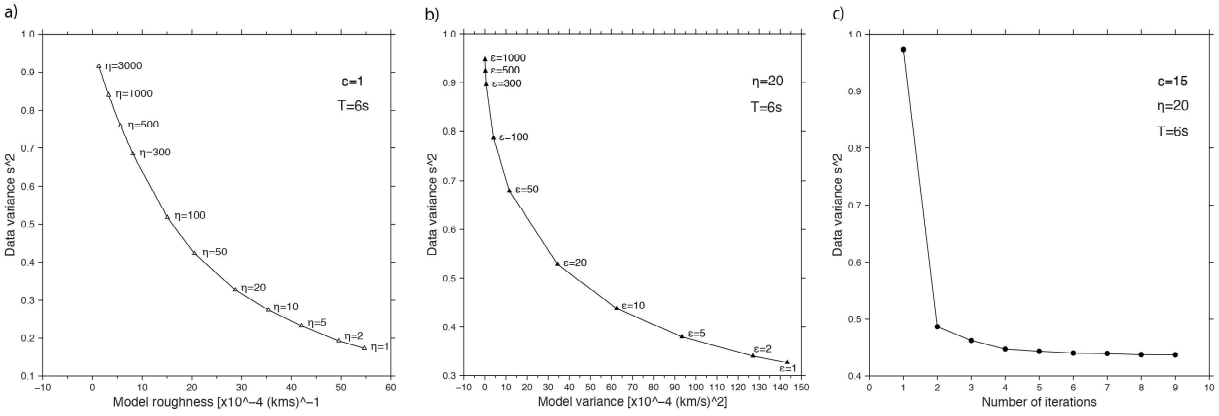

Figure 8.4: Trade-off curves between data variance and model roughness used to estimate the optimal damping and smoothing parameters. a) Variation of the smoothing parameter for a fixed damping parameter with $\epsilon = 1$ for the 2-D inversion of group velocities of Love waves at 6 s period. The value of $\eta = 20$ is chosen. b) Variation of the damping parameter fixing the smoothing at $\eta = 20$. $\epsilon = 15$ were chosen as optimum value. c) Evolution of data variance with iteration using the damping and smoothing parameters selected in a) and b). The inversion converges after 4 iterations.

8.1.3 Group velocity maps of Love waves

Love wave group velocity data from 4 s to 8.5 s were inverted using the previously defined smoothing and damping parameters. These period ranges were chosen because they contain the most observations. The velocity maps were calculated by using as initial reference velocity the average of the velocity map and the traveltimes for the respective period. Figure 8.5 show the Love wave group velocity maps together with the bathymetry contours. At 4 s period, the strongest low velocity anomaly with respect to the average of

the map is observed at the center of the array and is maintained until 6.5 s. In addition, an extra low velocity anomaly is observed in the east at 5 s period until at 6 s disappear. The strongest fast velocity anomaly appears around the station D07 and persists in all periods. At 6.5 s, two fast velocity anomalies appear to the northeast of station D04 and at the south between the stations D01 and D09, lasting until 8 s period. The inverted periods are most sensitive to the upper 10 km of the earth structure.

8.2 Shear-wave velocity

To build the 3-D shear-wave velocity model, it was used as initial model the 1-D shear-wave velocity model obtained in chapter 7, and as input data the Love wave group velocity maps in each node. For each 2-D grid node, it was performed a depth inversion, thus building a 3-D model. The 2-D grid used a total of 93 nodes covering the available rays of the Love wave group velocity maps for all periods (Figure 8.5). In addition, the dispersion curves in each node of the inverted maps were completed using the dispersion curves with the average of Love wave phase velocity dispersion curves of ambient noise between 4 s and 9 s and the two-station method between 14 s and 42 s. We used also the Rayleigh wave phase velocity dispersion curves of the two-station method between 15 s and 44 s. Figure 8.6 show the entire dataset of dispersion measurements used for the shear-wave inversion.

SURF96 was used to invert for a vertical velocity structure below each horizontal grid node, from the surface to 80 km depth, with the same initial parameters that were previously used for the 1-D shear-wave inversion described in section 7.3. A total of 20 iterations were performed for each node to obtain the shear-wave inversion for each coordinate, thus building the 3-D tomography. Figure 8.7 shows a density plot of the 1-D inverted shear-wave velocity depth profiles inferred at all nodes. In this figure, the depth models were grouped in bins of 0.1 km/s for each layer. The results show small variations with respect to the initial model in general. In the sedimentary layer the models generally present lower velocities than the a priory model. In the next 10 km of depth below the sediment layer, the models are well distributed around the initial model. This depth range has a maximum variation of $\pm$ 0.3 km/s with respect to the initial model. From 10 km to 25 km, most of the 1-D models slightly increased the velocity with respect to the initial

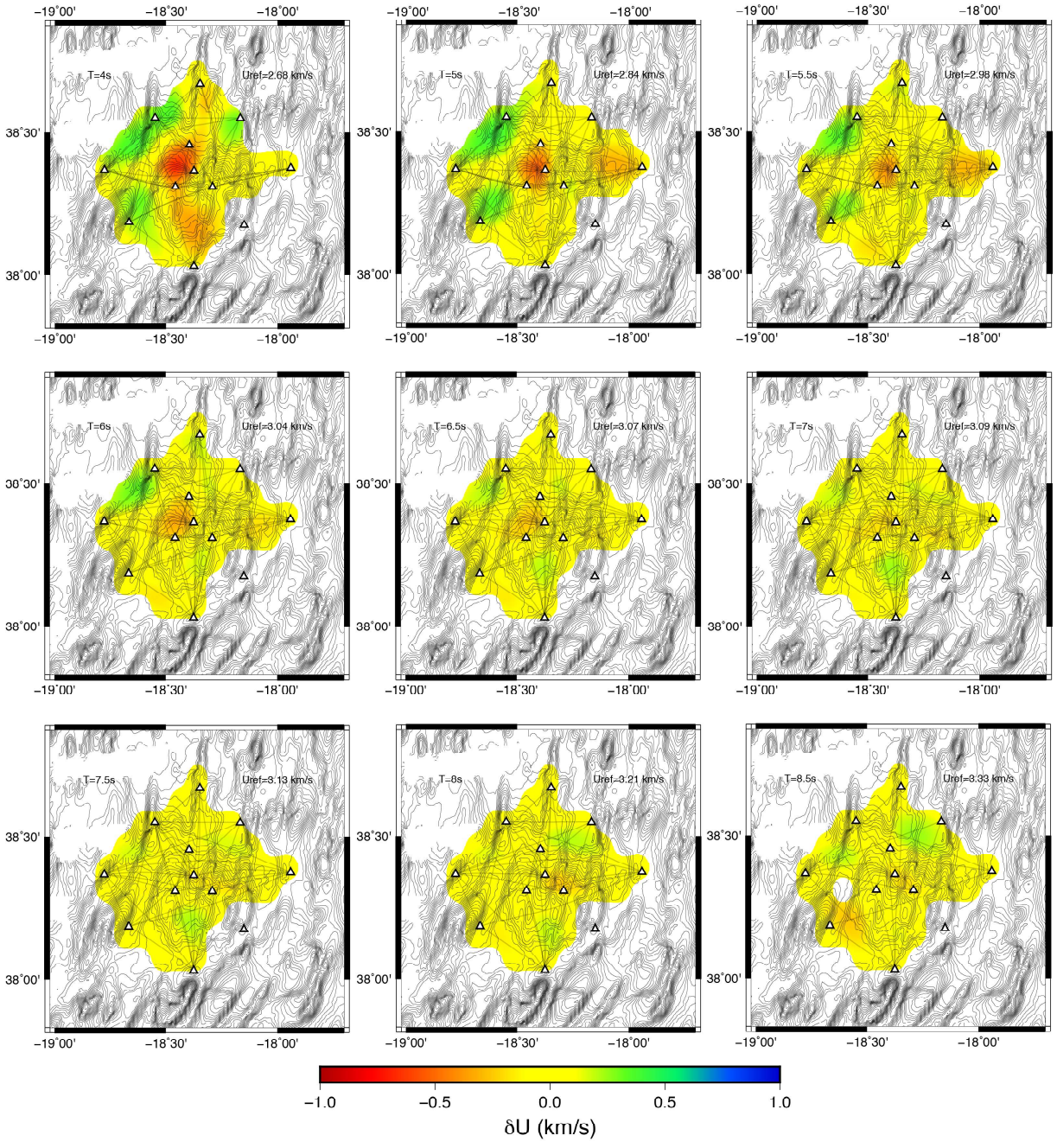

Figure 8.5: 2-D Love wave group velocity maps at increasing periods from 4 s to 8.5 s. The figure is plotted as a relative velocity with respect to the average of the velocity map.

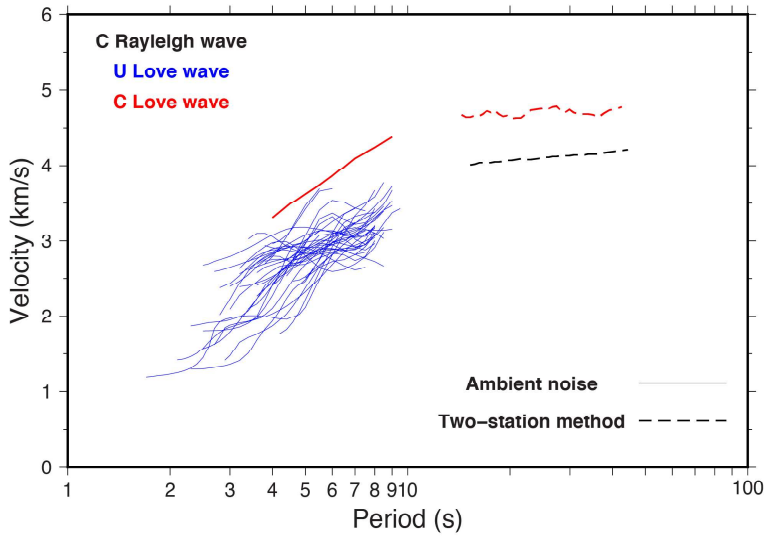

Figure 8.6: All the data used for the 3-D shear velocity inversion. Solid lines are the average of the dispersion curves obtained from ambient noise along with all the group velocity of Love waves in blue. The dashed lines represent the average of the dispersion curves inferred from the two-station method.

model with a maximum variation in the order of the 0.2 km/s. From 25 km depth until 70 km, there is a general decrease in the velocity with respect to the initial model. Most of the nodes are concentrated in the order of 0.2 km/s difference of the initial model and at 65-70 km depth all the nodes converge to the same value. Below 70 km depth, there is an increase in the velocity and the initial model is again in the middle of the density plot.

Figure 8.8 shows the resulting shear-wave models in horizontal slices at different depths, ranging from 2 km to 10 km, along with a bathymetric map. The velocity perturbations are shown in percentage with respect to the average shear-wave velocity at each depth, which is shown in each depth plot. At a depth of 2 km, a fast velocity anomaly is observed in the northwestern part of the array and a low velocity velocity anomaly in the central part. In addition, the strongest low velocity velocity anomaly starts to appear at 4 km depth in the southwest and a less strong low velocity anomaly in the northwest, which is best observed at 5 km depth. Both low velocity anomalies extend down to 9 km depth. In addition, fast velocity features become visible in the north, south, center and east of the array, located below small mountains, at 5 km depth below the ocean floor. These fast velocity anomalies extend to a depth of 7 km and the fast velocity feature in the center extends to a depth of 10 km. At 9 km and 10 km depth, the velocity anomalies generally appear to lose lateral resolution. This may be due to the data gap between the ambient noise and the two-station method data between 9 s and 14 s, and to the fact that the

Love wave group velocity is the only one changing in each node, but the rest of the data used is the average.

To better visualize the inferred 3-D tomographic model, several seismic profiles were plotted (Figure 8.9). Two profiles perpendicular to the Mid-Atlantic Ridge, three profiles parallel to the ridge and the last profile orientated southwest-northeast. The profiles extend from 1 km to 15 km depth below the seafloor and are plotted along with the corresponding bathymetric profile. The Moho boundary is marked as a reference at 7 km depth as a grey dashed line in each profile obtained from Crust1.0.

8.3 Discussion

Because the 3-D tomographic model is quite homogeneous, a general interpretation of the anomalies was done considering the limited geological knowledge of the structure below DOCTAR area. Below station D07 (Figure 8.8), it is observed a weak gradient of a low velocity anomaly surrounded by a strong high-velocity anomaly at 2 km depth. This fast velocity anomaly is followed by a low velocity anomaly at 5 km depth and just below station D07 the low velocity becomes a small fast velocity anomaly until 10 km depth.

To the southwest, between stations D08, D03 and D09, it is observed the strongest low velocity anomaly, which extends down to 9 km depth. This low velocity anomaly is clearly seen in the profile D08-D06 and P2-P2´ consistent with a thicker oceanic crust. Between stations D09 and D01, a fast velocity anomaly is evident at 4 km depth and reaches down to 8 km depth. This anomaly is observed in the profiles D09-D11 and again P2-P2´, which is consistent with a local thinning of the oceanic crust. In addition, comparing this fast velocity anomaly with marine free-air gravimetric map (Figure 8.10), it is observed that a fast velocity anomaly also exits in the south of the network. This anomaly may be related to a large submarine mountain. On the other hand, at the Northwest of the array we observe a low velocity anomaly in the gravimetric map. Because of the 1-min resolution of the gravimetric map, it is very difficult to make a detailed comparison between seismic velocities and densities.

In the center of the array (Figure 8.8), first is observed a low velocity anomaly at 2 km depth, followed by a fast velocity anomaly feature at 5 km depth between stations D03

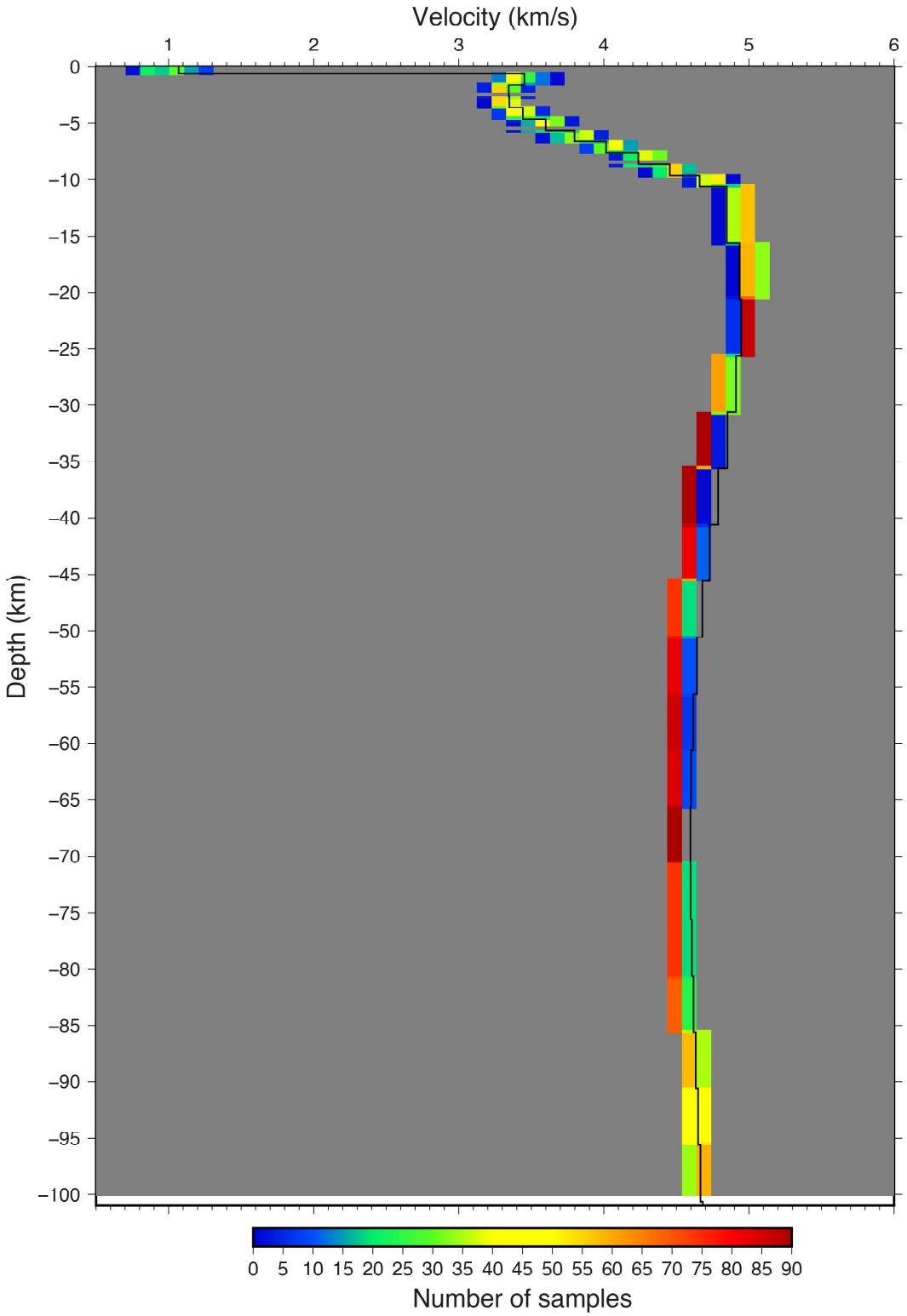

Figure 8.7: 1-D shear-wave velocity histogram based on the 1-D velocity models obtained for all the horizontal grid nodes, showing the velocity variations as a function of the depth each 0.1 km/s. For each velocity model obtained in each node it was used the Love waves group velocity maps between 4 s and 8.5 s plus the average of the Rayleigh and Love wave phase velocities. The black profile represents the initial model used for the shear-wave velocity inversions.

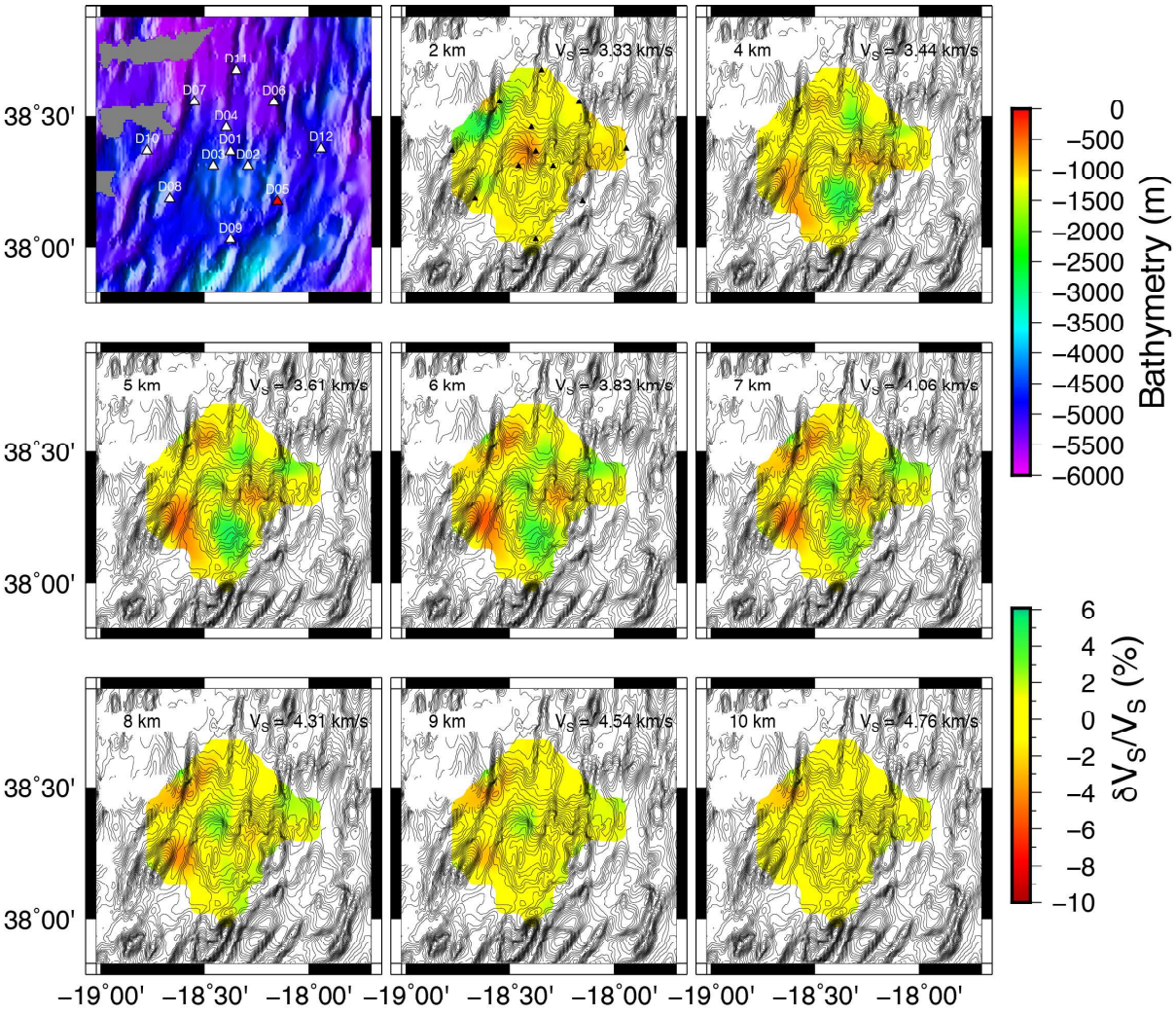

Figure 8.8: Shear-wave velocities horizontal slices at depths ranging from 2 km to 10 km, overlain on topography contours. We do not have information to the southeast of the study area because station D05 did not work.

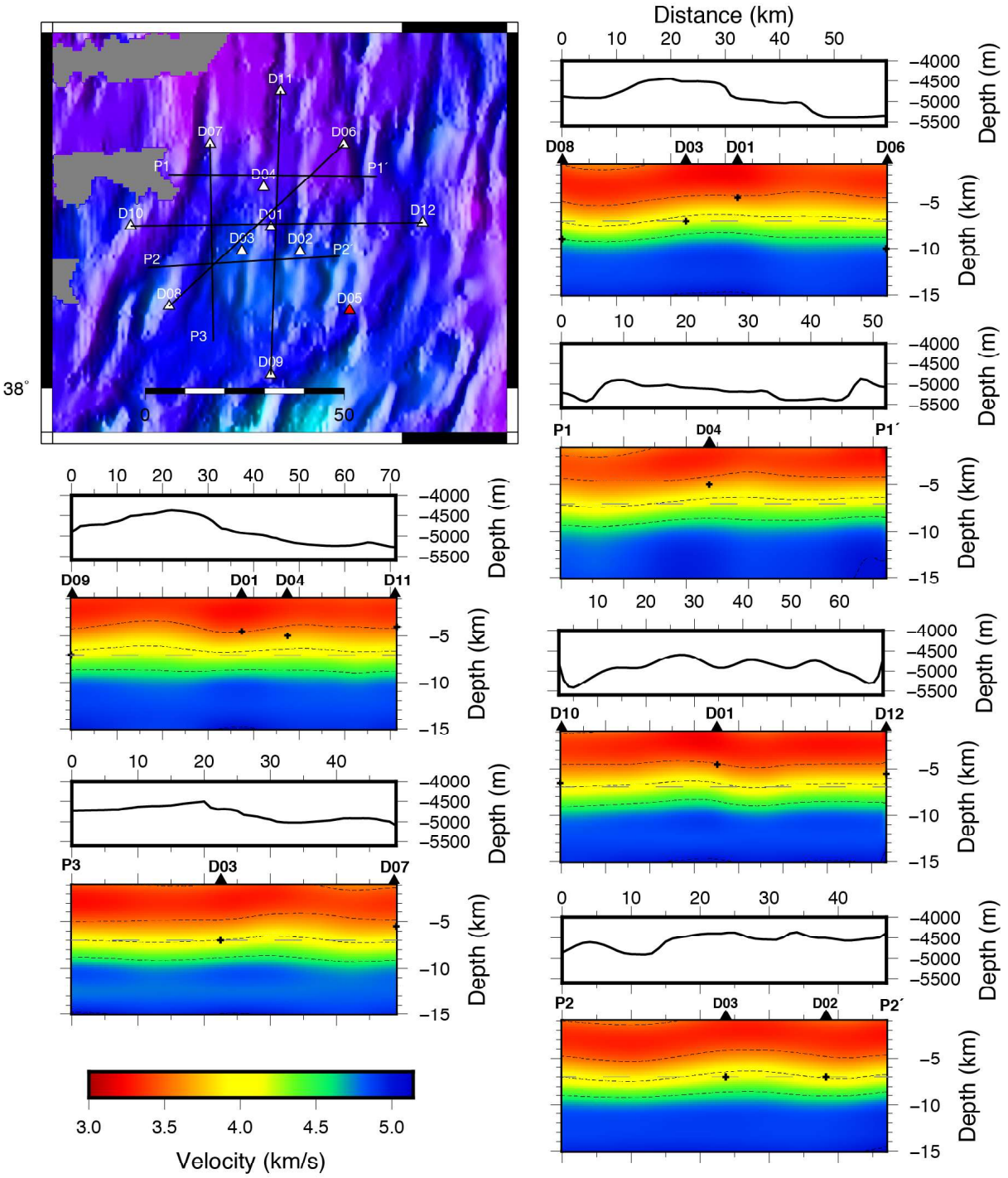

Figure 8.9: 2-D vertical profiles through the 3-D shear-wave velocity model. On the left is the map of the study area showing the three profiles chosen. On the right are the 2-D profiles showing the contours of 3.5, 4, 4.5 and 5 km/s. The black triangles represent the projection of the nearest station to the profile and the black crosses are the Moho depths found by *Hannemann et al.* (2016) under these stations. The profile starts at a depth of 1 km and extend until 15 km.

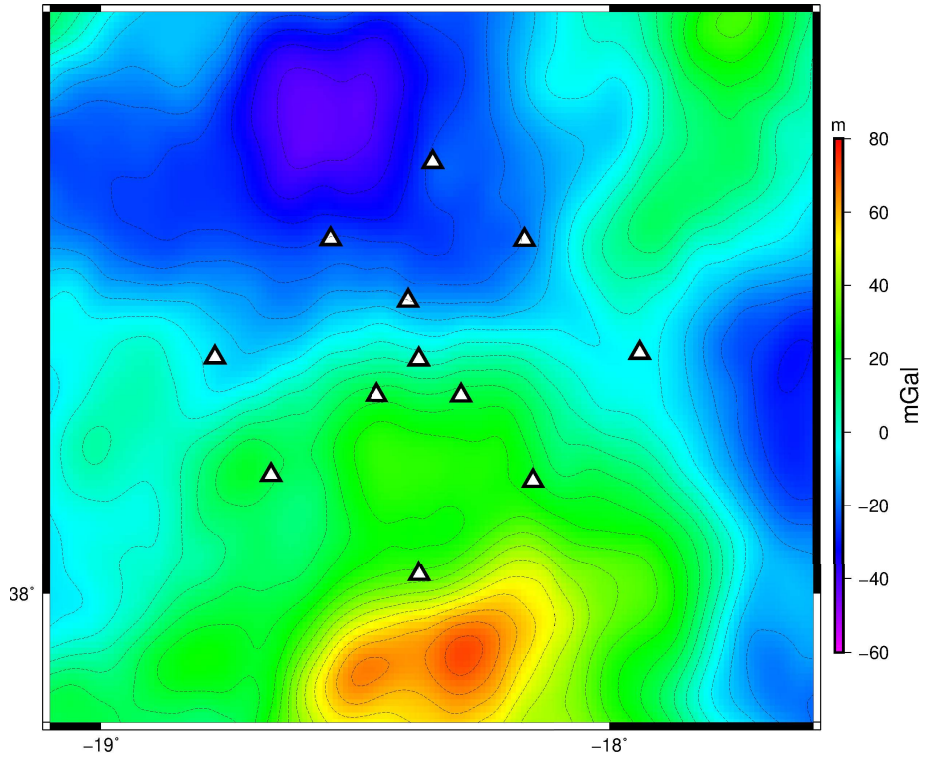

Figure 8.10: Marine free-air gravity map for the DOCTAR area (https://topex.ucsd.edu/pub/global_grav_1min/). There is a fast velocity anomaly to the south of the array related to a tall mountain and a low velocity anomaly to the northwest related to a very deep area.

and D04 and a low velocity anomaly in between stations D02 and D12. At 8 km depth, the the low velocity anomaly changes to a relatively homogeneous velocity structure maybe because we are losing resolution as previously mentioned. The D10-D12 profile passes through these two anomalies but also the D08-D10 profile crosses the fast velocity anomaly.

Another feature that can be observed in Figure 8.9 are the oscillations of the velocity contour lines along the profiles. As explained in the subsection 1.2.3, oscillations of crustal thickness in profiles perpendicular to the Mid-Atlantic Ridge have been observed in several studies.

Observing the N-S and W-E profiles of the Figure 1.4a, we can observe oscillations as well in the thickness of the oceanic crust. *Hannemann et al.* (2016) reported an increase in the thickness of the oceanic crust and a decrease in the shear-wave velocity towards the GF. Our results also found a thicker oceanic crust but at the SW observed in the profile D08-D06. Considering that the formation of new mountains or new material by the Mid-Atlantic Ridge are oriented N-S, the oscillations in the W-E direction should be more visible. In the Figure 8.9, the profiles that are parallel to the Mid-Atlantic Ridge,

such as profiles D09-D11 and P3-D07, show almost no oscillations in the 4.5 km/s velocity contour. On the other hand, the profiles that run perpendicular to the ridge, such as P1-P1', D10-D12 and P2-P2', show stronger oscillations in the 4.5 km/s contour. In addition, profile D08-D06 also shows very strong oscillations as this profile intersects the strongest low velocity anomaly. This can be due to the proximity of the GF and to the dextral transcurrent motion, which also exerts a deformation in the area. This deformation is also visible in the change of orientation of the nearest mountains to the GF, which could explain why we get strong oceanic crust oscillations at the profile D08-D06.

These oscillations are related to changes in crustal thickness and have an approximate wavelength of 25-30 km distance. According to *Bonatti et al.* (2003) the temporal variations in the crustal thickness have periods of ∼3-4 Ma. The DOCTAR area is located between 75 Ma and 85 Ma, with a difference is 10 Ma from station D10 to D12, so at least we should have 2 complete wavelengths in our observations, which is in agreement with our results in the profiles.

8.4 Summary

In a local study of the DOCTAR area, it was performed first 2-D velocity maps with the ambient noise dispersion curves using the FMST method. The tomographic resolution analysis was tested using the configuration of DOCTAR and the available data. Additionally, it was tested the regularization parameters to find the optimal setup of the inversion. Next, shear-wave velocity depth inversions were performed in each node of the Love wave group velocity maps to build a 3-D model. It was decided to use mostly the Love wave velocity maps because they are not affected by the water layer. The tomography inversion in each node was then built only using the velocity maps of Love wave group velocities from ambient noise (4 s to 8.5 s), complemented by the average of Love wave phase velocity of ambient noise (4 s to 9 s), and the average of Rayleigh and Love wave phase velocities of the two-station method (15 s to 44 s and 14 s to 42 s, respectively). The inversions were performed using the code SURF96 using as initial model the 1-D model inferred in chapter 7 and the same initial parameters.

Using a shear-wave velocity of 4 km/s as a reference for the Moho boundary, then our model indicates that the crustal thickness varies between 6 km and 8 km. Deeper levels

reflect therefore the structure of the mantle.

In general, is observed a thicker oceanic crust mainly at the southwest of the array related to a strong low velocity anomaly. On the contrary, at the south and center of the array, a thinner oceanic crust of ∼6 km is observed consistent with fast velocity anomalies. Free-air gravimetric data do not allow for a detailed comparison with the tomography results because of its resolution. Still, it is observed two main anomalies outside the array, a fast velocity anomaly related to a big submarine mountain to the south and a low velocity anomaly related to a deep valley to the northwest of the DOCTAR area.

Another important feature observed in the profiles are the crustal thickness oscillations best observed in profiles perpendicular to the Mid-Atlantic Ridge with wavelengths of ∼25-30 km. These may relate to changes in magma pulses in the Mid-Atlantic Ridge, as suggested by previous studies such us *Bonatti et al.* (2003); *Pariso et al.* (1995); *Tucholke et al.* (1997); *Shinevar et al.* (2019). In addition, there is an extra deformation in the DOCTAR area caused by the proximity of the GF, which we believe also influences the changes in the oceanic crustal thickness.

Chapter 9

Conclusions

The Gloria Fault is a strike-slip fault that divides the Eurasian and the Nubian tectonic plates and has a relative plate velocity motion of $\sim$ 4 mm/y (*Fernandes et al.*, 2003, 2006; *DeMets et al.*, 2010). In the Gloria Fault domain, at least three major earthquakes have been instrumentally recorded, on 1931, Ms=7.1; on 1939, Ms=7.1 and on 1941, Mw=8.3. Their focal mechanisms solutions are mainly strike-slip with some oblique motion at the east of the fault. The Deep OCean Test ARray (DOCTAR) was a mid-aperture temporary broadband of ocean bottom seismometers array deployed $\sim$70 km at north of segments 2 and 3 of the Gloria Fault. The array lies in an oceanic crust with an age of approximately 75 Ma and 85 Ma (*Müller et al.*, 2008). DOCTAR was installed from late-June 2011 to Mid-April 2012, recording in total 10 months of data continuously. The station D05 stopped working 1 month before recovery due to a high energy consumption because the vertical and one horizontal component were jammed. The hydrophone, on the other hand, worked well before the power loss so we could use that data. Ocean bottom seismometer data have a different processing from seismograms recorded on land stations because they are much more influenced by the conditions of the installation site and once recovered, the data requires several corrections in order for the data to be used. In addition, when processing the data, higher noise levels are often faced due to tilt noise, compliance noise, microseismic noise, local noise, self-noise, among others (*Webb*, 1998; *Crawford and Webb*, 2000; *Bell et al.*, 2015; *Matias and Harris*, 2015; *Janiszewski et al.*, 2019).

Previous studies performed by *Hannemann* (2016) inferred 1-D velocity models under each ocean bottom seismometer station, two velocity profiles for the region and evidence

of the lithosphere-asthenosphere boundary that gives us an idea of the influence of the Gloria Fault and of the geology of the study area.

Thus, our major goal was to characterize and image the 3-D lithospheric structure in the region, namely to map Vs changes and lateral variations in the thickness of the Earth's layers towards the Gloria Fault. In addition, this work applied other methods to obtain new insights below the DOCTAR area using surface-wave techniques based both on seismic ambient noise, teleseismic events and coda waves.

The secondary microseismic noise for the vertical component shows some sediment resonance at very short periods $\leq$4 s. In addition, at periods $\geq$10 s the self-noise becomes noticeable for the German instrument pool for amphibian seismology seismometer instruments. On the other hand, the hydrophone has shown to be very reliable in almost all the ocean bottom seismometers at all frequencies due to a wider response of the instrument. The horizontal components are very noisy, yet we were able to analyze these components. Some energy of the primary microseismic noise can be seen in the spectrogram at $\sim$12 s for the hydrophone but is not observed in the seismometer.

In chapter 3 we used the phase cross-correlation and the time-frequency Phase weighted stack to extract the Empirical Green's functions from ambient noise. The ambient seismic energy started to increase in the middle of August and remained stable during the rest of the deployment. It was observed that the predominant energy comes from the northwest and propagates towards the southeast. The hydrophone showed a higher amplitude signal compared to the vertical component. The horizontal components were rotated and cross-correlated to extract the Empirical Green's functions in the radial and transverse components. Additionally, symmetric stacking was applied to increase the arrival energy of all the paths of the station pairs.

To obtain the group and phase velocity dispersion curves from the cross-correlograms, the MFT and FTAN were used. It was used the hydrophone because of the number of dispersion curves are higher than those of the vertical component and it also has a higher amplitude signal in the cross-correlations.

To extract additional phase velocity dispersion curves at longer periods, the two-station method were used in chapter 4. The fundamental mode of Rayleigh wave phase velocity dispersion curves from 15 s to 44 s were used only considering the velocity range in which

the dispersion curve are already sensitive to the mantle structure. It was obtained 113 phase velocity dispersion curves for the hydrophone with an average velocity of 4.1 km/s between 20 s and 45 s. Dispersion curves $\geq$ 45 s were removed because the number of measurements to calculate the average decreased considerable leading to a different behavior in the average dispersion curve. It was only used the average phase velocity of Rayleigh and Love wave dispersion curves between 15 s to 45 s and 14 s to 43 s, respectively.

Plotting the dispersion curves from different azimuthal ranges show fast and low velocity dispersion curves. For instance, the velocity curves measured at azimuths ranging from 0 to 75 degrees and 200 to 245 degrees are faster than those between 270 and 360 degrees. In addition, the observations with a period of 20 s show a very small anisotropy, which, however, is not sufficient to clearly recognize an anisotropy.

The extraction of the Empirical Green's functions from the coda wave were done in chapter 5 to obtain some extra information of the shallow earth structure at periods between 5 s and 20 s. Beyond 20 s no information were retrieve due to a decay of the scattered seismic energy giving a hint of the nature of the scattered waves. Also, the array aperture limits the ability to extract dispersion curves at longer periods. To properly recover the seismic wavefield, is required a good distribution of energy from all directions between the two stations, which also requires a large number of earthquakes. Because of the lack of sufficient data for the coda analysis and the difficulties in observing the dispersion curves, the 1-D velocity structure inversion were carried out using only the measurements of the average Rayleigh wave phase velocity dispersion curves obtained with the two-station analysis from 15 s to 44 s, together with the average Love wave group and phase velocities obtained with ambient noise from 3 s to 9 s and from 4 s to 9 s, respectively. Finally, the average Love wave phase velocity dispersion curves of the two-station method between 14 s to 42 s were also used.

Systematically, we demonstrated the effect of the water, the sediments, the crustal structure and the lateral variation in the group and phase velocity dispersion curves in chapter 6 (manuscript in correction). Rayleigh waves observed in different oceanic settings confirm the existence of the three domains identified in synthetic tests, dominated by: (A) sediments; (B) water; and (C) lower crust and upper mantle structure, respectively.

Similar effects are observed in the dispersion curves for paths that cross water domains (e.g., between islands) as for those of paths between ocean bottom seismometers. The water layer must thus be taken into consideration, including variations in its thickness along the path between the stations. Concerning Love waves, as they are not affected by the water layer, an especial effort should be dedicated to extract their Empirical Green's functions whenever possible. To this end, the horizontal components must be carefully oriented and tilt noise reduced. Synthetic dispersion curves, including those of higher modes, should be computed using preliminary velocity models for the study region, using the appropriate water thicknesses to have a better interpretation in the selection of the dispersion curves. Dispersion curves should be picked or at least verified manually in the short-period band, where mode interference is likely to occur. The pressure channel can be used to identify the fundamental mode more clear, given that it is more energetic than the vertical seismometer component in the short period band.

In chapter 7, is first tested the reliability of the initial model used for the 1-D inversion of the vertical shear-wave structure. After testing several shear-wave inversions from different data sets, it was decided to perform the final velocity inversion using only the Rayleigh wave phase velocity data at long periods (two-station method) and the Love wave group (ambient noise) and phase velocity data (ambient noise and two-station method). The final 1-D shear-wave velocity model shows an oceanic crust with a thickness between 6 km and 9 km depending the reference velocity used.The final model reaches a maximum velocity of Vs=4.9 km/s at depths from 15.6 km to 35 km depth, which we attribute to the presence of harzburgite, a refractory residue of enhanced melting due to the proximity between the Mid-Atlantic Ridge and the Azores hotspot. The velocity then decreases reaching a minimum at ∼65-70 km depth interpreted as the lithosphere-asthenosphere boundary, which is in agreement with the depth reported by *Hannemann et al.* (2017). Geodynamically, a comparison between regional models and typical oceanic crust model was made. The sediment layer of all the models has on average the same thickness of ∼600 m, but only the Hannemann model shows similar velocities to those in our model. There is a considerable variation from model to model in the oceanic thickness, ranging on average from 6.41 km to 8.5 km.

Finally, chapter 8 presents the 2-D group velocity maps and the 3-D tomographic model. The tomography inversion in each node of the velocity maps were built using the Love

wave group velocity maps from ambient noise (4 s to 8.5 s). These measurements are complemented with the average of Love wave phase velocity of ambient noise (4 s to 9 s), and the average of Rayleigh and Love waves phase velocities of the two-station method (15 s to 44 s and 14 s to 42 s, respectively). The code SURF96 was applied using as initial model the 1-D model inferred in chapter 7 with the same initial parameters.

Because surface waves are not sensitive to discontinuities, it was used a shear-wave velocity of 4 km/s as a reference for the Moho boundary in the profiles of the 3-D tomography obtained from Crust1.0. Considering this value, then the crustal thickness varies between 6 km and 8 km. Overall, is observed a thicker oceanic crust mostly at the west and southwest of the DOCTAR area related to strong low velocity anomalies. On the contrary, at the south and center of the array, a thinner oceanic crust is observed consistent with fast velocity anomalies. The resolution of the free-air gravimetric data does not allow for a detailed comparison with the tomography results. In the free-air gravimetric map is observed two main anomalies with their maximum values outside the array. A fast velocity anomaly to the south related to a big submarine mountain and a low velocity anomaly to the north related to a deep valley.

Another important feature observed in the profiles are the oscillations of the oceanic crust thickness, which is best observed in profiles perpendicular to the Mid-Atlantic Ridge and with wavelengths of ∼25-30 km. These may relate to changes in magma pulses in the Mid-Atlantic Ridge. In addition, the proximity of the GF to the DOCTAR area may applies extra deformation observed in the change of orientation of the nearest mountains to the GF.

In conclusion, surface waves of ambient noise and earthquakes were used to image the oceanic crust and upper mantle structure below the DOCTAR area. With the 1-D and the 3-D models we infer an oceanic crustal thickness between 6 km and 9 km with oscillations every 25-30 km related to changes in mantle upwelling and flow during the formation of the lithosphere of the study area. In addition, we infer a thick layer of 25 km due to the presence of harzburgite, which generates very fast velocities in our final model. Finally, a decrease in the velocity is found at 65-70 km depth, which we assume to be the lithosphere-asthenosphere boundary. In addition, we demonstrated the impact of the water layer in the dispersion curves and compared theoretical predictions with real

observations in different scenarios such as deep water, island-water-island and continent-ocean transition.

Data and Resources

Data were obtained from the DEPAS pool (Deutsche Geräte-Pool für Amphibische Seismologie). Figures were generated with the Generic Mapping Tools software (GMT 6) (*Wessel et al.*, 2013). Synthetic eigenfunctions and seismograms, group velocity extraction with MFT and shear-wave inversion with SURF96 were computed using Computer Programs in Seismology (`http://www.eas.slu.edu/eqc/eqccps.html`). QSEIS is available at `https://github.com/pyrocko/fomosto-qseis`. SPECFEM3D can be downloaded at `https://geodynamics.org/cig/software/specfem3d`. FMST can be requested and downloaded at `http://iearth.edu.au/codes/FMST`.

Bibliography

Aki, K. (1957), Space and Time Spectra of Stationary Stochastic Waves, with Special Reference to Microtremors, *Bulletin of the Earthquake Research Institute*, *35*, 415–456.

Aki, K. (1969), Analysis of the seismic coda of local earthquakes as scattered waves, *Journal of Geophysical Research*, *74*(2), 615–631, doi:10.1029/JB074i002p00615.

Aki, K., and B. Chouet (1975), Origin of coda waves: Source, attenuation, and scattering effects, *Journal of Geophysical Research*, *80*(23), 3322–3342, doi:10.1029/JB080i023p03322.

Alfred-Wegener-Institut Helmholtz-Zentrum für Polar- und Meeresforschung et al.. (2017), DEPAS (Deutscher Geräte-Pool für amphibische Seismologie): German Instrument Pool for Amphibian Seismology, *Journal of largescale research facilities*, *3*, A122, doi:http://dx.doi.org/10.17815/jlsrf-3-165.

Ali, M. Y. (2002), A geophysical study of lithospheric flexure in the vicinity of Cape Verde islands, Ph.D. thesis, Worcester College and Department of Earth Sciences, University of Oxford.

Anderson, P. N., F. K. Duennebier, and R. K. Cessaro (1987), Ocean borehole horizontal seismic sensor orientation determined from explosive charges., *Journal of Geophysical Research*, *92*(B2), 3573–3579, doi:10.1029/jb092ib05p03573.

Ardhuin, F., E. Stutzmann, M. Schimmel, and A. Mangeney (2011), Ocean wave sources of seismic noise, *Journal of Geophysical Research: Oceans*, *116*(9), 1–21, doi:10.1029/2011JC006952.

Ardhuin, F., L. Gualtieri, and E. Stutzmann (2015), How ocean waves rock the Earth:

Two mechanisms explain microseisms with periods 3 to 300s, *Geophysical Research Letters*, *42*(3), 765–772, doi:10.1002/2014GL062782.

Asano, K., T. Iwata, H. Sekiguchi, K. Somei, K. Miyakoshi, S. Aoi, and T. Kunugi (2017), Surface wave group velocity in the Osaka sedimentary basin, Japan, estimated using ambient noise cross-correlation functions 4. Seismology, *Earth Planets Space*, *69*(1), doi:10.1186/s40623-017-0694-3.

Baptista, M. A., J. Miguel Miranda, L. Matias, and R. Omira (2017), Synthetic tsunami waveform catalogs with kinematic constraints, *Natural Hazards and Earth System Sciences*, *17*(7), 1253–1265, doi:10.5194/nhess-17-1253-2017.

Barruol, G., D. Reymond, F. R. Fontaine, O. Hyvernaud, V. Maurer, and K. Maamaatuaiahutapu (2006), Characterizing swells in the southern Pacific from seismic and infrasonic noise analyses, *Geophysical Journal International*, *164*(3), 516–542, doi:10.1111/j.1365-246X.2006.02871.x.

Bassin, C. (2000), The current limits of resolution for surface wave tomography in north america, *Eos, Transactions American Geophysical Union*.

Batista, L., C. Hübscher, P. Terrinha, L. Matias, A. Afilhado, and T. Lüdmann (2017), Crustal structure of the Eurasia–Africa plate boundary across the Gloria Fault, North Atlantic Ocean, *Geophysical Journal International*, *209*(2), 713–729, doi:10.1093/gji/ggx050.

Bell, S. W., D. W. Forsyth, and Y. Ruan (2015), Removing noise from the vertical component records of ocean-bottom seismometers: Results from year one of the cascadia initiative, *Bulletin of the Seismological Society of America*, *105*(1), 300–313, doi:10.1785/0120140054.

Bensen, G. D., M. H. Ritzwoller, M. P. Barmin, A. L. Levshin, F. Lin, M. P. Moschetti, N. M. Shapiro, and Y. Yang (2007), Processing seismic ambient noise data to obtain reliable broad-band surface wave dispersion measurements, *Geophysical Journal International*, *169*(3), 1239–1260, doi:10.1111/j.1365-246X.2007.03374.x.

Bensen, G. D., M. H. Ritzwoller, and N. M. Shapiro (2008), Broadband ambient noise

surface wave tomography across the United States, *Journal of Geophysical Research: Solid Earth*, *113*(5), doi:10.1029/2007JB005248.

Bensen, G. D., M. H. Ritzwoller, and Y. Yang (2009), A 3-D shear velocity model of the crust and uppermost mantle beneath the United States from ambient seismic noise, *Geophysical Journal International*, *177*(3), 1177–1196, doi:10.1111/j.1365-246X.2009.04125.x.

Bohlen, T., S. Kugler, G. Klein, and F. Theilen (2004), 1.5D inversion of lateral variation of Scholte-wave dispersion, *Geophysics*, *69*(2), 330–344, doi:10.1190/1.1707052.

Bonatti, E., M. Ligi, D. Brunelli, A. Cipriani, P. Fabretti, V. Ferrante, L. Gasperini, and L. Ottolini (2003), Mantle thermal pulses below the Mid-Atlantic Ridge and temporal variations in the formation of oceanic lithosphere, *Nature*, *423*(6939), 499–505, doi:10.1038/nature01594.

Bowden, D. C., M. D. Kohler, V. C. Tsai, and D. S. Weeraratne (2016), Offshore Southern California lithospheric velocity structure from noise cross-correlation functions, *Journal of Geophysical Research: Solid Earth*, *121*(5), 3415–3427, doi:10.1002/2016JB012919.

Buforn, E., A. Udías, and M. Colombás (1988), Seismicity, source mechanisms and tectonics of the Azores-Gibraltar plate boundary, *Tectonophysics*, *152*(1-2), 89–118, doi:10.1016/0040-1951(88)90031-5.

Campillo, M., and A. Paul (2003), Long range correlations in the diffuse seismic coda, *Science*, *299*(5606), 547–549, doi:10.1126/science.1078551.

Carvalho, J. (2020), Imaging the Cape Verde hotspot structure., Phd thesis, Universidade de Lisboa.

Carvalho, J., R. Bonadio, G. Silveira, S. Lebedev, J. Mata, P. Arroucau, T. Meier, and N. L. Celli (2019), Evidence for high temperature in the upper mantle beneath Cape Verde archipelago from Rayleigh-wave phase-velocity measurements, *Tectonophysics*, *770*(October), doi:10.1016/j.tecto.2019.228225.

Castagna, J. P., M. L. Batzle, and R. L. Eastwood (1985), Relationships between compressional and shear-wave velocities in clastic silicate rocks, *1984 SEG Annual Meeting, SEG 1984*, *50*(4), 582–584, doi:10.1190/1.1894108.

Corela, C., G. Silveira, L. Matias, M. Schimmel, and W. H. Geissler (2017), Ambient seismic noise tomography of SW Iberia integrating seafloor- and land-based data, *Tectonophysics*, *700-701*, 131–149, doi:10.1016/j.tecto.2017.02.012.

Crawford, W. C., and S. C. Webb (2000), Identifying and removing tilt noise from low-frequency (<0.1 Hz) seafloor vertical seismic data, *Bulletin of the Seismological Society of America*, *90*(4), 952–963, doi:10.1785/0119990121.

Crawford, W. C., S. C. Webb, and J. A. Hildebrand (1998), Estimating shear velocities in the oceanic crust from compliance measurements by two-dimensional finite difference modeling, *Journal of Geophysical Research: Solid Earth*, *103*(5), 9895–9916, doi:10.1029/97jb03532.

Dahlen, F. A., and J. Tromp (1998), *Theoretical global seismology*, Princeton University Press, Princeton, NJ.

DeMets, C., R. G. Gordon, and D. F. Argus (2010), Geologically current plate motions, *Geophysical Journal International*, *181*(1), 1–80, doi:10.1111/j.1365-246X.2009.04491.x.

Dick, H. J., R. L. Fisher, and W. B. Bryan (1984), Mineralogic variability of the uppermost mantle along mid-ocean ridges, *Earth and Planetary Science Letters*, *69*(1), 88–106, doi:https://doi.org/10.1016/0012-821X(84)90076-1.

Doran, A. K., and G. Laske (2017), Ocean-bottom seismometer instrument orientations via automated rayleigh-wave arrival-angle measurements, *Bulletin of the Seismological Society of America*, *107*(2), 691–708, doi:10.1785/0120160165.

Dziewonski, A., S. Bloch, and M. Landisman (1969), A technique for the analysis of transient seismic signals, *Bulletin of the Seismological Society of America*, *59*(1), 427–444.

Dziewonski, A., A. Hales, and E. Lapwood (1975), Parametrically simple earth models consistent with geophysical data, *Physics of the Earth and Planetary Interiors*, *10*(1), 12–48, doi:10.1016/0031-9201(75)90017-5.

Dziewonski, A. M., and D. L. Anderson (1981), Preliminary reference Earth model, *Physics of the Earth and Planetary Interiors*, *25*(4), 297–356, doi:10.1016/0031-9201(81)90046-7.

Ekström, G., G. A. Abers, and S. C. Webb (2009), Determination of surface-wave phase velocities across USArray from noise and Aki's spectral formulation, *Geophysical Research Letters*, *36*(18), 5–9, doi:10.1029/2009GL039131.

Ewing, M., and A. Vine (1938), Deep-sea measurements without wires or cables, *Eos, Transactions American Geophysical Union*, *19*(1), 248–251, doi:10.1029/TR019i001p00248.

Fang, H., H. Yao, H. Zhang, Y. C. Huang, and R. D. Van Der Hilst (2015), Direct inversion of surface wave dispersion for three-dimensional shallow crustal structure based on ray tracing: Methodology and application, *Geophysical Journal International*, *201*(3), 1251–1263, doi:10.1093/gji/ggv080.

Fernandes, R. M., B. A. Ambrosius, R. Noomen, L. Bastos, M. J. Wortel, W. Spakman, and R. Govers (2003), The relative motion between Africa and Eurasia as derived from ITRF2000 and GPS data, *Geophysical Research Letters*, *30*(16), 1–5, doi:10.1029/2003GL017089.

Fernandes, R. M., L. Bastos, J. M. Miranda, N. Lourenço, B. A. Ambrosius, R. Noomen, and W. Simons (2006), Defining the plate boundaries in the Azores region, *Journal of Volcanology and Geothermal Research*, *156*(1-2), 1–9, doi:10.1016/j.jvolgeores.2006.03.019.

Fischer, K. M., H. A. Ford, D. L. Abt, and C. A. Rychert (2010), The lithosphere-asthenosphere boundary, *Annual Review of Earth and Planetary Sciences*, *38*, 551–575, doi:10.1146/annurev-earth-040809-152438.

Forsyth, D. W., and A. Li (2005), Array analysis of two-dimensional variations in surface wave phase velocity and azimuthal anisotropy in the presence of multipathing interference, *Washington DC American Geophysical Union Geophysical Monograph Series*, *157*, 81–97, doi:10.1029/157GM06.

Gualtieri, L., E. Stutzmann, Y. Capdeville, F. Ardhuin, M. Schimmel, A. Mangeney, and A. Morelli (2013), Modelling secondary microseismic noise by normal mode summation, *Geophysical Journal International*, *193*(3), 1732–1745, doi:10.1093/gji/ggt090.

Gualtieri, L., E. Stutzmann, V. Farra, Y. Capdeville, M. Schimmel, F. Ardhuin, and A. Morelli (2014), Modelling the ocean site effect on seismic noise body waves, *Geophysical Journal International*, *197*(2), 1096–1106, doi:10.1093/gji/ggu042.

Gualtieri, L., E. Stutzmann, Y. Capdeville, V. Farra, A. Mangeney, and A. Morelli (2015), On the shaping factors of the secondary microseismic wavefield, *Journal of Geophysical Research: Solid Earth*, *120*(9), 6241–6262, doi:10.1002/2015JB012157.

Hannemann, K. (2016), Seismological investigation of the oceanic crust and upper mantle using an ocean bottom station array in the vicinity of the Gloria fault (eastern mid Atlantic), Ph.D. thesis.

Hannemann, K., F. Krüger, and T. Dahm (2013), Measuring of clock drift rates and static time offsets of ocean bottom stations by means of ambient noise, *Geophysical Journal International*, *196*(2), 1034–1042, doi:10.1093/gji/ggt434.

Hannemann, K., F. Kruger, T. Dahm, and D. Lange (2016), Oceanic lithospheric S-wave velocities from the analysis of P-wave polarization at the ocean floor, *Geophysical Journal International*, *207*(3), 1796–1817, doi:10.1093/gji/ggw342.

Hannemann, K., F. Krüger, T. Dahm, and D. Lange (2017), Structure of the oceanic lithosphere and upper mantle north of the Gloria Fault in the eastern mid-Atlantic by receiver function analysis, *Journal of Geophysical Research: Solid Earth*, *122*(10), 7927–7950, doi:10.1002/2016JB013582.

Hariharan, A., C. A. Dalton, Z. Ma, and G. Ekström (2020), Evidence of Overtone Interference in Fundamental-Mode Rayleigh Wave Phase and Amplitude Measurements, *Journal of Geophysical Research: Solid Earth*, *125*(1), 1–17, doi:10.1029/2019JB018540.

Harmon, N., and C. A. Rychert (2016), Joint inversion of teleseismic and ambient noise Rayleigh waves for phase velocity maps, an application to Iceland, *Journal of Geophysical Research: Solid Earth*, *121*(8), 5966–5987, doi:10.1002/2016JB012934.

Harmon, N., D. Forsyth, and S. Webb (2007), Using ambient seismic noise to determine short-period phase velocities and shallow shear velocities in young oceanic lithosphere, *Bulletin of the Seismological Society of America*, *97*(6), 2009–2023, doi:10.1785/0120070050.

Harmon, N., D. W. Forsyth, and D. S. Weeraratne (2009), Thickening of young Pacific lithosphere from high-resolution Rayleigh wave tomography: A test of the conductive cooling model, *Earth and Planetary Science Letters*, *278*(1-2), 96–106, doi:10.1016/j.epsl.2008.11.025.

Harmon, N., M. S. D. De La Cruz, C. A. Rychert, G. Abers, and K. Fischer (2013), Crustal and mantle shear velocity structure of Costa Rica and Nicaragua from ambient noise and teleseismic Rayleigh wave tomography, *Geophysical Journal International*, *195*(2), 1300–1313, doi:10.1093/gji/ggt309.

Hasselmann, K. (1963), A statistical analysis of the generation of microseisms, *Reviews of Geophysics*, *1*(2), 177–210, doi:10.1029/RG001i002p00177.

Herrmann, R. B. (2013), Computer programs in seismology: An evolving tool for instruction and research, *Seismological Research Letters*, *84*(6), 1081–1088, doi:10.1785/0220110096.

Herrmann, R. B., and C. J. Ammon (2002), Surface waves , receiver functions and crustal structure, Computer Programs in Seismology, *Saint Luis University*, (p. 133–135).

Janiszewski, H. A., J. B. Gaherty, G. A. Abers, H. Gao, and Z. C. Eilon (2019), Amphibious surface-wave phase-velocity measurements of the Cascadia subduction zone, *Geophysical Journal International*, *217*(3), 1929–1948, doi:10.1093/gji/ggz051.

Kawaguchi, K., S. Kaneko, T. Nishida, and T. Komine (2015), Construction of the DONET real-time seafloor observatory for earthquakes and tsunami monitoring, in *SEAFLOOR OBSERVATORIES*, vol. 21, pp. 211–228, Springer Berlin Heidelberg, Berlin, Heidelberg, doi:10.1007/978-3-642-11374-1_10.

Kawakatsu, H., P. Kumar, Y. Takei, M. Shinohara, T. Kanazawa, E. Araki, and K. Suyehiro (2009), Seismic evidence for sharp lithosphere-asthenosphere boundaries of oceanic plates, *Science*, *324*(5926), 499–502, doi:10.1126/science.1169499.

Keilis-Borok, V. I., A. L. Levshin, T. B. Yanovskaya, A. V. Lander, B. G. Bukchin, M. P. Barmin, L. I. Ratnikova, and E. N. Its (1989), *Seismic surface waves in a laterally inhomogeneous earth*, Springer, Dordrecht.

Kelemen, P. B., N. Shimizu, and V. J. Salters (1995), Extraction of mid-ocean-ridge basalt from the upwelling mantle by focused flow of melt in dunite channels, *Nature*, *375*(6534), 747–753, doi:10.1038/375747a0.

Kelley, D. S., J. R. Delaney, and S. K. Juniper (2014), Establishing a new era of submarine volcanic observatories: Cabling Axial Seamount and the Endeavour Segment of the Juan de Fuca Ridge, *Marine Geology*, *352*, 426–450, doi:10.1016/j.margeo.2014.03.010.

Kennett, B. L. N., M. S. Sambridge, and P. R. Williamson (1988), Subspace methods for large inverse problems with multiple parameter classes, *Geophysical Journal International*, *94*(2), 237–247, doi:10.1111/j.1365-246X.1988.tb05898.x.

Kohler, M. D., et al. (2020), A plan for a long-term, automated, broadband seismic monitoring network on the global seafloor, *Seismological Research Letters*, *91*(3), 1343–1355, doi:10.1785/0220190123.

Komatitsch, D., and J. Tromp (1999), Introduction to the spectral element method for three-dimensional seismic wave propagation, *Geophysical Journal International*, *139*(3), 806–822, doi:10.1046/j.1365-246X.1999.00967.x.

Komatitsch, D., Z. Xie, E. Bozdağ, E. S. de Andrade, D. Peter, Q. Liu, and J. Tromp (2016), Anelastic sensitivity kernels with parsimonious storage for adjoint tomography and full waveform inversion, *Geophysical Journal International*, *206*(3), 1467–1478, doi:10.1093/gji/ggw224.

Laske, G., G. Masters, Z. Ma, M. E. Pasyanos, and L. Livermore (2013), EGU2013-2658 Update on CRUST1 . 0 : A 1-degree Global Model of Earth ' s Crust, p. 2658.

Laughton, A. S., R. B. Whitmarsh, J. S. Rusby, M. L. Somers, J. Revie, B. S. Mccartney, and J. E. Nafe (1972), A continuous east-west fault on the Azores-Gibraltar Ridge, *Nature*, *237*(5352), 217–220, doi:10.1038/237217a0.

Le, B. M., T. Yang, Y. J. Chen, and H. Yao (2018), Correction of OBS clock errors using Scholte waves retrieved from cross-correlating hydrophone recordings, *Geophysical Journal International*, *212*(2), 891–899, doi:10.1093/gji/ggx449.

Le Pape, F., D. Craig, and C. J. Bean (2021), How deep ocean-land coupling controls the generation of secondary microseism Love waves, *Nature Communications*, *12*(1), 1–15, doi:10.1038/s41467-021-22591-5.

Lebedev, S., J. M. Adam, and T. Meier (2013), Mapping the Moho with seismic surface waves: A review, resolution analysis, and recommended inversion strategies, *Tectonophysics*, *609*(2013), 377–394, doi:10.1016/j.tecto.2012.12.030.

Levshin, A. L., and M. H. Ritzwoller (2001), Automated detection, extraction, and measurement of regional surface waves, *Pure and Applied Geophysics*, *158*(8), 1531–1545, doi:10.1007/pl00001233.

Lin, F. C., and M. H. Ritzwoller (2011), Helmholtz surface wave tomography for isotropic and azimuthally anisotropic structure, *Geophysical Journal International*, *186*(3), 1104–1120, doi:10.1111/j.1365-246X.2011.05070.x.

Lin, F. C., and V. C. Tsai (2013), Seismic interferometry with antipodal station pairs, *Geophysical Research Letters*, *40*(17), 4609–4613, doi:10.1002/grl.50907.

Lin, F. C., M. H. Ritzwoller, J. Townend, S. Bannister, and M. K. Savage (2007), Ambient noise Rayleigh wave tomography of New Zealand, *Geophysical Journal International*, *170*(2), 649–666, doi:10.1111/j.1365-246X.2007.03414.x.

Lin, F. C., M. P. Moschetti, and M. H. Ritzwoller (2008), Surface wave tomography of the western United States from ambient seismic noise: Rayleigh and Love wave phase velocity maps, *Geophysical Journal International*, *173*(1), 281–298, doi:10.1111/j.1365-246X.2008.03720.x.

Lodge, A., and G. Helffrich (2006), Depleted swell root beneath the Cape Verde Islands, *Geology*, *34*(6), 449–452, doi:10.1130/G22030.1.

Longuet-Higgins, M. S. (1950), A theory of the origin of microseisms, *Philosophical Transactions of the Royal Society of London. Series A, Mathematical and Physical Sciences*, *243*(857), 1–35, doi:10.1098/rsta.1950.0012.

Luis, J. F., and J. M. Miranda (2008), Reevaluation of magnetic chrons in the North Atlantic between 35°N and 47°N: Implications for the formation of the Azores Triple Junction and associated plateau, *Journal of Geophysical Research: Solid Earth*, *113*(10), 1–12, doi:10.1029/2007JB005573.

Luo, Y., Y. Yang, K. Zhao, Y. Xu, and J. Xia (2015), Unraveling overtone interferences in Love-wave phase velocity measurements by radon transform, *Geophysical Journal International*, *203*(1), 327–333, doi:10.1093/gji/ggv300.

Lynner, C., and M. Bodmer (2017), Mantle flow along the eastern North American margin inferred from shear wave splitting, *Geology*, *45*(10), 867–870, doi:10.1130/G38980.1.

Lynner, C., and R. W. Porritt (2017), Crustal structure across the eastern North American margin from ambient noise tomography, *Geophysical Research Letters*, *44*(13), 6651–6657, doi:10.1002/2017GL073500.

Maeda, T., H. Sato, and M. Ohtake (2006), Constituents of Vertical-component Coda Waves at Long Periods, *Pure and Applied Geophysics*, *163*(2), 549–566, doi:10.1007/s00024-005-0031-9.

Matias, L., and D. Harris (2015), A single-station method for the detection, classification and location of fin whale calls using ocean-bottom seismic stations, *Journal of the Acoustical Society of America*, *138*(1), 504–520, doi:10.1121/1.4922706.

Maupin, V. (2011), Upper-mantle structure in southern Norway from beamforming of Rayleigh wave data presenting multipathing, *Geophysical Journal International*, *185*(2), 985–1002, doi:10.1111/j.1365-246X.2011.04989.x.

McGuire, J. J., J. A. Collins, P. Gouédard, E. Roland, D. Lizarralde, M. S. Boettcher, M. D. Behn, and R. D. Van Der Hilst (2012), Variations in earthquake rupture properties along the Gofar transform fault, East Pacific Rise, *Nature Geoscience*, *5*(5), 336–341, doi:10.1038/ngeo1454.

McNutt, M. (1988), Thermal and mechanical properties of the Cape Verde Rise., *Journal of Geophysical Research*, *93*(B4), 2784–2794, doi:10.1029/JB093iB04p02784.

Meier, T., K. Dietrich, B. Stöckhert, and H. P. Harjes (2004), One-dimensional models of shear wave velocity for the eastern Mediterranean obtained from the inversion of

Rayleigh wave phase velocities and tectonic implications, *Geophysical Journal International*, *156*(1), 45–58, doi:10.1111/j.1365-246X.2004.02121.x.

Montagner, J. P., P. Lognonné, R. Beauduin, G. Roult, J. F. Karczewski, and E. Stutzmann (1998), Towards multiscalar and multiparameter networks for the next century: The French efforts, *Physics of the Earth and Planetary Interiors*, *108*(2), 155–174, doi:10.1016/S0031-9201(98)00093-4.

Mooney, W. D., G. Laske, and T. G. Masters (1998), CRUST 5.1: A global crustal model at 5° × 5°, *Journal of Geophysical Research: Solid Earth*, *103*(1), 727–747, doi:10.1029/97jb02122.

Mordret, A., M. Landés, N. M. Shapiro, S. C. Singh, and P. Roux (2014), Ambient noise surface wave tomography to determine the shallow shear velocity structure at Valhall: Depth inversion with a Neighbourhood Algorithm, *Geophysical Journal International*, *198*(3), 1514–1525, doi:10.1093/gji/ggu217.

Müller, R. D., M. Sdrolias, C. Gaina, and W. R. Roest (2008), Age, spreading rates, and spreading asymmetry of the world's ocean crust, *Geochemistry, Geophysics, Geosystems*, *9*(4), 1–19, doi:10.1029/2007GC001743.

Nakata, N., J. P. Chang, J. F. Lawrence, and P. Boué (2015), Journal of Geophysical Research : Solid Earth Body wave extraction and tomography at Long Beach , California , with ambient-noise interferometry, *Journal of Geophysical Research: Solid Earth*, *120*, 1159–1173, doi:10.1002/2015JB011870.Received.

Nettles, M., and A. M. Dziewoński (2011), Effect of higher-mode interference on measurements and models of fundamental-mode surface-wave dispersion, *Bulletin of the Seismological Society of America*, *101*(5), 2270–2280, doi:10.1785/0120110019.

Nishida, K. (2013), Earth's Background Free Oscillations, *Annual Review of Earth and Planetary Sciences*, *41*(1), 719–740, doi:10.1146/annurev-earth-050212-124020.

Nishida, K., H. Kawakatsu, Y. Fukao, and K. Obara (2008), Background Love and Rayleigh waves simultaneously generated at the Pacific Ocean floors, *Geophysical Research Letters*, *35*(16), 1–5, doi:10.1029/2008GL034753.

Olugboji, T. M., S. Karato, and J. Park (2013), Structures of the oceanic lithosphere-asthenosphere boundary: Mineral-physics modeling and seismological signatures, *Geochemistry, Geophysics, Geosystems*, *14*(4), 880–901, doi:10.1002/ggge.20086.

Pariso, J. E., J.-c. Sempéré, and C. Rommevaux (1995), Temporal and spatial variations in crustal accretion along the Mid-Atlantic Ridge (29°-31°30N) over the last 10 m.y.: Implications from a three-dimensional gravity study, *Journal of Geophysical Research: Solid Earth*, *100*(B9), 17,781–17,794, doi:10.1029/95JB01146.

Paul, A., M. Campillo, L. Margerin, E. Larose, and A. Derode (2005), Empirical synthesis of time-asymmetrical Green functions from the correlation of coda waves, *Journal of Geophysical Research: Solid Earth*, *110*(8), 1–13, doi:10.1029/2004JB003521.

Pekeris, C. L. (1948), Theory of propagation of explosive sound in shallow water, in *Propagation of Sound in the Ocean*, Mem Geol Soc Am, doi:10.1130/MEM27-2-p1.

Pim, J., C. Peirce, A. B. Watts, I. Grevemeyer, and A. Krabbenhoeft (2008), Crustal structure and origin of the Cape Verde Rise, *Earth and Planetary Science Letters*, *272*(1-2), 422–428, doi:10.1016/j.epsl.2008.05.012.

Poli, P., M. Campillo, H. Pedersen, and null null (2012), Body-wave imaging of earth's mantle discontinuities from ambient seismic noise, *Science*, *338*(6110), 1063–1065, doi:10.1126/science.1228194.

Poli, P., C. Thomas, M. Campillo, and H. A. Pedersen (2015), Imaging the D reflector with noise correlations, *Geophysical Research Letters*, *42*(1), 60–65, doi:10.1002/2014GL062198.

Poli, P., M. Campillo, and M. de Hoop (2017), Analysis of intermediate period correlations of coda from deep earthquakes, *Earth and Planetary Science Letters*, *477*, 147–155, doi:10.1016/j.epsl.2017.08.026.

Rawlinson, N. (2005), FMST: Fast Marching Surface Tomography package–Instructions., *Research School of Earth Sciences, Australian National University, Canberra.*, pp. 1–24.

Rawlinson, N., and M. Sambridge (2004), Wave front evolution in strongly heterogeneous layered media using the fast marching method, *Geophysical Journal International*, *156*(3), 631–647, doi:10.1111/j.1365-246X.2004.02153.x.

Rawlinson, N., and M. Sambridge (2005), The fast marching method: An effective tool for tomographic imaging and tracking multiple phases in complex layered media, *Exploration Geophysics*, *36*(4), 341–350, doi:10.1071/EG05341.

Rawlinson, N., S. Pozgay, and S. Fishwick (2010), Seismic tomography: A window into deep Earth, *Physics of the Earth and Planetary Interiors*, *178*(3-4), 101–135, doi:10.1016/j.pepi.2009.10.002.

Reis, C., R. Omira, L. Matias, and M. A. Baptista (2017), On the source of the 8 May 1939 Azores earthquake–tsunami observations and numerical modelling, *Geomatics, Natural Hazards and Risk*, *8*(2), 328–347, doi:10.1080/19475705.2016.1218944.

Romanowicz, B., P. McGill, D. Neuhauser, and D. Dolenc (2009), Acquiring real time data from the broadband ocean bottom seismic observatory at Monterey bay (MObb), *Seismological Research Letters*, *80*(2), 197–202, doi:10.1785/gssrl.80.2.197.

Rospabé, M., G. Ceuleneer, V. Le Guluche, M. Benoit, and M. A. Kaczmarek (2021), The Chicken and Egg Dilemma Linking Dunites and Chromitites in the Mantle-Crust Transition Zone beneath Oceanic Spreading Centres: A Case Study of Chromite-hosted Silicate Inclusions in Dunites Formed at the Top of a Mantle Diapir (Oman Ophiolite), *Journal of Petrology*, *62*(4), 1–27, doi:10.1093/petrology/egab026.

Roux, P., K. G. Sabra, P. Gerstoft, W. A. Kuperman, and M. C. Fehler (2005), P-waves from cross-correlation of seismic noise, *Geophysical Research Letters*, *32*(19), 1–4, doi:10.1029/2005GL023803.

Rusell, D. R. (1987), Multi-channel processing of dispersed surface waves, Dissertation, St. Louis University, 1–162.

Ryberg, T., W. Geissler, W. Jokat, and S. Pandey (2017), Uppermost mantle and crustal structure at tristan da cunha derived from ambient seismic noise, *Earth and Planetary Science Letters*, *471*, 117–124, doi:10.1016/j.epsl.2017.04.049.

Sallarès, V., A. Gailler, M. A. Gutscher, D. Graindorge, R. Bartolomé, E. Gràcia, J. Díaz, J. J. Dañobeitia, and N. Zitellini (2011), Seismic evidence for the presence of Jurassic oceanic crust in the central Gulf of Cadiz (SW Iberian margin), *Earth and Planetary Science Letters*, *311*(1-2), 112–123, doi:10.1016/j.epsl.2011.09.003.

Sallarès, V., et al. (2013), Seismic evidence of exhumed mantle rock basement at the Gorringe Bank and the adjacent Horseshoe and Tagus abyssal plains (SW Iberia), *Earth and Planetary Science Letters*, *365*, 120–131, doi:10.1016/j.epsl.2013.01.021.

Sato, H., M. C. Fehler, and T. Maeda (2012), *Seismic Wave Propagation and Scattering in the Heterogeneous Earth : Second Edition*, Springer Berlin Heidelberg, Berlin, Heidelberg, doi:10.1007/978-3-642-23029-5.

Sato, Y. (1955), Analysis of Dispersed Surface Waves by means of Fourier Transform I.

Savage, M. K., F. C. Lin, and J. Townend (2013), Ambient noise cross-correlation observations of fundamental and higher-mode Rayleigh wave propagation governed by basement resonance, *Geophysical Research Letters*, *40*(14), 3556–3561, doi:10.1002/grl.50678.

Schimmel, M. (1999), Phase cross-correlations: Design, comparisons, and applications, *Bulletin of the Seismological Society of America*, *89*(5), 1366–1378.

Schimmel, M., and J. Gallart (2007), Frequency-dependent phase coherence for noise suppression in seismic array data, *Journal of Geophysical Research: Solid Earth*, *112*(4), 1–14, doi:10.1029/2006JB004680.

Schimmel, M., and H. Paulssen (1997), Noise reduction and detection of weak, coherent signals through phase-weighted stacks, *Geophysical Journal International*, *130*(2), 497–505, doi:10.1111/j.1365-246X.1997.tb05664.x.

Schimmel, M., E. Stutzmann, and J. Gallart (2011), Using instantaneous phase coherence for signal extraction from ambient noise data at a local to a global scale, *Geophysical Journal International*, *184*(1), 494–506, doi:10.1111/j.1365-246X.2010.04861.x.

Schimmel, M., E. Stutzmann, and S. Ventosa (2017), Measuring Group Velocity in Seismic Noise Correlation Studies Based on Phase Coherence and Resampling Strategies, *IEEE Transactions on Geoscience and Remote Sensing*, *55*(4), 1928–1935, doi:10.1109/TGRS.2016.2631445.

Scholz, J. R., G. Barruol, F. R. Fontaine, K. Sigloch, W. C. Crawford, and M. Deen (2017), Orienting ocean-bottom seismometers from P-wave and Rayleigh wave polarizations, *Geophysical Journal International*, *208*(3), 1277–1289, doi:10.1093/gji/ggw426.

Sethian, J. A. (1996), A Fast Marching Level Set Method for Monotonically Advancing Fronts, *Proceedings of the National Academy of Science*, *93*(4), 1591–1595, doi:10.1073/pnas.93.4.1591.

Shapiro, N. M., and M. Campillo (2004), Emergence of broadband Rayleigh waves from correlations of the ambient seismic noise, *Geophysical Research Letters*, *31*(7), 8–11, doi:10.1029/2004GL019491.

Shapiro, N. M., M. Campillo, L. Stehly, and M. H. Ritzwoller (2005), High-resolution surface-wave tomography from ambient seismic noise, *Science*, *307*(5715), 1615–1618, doi:10.1126/science.1108339.

Shinevar, W. J., et al. (2019), Causes of Oceanic Crustal Thickness Oscillations Along a 74-M Mid-Atlantic Ridge Flow Line, *Geochemistry, Geophysics, Geosystems*, *20*(12), 6123–6139, doi:10.1029/2019GC008711.

Simons, F. J., G. Nolet, J. M. Babcock, R. E. Davis, and J. A. Orcutt (2006), A future for drifting seismic networks, *Eos, Transactions American Geophysical Union*, *87*(31), 305–307, doi:10.1029/2006eo310002.

Snieder, R. (2006), The theory of coda wave interferometry, *Pure and Applied Geophysics*, *163*(2-3), 455–473, doi:10.1007/s00024-005-0026-6.

Socco, L. V., S. Foti, and D. Boiero (2010), Surface-wave analysis for building near-surface velocity models - Established approaches and new perspectives, *Geophysics*, *75*(5), doi:10.1190/1.3479491.

Soomro, R. A., et al. (2016), Phase velocities of Rayleigh and Love waves in central and northern Europe from automated, broad-band, interstation measurements, *Geophysical Journal International*, *204*(1), 517–534, doi:10.1093/gji/ggv462.

Stachnik, J. C., A. F. Sheehan, D. W. Zietlow, Z. Yang, J. Collins, and A. Ferris (2012), Determination of New Zealand Ocean bottom seismometer orientation via rayleigh-wave polarization, *Seismological Research Letters*, *83*(4), 704–713, doi:10.1785/0220110128.

Stähler, S. C., et al. (2016), Performance report of the RHUM-RUM ocean bottom seismometer network around la Réunion, western Indian Ocean, *Advances in Geosciences*, *41*, 43–63, doi:10.5194/adgeo-41-43-2016.

Stockwell, R., L. Mansinha, and R. Lowe (1996), Localization of the complex spectrum: the s transform, *IEEE Transactions on Signal Processing*, *44*(4), 998–1001, doi:10.1109/78.492555.

Suetsugu, D., and H. Shiobara (2014), Broadband ocean-bottom seismology, *Annual Review of Earth and Planetary Sciences*, *42*, 27–43, doi:10.1146/annurev-earth-060313-054818.

Takeuchi, H., and M. Saito (1972), *Seismis surface waves, in Seismology: Surface Waves and Earth Oscillations*, B. A. Bolt (Editor), Academic Press, New York, New York, 217–295.

Tanimoto, T., and C. Alvizuri (2006), Inversion of the HZ ratio of microseisms for S-wave velocity in the crust, *Geophysical Journal International*, *165*(1), 323–335, doi:10.1111/j.1365-246X.2006.02905.x.

Tanimoto, T., C. Hadziioannou, H. Igel, J. Wasserman, U. Schreiber, and A. Gebauer (2015), Estimate of Rayleigh-to-Love wave ratio in the secondary microseism by colocated ring laser and seismograph, *Geophysical Research Letters*, *42*(8), 2650–2655, doi:10.1002/2015GL063637.

Tian, Y., and M. H. Ritzwoller (2015), Directionality of ambient noise on the Juan de Fuca plate: Implications for source locations of the primary and secondary microseisms, *Geophysical Journal International*, *201*(1), 429–443, doi:10.1093/gji/ggv024.

Tian, Y., and M. H. Ritzwoller (2017), Improving ambient noise cross-correlations in the noisy ocean bottom environment of the Juan de Fuca plate, *Geophysical Journal International*, *210*(3), 1787–1805, doi:10.1093/gji/ggx281.

Tomar, G., E. Stutzmann, A. Mordret, J. P. Montagner, S. C. Singh, and N. M. Shapiro (2018), Joint inversion of the first overtone and fundamental mode for deep imaging at the Valhall oil field using ambient noise, *Geophysical Journal International*, *214*(1), 122–132, doi:10.1093/gji/ggy122.

Tozer, B., D. T. Sandwell, W. H. Smith, C. Olson, J. R. Beale, and P. Wessel (2019), Global Bathymetry and Topography at 15 Arc Sec: SRTM15+, *Earth and Space Science*, *6*(10), 1847–1864, doi:10.1029/2019EA000658.

Tucholke, B. E., J. Lin, M. C. Kleinrock, M. A. Tivey, T. B. Reed, J. Goff, and G. E. Jaroslow (1997), Segmentation and crustal structure of the western Mid-Atlantic Ridge flank, 25°25-27°10N and 0-29 m.y., *Journal of Geophysical Research: Solid Earth*, *102*(B5), 10,203–10,223, doi:10.1029/96jb03896.

Udías, A., A. Arroyo, and J. Mezcua (1976), Seismotectonic of the Azores-Alboran region, *Tectonophysics*, *31*(3-4), 259–289, doi:10.1016/0040-1951(76)90121-9.

Wang, Q., N. Bagdassarov, and S. Ji (2013), The Moho as a transition zone: A revisit from seismic and electrical properties of minerals and rocks, *Tectonophysics*, *609*, 395–422, doi:10.1016/j.tecto.2013.08.041.

Wang, R. (1999), A simple orthonormalization method for stable and efficient computation of Green's functions, *Bulletin of the Seismological Society of America*, *89*(3), 733–741.

Wang, S., and H. Tkalčić (2020), Seismic event coda-correlation's formation: Implications for global seismology, *Geophysical Journal International*, *222*(2), 1283–1294, doi:10.1093/gji/ggaa259.

Webb, S. C. (1998), Broadband seismology and noise under the ocean, *Reviews of Geophysics*, *36*(1), 105–142, doi:10.1029/97RG02287.

Weber, M., G. Silveira, and A. Schulze (2007), The COBO/CV-PLUME temporary seismic network. GFZ Data Services. Other/Seismic Network., doi:10.14470/4N7552467332.

Wessel, P., W. H. Smith, R. Scharroo, J. Luis, and F. Wobbe (2013), Generic mapping tools: Improved version released, *Eos, Transactions American Geophysical Union*, *94*(45), 409–410, doi:10.1002/2013EO450001.

White, R. S. (1984), Atlantic oceanic crust: Seismic structure of a slow-spreading ridge, *Geological Society Special Publication*, *13*, 101–111, doi:10.1144/GSL.SP.1984.013.01.09.

White, R. S., D. McKenzie, and R. K. O'Nions (1992), Oceanic crustal thickness from seismic measurements and rare earth element inversions, *Journal of Geophysical Research*, *97*(B13), 19,683, doi:10.1029/92JB01749.

Yang, H. Y., L. Zhao, and S. H. Hung (2010), Synthetic seismograms by normal-mode summation: A new derivation and numerical examples, *Geophysical Journal International*, *183*(3), 1613–1632, doi:10.1111/j.1365-246X.2010.04820.x.

Yao, H., X. Campman, M. V. de Hoop, and R. D. van der Hilst (2009), Estimation of surface wave Green's functions from correlation of direct waves, coda waves, and ambient noise in SE Tibet, *Physics of the Earth and Planetary Interiors*, *177*(1-2), 1–11, doi:10.1016/j.pepi.2009.07.002.

Yao, H., P. Gouédard, J. A. Collins, J. J. McGuire, and R. D. van der Hilst (2011), Structure of young East Pacific Rise lithosphere from ambient noise correlation analysis of fundamental- and higher-mode Scholte-Rayleigh waves, *Comptes Rendus - Geoscience*, *343*(8-9), 571–583, doi:10.1016/j.crte.2011.04.004.

Zha, Y., S. C. Webb, and W. Menke (2013), Determining the orientations of ocean bottom seismometers using ambient noise correlation, *Geophysical Research Letters*, *40*(14), 3585–3590, doi:10.1002/grl.50698.

Zha, Y., S. C. Webb, S. S. Wei, D. A. Wiens, D. K. Blackman, W. Menke, R. A. Dunn, and J. A. Conder (2014), Seismological imaging of ridge-arc interaction beneath the Eastern Lau Spreading Center from OBS ambient noise tomography, *Earth and Planetary Science Letters*, *408*, 194–206, doi:10.1016/j.epsl.2014.10.019.

Zhan, Z. (2019), Distributed acoustic sensing turns fiber-optic cables into sensitive seismic antennas, *Seismological Research Letters*, *91*(1), 1–15, doi:10.1785/0220190112.

Zhao, D., Y. Xu, D. A. Wiens, L. R. Dorman, J. Hildebrand, and S. Webb (1997), Depth extent of the Lau back-arc spreading center and its relation to subduction processes, *Science*, *278*(5336), 254–257, doi:10.1126/science.278.5336.254.

Zhu, G., H. Yang, J. Lin, and Q. You (2020), Determining the Orientation of Ocean-Bottom Seismometers on the Seafloor and Correcting for Polarity Flipping via Polarization Analysis and Waveform Modeling, *Seismological Research Letters*, *91*(2A), 814–825, doi:10.1785/0220190239.